Dissertation
submitted to the
Combined Faculty of Natural Sciences and Mathematics
of Heidelberg University, Germany
for the degree of
Doctor of Natural Sciences

Put forward by

Ragandeep Singh Sidhu
Born in: Chandigarh, India
Oral examination: 21.07.2021

Measurement of the bound-state beta decay of bare $^{205}Tl^{81+}$ ions at the ESR

Referees:	Apl. Prof. Dr. Yuri A. Litvinov
	Priv.-Doz. Dr. Adriana Pálffy
Supervisors:	Apl. Prof. Dr. Yuri A. Litvinov
	Prof. Dr. Klaus Blaum

Truth is the highest virtue,
but higher still is truthful living
- Guru Nanak

Dedicated to:
my parents

Late S. Rukmani Devi,
S. Harjit Singh Sidhu

Kurzfassung

Seit dem Bau des Experimentier Speicher Rings (ESR) bei GSI war die Messung des gebundenen Betazerfalls von $^{205}Tl^{81+}$-Ionen einer der wesentlichen physikalischen Prozesse, die untersucht werden sollten. Der gebundene Betazerfall (β_b) ist ein besonderer Zerfallskanal der schwachen Wechselwirkung, bei dem das Elektron in einem gebundenen atomaren Zustand bleibt, anstatt in das Kontinuum emittiert zu werden.

In dieser Doktorarbeit berichte ich über die erste Messung des gebundenen Betazerfalls für vollständig ionisierte $^{205}Tl^{81+}$-Ionen. Für das Experiment wurden $^{205}Tl^{81+}$-Ionen durch Projektilfragmentation eines ^{206}Pb-Primästrahls im FRagmentSeparator (FRS) produziert und von $^{205}Pb^{81+}$-Kontamination mittels der $B\rho$-ΔE-$B\rho$-Methode getrennt. Im ESR wurden die $^{205}Tl^{81+}$-Ionen unter Anwendung von Elektronenkühlung und stochastischer Kühlung akkumuliert und für unterschiedlich lange Zeiten gespeichert mit dem Ziel die Halbwertszeit zu bestimmen. Der ermittelte Wert beträgt 229 ± 36 Tage, was innerhalb von 3σ mit dem theoretischen Wert von 122 Tagen übereinstimmt.

Die Messung unterliegt zwei physikalischen Motivationen: Die erste ist mit dem LOREX Projekt (Abkürzung für LORandite EXperiment) verbunden, bei dem die Messung zur Bestimmung des Kernmatrixelementes für den solaren pp-Neutrino-Einfang durch den Grundzustand von ^{205}Tl in den mit 2.3 keV angeregten Zustand von ^{205}Pb benötigt wird. Mit der längeren Halbwertszeit wird das Kernmatrixelement kleiner, was für die Studien von solaren pp-Neutrinos von zentraler Bedeutung ist. Die zweite Motivation ist verbunden mit dem $^{205}Pb/^{205}Tl$-Paar als s-Prozess-Kosmochronometer. Im stellaren Medium kann ^{205}Tl in ionisierter Form existieren, und der β_b-Zerfall in den ersten angeregten Zustand von ^{205}Pb kann die Verringerung von ^{205}Pb durch Elektroneneinfang ausgleichen. Durch die längere Halbwertszeit des β_b-Zerfalls ist eine geringere Vernichtung von ^{205}Tl in stellaren Plasmen zu erwarten. Dies kann kritisch sein für das Verständnis der Entwicklung von ^{205}Pb im frühen Sonnensystem.

Abstract

Ever since the construction of the Experimental Storage Ring (ESR) at GSI, measurement of the bound-state beta decay of $^{205}Tl^{81+}$ ions was one of the main physics cases to be performed. Bound-state beta decay (β_b), is a particular weak interaction decay mode, in which the electron remains in a bound atomic state rather than being emitted into the continuum, which is favored in the case of highly-ionized atoms.

In this thesis, I report on the first measurement of the bound-state beta decay of fully-ionized $^{205}Tl^{81+}$ ions. For the experiment, $^{205}Tl^{81+}$ ions were produced via the projectile fragmentation of a primary ^{206}Pb beam in the FRagment Separator (FRS), which were well separated from the $^{205}Pb^{81+}$ contaminants by using the $B\rho$-ΔE-$B\rho$ technique. $^{205}Tl^{81+}$ ions were then accumulated, stochastically and electron cooled, and stored for different storage times in the ESR in order to determine the half-life. The obtained value is 229 $\pm$ 36 days which agrees within 3σ with the theoretically predicted value of 122 days.

The measurement is essential for two physics cases. The first one is linked with the LOREX project (acronym of LORandite EXperiment), wherein, the measurement is needed to determine the nuclear matrix element of the solar pp neutrino capture by the ground state of ^{205}Tl to the 2.3 keV excited state in ^{205}Pb. With the longer measured half-life, the nuclear matrix element will become smaller which is pivotal for the solar pp neutrino studies. The second physics case is associated with the $^{205}Pb/^{205}Tl$ pair as an s-process cosmochronometer. In stellar medium, ^{205}Tl can exist in the ionized form and β_b decay to the first excited state of ^{205}Pb can counter-balance the reduction of ^{205}Pb ions due to the electron capture process. Smaller destruction of ^{205}Tl is expected in the stellar plasmas due to the longer measured half-life of β_b decay. This is crucial for the clarification of the fate of ^{205}Pb in the early solar system.

Contents

Chapter 1

Introduction

1.1 A brief history

The history of the birth of radioactivity [1] can be traced back to the end of 19^{th} century when the French scientist Henri Becquerel in 1896 discovered the phenomenon while working with phosphorescent materials. More scientific studies with the span of time revealed that the radioactivity can be distinguished by the emitted particle as α, β or γ [2, 3, 4] radioactivity, when the natural radioactive substance is kept in the presence of an electric or magnetic field. Each of the three types of processes was found to entail a characteristic change in the state of some atomic nuclei. This was first realized by Ernest Rutherford [5], who took up the study of these radiations and their properties. α radiations [2] were identified as nuclei of helium, which were understood as fragments of nuclear matter which were thrown off to obtain a more stable structure. γ radiations [4] were identified as the electromagnetic radiations, which were emitted during motions within the systems of charges. They were also expected to be released whenever α or β process leaves the product nucleus in an excited state, requiring internal redistributions of the nucleons. β radiations [3] were identified as the emission of ordinary electrons, the understanding of which required a radical enlargement of conceptions about the underlying physical processes.

The emission of electrons from the nuclei [6] themselves in the decay was understood as the daughter and the parent nuclei differed in charge by one. But, there was no question for pre-existing electrons [7], waiting to be emerged from the nuclei as the nuclei were very well known to be composed of neutrons and protons. A revolution occurred in this field when L. Meitner *et al.* and later J. Chadwick [8] observed a continuous energy spectrum of the electrons emitted from the nucleus as shown in Figure 1.1.

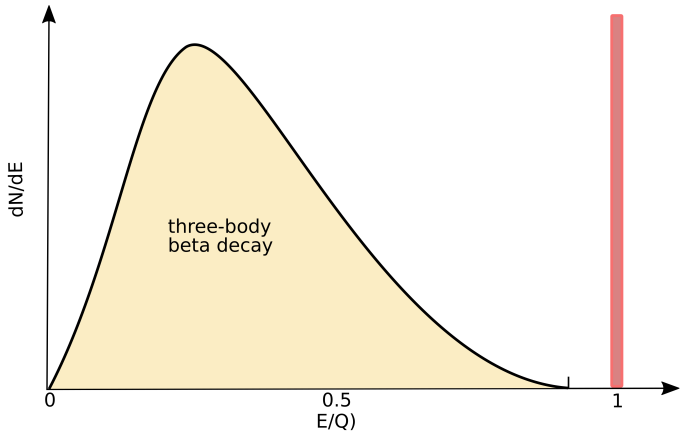

Figure 1.1: The yellow area represents the energy distribution of the emitted electrons in β^- decay, which is a three-body decay. In case of a two-body decay, the shape of the distribution would have been discrete as shown by the red rectangular bar.

The continuous spectrum was surprising as in a given β decay, the parent and the daughter nuclei have definite masses and thus a monoenergetic spectrum was expected for the emitted electrons. The problem was later put to a halt in 1930 [6, 7] when Wolfgang Pauli postulated a new particle of no electrical charge and spin 1/2. This particle was named "neutrino" by E. Fermi in 1932 and in 1934, he published the very first and famous "Fermi's theory of beta decay" [3]. In a β decay, the released energy (Q-value of the reaction) is distributed among: the electron, the neutrino, and the recoil of the daughter nucleus (this is merely a few keV and thus may be often neglected). From the continuous spectrum of the decay, the mass of the neutrino was assumed to be nil until the discovery of neutrino oscillations [9]. However, the journey of understanding the nature of β decay was always a roller coaster ride. In 1956, an experiment proposed by Tsung-Dao Lee & Chen-Ning Yang [10, 11] puzzled the physics community again. From the famously known as the Wu experiment, it was found that parity, which is conserved in the electromagnetic and strong interactions, is not conserved in the weak interactions.

In Fermi's basic theory [3], he explained the decay through a four-fermion interaction, involving a contact force with no range [6, 7]. However, the decay is better described by a non-contact force having a very short finite range. In 1968, Glashow, Salam, and Weinberg [12] unified the electromagnetic and weak interaction into the electroweak interaction. Thus, in a modern

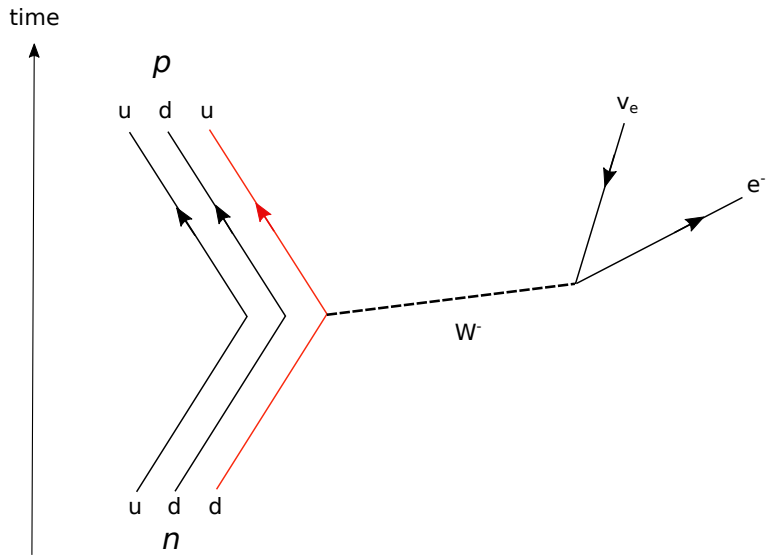

Figure 1.2: Leading order Feynman diagram of β^- decay. One of the d quarks constituting neutron transmutes into an u quark with an emission of W^- boson which then decays into an electron and an electron anti-neutrino.

description of the weak interaction, the decay process can be described in terms of the exchange of heavy $W^{\pm}$, Z bosons [13].

1.2 Beta decay

Beta decay is a radioactive process in which a parent nucleus decays via the emission of an electron e^- (or a positron e^+) and an electron anti-neutrino $\bar{\nu}_e$ (or an electron neutrino ν_e) through weak interaction (by conserving lepton number [13]). This can be expressed as:

for β^-:

$$n \rightarrow p + e^- + \bar{\nu}_e \quad \text{or} \quad d \rightarrow u + e^- + \bar{\nu}_e \ ,$$

where d and u are the down and up quarks [13], respectively (see Figure 1.2). The half-life of a free neutron is 10.1(7) minutes [14].

for β^+:

$$p \rightarrow n + e^+ + \nu_e \quad \text{or} \quad u \rightarrow d + e^+ + \nu_e \ .$$

Intermediate vector bosons $W^{\pm}$ are the weak force carriers in β^- and β^+ decays, respectively.

Since there is an overlap between the nucleus and the bound electron wave functions, there exists an alternative mode of β^+ decay, namely the electron capture (EC) [15], where a quasi-monochromatic electron neutrino is emitted.

for EC:

$$p + e^- \rightarrow n + \nu_e \quad \text{or} \quad u + e^- \rightarrow d + \nu_e \ .$$

The electron capture process can occur for both bound and free electrons (for e.g. in stellar plasmas) and is thus termed as the bound and free electron capture, respectively.

This thesis work concentrates on the further decay mode known as the bound-state beta decay (β_b). It was first proposed by Daudel *et al.* in 1947 [16, 17, 18]. In a β_b decay, the created electron stays bound in one of the free electron orbit and a quasi-monochromatic electron anti-neutrino is emitted.

for β_b:

$$n \rightarrow p + e_b^- + \bar{\nu_e} \quad \text{or} \quad d \rightarrow u + e_b^- + \bar{\nu_e} \ .$$

All of the above decays occur only if they are energetically allowed. It may be noted that β^- and β^+ are three-body β decay processes and EC and β_b are two-body β decay processes [13], which are also time-mirrored processes of each other.

1.3 Kinematics of β decay

For a beta decay to occur, the Q-value [19, 20, 21], which is defined as the difference between the parent and daughter atomic masses must be positive. Let us denote m as the atomic mass and m_N as the nuclear mass for the parent nucleus ${}^A_Z X$ decaying to the daughter nucleus ${}^A_{Z+1} Y$. The energetics of the decays are addressed in the following [19, 20, 21]

for β^-:

$$Q_{\beta^-} = \Big(m_N({}^A_Z X) - m_N({}^A_{Z+1} Y) - m_e - m_{\bar{\nu_e}} \Big) c^2 \ , \tag{1.1}$$

or

$$Q_{\beta^-} = \Bigg[\Bigg(m({}^A_Z X) - Z m_e + \sum_{n=1}^{Z} B_n/c^2 \Bigg) - \Bigg(m({}^A_{Z+1} Y) - (Z+1) m_e + \sum_{n=1}^{Z+1} B_n/c^2 \Bigg) - m_e - m_{\bar{\nu_e}} \Bigg] c^2 \ , \tag{1.2}$$

where B_n represents the binding energy of the n^{th} electron. Since the rest masses of ν_e and $\bar{\nu_e}$ are very small in comparison to the masses of other particles involved in a β decay, we can safely neglect them

$$Q_{\beta^-} = \Big(m(^A_Z X) - m(^A_{Z+1} Y)\Big)c^2 + \Big(\sum_{n=1}^{Z} B_n - \sum_{n=1}^{Z+1} B_n\Big) \ . \tag{1.3}$$

The second term in the above equation is the difference of the electron binding energies of the parent and the daughter nuclei. For low-Z nuclei, this difference is tiny [19] and could be neglected, but in the case of large-Z nuclei, it has a value of a few keV and must be incorporated for an accurate determination of the Q-value.

for β^+:

$$Q_{\beta^+} = \Big(m_N(^A_Z X) - m_N(^A_{Z-1} Y) - m_{e^+} - m_{\nu_e}\Big)c^2 \ , \tag{1.4}$$

or

$$Q_{\beta^+} = \Bigg[\Big(m(^A_Z X) - Zm_e + \sum_{n=1}^{Z} B_n/c^2\Big) - \Big(m(^A_{Z-1} Y) - (Z-1)m_e + \sum_{n=1}^{Z-1} B_n/c^2\Big) - m_{e^+} - m_{\nu_e}\Bigg]c^2 \ . \tag{1.5}$$

Assuming $m_e = m_{e^+}$,

$$Q_{\beta^+} = \Big(m(^A_Z X) - m(^A_{Z-1} Y) - 2m_e\Big)c^2 + \Big(\sum_{n=1}^{Z} B_n - \sum_{n=1}^{Z-1} B_n\Big) \ . \tag{1.6}$$

Thus, in the case of β^+ decay an additional threshold of $2m_e c^2$ is required for the decay to be exothermic.

for EC:

$$Q_{\rm EC} = \Big(m_N(^A_Z X) + m_e - B_e/c^2 - m_N(^A_{Z-1} Y) - m_{\nu_e}\Big)c^2 \ , \tag{1.7}$$

where B_e is the binding energy of the captured electron. Hence,

$$Q_{\rm EC} = \Bigg[\Big(m(^A_Z X) - Zm_e + \sum_{n=1}^{Z} B_n/c^2\Big) + m_e - \Big(m(^A_{Z-1} Y) - (Z-1)m_e + \sum_{n=1}^{Z-1} B_n/c^2\Big) - m_{\nu_e}\Bigg]c^2 - B_e \ . \tag{1.8}$$

By rearranging the terms,

$$Q_{\rm EC} = \Big(m(^{A}_{Z}X) - m(^{A}_{Z-1}Y)\Big)c^2 - B_e + \Big(\sum_{n=1}^{Z} B_n - \sum_{n=1}^{Z-1} B_n\Big) \ . \tag{1.9}$$

EC is a process which is very similar to β^+ decay [13] as the nuclear charge in both these decays decreases by one unit. However, if the difference in atomic mass is less than $2m_ec^2$, then only the electron capture process is energetically allowed [19, 21]. The kinematics for the bound-state beta decay will be discussed in details in Chapter 2.

1.4 Theory of β decay

Enrico Fermi [3, 6, 19, 22] developed the initial theory of β decay in 1934, wherein the neutrino assumption from Pauli was taken into consideration. In parallel to the quantum mechanical treatment of the electromagnetic theory, Fermi worked out the theory of weak interaction [13]. According to Fermi's golden rule, the probability $N(p)dp$ per unit time that an electron (or a positron) is emitted with momentum in the range p and $p + dp$ is given by [19, 21]

$$d\lambda = N(p)dp = \frac{2\pi}{\hbar} \mid H_{fi} \mid^2 \rho(E_0) \ , \tag{1.10}$$

where $\hbar$ is the Planck's constant, $\mid H_{fi} \mid$ is the matrix element for the transition and $\rho(E_0)$ is the density of the final states per unit energy, which can also be written as dn/dE_0. dn is the number of final states in the energy interval dE_0. The probability of the transition is more likely if the number of accessible final states is large. The matrix element of the transition, which depends weakly on energy, determines the overall magnitude of the decay probability. It can be expressed as the integral of the interaction O [6, 7] between the initial and final quasi-stationary states of the nuclear system:

$$H_{fi} = g \int \Psi_f^* O \Psi_i dV \ , \tag{1.11}$$

where the coupling constant g [13] determines the strength of the interaction. In the final state in β decay, we have the daughter nucleus and the leptons (electron or positron and anti-neutrino or neutrino)

$$\Psi_f^* = \psi_f^* \phi_e^* \phi_\nu^* \ . \tag{1.12}$$

The lepton wave functions have the usual free-particle form as they interact only weakly. Thus, the wave functions normalized within the nuclear volume

V are

$$\phi_e(\vec{r}) = \frac{1}{\sqrt{V}} e^{i\vec{p}\cdot\vec{r}/\hbar} \ , \tag{1.13}$$

$$\phi_\nu(\vec{r}) = \frac{1}{\sqrt{V}} e^{i\vec{q}\cdot\vec{r}/\hbar} \ , \tag{1.14}$$

where $\vec{p}$ and $\vec{q}$ are the linear momenta of the electron (or positron) and anti-neutrino (or neutrino), respectively. Since the leptonic wavelengths are many times the size of the nucleus [13], it is reasonable to expand the wave functions in a Taylor series. For an emitted electron, a typical kinetic energy of 1 MeV corresponds to an electron momentum $p = 1.4$ MeV/c [19]. For a nuclear radius of $r \approx 5$ fm, $pr/\hbar = 0.035 << 1$ and thus by considering only the first term in the expansion

$$e^{i\vec{p}\cdot\vec{r}/\hbar} = 1 + \frac{i\vec{p}\cdot\vec{r}}{\hbar} + ... \cong 1 \ , \tag{1.15}$$

$$e^{i\vec{q}\cdot\vec{r}/\hbar} = 1 + \frac{i\vec{q}\cdot\vec{r}}{\hbar} + ... \cong 1 \ . \tag{1.16}$$

This is known as the allowed approximation [6, 7]. For an electron, a pure plane wave approximation is too crude and the distortion of the electron wave function caused by interaction with the Coulomb potential of the daughter nucleus should be considered. Thus, an additional factor, the Fermi function $F(Z^{'}, p)$ [6, 7], is introduced, where $Z^{'}$ is the atomic number of the daughter nuclei. Thus, the transition matrix element becomes [21]

$$\mid H_{fi} \mid^2 = \frac{1}{V^2} F(Z^{'}, p) \mid g \int \psi_f^* O \psi_i \mid^2 = \frac{1}{V^2} F(Z^{'}, p) g^2 M^2 \ , \tag{1.17}$$

where the nuclear matrix element, M, describes the transition probability between the initial and the final nuclear states. In his theory, Fermi [3], in an analogy with the electromagnetic theory, took the vector form of the interaction explaining only the allowed β transitions. But with a proper relativistic treatment of β decay, the operator O can take five different mathematical forms for the Hamiltonian to be relativistically invariant [6, 7, 21]. These were identified as scalar S, pseudoscalar P, vector V, axial-vector A, and tensor T [6, 13]. Considering the maximal parity violation in β decay from the experiment of Wu [12], it was found that the electrons and anti-neutrinos exhibit polarization and were observed with a negative and a positive helicity, that is being left- and right-handed [13], respectively. This lead only the vector V and the axial-vector A contribute to the overall transition probability. Thus, we have [21]

$$\mid H_{fi} \mid^2 = \frac{1}{V^2} F(Z^{'}, p) \Big(G_V^2 M_F^2 + G_A^2 M_{GT}^2 \Big) \ , \tag{1.18}$$

where G_V and G_A are the vector and axial-vector coupling constants with G_A to be larger than G_V, and M_F and M_{GT} are the Fermi and Gamow-Teller matrix elements [13], respectively.

In the above treatment of the transition matrix element, the assumption of constant lepton wave functions over the nuclear volume results in nuclear matrix elements which are independent of the lepton energies and are termed as the allowed β transitions [6, 21]. Whereas, in some decays, it turns out that the angular momentum and parity selection rules prevent the allowed transitions. In such a case, the next terms in the plane wave expansions must be taken into account and the nuclear matrix element is no longer independent of the energy. These transitions are termed as forbidden [6] as they are less likely to occur as compared to the allowed transitions. The degree, to which a transition is forbidden, depends on how many terms have to be taken in the expression of the plane wave to find a non-vanishing nuclear matrix element (see Section 1.6).

To determine the density of states in the momentum space, let us consider an electron (or a positron) and an anti-neutrino (or a neutrino) emitted with momenta $\vec{p}$ and $\vec{q}$, respectively. The momentum volume in the space between two spheres of radius p and $p + dp$ is $4\pi p^2 dp$. Thus, the number of electrons confined to a nuclear volume V in the momentum range $p + dp$ is [19, 20, 21]

$$dn_e = \frac{4\pi p^2 dp V}{h^3} \quad , \tag{1.19}$$

where h^3 is the volume of a unit cell in the momentum space.
Similarly for anti-neutrinos

$$dn_\nu = \frac{4\pi q^2 dq V}{h^3} \quad , \tag{1.20}$$

and the number of final states having electron and anti-neutrino is

$$dn = (dn_e)(dn_\nu) = \frac{16\pi^2 V^2 p^2 q^2 dp dq}{h^6} \quad . \tag{1.21}$$

The total kinetic energy of the final state is $E_0 = Q = E_R + E_e + E_\nu$, where Q is the energy release in the decay, E_R is the recoil of the daughter nucleus, E_e is the electron kinetic energy and E_ν is the neutrino energy (including the rest mass). Recoil energy of the daughter nucleus is a few keV and can be neglected. For neutrino, from relativistic kinematics [21], $E_\nu^2 = q^2c^2 + m_\nu^2 c^4$ and $E_\nu dE_\nu = c^2 q dq$. For a constant E_e, $d/dE_0 = d/dE_\nu$. Hence, the density of final states becomes [21]

$$\frac{dn}{dE_o} = \frac{16\pi^2 V^2 p^2}{h^6} \sqrt{\frac{E_\nu^2 - m_\nu^2 c^4}{c^2}} \left(\frac{dp E_\nu}{c^2} \right) \quad . \tag{1.22}$$

On further simplification, we get

$$\frac{dn}{dE_o} = \frac{V^2}{4\pi^4\hbar^6c^3}p^2(E_0 - E_e)^2\sqrt{1 - \frac{m_\nu^2c^4}{(E_0 - E_e)^2}}dp \ . \tag{1.23}$$

The above expression reduces to a simpler form for $m_\nu \approx 0$. Thus, the partial decay probability of emitting an electron in an energy interval E_e, $E_e + dE_e$ and momentum interval p, $p + dp$ is [6, 21]

$$d\lambda = N(p)dp = \frac{1}{2\pi^3\hbar^7c^3}F(Z^{'},p)\Big(G_V^2M_F^2+G_A^2M_{GT}^2\Big)p^2(E_0-E_e)^2\sqrt{1 - \frac{m_\nu^2c^4}{(E_0 - E_e)^2}}dp \ . \tag{1.24}$$

This distribution describes the β decay spectrum, which vanishes for $p = 0$ and at the endpoint, where the maximum electron or positron energy is equal to the total decay energy. The total decay constant (considering $m_\nu \approx 0$) is given by the integral

$$\lambda = \frac{\ln 2}{t_{1/2}} = \frac{\Big(G_V^2M_F^2 + G_A^2M_{GT}^2\Big)}{2\pi^3\hbar^7c^3}\int_0^{p_{\max}} F(Z^{'},p)p^2(E_0 - E_e)^2dp \ , \tag{1.25}$$

$$\lambda = \frac{\ln 2}{t_{1/2}} = \frac{m_e^5c^4}{2\pi^3\hbar^7}\Big(G_V^2M_F^2 + G_A^2M_{GT}^2\Big)f(Z^{'},E_e^{\max}) \ . \tag{1.26}$$

The dimensionless quantity

$$f(Z^{'},E_e^{\max}) = \frac{1}{m_e^5c^7}\int_0^{p_{\max}} F(Z^{'},p)p^2(E_e^{\max} - E_e)^2dp \ , \tag{1.27}$$

is called the Fermi integral [3, 13] which depends on the charge of the daughter nucleus $Z^{'}$ and the maximum energy of the electron $E_e^{\max}$. For $E_0 >> 1$ $f(Z^{'},E_e) \approx E^5/30$ and thus the decay rate is $\propto E^5$. This is called the Sargent's rule [19]. We can rewrite the equation to be

$$f(Z^{'},E_e^{\max})t_{1/2} = \frac{2\pi^3\hbar^7}{m_e^5c^4}\frac{\ln 2}{\Big(G_V^2M_F^2 + G_A^2M_{GT}^2\Big)} \ . \tag{1.28}$$

The above quantity is called the ft-value [6, 7], which is a standard measure for the strength of β decay and yields the information about the nuclear matrix elements and the coupling constants.

1.5 Electron capture

Due to the overlap between the nucleus and the bound electron wave functions [6, 19, 21], there exist chances for the electrons to be absorbed by the nucleus. When such an absorption occurs, the energy spectrum of the emitted neutrino is not continuous, but is quasi-monoenergetic with $Q = E_0 \approx E_\nu$ (E_R is a few keV and is thus neglected) [19]. As soon as the capture occurs, the atomic shell rearranges, leading to the emission of X-rays or Auger electrons [19]. In some cases, the daughter nucleus is produced in an excited state and a series of γ rays may be emitted. For the electron capture process (EC), the decay rate can be written as [21]

$$\lambda = \frac{2\pi}{\hbar} \mid H_{fi} \mid^2 \frac{dn_\nu}{dE_0} \quad . \tag{1.29}$$

The density of final states, in this case, is given by

$$\frac{dn_\nu}{dE_0} = \frac{Vq^2}{2\pi^2\hbar^3}\frac{dq}{dE_0} = \frac{VE_\nu^2}{2\pi^2\hbar^3c^3} \quad , \tag{1.30}$$

where $E_\nu = qc$ (assuming $m_\nu \approx 0$). In EC, the total wave functions before and after the decay are given by $\Psi_i = \psi_i\phi_e$ and $\Psi_f = \psi_f\phi_\nu$. It is likely that an electron is captured from the atomic K-shell [6] as its wave function has the largest overlap with the nucleus [13]. But, since the electron is bound in this case, it cannot be represented with the plane wave approximation as considered in Section 1.4. Here, we can approximate ϕ_e by the electron wave function ϕ_K of the K-orbit at the location of the nucleus [21]

$$\phi_e(\vec{r}) = \phi_K(\vec{r}) = \frac{1}{\sqrt{\pi}}\left(\frac{Z}{a_0}\right)^{3/2} e^{-Zr/a_0} \quad , \tag{1.31}$$

$$\phi_e(\vec{r}) \approx \phi_K(0) = \frac{1}{\sqrt{\pi}}\left(\frac{Z}{a_0}\right)^{3/2} = \frac{1}{\sqrt{\pi}}\left(\frac{Zm_ee^2}{\hbar^2}\right)^{3/2} \quad , \tag{1.32}$$

where Z is the atomic number of the parent nucleus, a_0 is the Bohr radius, $a_0 = \hbar^2/(m_ee^2)$. The plane wave approximation is used again for the neutrino wave function and thus the decay constant for the allowed electron capture process is

$$\lambda_K = \frac{2\pi}{\hbar}\Big(G_V^2M_F^2 + G_A^2M_{GT}^2\Big)\frac{1}{\pi V}\left(\frac{Zm_ee^2}{\hbar^2}\right)^3\frac{VE_\nu^2}{2\pi^2\hbar^3c^3} \quad . \tag{1.33}$$

On simplifying the above expression

$$\lambda_K = \frac{Z^3m_e^3e^6}{\pi^2\hbar^{10}c^3}\Big(G_V^2M_F^2 + G_A^2M_{GT}^2\Big)E_\nu^2 \quad . \tag{1.34}$$

The nuclear matrix element of EC is identical to that of β^+ decay [13] as the very same nuclear states are involved. In fact, there comes an additional factor of 2 in the decay constant since either of the two electrons can be captured from the K-shell. Z^3 dependence of the decay constant makes EC greatly favored over β^+ for a heavy nuclei [19]. Here, the spin orientation of the captured electron is not taken into account, which can significantly modify the decay rate in highly-ionized ions.

As mentioned before, β_b and EC are time-mirrored processes of each other and thus, the probability of allowed K-capture of an electron in EC process is similar to that of the probability of creation of an electron in the K-shell in β_b process. A more quantitative discussion of the probability of β_b decay can be found in Section 2.2.

1.6 Selection rules

As discussed in the theory of β decay [19, 20, 21], we can subdivide them into allowed and forbidden transitions [6, 19] depending on the terms considered in the plane wave approximation. The Taylor series expansion of the plane wave is

$$e^{i\vec{p}\cdot\vec{r}/\hbar} = 1 + \frac{i\vec{p}\cdot\vec{r}}{\hbar} + ... \quad . \tag{1.35}$$

The first order in the expansion corresponds to the allowed transitions, where the orbital angular momentum carried by the leptons is null. The higher orders ($l \neq 0$) are called l^{th}-order forbidden transitions [6].

1) Allowed transitions:

Electron and neutrino have an intrinsic spin 1/2. From the law of conservation of total angular momentum

$$\vec{I_p} = \vec{I_d} + \vec{L} + \vec{S} \ ,$$

where $\vec{I_p}$, $\vec{I_d}$ are the angular momenta of the parent and the daughter nuclei, respectively, and $\vec{L}$, $\vec{S}$ are the orbital and the spin angular momenta of the electron neutrino pair. The change in the angular momentum is given by $\vec{L}+\vec{S}$, where $\vec{S} = 0$ or 1 due to coupling of the spins of electron and neutrino. For the allowed transitions, $\vec{L} = 0$ as we replaced the electron and neutrino wave functions with their values at the origin [21]. In this case, they do not carry any orbital angular momentum. Transitions with $\vec{L} = 0$ and $\vec{S} = 0$ (when electron and neutrino spins are anti-aligned) are called Fermi transitions [3] and with $\vec{L} = 0$ and $\vec{S} = 1$ (when electron and neutrino spins are aligned) are

called Gamow-Teller (GT) transitions [13]. For an electron and a neutrino carrying no orbital angular momentum, the initial and the final parity (π) must be the same as the parity is associated with the momentum l as $(-1)^l$. Thus, for the allowed β decay, the selection rules are

$$\Delta\vec{I} = 0 \text{ and } \pi_i = \pi_f \quad \text{for Fermi transitions,} \tag{1.36}$$

$$\Delta\vec{I} = 0, \pm 1 \text{ and } \pi_i = \pi_f \quad \text{for Gamow-Teller transitions (except for } 0^+ \rightarrow 0^+\text{).} \tag{1.37}$$

2) Forbidden transitions:

In the case, when the leptons carry angular momentum, $\vec{L} \neq 0$ [19, 20, 21]. The $\vec{p}\cdot\vec{r}$ term in the plane wave expression is of the order of 10^{-2} and it enters as a square into the equation for the decay constant [13]. Thus, the decay constant for each l^{th}-order forbidden transition is suppressed by a factor of 10^4 compared to the $(l-1)^{th}$-order forbidden transition. $\vec{L} = 1$, corresponds to 1^{st} forbidden transitions ($\vec{L} = 2$, 2^{nd} forbidden transitions and so on) which can further be classified as Fermi 1^{st} forbidden transitions (for $\vec{S} = 0$) and Gamow-Teller 1^{st} forbidden transitions (for $\vec{S} = 1$) [6, 13]. For 1^{st} forbidden transitions, the selection rules are [19]

$$\Delta\vec{I} = 0, \pm 1 \text{ and } \pi_i \neq \pi_f \quad \text{for Fermi transitions,} \tag{1.38}$$

$$\Delta\vec{I} = 0, \pm 1, \pm 2 \text{ and } \pi_i \neq \pi_f \quad \text{for Gamow-Teller transitions (except for } 0^+ \rightarrow 0^+\text{).} \tag{1.39}$$

For $\Delta I = \pm 2$, it is a pure GT transition and it is termed as unique 1^{st} forbidden transition. For $\Delta I = 0, \pm 1$, the transition type is not unambiguous. Such transition is then called non-unique 1^{st} forbidden transition.

Chapter 2

Bound-state beta decay

2.1 Introduction

In an ordinary beta decay [3, 6, 7], a neutron transforms into a proton and an electron and a corresponding electron anti-neutrino are emitted into the continuum state. However, in the case of a bound-state beta decay β_b [16, 17, 18, 23], a neutron transforms into a proton, an electron anti-neutrino is produced in a free state, and an electron is created in a bound atomic state, as shown in Figure 2.1. The possibility of a bound-state beta decay was first pointed out by Daudel *et al.* [16, 17, 18] in 1947 and the first detailed theory was given by Bahcall [23] in 1961. After almost three decades, the first direct experimental observation of β_b was seen in the case of bare ^{163}Dy [24, 25] ions in 1992 at GSI Helmholtzzentrum für Schwerionenforschung (the facility is described in details in Chapter 4) in Darmstadt, Germany.

2.2 Theory of β_b decay

In neutral atoms, the lowest electronic orbitals are occupied and thus, due to the Pauli exclusion principle, the probability of the bound-state beta decay is tiny. Whereas, in the case of Highly Charged Ions (HCIs), inner electronic orbitals are vacant and thus, the bound-state beta decay becomes a possible decay path. The decay rate for β_b [16, 17, 18] is given by

$$\lambda_{\beta_b} \propto \sum_x n_x \left|M_{fi}\right|^2 \left|\Psi_e^x(R)\right|^2 E_{\bar{\nu_e}}^2 \quad , \tag{2.1}$$

where n_x is the number of electron vacancies at orbital x, $\Psi_e^x(R)$ is the wave function of the electron at orbital x, and $E_{\bar{\nu_e}} = E_0 - m_0c^2 + \epsilon$ is the total available energy for the quasi-monochromatic anti-neutrino emitted in the

continuum, with ϵ being the binding energy of the level in which the electron is created. For the creation of an electron in the K-shell (for fully-ionized atom) [16, 17, 18]

$$\lambda_{\beta_b} \propto Z^3 \left|M_{fi}\right|^2 E_{\bar{\nu}_e}^2 \quad , \tag{2.2}$$

or

$$\lambda_{\beta_b} \propto Z^3 \left|M_{fi}\right|^2 \left(E_0 - m_0c^2 + \epsilon_K\right)^2 \quad . \tag{2.3}$$

1. The probability of the creation of an electron increases as the cube of the atomic number of the daughter nucleus (Z^3). For the case of β_c, the rate varies linearly with Z. Thus, β_b is maximized for higher Z.

2. E^2 dependence of λ_{β_b}, as compared to the E^5 dependence from the Sargent's rule, reveals that for the same Z, β_b is more probable for smaller Q-values.
After a careful quantum treatment, the decay rate [16] can be written as

$$\lambda_{\beta_b} = 2\pi \left|H_{fi}\right|^2 \rho \quad . \tag{2.4}$$

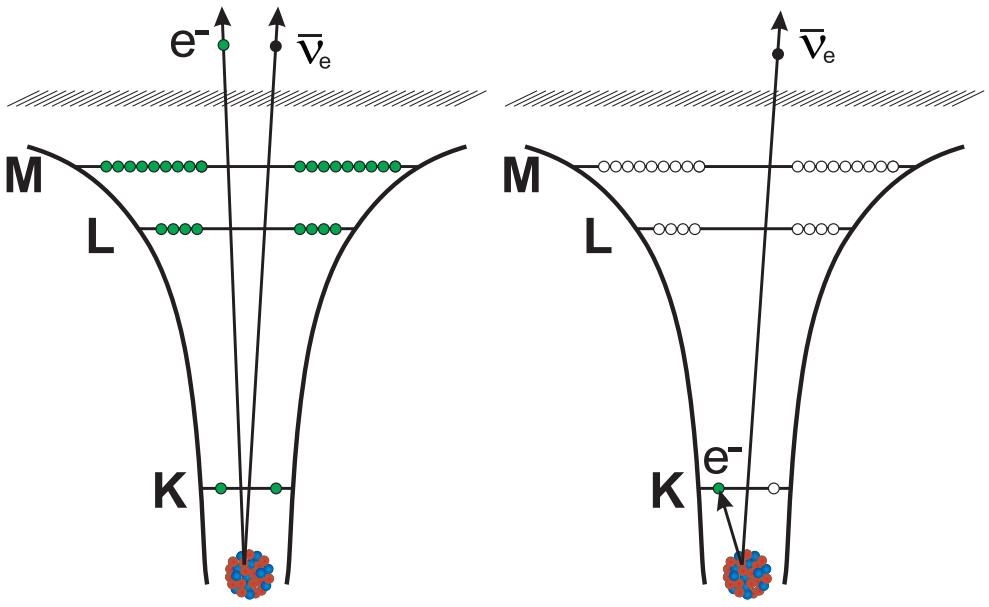

Figure 2.1: Left: β_c decay in which both the electron and anti-neutrino are emitted into the continuum. Right: β_b decay in which the electron is created in one of the vacant orbitals and the anti-neutrino is emitted into the continuum.
Source: Taken with permission from [26].

As discussed in Section 1.4, the transition matrix element consists of hadronic (nuclear) and leptonic contributions [13], wherein the nuclear matrix element contains contributions from the vector V and the axial-vector A parts of the weak interaction [6, 13]. It can be expanded and written in the form [16]

$$H = g\Big[(\Psi_p^* O \Psi_n^*)(\phi_e^* \phi_\nu) - (\Psi_p^* O \vec{\alpha} \Psi_n^*)(\phi_e^* \vec{\alpha} \phi_\nu)\Big] \ , \tag{2.5}$$

where O and O^* are the operators which transform a neutron into a proton and vice versa, g is the strength of the interaction, $\vec{\alpha}$ is the Dirac's matrix vector [6] and the rest are the hadronic and leptonic wave functions as defined before. The rate can be written as [16, 17]

$$\lambda_{\beta_b} = \frac{g^2}{2\pi^2} \int d\omega_n \sum_{jlm} \left| \int \Big[(\Psi_p^* O \Psi_n^*)(\phi_e^* \phi_\nu) - (\Psi_p^* O \vec{\alpha} \Psi_n^*)(\phi_e^* \vec{\alpha} \phi_\nu)\Big] d\tau \right|^2 q^2 \ , \tag{2.6}$$

where $\int d\omega_n$ covers all the directions of the emitted anti-neutrino with momentum $\vec{q}$ and $\sum_{jlm}$ accounts for the quantum numbers of the electron.

In the case of allowed transitions [6], the second part of the matrix element can be neglected and for the wave functions to be constant inside the nucleus, the remaining term can be taken outside the integral [16]

$$\lambda_{\beta_b} = \frac{g^2}{2\pi^3} \left|M_{fi}\right|^2 n_K \frac{\pi}{4} g_K^2 \Big(E_0 - m_0 c^2 + \epsilon_K\Big)^2 \ , \tag{2.7}$$

where n_K is the number of unoccupied places in the K-shell (it is 2 for fully-ionized atoms) and g_K^2 is the radial part of the Dirac function for a value of the argument equal to the nuclear radius R [21]. By limiting the expression of g_K^2 to the first non-zero term and by using the Born's approximation [27]

$$\lambda_{\beta_b} = \frac{g^2}{2\pi^3} \left|M_{fi}\right|^2 n_K \phi_K \Big(E_0 - m_0 c^2 + \epsilon_K\Big)^2 \ , \tag{2.8}$$

where ϕ_K is the K-shell electron wave function, which scales as Z^3. To understand the relative frequency of β_b w.r.t. β_c, their ratio can be examined. The ratio of the probability of an electron created in the K-shell to the continuum emission is given by [16]

$$\frac{\lambda_{\beta_b}(K)}{\lambda_{\beta_c}} = n_K \frac{\phi_K \Big(E_0 - m_0 c^2 + \epsilon\Big)^2}{f(Z, E_0)} = n_K \sigma(Z, E_0) \ , \tag{2.9}$$

where $f(Z, E_0)$ is the Fermi function [3, 6] for β_c and E_0 (or the Q_{β_b}-value) is the total energy released in the process. It may be noted that the above

ratio [28] is independent of the nuclear matrix element, which enables one to calculate the bound-state decay rate of a nucleus if its continuum decay rate is known. Also, $\sigma(Z, E_0)$ depends on two parameters: Z and E_0.

In the above treatment, fully-ionized atoms were considered with the creation of an electron in the K-shell. It was generalized to ionized atoms (may or may not be fully-ionized) by Bahcall (in 1961) [23] and the relative frequency of bound-state to continuum-state beta decay is given by [23]

$$\frac{\lambda_{\beta_b}}{\lambda_{\beta_c}} \approx n_f \frac{E_{\bar{\nu}_e}^2 \left|M_{fi}\right|^2}{f(Z, E_0)} \approx n_f (E_0 - 1)^2 \frac{(\alpha Z)^2}{n^3 f(Z, E_0)} \quad , \tag{2.10}$$

where n_f is the number of unoccupied places in the lowest unoccupied atomic orbit with the principal quantum number $n(\lambda_{\beta_b})$ and α is the fine structure constant.

2.3 Kinematics of β_b decay

For fully-ionized atoms, the Q-value for β_b decay into the K, L,... shell is given by

$$Q_{\beta_b}(Z \to Z+1) = \Big[m_N({}^A_Z X) - m_N({}^A_{Z+1} Y) - m_e - \mid B_e^{K,L,\cdots} \mid /c^2 - m_{\bar{\nu_e}} \Big] c^2 \quad , \tag{2.11}$$

where $\mid B_e^{K,L,\cdots} \mid$ is the binding energy of the created electron in the K, L,... shell of the hydrogen-like (H-like) daughter atom and the rest of the symbols carries the same definition as before.

$$Q_{\beta_b} = \Bigg[\Bigg(m({}^A_Z X) - Z m_e + \sum_{n=1}^{Z} B_n/c^2 \Bigg) - \Bigg(m({}^A_{Z+1} Y) - (Z+1) m_e + \sum_{n=1}^{Z+1} B_n/c^2 \Bigg) - m_e - \mid B_e^{K,L,\cdots} \mid /c^2 - m_{\bar{\nu_e}} \Bigg] c^2 \quad . \tag{2.12}$$

By neglecting the mass of the anti-neutrino and after rearranging the terms we get

$$Q_{\beta_b} = \Big((m({}^A_Z X) - m({}^A_{Z+1} Y) \Big) c^2 - \mid B_e^{K,L,\cdots} \mid - \Big(\sum_{n=1}^{Z+1} B_n - \sum_{n=1}^{Z} B_n \Big) \quad , \tag{2.13}$$

where the first term stands for Q_{β_c}, which is the Q-value of the continuum beta decay β_c [6]. The above expression can be rewritten as

$$Q_{\beta_b}^{K,L}(Z \to Z+1) = Q_{\beta_c} - \mid \Delta B_e \mid + \mid B_e^{K,L,\cdots} \mid \quad , \tag{2.14}$$

where $\mid \Delta B_e \mid$ is the difference of the total binding energies of the neutral daughter and parent atoms. In the case of HCIs, containing no or a few electrons, β_b is energetically possible if the condition

$$\mid B_e^{K,L,\cdots} \mid > \mid Q_{\beta_c} \mid + \mid \Delta B_e \mid \ , \tag{2.15}$$

is fulfilled, where of course the atoms are stable in their neutral state ($Q_{\beta_c} < 0$).

Chapter 3

Bound-state beta decay in ^{205}Tl ions

3.1 Motivation

Ever since the construction of the Experimental Storage Ring (ESR) [29, 30], measurement of the bound-state beta decay [31, 32, 33] of $^{205}Tl^{81+}$ ions was one of the main physics cases to be performed. Very soon after the first direct experimental observation of β_b decay in the case of fully-ionized ^{163}Dy ions [24, 25] in 1992, the proposal to measure the β_b decay in bare ^{205}Tl ions was submitted and approved with the "highest physics priority". But owing to the exceedingly poisonous nature of ^{205}Tl vapors, it was hesitated to accelerate ^{205}Tl ions from the ion-source. Hence, at that time it was forced to cancel or at least to shift the experiment for an unknown time span.

After almost two decades, with the continuous development of GSI accelerator facilities (see Chapter 4), it became possible to produce and separate sufficient amount of bare ^{205}Tl ions via the projectile fragmentation technique. In 2015, the proposal was evaluated by the European Research Council within the ERC Consolidator Grant application ASTRUm (Astrophysics with Stored Highly Charged Radionuclides) [34]. The physics case was found to be outstanding and the funding was approved. In 2017, the proposal [35] was again submitted to the General Program Advisory Committee (G-PAC) of GSI, wherein the experiment was granted grade "A" and 21 shifts i.e. 7 days (including the shifts for beam setting) of the beam time were granted for the experiment.

Apart from the nuclear structure aspects, the measurement of the bound-state beta decay of fully-ionized ^{205}Tl ions is motivated by two astrophysics cases. The first one is linked with the LOREX project (acronym of LORan-

dite EXperiment) [36, 37] wherein the measurement is needed to determine the nuclear matrix element of the solar pp neutrino capture by the ground state of ^{205}Tl to the 2.3 keV excited state in ^{205}Pb. This capture reaction has by far the lowest threshold (E_{ν_e} >53 keV) [36, 37]. The second physics case is associated with the ^{205}Pb/^{205}Tl pair as an s-process cosmochronometer [38]. In stellar medium, ^{205}Tl can exist in the ionized form and β_b decay to the first excited state of ^{205}Pb can counter-balance the reduction of ^{205}Pb ions due to the electron capture process (discussed in Section 3.1.2). The measurement is thus crucial for the clarification of the fate of ^{205}Pb in the early solar system [35].

3.1.1 The flux of solar pp neutrinos

The Sun is the only star in our solar system. In the past 5 billion years, it has produced a lot of energy through fusion reactions. As a result, neutrinos are produced and emitted from the Sun's interior [39]. The main contribution ($\sim$ 86%) comes from the proton-proton reaction [39]

$$p + p \rightarrow d + e^+ + \nu_e \ .$$

Other contributions include: ^{7}Be neutrinos, CNO neutrinos, ^{8}B neutrinos, etc [39]. The spectroscopy of solar neutrinos provides important information about the solar structure and is an important tool to verify and constrain solar models [40].

Accounting for most of the solar neutrinos, pp neutrinos are difficult to detect on earth owing to their low energy. Till date, there have been various neutrino projects [41] which aimed to measure and study solar neutrinos. LOREX (LORandite EXperiment) [36, 37] is the last remaining geochemical project which aims at determining the long-time average (over 4.31(2) million years Myr) of the solar pp neutrino flux ϕ_ν via the neutrino capture reaction. The capture of solar pp neutrinos ($0 \leq E_{\nu_e} \leq 420$ keV) transforms the nucleus ^{205}Tl ($I^\pi = 1/2^+$) into ^{205}Pb ($I^\pi = 5/2^-$, $t_{1/2}$ = 17.3(7) Myr), and according to the selection rules, predominantly populating the first excited state (E^* = 2.3 keV, $I^\pi = 1/2^-$)

$$^{205}\mathrm{Tl} + \nu_e(\geq 53 \text{ keV}) \rightarrow {}^{205}\mathrm{Pb}^*(E^* = 2.3 \text{ keV}) + e^- \ .$$

The energy threshold for this reaction amounts to $E \geq 53$ keV, and is by far the lowest threshold for any known neutrino induced nuclear reaction. We can safely restrict ourselves to the capture of solar pp neutrinos as their flux is orders of magnitude larger than the flux of neutrinos from other reactions [39] (see Figure 3.1). The corresponding threshold for capturing solar pp

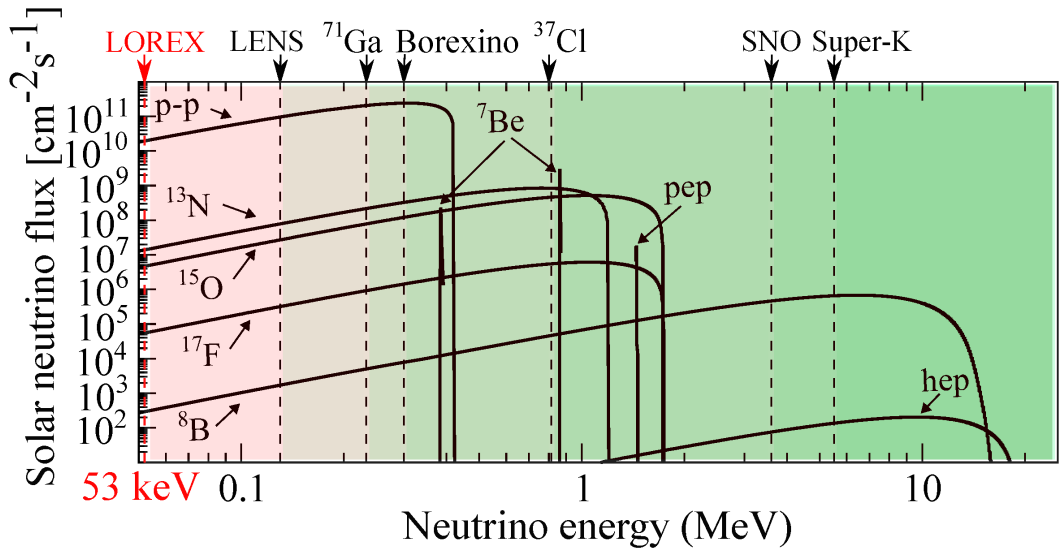

Figure 3.1: Solar neutrino flux vs neutrino energy. The LOREX project aims at extending the detection range down to 53 keV.
Courtesy: Dr. R. J. Chen.

neutrinos by ^{71}Ga nuclei (GALLEX and SAGE experiments [41]) amounts to $E \geq 233$ keV.

The geochemical experiment using ^{205}Tl was proposed by Freedman [42] in 1976. Along with the motivation to solve the solar neutrino problem, an international collaboration LOREX was formed by Pavićević in 1986. The solar neutrino problem was solved around the year 2002 with the discovery of neutrino oscillations [9] by the SNO and SKO experiments [41]. At present, the BOREXINO [43, 44] and the LOREX are the only active experiments which aim to precisely [44] measure the solar neutrino flux.

Lorandite is the Tl-bearing mineral ($TlAsS_2$), which is amply available in the mine of Allchar (FYR Macedonia). The average neutrino flux ϕ_ν over the exposure time a (age of lorandite since its mineralization) follows from the common activation equation [36, 37]

$$\phi_\nu = N^{-1}(T - B)(\sigma\epsilon)^{-1}\lambda[1 - \exp(-\lambda a)]^{-1} \quad , \tag{3.1}$$

where N is the total number of ^{205}Tl atoms, T is the total number of ^{205}Pb atoms, B is the background induced number of ^{205}Pb atoms (obtained mainly via $^{205}\mathrm{Tl}(\mu p, n)^{205}\mathrm{Pb}$ reaction [36, 37]), σ is the neutrino capture cross section, ϵ is the overall detection efficiency, $\lambda = 4.68{\times}10^{-8}$/yr is the decay constant of neutral ^{205}Pb, and $a = 4.31(2)$ Myr [36, 37] is the age of

Figure 3.2: Lorandite collected from the mine Allchar and transported to GSI, Darmstadt. To avoid the background induced ^{205}Pb atoms, Lorandite will be transferred to Felsenkeller underground laboratory, Dresden.
Courtesy: Prof. G. Amthauer.

lorandite. This finally renders the mean solar pp neutrino flux, i.e. the mean luminosity of the Sun during the last 4.31(2) million years, the geological age a of lorandite [36, 37].

For the determination of the mean solar pp neutrino flux, the solar pp neutrino capture cross section transmuting ^{205}Tl to ^{205}Pb has to be determined. According to the β decay selection rules, the neutrino is captured in the 2.3 keV excited state in ^{205}Pb. Measurement of the bound-state beta decay of $^{205}Tl^{81+}$ ions to $^{205}Pb^{81+}$ ions is the only direct method [35] that can be employed as this decay shares the same nuclear transition matrix element with the neutrino capture process.

3.1.2 ^{205}Pb/^{205}Tl pair as an s-process cosmochronometer

The short-lived radioactivities (SLRs) are radioactive nuclei with half-lives ranging from 1 Myr to 100 Myr. Their abundance in the early solar system is known from excesses of their daughter isotopes in primitive meteorites that correlate with the abundance of stable isotopes of the parent elements. Up to now, roughly ten such SLRs have been confirmed and their abundances relative to their stable reference isotope inferred [45]. Among these, ^{205}Pb [38] is unique SLR as it is the only purely slow neutron capture process

(s-process) [46] SLR. The slow neutron capture process (s-process) [46] and the rapid neutron capture process (r-process) [47] are responsible for the production of the majority of the heavy elements beyond iron.

The study of a short-lived s-process chronometer is decisive for nuclear astrophysics as it provides estimates independent of the model, of the time interval between the solidification of material in the solar system and the last s-process nucleosynthesis events contributing to the elemental abundances of the solar system [38]. Nucleosynthesis activity just prior to the Sun's birth and the circumstances of solar system formation are constrained by the abundance of an SLR relative to a stable reference isotope. In particular, the pivotal quantity is the SLR to reference isotope ratio compared to the value expected from the continuous galactic nucleosynthesis [48]. If there exists an agreement between the ratios, then no special circumstances are required to elucidate the SLRs abundance since the solar system simply inherited it from the interstellar medium (ISM) [48, 49]. If the abundance ratio exceeds the expected value, then an input from a special stellar source just prior to the Sun's birth is necessary.

The expected ratio for radioactive ^{205}Pb and stable ^{204}Pb, which are both secondary nucleosynthesis species, in the ISM is [45]

$$\frac{N_{^{205}\mathrm{Pb}}}{N_{^{204}\mathrm{Pb}}} = (k+2)\frac{P_{^{205}\mathrm{Pb}}}{P_{^{204}\mathrm{Pb}}}\frac{\tau}{T} \quad , \tag{3.2}$$

where $N_{^{205}\mathrm{Pb}}$ and $N_{^{204}\mathrm{Pb}}$ are the ISM abundances of ^{205}Pb and ^{204}Pb, respectively, $P_{^{205}\mathrm{Pb}}/P_{^{204}\mathrm{Pb}}$ is the production rate ratio of the two species at their stellar source, τ is the mean life of ^{205}Pb, and T is the age of the galactic disk ($\sim$ 8.5 billion years). k is the infall parameter in Clayton's standard galactic chemical evolution model [50] with a typical value in the range from 1 to 3. From equation 3.2, it is clear that the ISM abundance ratio is proportional to the production ratio in the s-process.

In stellar plasmas, the ground and the 2.3 keV excited states in ^{205}Pb are thermally populated. Due to the weak-decay selection rules (see Section 1.6), the electron capture decay of the 2.3 keV excited state is expected to be significantly faster than the electron capture decay of the ground state ($t_{1/2}$ = 17.3(7) Myr). This raised concern for the validity of the ^{205}Pb chronometer as $P_{^{205}\mathrm{Pb}}/P_{^{204}\mathrm{Pb}}$ might be strongly affected by it [51]. As a consequence, the production of ^{205}Pb in the s-process could be dramatically reduced [52]. However, in stellar plasmas, ^{205}Tl can exist in highly-ionized form (with a few or no electrons). Yokoi *et al.* [53] pointed out that the bound-state beta decay of $^{205}\mathrm{Tl}^{81+}$ [54, 55] could counter-balance the electron capture of ^{205}Pb and keep the ^{205}Pb production high. Current s-process models [46], by using theoretical estimates for the rate of ^{205}Tl bound-state beta decay,

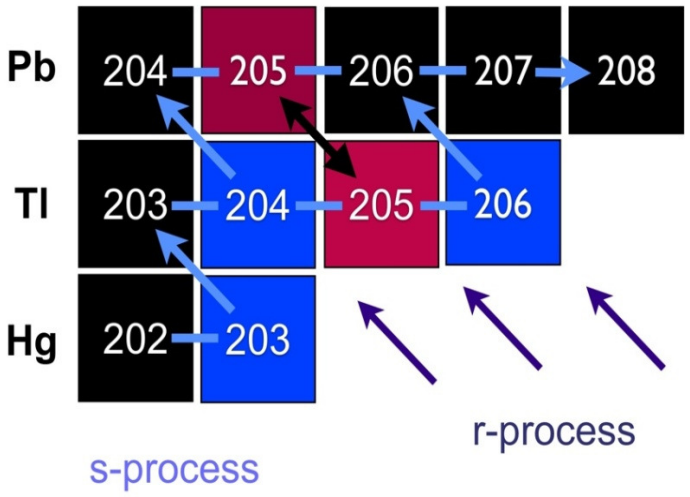

Figure 3.3: The s-process path in the Pb-Tl region.
Courtesy: Prof. Yu. A. Litvinov.

provide $P_{^{205}\mathrm{Pb}}/P_{^{204}\mathrm{Pb}}$ value near unity. Hence, due to the importance of the ^{205}Pb chronometer an experimentally determined value for the rate of ^{205}Tl bound-state beta decay is crucial to clarify the plausibility for the source of the live ^{205}Pb in the early solar system.

3.2 Kinematics of β_b decay in $^{205}\mathrm{Tl}^{81+}$ ions

The neutral ^{205}Tl atom is stable but shall decay by bound-state beta decay if all or most of its electrons are stripped off. For fully-stripped $^{205}\mathrm{Tl}^{81+}$ ions, β_b decay occurs from the ground state of $^{205}\mathrm{Tl}^{81+}$ ($I^\pi = 1/2^+$) with an almost 100% branching ratio to the first excited state of $^{205}\mathrm{Pb}^{81+}$ ($E^* = 2.3$ keV, $I^\pi = 1/2^-$) with the created electron bound in the K-shell of $^{205}\mathrm{Pb}^{81+}$ (see Figure 3.4). This is a non-unique first-forbidden transition [35].

The Q_{β_b} for bare $^{205}\mathrm{Tl}^{81+}$ ions is given by

$$Q_{\beta_b}(\text{bare} \rightarrow \mathrm{K}, E^*) = -Q_{\mathrm{EC}} - \mid \Delta B_e \mid - \mid E^* \mid + \mid B_K \mid \ , \qquad (3.3)$$

where Q_{EC} is the Q-value for the EC decay from the ground state of neutral ^{205}Pb atom to the ground state of neutral ^{205}Tl atom, ΔB_e is the difference

of the sum of the binding energies of all electrons in neutral ^{205}Tl and ^{205}Pb atoms, $E^* = 2.3$ keV is the excitation energy of the ^{205}Pb nucleus, and B_K is the K-shell binding energy of the created electron in the H-like ^{205}Pb daughter atom. With $Q_{\rm EC} = 50.5(5)$ keV, $\Delta B_e = 17.35$ keV, $B_K = 101.32$ keV and $E^* = 2.329$ keV one obtains

$$Q_{\beta_b}(\text{bare} \rightarrow \text{K}, E^*) = +31.14 \text{ keV}.$$

It shall be noted that the creation of the electron in the L-shell is energetically prohibited as $B_L = 24.94$ keV and $Q_{\beta_b}(\text{bare} \rightarrow \text{L}, E)$ = -42.91 keV.

The $\log(ft)$ value of the unknown nuclear matrix element for this transition is estimated to be [54]

$$\log(ft) \text{ (g.s. of } ^{205}\text{Tl} \rightarrow ^{205}\text{Pb}^*(2.3 \text{ keV})) = 5.4,$$

where a large error margin of about a factor of 3 shall be taken into account. Hence, one derives for bare ^{205}Tl^{81+} ions a half-life of about $t_{1/2}(\beta_b) = 122$ days, or a decay probability in the ^{205}Tl rest frame of $\lambda_{\rm CM}(\beta_b) = \ln 2/t_{1/2} = 6.6 \times 10^{-8}$ s^{-1} [54].

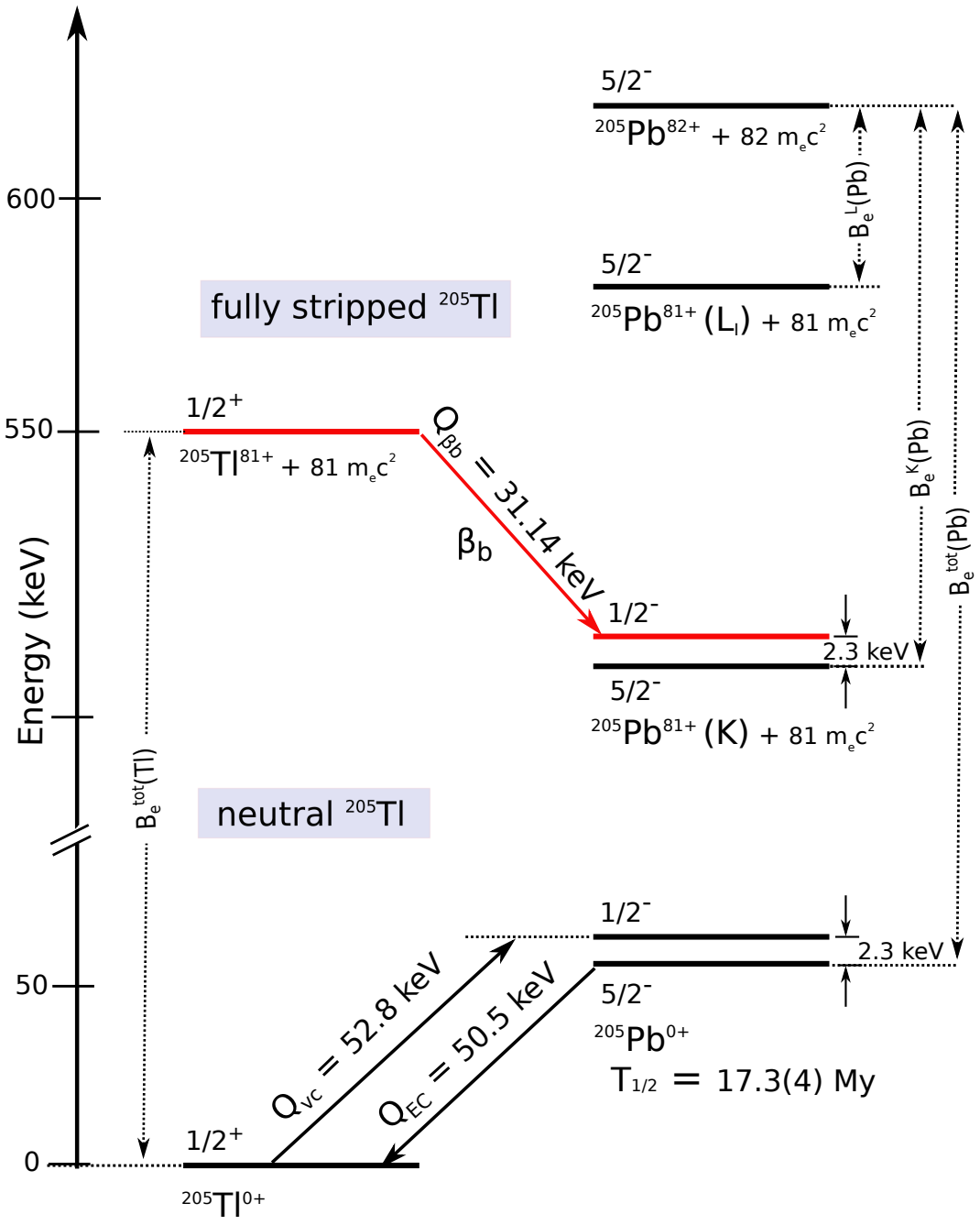

Figure 3.4: Level diagram of neutral and fully-ionized ^{205}Tl and ^{205}Pb.

Chapter 4

Experiment

The measurement of the bound-state beta decay experiment discussed in this thesis was performed at GSI Helmholtzzentrum für Schwerionenforschung in Darmstadt, Germany. The experiment was conducted in March-April, 2020 after waiting for almost three decades, amidst the corona pandemic. The experiment put into use almost all of the experimental facilities at GSI: the ion-source, the UNILAC (UNIversal Linear ACcelerator), the Heavy Ion Synchrotron (German: Schwer-Ionen-Synchrotron) SIS-18, complemented by the FRagment Separator (FRS) and the Experimental Storage Ring (ESR).

Enriched ^{206}Pb source was used and ^{206}Pb ions were accelerated in the UNILAC up to 11.4 MeV/u, injected into the SIS-18 and accelerated up to 600 MeV/u. $^{205}Tl^{81+}$ ions were produced via the projectile fragmentation nuclear reaction of a $^{206}Pb^{67+}$ primary beam on a ^{9}Be target in the FRS and separated by using the $B\rho$-ΔE-$B\rho$ technique (described in Section 4.2.5). Well separated $^{205}Tl^{81+}$ ions were then injected into the ESR where the ions were pre-cooled stochastically and then by electron cooling techniques, accumulated and stored for different storage times, and detected via a resonant Schottky cavity and dedicated particle detectors (described in details in Chapter 5) after the argon (Ar) gas jet target was turned on at the end of each storage measurement. In this Chapter, the techniques to produce, separate, store and measure the β_b in $^{205}Tl^{81+}$ ions are described.

4.1 Projectile fragmentation

Projectile fragmentation [56] can be understood as a two step process where the projectile loses a certain number of nucleons when bombarded on a light target. The first step involves the removal of the nucleons from the projectile, leading to the formation of pre-fragments and is termed as “abrasion”.

The second step is followed with the de-excitation of the pre-fragments by evaporation cascades of the nucleons and is termed as "ablation". At the energies relevant to this work, the fragmentation cross section is almost independent of the incident energy and the projectile fragments have almost the same velocity as that of the projectile. For the projectile fragmentation, the cross section decreases with the number of removed nucleons. Therefore, a ^{206}Pb primary beam was used to produce the $^{205}Tl^{81+}$ ions via the projectile fragmentation reaction as only one nucleon (a proton) was to be removed.

For the produced fragments, the width of the longitudinal momentum spread $\sigma(p_{\parallel})$, is essentially independent of the target mass and the beam energy but does depend on the mass number of the projectile (A_p) and that of the fragment (A_f). The dependence of $\sigma(p_{\parallel})$ on A_p and A_f is given by [57]

$$\sigma(p_{\parallel}) = \sigma_0 \sqrt{\frac{A_f(A_p - A_f)}{A_p - 1}} \quad , \tag{4.1}$$

where $\sigma_0 \sim 90$ MeV/c and $\sigma(p_{\parallel})$ takes its maximum value when $A_f = A_p/2$. In order to minimize the momentum spread of produced fragments, it is important to use a primary beam of which the mass number is close to that of the desired nucleus. This also made ^{206}Pb well suited in the experiment.

Since the removal of a proton from ^{206}Pb is involved in the formation of ^{205}Tl ions, this process is known as the cold fragmentation [58]. By the term "cold", it is meant that the excitation energy of the pre-fragments is low in order to avoid the emission of neutrons (having no Coulomb barrier).

4.2 Production and storage of bare ^{205}Tl ions

Figure 4.1 represents the schematic layout of the existing accelerator facility at GSI. In the following subsections, brief details about the different accelerator facilities will be presented which were employed in the experiment.

4.2.1 Ion Source

Dedicated cathodes made out of enriched ^{206}Pb were used in the VARIS (Vacuum ARc Ion Source). The VARIS, installed in the north source station, is optimized for the production of highly charged ions (up to 6-fold) and therefore it is foreseen for operation with heavy elements. The cathode flange has a revolver system and is equipped with 18 cathode positions. By stripping off the electrons, the desired ions are extracted and inserted into the accelerators at an energy corresponding to about 2% of the speed of light. In the experiment, four ^{206}Pb electrodes were put into use.

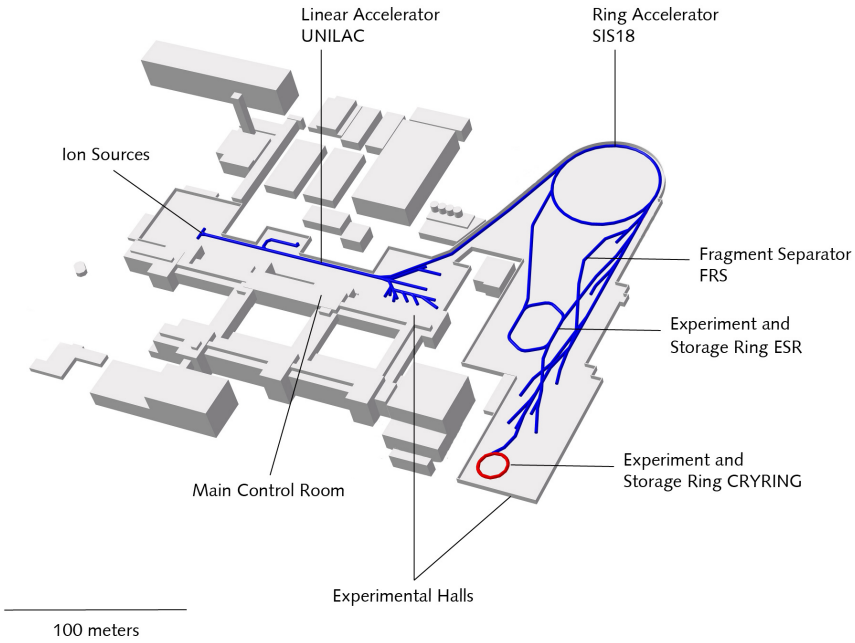

Figure 4.1: Schematic illustration of the GSI accelerator facility [59, 60].

4.2.2 Universal Linear Accelerator

The first accelerating facility of GSI is the UNIversal Linear ACcelerator (UNILAC), wherein the particles can be accelerated to a maximum energy of 11.4 MeV/u. The dc-beam from the ion source is bunched and pre-accelerated by a Radio Frequency Quadrupole (RFQ) and then accelerated by interdigital H-mode structures followed by a gas stripper to increase the charge states of the accelerated ions. The ions are then transferred via a low-energy beam transport line to the high current injector into the 120 m long accelerator which consists of five Alvarez-type cavities. After the final acceleration in the UNILAC, the beam is transferred to the SIS-18 via a transfer channel (TK).

4.2.3 Heavy Ion Synchrotron

The SIS-18 is a heavy ion synchrotron. Having a circumference of 216 m, it can accelerate ions up to about 90% of the speed of light. The number 18 in the abbreviation SIS-18 stands for the maximum magnetic rigidity of the synchrotron i.e. $B\rho = 18$ Tm. Consisting of 24 bending dipole magnets and

two RF cavities, $^{206}Pb^{67+}$ ions were accelerated up to 592 MeV/u. A multi-multi injection technique was employed to achieve high intensity ($\sim 10^9$ particles per second pps) of Pb beam in the experiment. The maximum intensity was limited by several facts including the beam current from the UNILAC, injection and accumulation efficiency in the SIS, as well as the acceleration and extraction efficiencies. The beam finally delivered had an energy resolution ($\Delta p/p < 10^{-3}$).

4.2.4 Production target

A relatively thin 1606.7 mg/cm^2 ^{9}Be target with 223 mg/cm^2 niobium (Nb) backing on the back side was used. When $^{206}Pb^{67+}$ beam at an energy of about 590 MeV/u hits ^{9}Be target, fragmentation reactions take place. Based on the EPAX code [61], production cross section of $^{205}Tl^{81+}$ fragments is 2.3 mb. One can estimate the number of produced fragments of a given species per injection by the following expression

$$N_f = N_i N_t \sigma \epsilon \ , \tag{4.2}$$

where N_i is the number of particles in one extraction spill of the primary beam from the SIS-18, N_t is the number of particles in the target per cm^2 of the target surface, σ is the corresponding production cross section in barn and ϵ is the transmission of the ion-optical system between the target and the detector. The value of N_i in the experiment was $\sim 10^9$ pps. N_t can be determined by

$$N_t = \frac{\rho(\mathrm{g/cm^2}) N_A}{m(u)} \ , \tag{4.3}$$

where ρ is the target thickness, N_A is the Avogadro's constant and $m(u)$ is the mass of an atom of the target material in atomic units. For a 1606 mg/cm^2 ^{9}Be target, $N_t = 1.07 \times 10^{23}$ cm^{-2}. Thus, the number of $^{205}Tl^{81+}$ fragments produced in one extraction spill of the primary beam $^{206}Pb^{67+}$ from the SIS-18 is

$$N_f = 10^9 \times 1.07 \times 10^{23} \times 2.31 \times 10^{-27} \times 10^{-2} \sim 5 \times 10^3 \ ,$$

where $\epsilon = 1\%$ is taken which is the transmission efficiency of the FRS-ESR system. It has to be noted, that the cross section value from the EPAX code [61] is underestimated by about one order of magnitude than the one measured in the cold fragmentation studies. Thus, $N_f \sim 5 \times 10^4$. A storage of $\sim 10^6$ particles was aimed in the ESR. Therefore, an accumulation of 20-25 injections was needed.

4.2.5 Fragment Separator

The FRagment Separator (FRS) [62, 63] is a high-resolution spectrometer, wherein, secondary beams of radioactive ions can be produced via various nuclear reactions and can be efficiently separated. For the FRS-ESR beam line, the system contains four independent stages, each consisting of a 30° dipole magnet and a set of quadrupoles before and after the dipole to fulfill first-order focusing conditions with a maximum bending power of 18 Tm. The magnetic fields are controlled by the Hall probes with a precision and stability of about 10^{-4}. Five focal planes namely S1-S3, S5 and S6 are established in the FRS-ESR beam line (see Figure 4.2).

For the production of radioactive $^{205}Tl^{81+}$ secondary beam, projectile fragmentation of the $^{206}Pb^{67+}$ beam from the SIS-18 on ^{9}Be target was employed as explained in Section 4.2.4.

Having a transmission acceptance in magnetic rigidity $B\rho$ of about ± 2 % for centered fragments, $B\rho$-ΔE-$B\rho$ separation technique was used in the experiment to extract the secondary beam of $^{205}Tl^{81+}$ ions. The fragments with different A/Z were first separated by the dipole magnets D1 and D2. The magnetic field B of the magnets of the FRS is related to the mass-over-charge ratio (m/q) and velocity v of the fragments, as

$$B\rho = \frac{m}{q} v\gamma \quad \propto \quad \frac{A}{Z} \ , \tag{4.4}$$

where γ is the relativistic Lorentz factor. The fragments having higher velocities and/or larger A/Z ratio follow the trajectory with a larger radius or they are bent less in the given magnetic field B. On the contrary, fragments with lower velocities (or smaller A/Z) are bent more as a consequence of which, fragments land at different horizontal positions (x) in the intermediate focal plane. The relative displacement (dx) and the magnetic rigidity are related as

$$D(x) = \frac{dx}{d(B\rho)/(B\rho)} \quad [\text{cm}/\%] \ , \tag{4.5}$$

where D is the dispersion function which defines the change in the horizontal position w.r.t. 1% change in the magnetic rigidity. In the achromatic operation mode [62] (also known as the energy-loss spectrometer mode) of the FRS, the total dispersion of the two stages is equal to zero. This means that the dispersion due to the momentum spread coming from the target is matched to zero in position and angle at the final focal plane. Thus, the dispersive effect of D1 and D2 dipole magnets is compensated by the inverse dispersive effect of D3 and D4 dipole magnets.

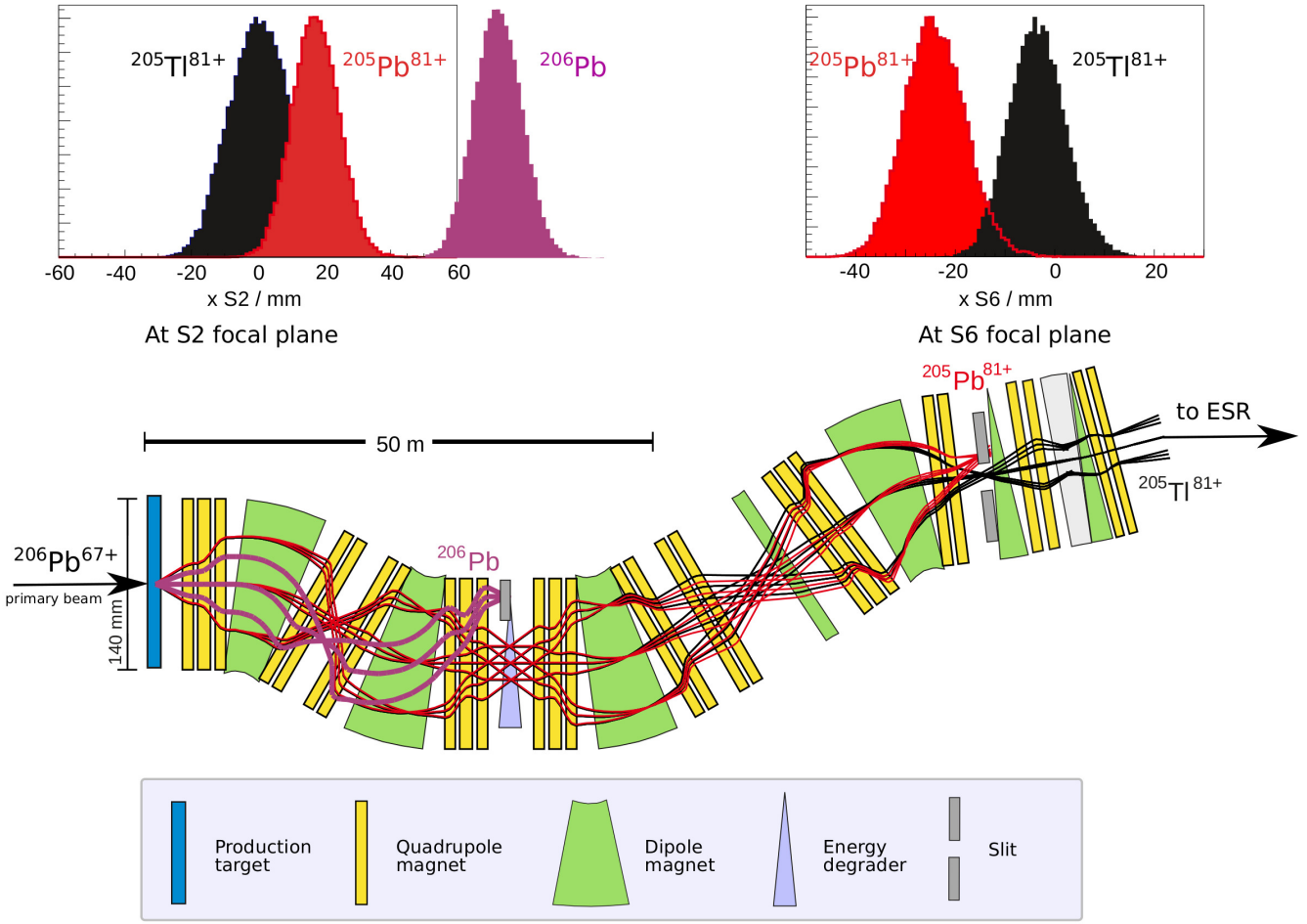

Figure 4.2: Schematic picture of the lattice of the FRS. $B\rho$-ΔE-$B\rho$ separation technique was used to separate $^{205}\mathrm{Tl}^{81+}$ and $^{205}\mathrm{Pb}^{81+}$ isobaric fragments. Energy degrader placed in the middle displaces the two mixed isobaric fragments due to their different energy losses.

The fragments produced with the same A/Z are separated with the aid of an energy degrader in the S2 focal plane. A wedge-shaped aluminium (Al) energy degrader ($\sim$ 735 mg/cm^2) was used for the separation of $^{205}Tl^{81+}$ and $^{205}Pb^{81+}$ ions. The separation in the energy degrader lies on the principle of the Bethe equation that the energy loss ΔE for a given nuclide passing through a matter is $\propto Z^2/v^2$ (Z and v are the atomic number and velocity of the nuclide, respectively). Due to the energy loss in the degrader, every fragment is slowed down and its magnetic rigidity is lowered in accordance with its nuclear charge and velocity. The second stage of the FRS then completes the separation with $B\rho$ selection again with D3 and D4 dipole magnets.

The crucial part of the experiment was the well separation of the isobaric contaminants $^{205}Pb^{81+}$ ions from $^{205}Tl^{81+}$ ions with the FRS. The separation is important as β_b decayed products of $^{205}Tl^{81+}$ ions are the same as the $^{205}Pb^{81+}$ contaminant ions. Thus, $^{205}Pb^{81+}$ ions produced via the projectile fragmentation in the FRS will act as a background in the number of β_b decayed daughter ions in the storage measurement. It is to be emphasized that the condition is concerning if the amount of the background is several orders of magnitude larger than the number of β_b decayed ion. In the separation process, there is also a reduction in $^{205}Tl^{81+}$ ions, and thus a compromise had to be made during setting up the accelerator. The lattice of the FRS for the separation purpose is shown in Figure 4.2. On the top of Figure 4.2 are the MOCADI [64, 65] simulation results which show the isobaric fragments $^{205}Tl^{81+}$ and $^{205}Pb^{81+}$ at S2 and S6 focal planes.

Different positions of the x-slits in the S2 and S6 focal planes as listed in Table 4.1, were used to minimize the $^{205}Pb^{81+}$ contaminants as much as possible. The best reduction of $^{205}Pb^{81+}$ ions was achieved with the position of the x-slits to be S2: 0/35 mm and S6: -20/7 mm, for which most of the storage measurements were performed. The FRS was set to $B\rho = 8.6959$ Tm from the target area to the S2 focal plane and $B\rho = 8.0292$ Tm from the S2 focal plane to the ESR for the transmission of $^{205}Tl^{81+}$ fragments with the least amount of contaminant ions.

4.2.6 Experimental Storage Ring

After the separation of $^{205}Tl^{81+}$ ions from the contaminants, they were injected into the Experimental Storage Ring (ESR) [29, 30]. ESR has a circumference of 108.36 m and a maximum magnetic rigidity of 10 Tm. The ring consists of six bending dipole magnets (with a deflection angle of 60°), twenty quadrupole and eight sextupole magnets for focusing the beam. Having an ultra-high vacuum (UHV) of about 10^{-11} mbar, the ring allows the storage

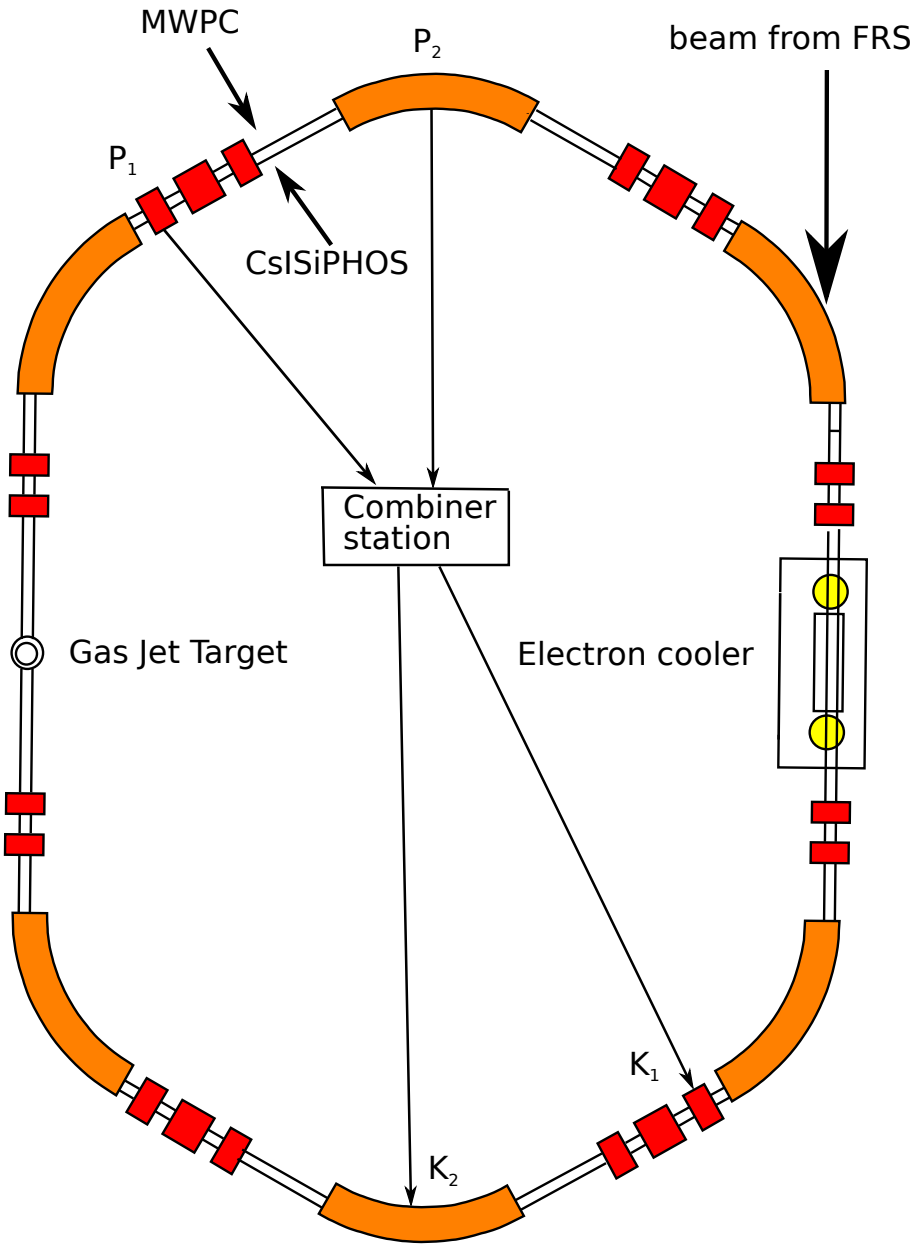

Figure 4.3: Schematic view of the Experimental Storage Ring (ESR). The orange blocks represent the dipole magnets, whereas the red blocks represent the quadrupole and sextupole magnets. P_1 and P_2 are the pick-ups & K_1 and K_2 are the kickers for stochastic cooling. The positions of the gas jet target, the electron cooler and the particle detectors are indicated.

Table 4.1: Different positions of the x-slits in the S2 and S6 focal planes used in the experiment.

S2	S6
-10/35 mm	open
0/35 mm	open
0/35 mm	-20/7 mm

of ions ranging from H^+ to U^{92+} between a few MeV/u up to approximately 400 MeV/u. It has an injection acceptance from the FRS of about ± 0.2%, and a storage acceptance of about ± 1.5% in $B\rho$. To reduce the momentum spread (in the longitudinal direction) and betatron oscillations [66] (in the transverse direction) of the ions in the ring, two types of cooling techniques are used.

Stochastic cooling

In the stochastic cooling technique, spatial deviation of ions from the reference orbit is measured with the aid of capacitive pick-up metal plates. This signal is then amplified and sent to a kicker module, which is located on the opposite side of the ring. The kicker is located at a distance $(n+1/4)\lambda_b$, where n is an integer number and λ_b is the betatron wavelength [66]. Obeying this condition, the phase-space ellipse [66, 67] is rotated by $\pi/2$ and the spatial deviation is transformed into angular deviation, which can now be corrected at the same turn by the transmitted, amplified signal. The cooling rate $1/\tau$ is given by [66]

$$1/\tau \propto \frac{W}{N} \cdot R \ , \tag{4.6}$$

where W is the bandwidth of the pick-up system, pre- and amplifier electronics and the kicker system, N is the number of stored ions and R is a reduction factor, which takes into account the incoherent heating effects for already cooled particles as well as the electronic noise.

The stochastic cooling at the ESR is a pre-cooling process prior to the electron cooling. The stochastic pre-cooling reduces the momentum spread from up to $\delta p/\mathrm{p} = \pm$ 0.35 % down to $\delta p/\mathrm{p} = \pm$ 0.1 % and transverse emittances from up to $\epsilon_{x,y} = 20$ πmm mrad down to $\epsilon_{x,y} = 2.5$ πmm mrad. It has to be noted, that the stochastic cooling at the ESR is optimized such that the ions with energies around 400 MeV/u are cooled, which is defined by the delay line between the pick-up and the kicker.

Electron cooling

In electron cooling [68], a beam of electrons with a velocity equal to the mean ion velocity is merged with an ion beam with the help of a weak toroidal magnetic field over the length of a few meters. The ions undergo Coulomb scattering in an electron soup and lose or gain energy, which is transferred from the co-streaming electrons. Finally, the electron beam is bent away to the electron collector. Many cycles are required wherein the two beams continuously merge until a thermal equilibrium is attained. Continuous cooling of the beam is required to keep the velocity spread of the ions small [69], as inter-beam collisions cause the ion beam to blow up. The electron cooling rate [66] is given by

$$1/\tau \propto \frac{Q^2}{A} n_e \eta_e (\delta v)^{-3} \ , \tag{4.7}$$

where n_e is the electron density of the electron beam, $\eta_e = L/C$ is the ratio of the length L of the cooling section to the ring circumference C, Q and A are the charge and atomic mass of the ion, respectively. The electron cooling force scales as $1/\delta v^3$, where δv is the difference between the electron and ion velocities. Thus, electron cooling is most effective if the difference between the velocities of the electrons and ions is small and thus stochastic pre-cooling is done before. After applying both the cooling techniques, the velocity spread of the stored ions can be reduced from $\delta v/v \sim 10^{-2}$ to $\delta v/v \sim 10^{-6}$-10^{-7}, depending on the number of stored ions [66].

4.3 Storage measurements in the ESR with $^{205}Tl^{81+}$ ions

For the design value of $\sim 10^6$ stored $^{205}Tl^{81+}$ ions and a very cautiously estimated β_b half-life of 1 year (considering large error margin), corresponding to a decay probability in the ^{205}Tl rest frame of $\lambda_{CM}(\beta_b) = 6.6\times10^{-8}$ s^{-1} [35], one would expect a number of about 40 β_b decays within a storage time of 1 hour. Thus, ensuring a high intensity (above 10^6) of ^{205}Tl ions with keeping the number of contaminant $^{205}Pb^{81+}$ ions as small as possible in the ESR was crucial to see a significant amount of decay atoms at the end of the storage measurements. Also, as discussed in Section 4.2.4, $\sim 10^4$ $^{205}Tl^{81+}$ ions were injected in the ESR per spill from the FRS and thus, accumulation/stacking of $^{205}Tl^{81+}$ ions were done in order to achieve the desired intensity.

For this purpose, $^{205}Tl^{81+}$ ions at 400 MeV/u were injected on the outer orbit in the ESR. After fast stochastic pre-cooling, the injected beam was shifted to the inner part of the ESR via an applied radio-frequency bucket.

Each newly injected beam was then added to the stack. The process was repeated until the required intensity was achieved (see Figure 7.8). During the stacking process, both stochastic and electron cooling ($I_e = 200$ mA) were in operation. Once, the desired amount of intensity was achieved, stochastic cooling was switched off and the stacked beam was shifted from the inner orbit to the outer orbit of the ring via the ramping of the dipole magnet, which was done by changing the dipole field of all six dipoles of the ESR (see Figure 4.4).

The accumulated $^{205}Tl^{81+}$ ions ($\sim$ 1-2$\times10^6$) were stored for different storage times with $I_e = 20$ mA, so that the recombination rate of the ions with the cooler electrons is minimized. During the storage process, some of the $^{205}Tl^{81+}$ ions will decay by β_b decay to hydrogen-like (H-like) ^{205}Pb ions with the electron created in the K-shell of $^{205}Pb^{81+}$.

Table 4.2: Setting 1.

S2: -10/35 mm, S6: open	
Storage time (in hours)	Number of measurements
0	1
1	1

Table 4.3: Setting 2.

S2: 0/35 mm, S6: open	
Storage time (in hours)	Number of measurements
0	3
0.5	3
1	2
2	4
3	1
4	1
8	1

Due to the small Q_{β_b}(K) value of only 31 keV, the orbits of β_b $^{205}Pb^{81+}$ daughters remain "hidden" in a common beam. Therefore, to reveal the creation of H-like β_b daughter ions, at the end of each storage times, argon

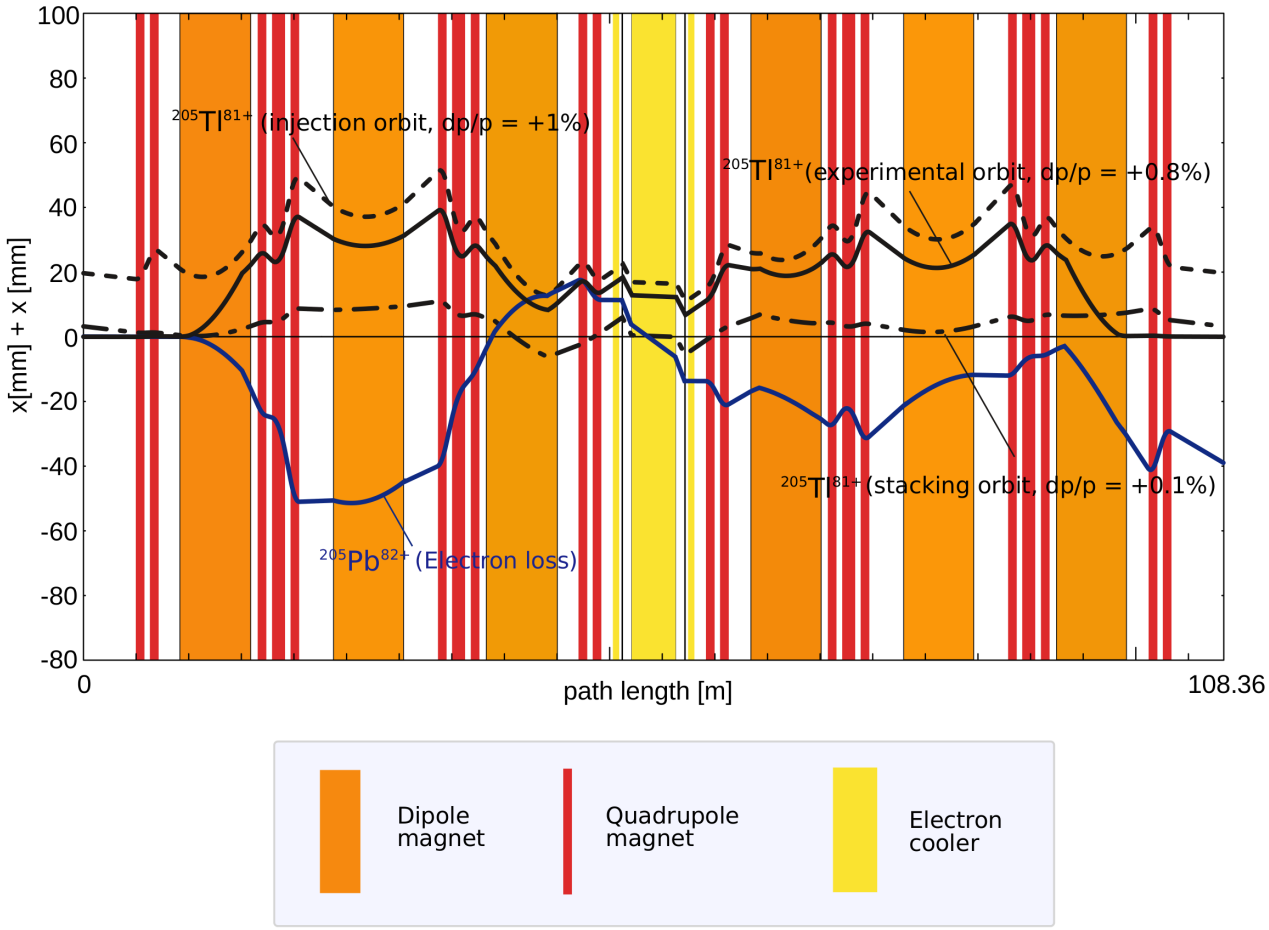

Figure 4.4: The lattice of the ESR where the path length 0 m corresponds to the position of the internal gas jet target. $^{205}Tl^{81+}$ ions were injected on the outer orbit of the ring and were then shifted to the inner orbit after pre-cooling where they were accumulated. Once the accumulation was completed, the $^{205}Tl^{81+}$ beam was shifted to the outer orbit where the storage measurement took place.

(Ar) gas jet target with a density $\sim 2-4\times10^{12}$ atoms/cm^2 was switched on for 10 minutes. During this period, the electron in the K-shell of the $^{205}Pb^{81+}$ ions was stripped off, transforming H-like $^{205}Pb^{81+}$ ions to bare $^{205}Pb^{82+}$ ions, which have a significant different A/Z value. Thus they could be detected in the inner orbit of the ring. This detection was done by employing a non-destructive Schottky cavity (details in Section 5.3). Different trajectories of the ions within the ESR acceptance can be seen in Figure 4.4.

Different storage time measurements were taken for different settings of the x-slits in the FRS which are listed in Tables 4.2, 4.3 and 4.4. Different settings of the x-slits aimed for the reduction of $^{205}Pb^{81+}$ contaminant ions in the FRS and the optimum setting was obtained in the case described in Table 4.4.

Table 4.4: Setting 3.

S2: 0/35 mm, S6: -20/7 mm	
Storage time (in hours)	Number of measurements
0	5
0.5	4
1	1
1.5	1
2	1
3	1
4	1
5	1
6	1
10	2

4.4 Storage measurements in the ESR with $^{206}Pb^{81+}$ ions

When the gas jet target is on, H-like $^{205}Pb^{81+}$ ions may also capture an electron and thus, $^{205}Pb^{82+}$ ions seen in the inner orbit of the ring needs to be corrected by the ratio $(\sigma_{I,\mathrm{Pb}}+\sigma_{c,\mathrm{Pb}})/\sigma_{I,\mathrm{Pb}}$ to determine the true number of β_b daughters, where $\sigma_{I,\mathrm{Pb}}$ and $\sigma_{c,\mathrm{Pb}}$ are the ionization and capture cross section for Pb ions colliding with the Ar atoms, respectively. To obtain these quantities a dedicated measurement was conducted with the primary ^{206}Pb

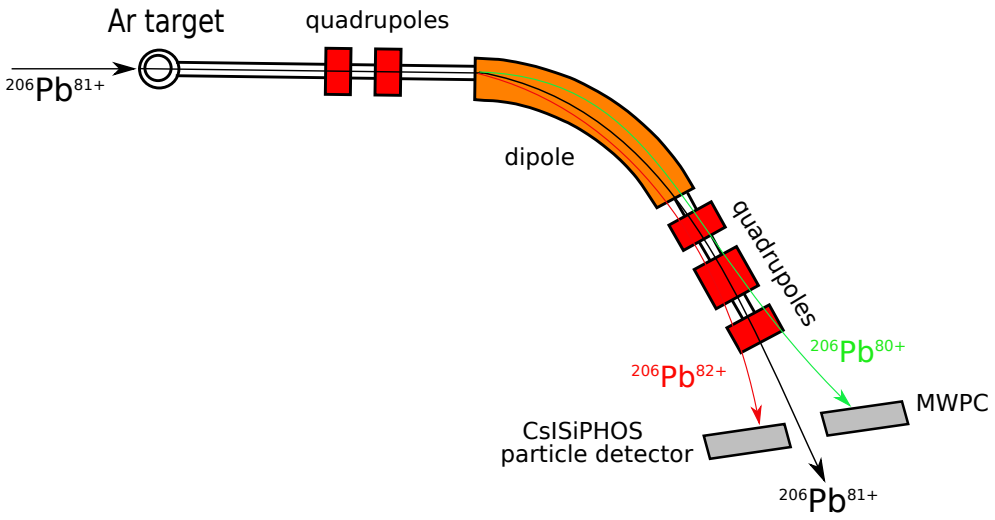

Figure 4.5: The experimental setup at the ESR from the gas jet to the next dipole magnet. $^{206}Pb^{80+}$ ions produced due to the electron capture in the gas jet target are detected by a MWPC placed in the outer pocket after the dipole magnet, whereas $^{206}Pb^{82+}$ ions produced due to ionization in the gas jet target are detected by a ΔE-E telescope (CsISiPHOS) placed in the inner pocket after the dipole magnet.

beam. $^{206}Pb^{67+}$ beam from the SIS-18 at an energy of 401.17 MeV/u and intensity $\sim$ 2-3$\times 10^8$ pps was extracted. Only a thin SEETRAM was used in the target area in the FRS. SEETRAM consists of three Ti foils ($\sim$ 10 µm each) which was used to strip off the electrons to obtain H-like $^{206}Pb^{81+}$ ions. All magnets of the FRS were set at $B\rho$ = 8.06838 Tm.

With a very similar pattern as discussed in Section 4.3, $^{206}Pb^{81+}$ ions were injected on the outer orbit of the ESR. No accumulation was needed as the intensity of the primary beam was high enough. Both stochastic and electron cooling (I_e = 200 mA) were employed. Then, the beam orbit was changed via ramping of the dipole magnets. Dedicated particle detectors (explained in details in Sections 5.1 and 5.2), the CsI-Silicon Particle detector for Heavy ions Orbiting in Storage rings (CsISiPHOS) [70] (in the outer pocket) and a Multi-Wire Proportional Chamber (MWPC) [71] (in the inner pocket) were placed after the first dipole magnet downstream the gas jet target at positions 60 mm and -10 mm (0 mm being the nominal beam orbit), respectively (see Figure 4.5). Ar gas jet target was switched on and $^{206}Pb^{82+}$ and $^{206}Pb^{80+}$ ions were detected by the CsISiPHOS and the MWPC detectors, respectively.

4.5 Measurement principle

The basic principle for the measurement of the decay constant (λ_{β_b}) for the bound-state beta decay is the following equation, which describes the ratio $N^*_{\mathrm{Pb}}(t_s)/N_{\mathrm{Tl}}(t_s)$ as a function of the storage time t_s

$$\frac{N^*_{\mathrm{Pb}}(t_s)}{N_{\mathrm{Tl}}(t_s)} = \frac{\lambda_{\beta_b}}{\gamma} t_s \Big(1 + 1/2(\lambda^{cc}_{\mathrm{Tl}} - \lambda^{cc}_{\mathrm{Pb}})t_s + \cdots\Big) \ , \tag{4.8}$$

where

$$N^*_{\mathrm{Pb}}(t_s) = N_{\mathrm{Pb}}(t_s) - N_{\mathrm{Pb}}(0)\exp(-\lambda^{cc}_{\mathrm{Pb}} t_s) \ , \tag{4.9}$$

$N_{\mathrm{Pb}}(t_s)$ is the number of $^{205}\mathrm{Pb}^{81+}$ ions at time t_s (end of storage) and $N_{\mathrm{Pb}}(0)$ is the number of $^{205}\mathrm{Pb}^{81+}$ ions at $t = 0$ seconds (s) (beginning of storage). $\lambda^{cc}_{\mathrm{Pb}}$ and $\lambda^{cc}_{\mathrm{Tl}}$ are the beam loss factors due to the atomic charge changing processes in the electron cooler and in the residual gas during the storage of $^{205}\mathrm{Pb}^{81+}$ and $^{205}\mathrm{Tl}^{81+}$ ions, respectively.
The number of parent ions stored at time t_s is given by

$$N_{\mathrm{Tl}}(t_s) = N_{\mathrm{Tl}}(0)\exp(-\lambda t_s) \ , \tag{4.10}$$

or

$$N_{\mathrm{Tl}}(t_s) = N_{\mathrm{Tl}}(0)\exp[-(\lambda_{\beta_b}/\gamma + \lambda^{cc}_{\mathrm{Tl}})t_s] \ , \tag{4.11}$$

where $N_{\mathrm{Tl}}(0)$ is the number of parent ions at time $t = 0$ s (beginning of storage) and $\lambda = \lambda_{\beta_b}/\gamma + \lambda^{cc}_{\mathrm{Tl}}$ is the total decay constant in the rest frame of the ion.
The number of daughter ions can be described by the following differential equation

$$\frac{dN_{\mathrm{Pb}}(t_s)}{dt_s} = -\lambda^{cc}_{\mathrm{Pb}} N_{\mathrm{Pb}}(t_s) + N_{\mathrm{Tl}}(t_s)\lambda_{\beta_b}/\gamma \ . \tag{4.12}$$

By using equation 4.11

$$\frac{dN_{\mathrm{Pb}}(t_s)}{dt_s} = -\lambda^{cc}_{\mathrm{Pb}} N_{\mathrm{Pb}}(t_s) + N_{\mathrm{Tl}}(0)\cdot\lambda_{\beta_b}/\gamma\cdot\exp[-(\lambda_{\beta_b}/\gamma + \lambda^{cc}_{\mathrm{Tl}})t_s] \ . \tag{4.13}$$

On solving the above equation, we get the number of daughter ions as a function of storage time t_s

$$N_{\mathrm{Pb}}(t_s) = N_{\mathrm{Tl}}(0)\frac{\lambda_{\beta_b}/\gamma}{\lambda_{\beta_b}/\gamma + \lambda^{cc}_{\mathrm{Tl}} - \lambda^{cc}_{\mathrm{Pb}}}\Bigg(\exp(-\lambda^{cc}_{\mathrm{Pb}} t_s) - \exp\Big[-(\lambda_{\beta_b}/\gamma + \lambda^{cc}_{\mathrm{Tl}})t_s\Big]\Bigg) + N_{\mathrm{Pb}}(0)\exp(-\lambda^{cc}_{\mathrm{Pb}} t_s) \ . \tag{4.14}$$

Using equation (4.11) and (4.14), we get

$$\frac{N^*_{\mathrm{Pb}}(t_s)}{N_{\mathrm{Tl}}(t_s)} = \lambda_{\beta_b}/\gamma\left(- \frac{1}{\lambda_{\beta_b}/\gamma + \lambda^{cc}_{\mathrm{Tl}} - \lambda^{cc}_{\mathrm{Pb}}} + \frac{\exp(\lambda_{\beta_b}/\gamma + \lambda^{cc}_{\mathrm{Tl}} - \lambda^{cc}_{\mathrm{Pb}})t_s}{\lambda_{\beta_b}/\gamma + \lambda^{cc}_{\mathrm{Tl}} - \lambda^{cc}_{\mathrm{Pb}}}\right) . \tag{4.15}$$

Using the Taylor series, the last term on the right hand side can be expanded as

$$\frac{\exp(\lambda_{\beta_b}/\gamma + \lambda^{cc}_{\mathrm{Tl}} - \lambda^{cc}_{\mathrm{Pb}})t_s}{\lambda_{\beta_b}/\gamma + \lambda^{cc}_{\mathrm{Tl}} - \lambda^{cc}_{\mathrm{Pb}}} = \frac{1}{\lambda_{\beta_b}/\gamma + \lambda^{cc}_{\mathrm{Tl}} - \lambda^{cc}_{\mathrm{Pb}}}\Big[1 + (\lambda_{\beta_b}/\gamma + \lambda^{cc}_{\mathrm{Tl}} - \lambda^{cc}_{\mathrm{Pb}})t_s + \frac{1}{2!}(\lambda_{\beta_b}/\gamma + \lambda^{cc}_{\mathrm{Tl}} - \lambda^{cc}_{\mathrm{Pb}})^2 t_s^2 + \frac{1}{3!}(\lambda_{\beta_b}/\gamma + \lambda^{cc}_{\mathrm{Tl}} - \lambda^{cc}_{\mathrm{Pb}})^3 t_s^3 + \cdots\Big] . \tag{4.16}$$

On putting the above in equation (4.15) we get

$$\frac{N^*_{\mathrm{Pb}}(t_s)}{N_{\mathrm{Tl}}(t_s)} = \lambda_{\beta_b}/\gamma \cdot t_s\Big[1 + \frac{1}{2!}(\lambda_{\beta_b}/\gamma + \lambda^{cc}_{\mathrm{Tl}} - \lambda^{cc}_{\mathrm{Pb}})t_s + \frac{1}{3!}(\lambda_{\beta_b}/\gamma + \lambda^{cc}_{\mathrm{Tl}} - \lambda^{cc}_{\mathrm{Pb}})^2 t_s^2 + \cdots\Big] . \tag{4.17}$$

Also, λ_{β_b}/γ is negligible as compared to the loss constants $\lambda^{cc}_{\mathrm{Tl}}$ and $\lambda^{cc}_{\mathrm{Pb}}$ [$\lambda_{\beta_b}/\gamma << (\lambda^{cc}_{\mathrm{Tl}} - \lambda^{cc}_{\mathrm{Pb}})$] and thus

$$\frac{N^*_{\mathrm{Pb}}(t_s)}{N_{\mathrm{Tl}}(t_s)} = \lambda_{\beta_b}/\gamma \cdot t_s\Big[1 + \frac{1}{2!}(\lambda^{cc}_{\mathrm{Tl}} - \lambda^{cc}_{\mathrm{Pb}})t_s + \frac{1}{3!}(\lambda^{cc}_{\mathrm{Tl}} - \lambda^{cc}_{\mathrm{Pb}})^2 t_s^2 + \cdots\Big] . \tag{4.18}$$

For $(\lambda^{cc}_{\mathrm{Tl}} - \lambda^{cc}_{\mathrm{Pb}})t_s << 1$, the higher order terms in the Taylor series are negligible and thus,

$$\frac{N^*_{\mathrm{Pb}}(t_s)}{N_{\mathrm{Tl}}(t_s)} = \frac{\lambda_{\beta_b}}{\gamma} t_s\Big[1 + 1/2(\lambda^{cc}_{\mathrm{Tl}} - \lambda^{cc}_{\mathrm{Pb}})t_s\Big] . \tag{4.19}$$

The above is the basic equation which is employed for the determination of the decay constant of the bound-state beta decay of $^{205}\mathrm{Tl}^{81+}$ ions.

Chapter 5

Detectors

During the entire experimental campaign, three detectors were employed: the CsI-Silicon Particle detector for Heavy ions Orbiting in Storage rings (CsISiPHOS) [70], a Multi-Wire Proportional Chamber (MWPC) [71] and a non-destructive resonant Schottky cavity [72]. In this Chapter, these detectors and their corresponding data-acquisition systems (DAQ) are introduced.

5.1 CsISiPHOS

CsISiPHOS [70] is a heavy-ion detector which was developed for decay studies in the ESR. CsISiPHOS was used for counting the number of $^{206}Pb^{82+}$ ions during the storage of H-like $^{206}Pb^{81+}$ primary beam in the ring. This detector is also a complementary tool serving several tasks at a time, e.g. for independent half-life measurements, unique particle identification (PID) in mass and charge, and as an additional beam diagnostics tool. It has been built under the flagship of ILIMA (Isomeric states, LIfetimes, and MAsses) collaboration [73] which is a branch of the NUSTAR (NUclear STructure, Astrophysics and Reactions) pillar of the FAIR [74, 75] program. As the detector is designed for the nuclei of interest having typical decay times of more than a second, the rate capability, time resolution, and the dead time constraints are less crucial requirements. Owing to the detector concept and its complexity, its direct implementation inside the ultra high-vacuum (UHV) of the ring is not possible. A very compact pocket structure is used to insert the CsISiPHOS close to the beam trajectory in the ring, while leaving the detector itself outside of the ring vacuum in a closed volume continuously flushed with dry nitrogen. The detector can be mounted in different movable detector pocket positions in the ESR and in the future Collector Ring (CR) [76] in the FAIR project. These pockets are equipped with thin win-

dows made of 25 µm stainless steel, which separates the gas pressure inside the pocket from the UHV of $\sim 10^{-11}$ mbar in the ring. The detector for this experiment was installed in the inner pocket of the ESR after the first dipole magnet downstream the gas jet target area (see Figure 4.5). The drive specific accelerator nomenclature of the device is GE01DD2IG.

5.1.1 Configuration of the CsISiPHOS

The CsISiPHOS [70] having an active area of 40×60 mm^2, consists of a stack of six large-area Si pads, a double-sided silicon strip detector (DSSD), one passive energy degrader and a massive CsI(Tl) scintillator crystal. Each Si pad sensor is 500 µm thick with no segmentation on the n-side, whereas the p-side consists of seven individual strips. It is used for high resolution energy loss ΔE measurement from where the nuclear charge of the reaction products impinging on the detector can be identified. For the determination of the two-dimensional impact coordinates of particles, a 300 µm thick DSSD is used where a single resistive readout chain is employed on each side of the detector to determine the position with a single strip resolution. For the mass identification of the particles, a 10 mm thick CsI(Tl) crystal having an area

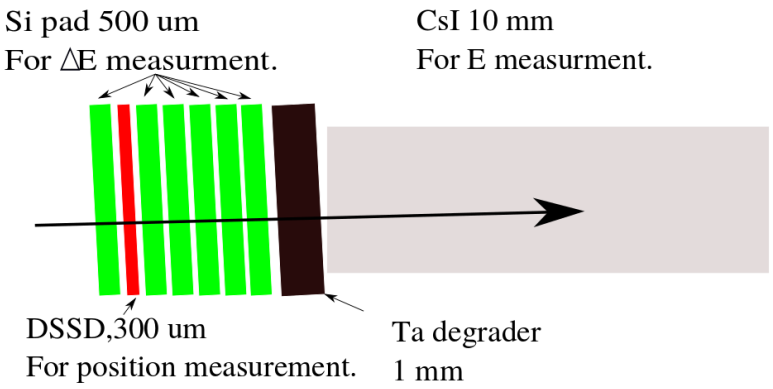

Figure 5.1: Schematic drawing of the CsISiPHOS. The Si pad sensors, the DSSD and the passive degrader are tilted by 3° to reduce the channeling effect.

of 24×24 mm^2 is used which is coupled to a Si photodiode to stop particles and reconstruct their full energy E. Also a passive energy degrader is used which is a 1000 µm thick slab of tantalum (Ta). To reduce the channeling effect [70], all Si pad sensors, DSSD and passive degrader are tilted by an angle of 3° with respect to the entrance window of the frame as shown in Figure 5.1.

The detector frame consists of 10 positions, which are filled as shown in Table 5.1 and the CsI(Tl) crystal is already attached to the frame. The detector has a total of 54 channels: 8×6 readout channels for the Si pad sensors (the p-side having 7 strips and no segmentation on the n-side), 4 readout channels for the DSSD (the p-side having 60 strips and the n-side having 40 strips) and 2 readout channels for the photodiode coupled to the CsI(Tl).

The DSSD which is used for the determination of the position coordinates of each hitting particle consists of 100 strips. The strips of each side are connected to a chain of resistors with a total resistance of 3000 Ω (60 resistors of 50 Ω on the p-side and 40 resistors of 75 Ω on the n-side equally distributed over the active area). The position information of ions can be constructed by the following equation

$$\mathrm{x} = a_0 + a_1 . \frac{Q_L - Q_R}{Q_L + Q_R} \quad , \tag{5.1}$$

$$\mathrm{y} = b_0 + b_1 . \frac{Q_T - Q_B}{Q_T + Q_B} \quad , \tag{5.2}$$

where Q_L and Q_R are the charge from the left and right side of the DSSD, Q_T and Q_B are charge from the top and bottom side of the DSSD, respectively. A required condition is that the sum of the signals from both the p- and n-sides is constant. a_0, a_1, b_0 and b_1 are the calibration parameters.

Table 5.1: Details about the CsISiPHOS.

Position in the frame	Detector components
Position 1	Si pad sensor
Position 2	DSSD
Position 3-7	Si pad sensor
Position 8	passive energy degrader (Ta)
Position 9-10	empty

The CsI coupled to the photodiode has two readout channels, which are generated from the front and back side of the photodiode. Charged particles lose their energy inside the CsI scintillator and produce photons, which are collected by the photodiode and converted into a charge pulse.

5.1.2 Electronics and DAQ

The analog signals from the detector are transferred to the flange of the pocket using two 50 Ω flat cables (each cable consisting of 60 individually shielded wires) which are then sent to MSI-8 and MPR-32 charge sensitive preamplifiers via lemo and ribbon cables, respectively. The p-side strips of the silicon pad sensors (6×7 channels) are sent to two MPR-32 modules as their output signals have the same characteristics. The output signals from the DSSD (4 channels), the CsI coupled with a photodiode (2 channels) and the n-side strips of the silicon pad sensors (6×1 channels) are sent to two MSI-8 modules. MSI-8 is a flexible module which has a possibility of reading signals with different polarities on different channels and is also used for applying a bias voltage to different detector components. Five MSCF amplifier modules are used to shape (shaping time 2 µs) and further amplify the signals, which are then sent to three 12-bit 32-channel CAEN V785 analog to digital converter (ADC) modules for the digitization process. A high voltage of 32 V, -50 V, and -100 V, is applied as a bias voltage via MSI-8 modules to the n-side of the six Si-pad sensors, to the p-side of the DSSD and to the p-side of the photodiode, respectively. Various parameters of the high voltage and amplifier modules are controlled by a raspberry pi during the experiment.

The data is transferred to a storage disk via a Versa Module Europa bus (VMEbus) operated by the data acquisition software Multi-Branch System (MBS), developed at GSI. For the on-line streaming of the data Go4 (GSI Object Oriented On-line Off-line system) is used which is an object-oriented system based on ROOT as shown in Figure 5.3. For the off-line storage of data, the files are saved in lmd (list mode data) format which are converted by a ROOT unpacker to ROOT files for the further off-line analysis.

5.2 MWPC

A position-sensitive MWPC [71] with delay-line readouts, having an active area of 121×42 mm^2 was used in this experiment. It was placed in the outer pocket of the ESR after the first dipole magnet downstream the gas jet target (see Figure 4.5). The accelerator nomenclature of the device is GE01DD2AG.

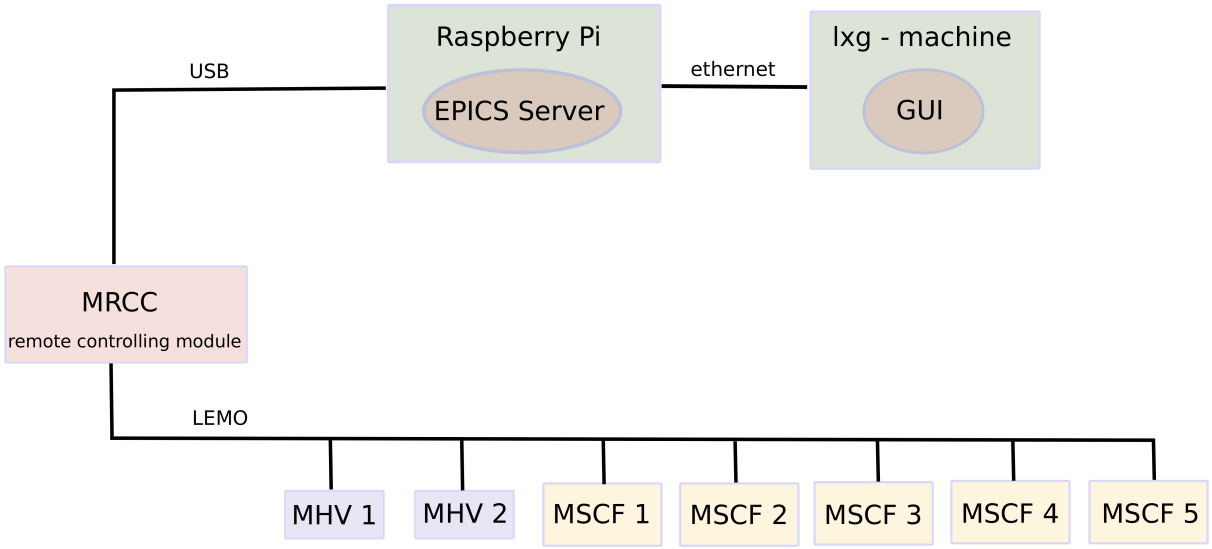

Figure 5.2: Block diagram showing the slow control.

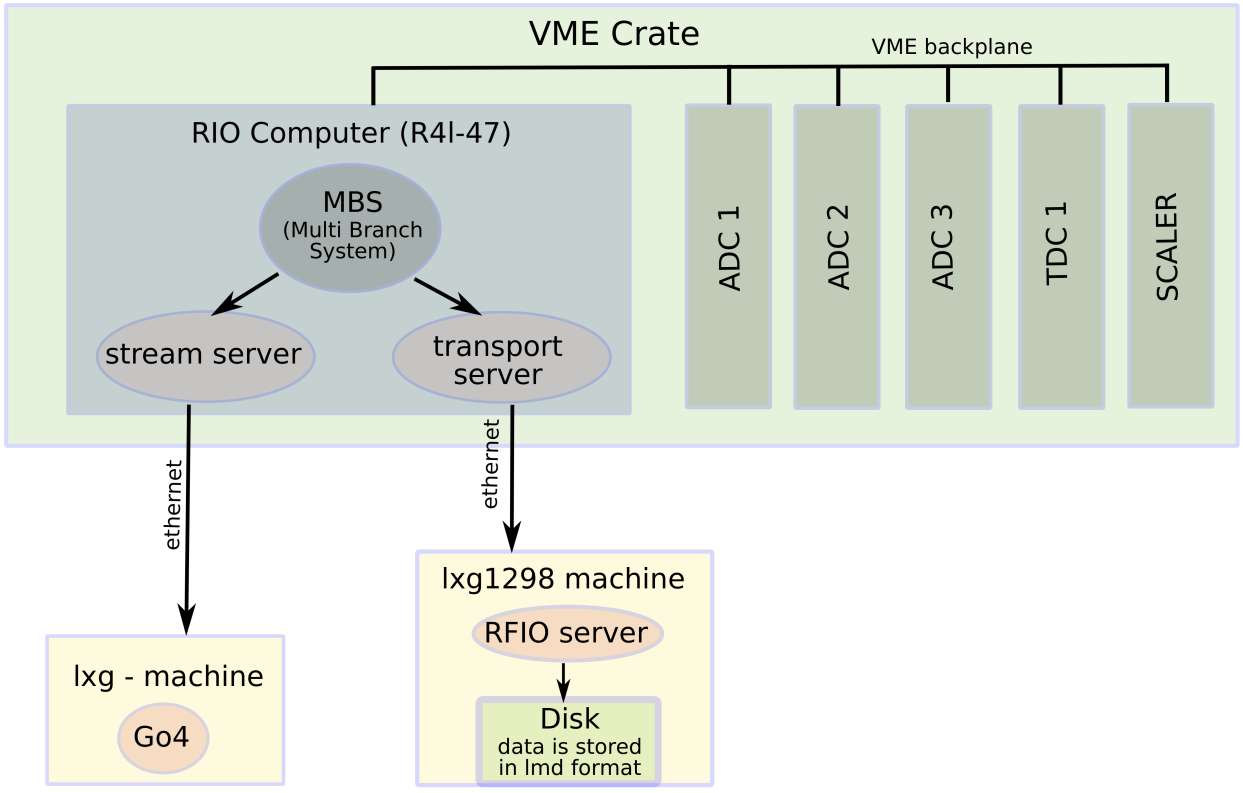

Figure 5.3: Block diagram of the data storage system.

The detector consists of an anode plane and two cathode planes with the distance between the wire planes to be 5 mm. The anode plane consists of 15 µm gold plated tungsten wires with a pitch of 2 mm whereas two cathode planes consist of 50 µm gold plated tungsten wires with a pitch of 1 mm. The wire directions in the two cathode planes are orthogonal to each other whereas the wires of the anode plane are in the diagonal direction. The detector gas (argon + CO_2 + heptane: 80:20:1.5) fills the whole pocket tube at atmospheric pressure.

Ions that hit the active area of the chamber produce primary electrons in the chamber gas which are multiplied in the high electric field of the planar electrode structure. The avalanche then drifts to the anode plane inducing a negative signal. Positive signals are induced on the adjacent orthogonal (X and Y direction) cathodes. All analog signals are sent to a Constant Fraction Discriminator (CFD), and the anode signal is sent to a Leading Edge Discriminator (LED) additionally. The output signals from the CFD are then processed with a time to digital converter (TDC) where the time information is recorded. The LED signal is used for trigger generation due to its high precision threshold feature. For both the CsISiPHOS and the MWPC, a common DAQ system was used. The signal map and the data structure are shown in Figure 5.4 and Figure 5.5, respectively. The DAQ system also contains a scaler module where other important signals (see Figure 5.5) were recorded during the experiment.

Each wire of the cathode planes is connected to a tap of delay chip and the signal propagates from the left and the right side of the delay line. The delay time between the two adjacent delay chains is 4 ns/2 mm. The time difference between the two sides of the delay line gives the position of the particle, where the sum of the two sides is constant. The time difference between the start and stop signals from each side of t_{x} (t_{y}) cathode wire provides the information on the x-left and x-right (y-top and y-bottom) positions. The exact position in millimeters is determined from the difference of the signals on both ends of the wire

$$\mathrm{x} = a_0(t_{\mathrm{x}_L} - t_{\mathrm{x}_R}) + b_0 \quad , \tag{5.3}$$

$$\mathrm{y} = a_1(t_{\mathrm{y}_T} - t_{\mathrm{y}_B}) + b_1 \quad , \tag{5.4}$$

where a_0, a_1, b_0 and b_1 are the calibration parameters. The detection efficiency of the MWPC is better than 99% with a position resolution (full width at half maximum) of about 1.9 mm.

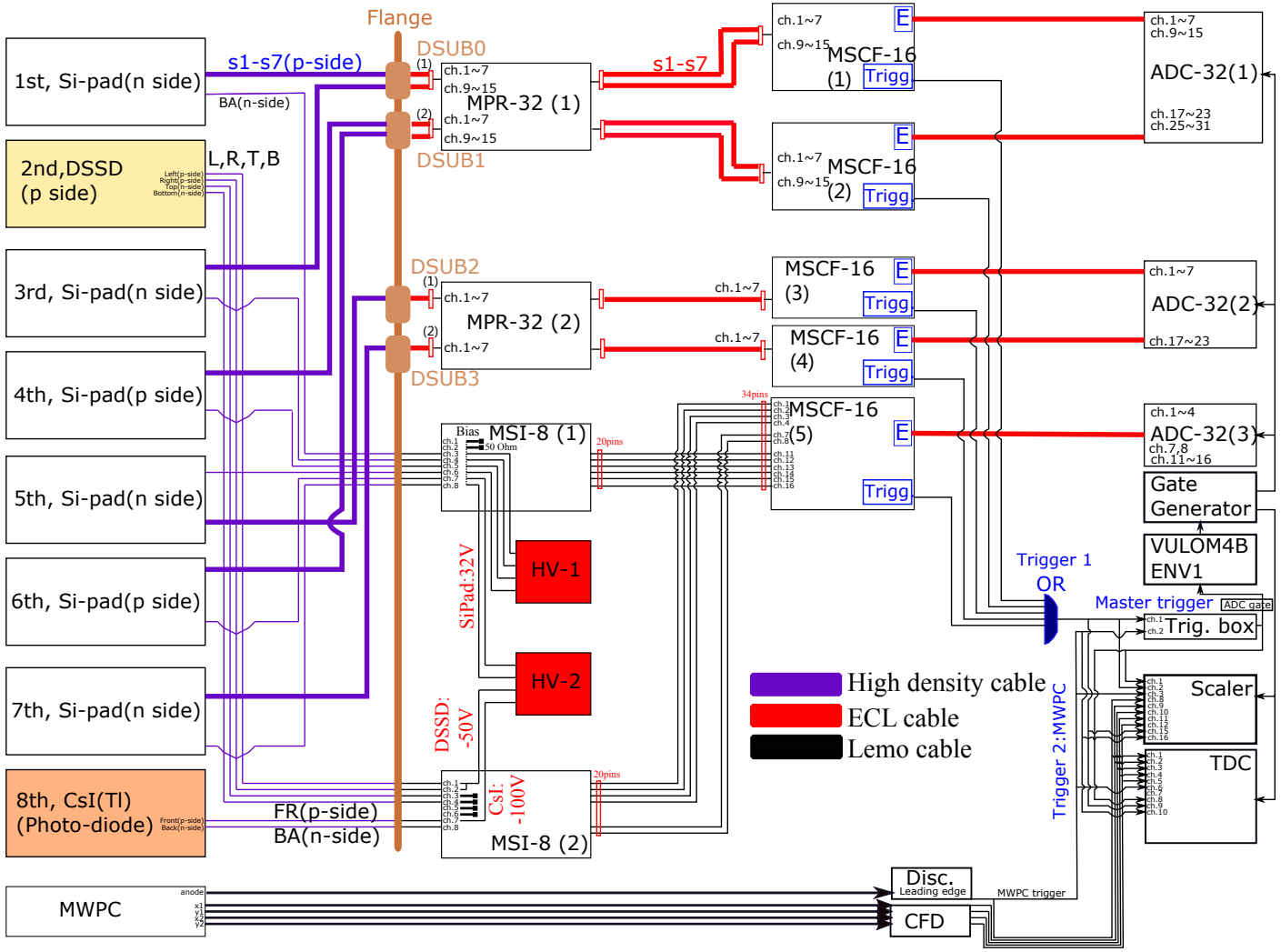

Figure 5.4: The signal map of the CsISiPHOS and the MWPC detectors.

Data structure									
Name	**Value**	**Name**	**Value**	**Name**	**Value**	**Name**	**Value**	**Name**	**Value**
ADC1_1	1st Det: Si S1	ADC2_1	5th Det: Si S1	ADC3_1	2nd Det: DSSD Left	SC1_1	Master trigger.	TDC1_1	MWPC anode
ADC1_2	1st Det.: Si S2	ADC2_2	5th Det.: Si S2	ADC3_2	2nd Det: DSSD Right	SC1_2	Si or.	TDC1_2	MPWC X1
ADC1_3	1st Det.: Si S3	ADC2_3	5th Det.: Si S3	ADC3_3	2nd Det: DSSD Top	SC1_3	MWPC trigger raw	TDC1_3	MPWC X2
ADC1_4	1st Det.: Si S4	ADC2_4	5th Det.: Si S4	ADC3_4	2nd Det: DSSD Bottom	SC1_4	Gas target density (S1)	TDC1_4	MPWC Y1
ADC1_5	1st Det.: Si S5	ADC2_5	5th Det.: Si S5	ADC3_5		SC1_5	I-Ecool	TDC1_5	MPWC Y2
ADC1_6	1st Det.: Si S6	ADC2_6	5th Det.: Si S6	ADC3_6		SC1_6	DC Trafo	TDC1_6	MWPC trigger raw
ADC1_7	1st Det.: Si S7	ADC2_7	5th Det.: Si S7	ADC3_7	7th Det: CsI FR.	SC1_7	Inhibit	TDC1_7	
ADC1_8		ADC2_8		ADC3_8	7th Det: CsI BK.	SC1_8	MWPC anode	TDC1_8	Master trigger
ADC1_9	3rd Det: Si S1	ADC2_9		ADC3_9		SC1_9	MPWC X1	TDC1_9	Trigger 1
ADC1_10	3rd Det.: Si S2	ADC2_10		ADC3_10		SC1_10	MPWC X2	TDC1_10	Trigger 2
ADC1_11	3rd Det.: Si S3	ADC2_11		ADC3_11	1st Det.: Si n side	SC1_11	MPWC Y1		
ADC1_12	3rd Det.: Si S4	ADC2_12		ADC3_12	3rd Det.: Si n side	SC1_12	MPWC Y2		
ADC1_13	3rd Det.: Si S5	ADC2_13		ADC3_13	4th Det.: Si n side	SC1_13	Clock(1.5MHz)		
ADC1_14	3rd Det.: Si S6	ADC2_14		ADC3_14	5th Det.: Si n side	SC1_14	Gas target density (S2)		
ADC1_15	3rd Det.: Si S7	ADC2_15		ADC3_15	6th Det.: Si n side	SC1_15	Trigger 1		
ADC1_16		ADC2_16		ADC3_16	7th Det.: Si n side	SC1_16	Trigger 2		
ADC1_17	4th Det: Si S1	ADC2_17	7th Det: Si S1	ADC3_17					
ADC1_18	4th Det.: Si S2	ADC2_18	7th Det.: Si S2	ADC3_18					
ADC1_19	4th Det.: Si S3	ADC2_19	7th Det.: Si S3	ADC3_19					
ADC1_20	4th Det.: Si S4	ADC2_20	7th Det.: Si S4	ADC3_20					
ADC1_21	4th Det.: Si S5	ADC2_21	7th Det.: Si S5	ADC3_21					
ADC1_22	4th Det.: Si S6	ADC2_22	7th Det.: Si S6	ADC3_22					
ADC1_23	4th Det.: Si S7	ADC2_23	7th Det.: Si S7	ADC3_23					
ADC1_24		ADC2_24		ADC3_24					
ADC1_25	6th Det: Si S1	ADC2_25		ADC3_25					
ADC1_26	6th Det.: Si S2	ADC2_26		ADC3_26					
ADC1_27	6th Det.: Si S3	ADC2_27		ADC3_27					
ADC1_28	6th Det.: Si S4	ADC2_28		ADC3_28					
ADC1_29	6th Det.: Si S5	ADC2_29		ADC3_29					
ADC1_30	6th Det.: Si S6	ADC2_30		ADC3_30					
ADC1_31	6th Det.: Si S7	ADC2_31		ADC3_31					
ADC1_32		ADC2_32		ADC3_32					
Name	**Value**			**Name**		**Value**			
TB_SI_IN	Trigger of Si or before scaling down.			TB_MWPC_IN		Trigger of MWPC or before scaling down.			
TB_SI_RED	Trigger of Si or after scaling down.			TB_MWPC_Out		Trigger of MWPC or after scaling down.			

Figure 5.5: The data structure of the DAQ signals.

5.3 Schottky detector

This Section describes the origin and recording of the Schottky signals. Schottky signals are the basis for the non-destructive Schottky spectroscopy, which is used for beam diagnostics in circular accelerators and storage rings. With Schottky beam diagnosis, a lot of information about the stored ion beam such as the revolution frequency, beam intensity, distribution width or number of particles etc. can be determined. This information can be extracted by means of the Fourier transform of the Schottky noise.

In the ESR ring, there are two non-destructive Schottky detectors: one is a parallel plate Schottky pick-up made up of copper plates [77] and another is a resonant Schottky cavity [72]. On passage of the ions in the ring, the Schottky noise can be picked up by means of either image charge induced by the ions on a pair of capacitive plates or by means of excited electromagnetic fields inside a resonant cavity. The latter has a much higher quality factor and for the same data recorded from the two detectors, the signal to noise ratio is about a factor of 100 times better than the capacitive detector.

The ions revolving in the storage ring induce a signal which is proportional to the current density of the stored ions. For a single ion with the charge Z circulating in the ring with revolution time $T_0 = 1/f_0$ (f_0 being the revolution frequency), the amplitude of the induced signal [78, 79] can be written as a sequence of sharp Dirac δ pulses

$$i(t) = Ze \sum_m \delta(t - t_i - mT_0) \ , \tag{5.5}$$

where e is the elementary charge, t_i is the time when an ion is injected, and m is the revolution number which is an integer. For further analysis, the delta function can be approximated by a Fourier series given by

$$i(t) = a_0 + \sum_{h=1}^{\infty} \big(a_1 \cos(hw_0 t) + a_2 \sin(hw_0 t)\big) \ , \tag{5.6}$$

where the coefficients are

$$a_0 = \frac{1}{T_0} \int_{T_i}^{T_i+T_0} i(t)dt \ , \tag{5.7}$$

$$a_1 = \frac{2}{T_0} \int_{T_i}^{T_i+T_0} i(t) \cos(hw_0 t)dt \ , \tag{5.8}$$

$$a_2 = \frac{2}{T_0} \int_{T_i}^{T_i+T_0} i(t) \sin(hw_0 t)dt \ . \tag{5.9}$$

Here $w_0 = 2\pi/T_0$, T_i is the interval constant for the integration which can be chosen arbitrarily. The coefficients are calculated using the relations

$$\int_{-\infty}^{\infty} \delta(t)dt = 1 \text{ and } \int_{-\infty}^{\infty} f(t)\delta(t-a)dt = f(a) \ . \tag{5.10}$$

Thus, the Fourier series of the current signal becomes

$$i(t) = i_0 + 2i_0 \sum_{h=1}^{\infty} \Big(\cos(hw_0 t_i)\cos(hw_0 t) + \sin(hw_0 t_i)\sin(hw_0 t) \Big) \ , \tag{5.11}$$

where $i_0 = Ze/T_0 = Zef_0$ is referred to as DC current which represents the macroscopic beam current and the second term represents the random current fluctuations. In the Schottky spectrum, this is represented by bands around the harmonics of frequency hf_0 [79].

The spectrum for another particle at a slightly different frequency $f' = f_0 + \Delta f$ with $\Delta f = f_0 \eta \Delta p/p$ where η is the frequency slip factor of the ring, is given by the superposition of the individual line spectra. The frequency difference between the single lines of the two particles is proportional to the harmonic number. This means the two lines are better separated for a higher harmonic number. Let us consider a continuous beam of N stored particles all with the same revolution frequency f_0 and with random injection times $0 \leq t_i \leq T$. This is represented in the time domain by a fluctuating current signal (noise trace with some DC offset), called the Schottky noise current [72, 79]

$$I(t) = \sum_{i=1}^{N} \Big[i_0 + 2i_0 \sum_{h=1}^{\infty} \Big(\cos(hw_0 t_i)\cos(hw_0 t) + \sin(hw_0 t_i)\sin(hw_0 t) \Big) \Big] \ . \tag{5.12}$$

The average of the above over a sufficiently long time is given by

$$\langle I(t) \rangle_{T_0} = \frac{1}{T_0} \int_0^{T_0} I(t)dt = i_0 N \ , \tag{5.13}$$

where only the macroscopic beam current (DC current) survives and the random current fluctuations vanish. In order to obtain the harmonic band intensity, the root mean square (r.m.s.) value of the current noise signal has to be calculated

$$(I_{\mathrm{rms}}(t)_h)^2 = \frac{1}{T_0} \int_0^{T_0} \big(I(t) - \langle I(t) \rangle_{T_0} \big) \, dt = 2i_0^2 N = 2(Ze)^2 f_0^2 N \ . \tag{5.14}$$

Thus, the integrated Schottky noise spectral density in each band does not depend on the harmonic number h, but on the number of circulating particles,

their revolution frequency and charge. Of course, it is not realistic to assume that all the particles have the same revolution frequency as this would imply either $\eta = 0$ or a vanishing momentum spread which is never the case. Thus, by considering the fact that the ion revolution frequency is distributed within $f_0 \pm \Delta f/2$, the number of particles N for a subgroup of particles over a very narrow range df is

$$\left(\frac{dN}{df}\right) df \quad , \tag{5.15}$$

and

$$d(I_{\mathrm{rms}}(f)_h)^2 = 2(Ze)^2 f_0^2 \left(\frac{dN}{df}\right) df \quad , \tag{5.16}$$

$$\frac{d(I_{\mathrm{rms}}(f)_h)^2}{df} = 2(Ze)^2 f_0^2 \left(\frac{dN}{df}\right) \quad . \tag{5.17}$$

The above represents the spectral density (in units of A^2/Hz) of the noise at the h^{th} harmonic. Integrating the above over the band $f_0 \pm \Delta f$, we get the total noise power per band

$$(I_{\mathrm{rms}}(f)_h)^2 = 2(Ze)^2 f_0^2 N = 2ZeI_0 f_0 \quad . \tag{5.18}$$

The above equation concludes that the total noise power for each Schottky band is constant [72, 79]. But since the width of the Schottky band is increasing proportionally to the harmonic number, the amplitudes must decrease by $1/h$.

5.3.1 NTCAP

A radio frequency (RF) signal from the Schottky resonator [80, 81] goes through a low-noise amplifier (LNA) which is a wideband amplifier. The signal then passes through a bandpass filter (f_c = 245 MHz, bandwidth $\mathrm{BW}_{-3\mathrm{dB}}$ = 27 MHz) followed by a series of amplifiers (A) through a long co-axial wire to the main control room. The RF signal is split and given to: a spectrum analyzer (for on-line monitoring) and to the NTCAP for the data recording purpose.

NTCAP [82] is a data acquisition system for the Schottky detector which has been developed by C. Trageser *et al.* [83] at GSI. It consists of different commercial National Instruments(NI)-hardware modules. The Schottky signals are analyzed by a vector signal analyzer (VSA) (PXIe-5663E) which consists of three sub-modules: a local oscillator (NI 5601), a down-converter (NI 5652) and a digitizer (NI 5622). A voltage controlled oscillator source is

used as a generator of mixed frequency (f_{LO}) which is fed to a RF downconverter where the RF Schottky signal (f_{in}) is present. The downconverter gives $f_{in} \pm f_{\mathrm{LO}}$ as the output signals where the higher frequency signal ($f_{in} + f_{\mathrm{LO}}$) is suppressed by a low-pass filter (53 MHz, 20 MHz BW). The low frequency analog signal ($f_{in} - f_{\mathrm{LO}}$) (intermediate frequency IF) is digitized by an ADC which is a 16 bit digitizer at a fixed sampling rate of 150 MS/s (mega samples per second). IF signal = 53 MHz (20 MHz BW) for 119 MHz $< f_{in} <$ 330 MHz and $f_{\mathrm{LO}} = (53 + f_{in})$ MHz. The digitized signal is then passed to an onboard signal processing (OSP) module. OSP consists of a digital down converter (DDC) which generates complex I (in-phase)-Q (quadrature-phase) baseband signals. IQ signals are generated by mixing the digitized IF signal with 90° phase-shifted cosine (to get I signal) and sine signals (to get Q signal) which are generated by a numerically-controlled oscillator (NCO). The IQ data obtained are then filtered and decimated according to the desired settings, merged and pushed into the internal 64 MB (megabyte) device memory storage. The data in the device memory is sent from a control program via the interface card to the computer. The NTCAP allows for a variable IQ rate and can be set between 1 MS/s to 75 MS/s. For the experiment, an IQ rate of 8 MS/s was used covering 8 MHz of the bandwidth and containing three Schottky (124^{th}, 125^{th} and 126^{th}) harmonics. The recorded data is in the time domain which is stored in the complex samples $U_{\mathrm{I}} + iU_{\mathrm{Q}}$ in a Technical Data Management Streaming (TDMS) format.

Each TDMS file is 4.29 GB (gigabyte) long containing 134.217 seconds of recording time with 2^{12} frames and each frame containing 2^{18} IQ (I point: 2 MB and Q point: 2 MB in size) data points. In the experiment, which ran for one week, a total of $\sim$ 20 TB (terabyte) of Schottky data was recorded with the NTCAP.

Table 5.2: The components of the NTCAP.

Module Name	Quantity	Module description
NI PXIe-1075 PXIe	1	NI-Chassis
NI PXIe-PCIe8375	1	Connection to the control computer
NI PXIe-5663E	1	Vector Signal Analyzer (VSA)
NI PXIe-6612	2	Scalar card with eight inputs
NI PXIe-6674T	1	Time and synchronization module

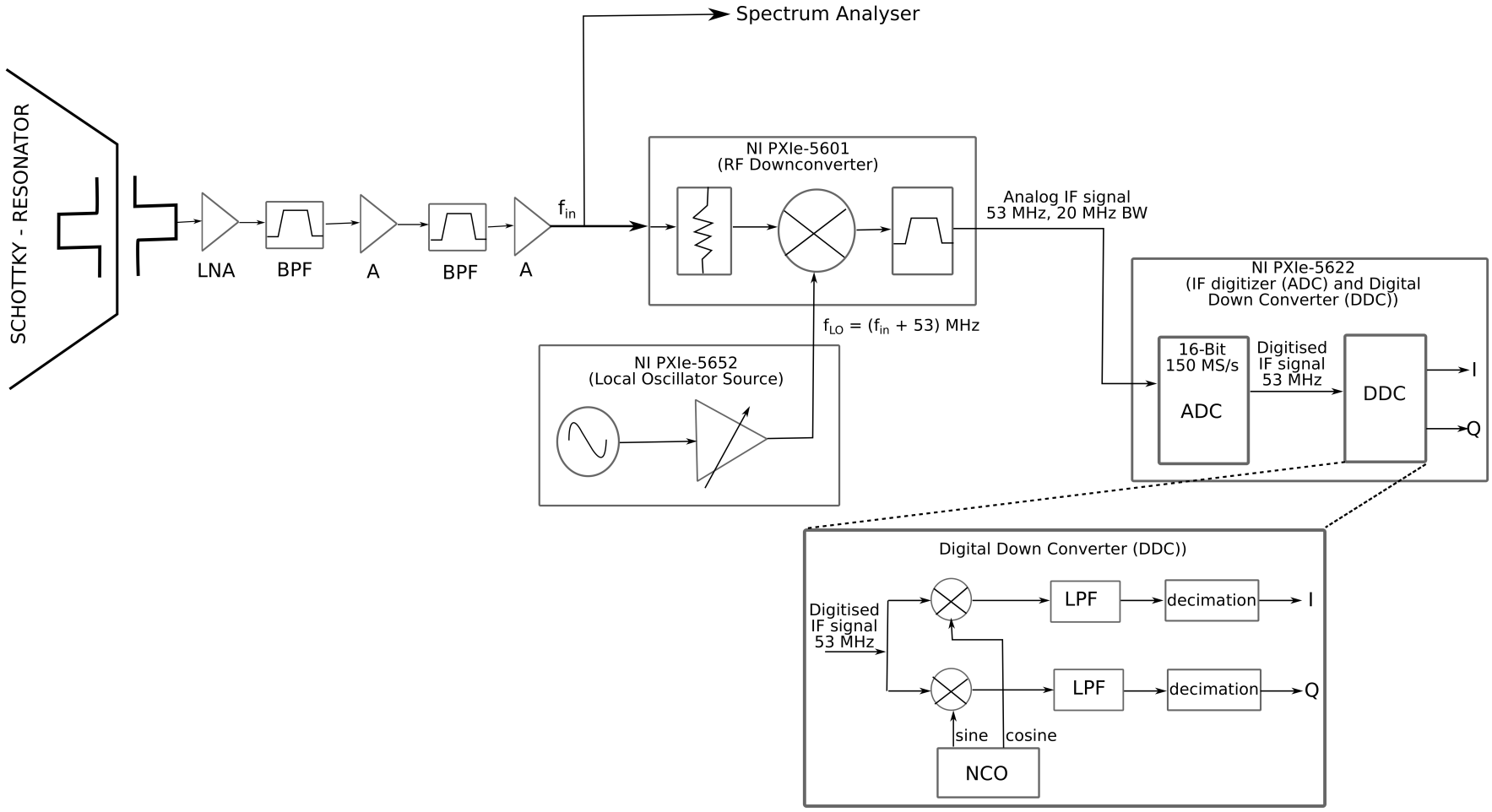

Figure 5.6: Block diagram of the NTCAP (adopted from [84]).

Chapter 6

Particle detector data analysis and results

As described in Section 4.4, the main experiment was performed in two parts. In the first part, $^{206}Pb^{81+}$ beam was used, wherein, both the particle detectors, namely the CsISiPHOS and a MWPC were employed. In the second part, $^{205}Tl^{81+}$ beam was used in the ESR for which a Schottky resonator and a MWPC were used. In this Chapter, I will discuss the data analysis and the results obtained by using the two particle detectors in the first part of the experiment with the $^{206}Pb^{81+}$ beam. The data analysis and results obtained using the Schottky resonator will be discussed in Chapter 7.

The idea of the measurement with the stable $^{206}Pb^{81+}$ beam was to measure the ratio $(\sigma_{I,\mathrm{Pb}} + \sigma_{c,\mathrm{Pb}})/\sigma_{I,\mathrm{Pb}}$ where $\sigma_{I,\mathrm{Pb}}$ and $\sigma_{c,\mathrm{Pb}}$ are the ionization and electron capture cross sections for H-like Pb ions, respectively. For the measurement, H-like $^{206}Pb^{81+}$ ions were injected in the ESR at 400 MeV/u, where both stochastic and electron cooling were active. As soon as the ions were cooled, the argon (Ar) gas jet target was switched on for ~ 300 s. With turning on of the gas jet target, we can have the following two dominant processes.

1. Ionization process:

The bound electron from the H-like $^{206}Pb^{81+}$ ions is stripped off and the formed $^{206}Pb^{82+}$ ions hit the CsISiPHOS detector placed in the inner pocket after the first dipole magnet downstream the gas jet target.

2. Capture process:

H-like $^{206}Pb^{81+}$ ions can capture an electron(s) from the Ar gas jet target

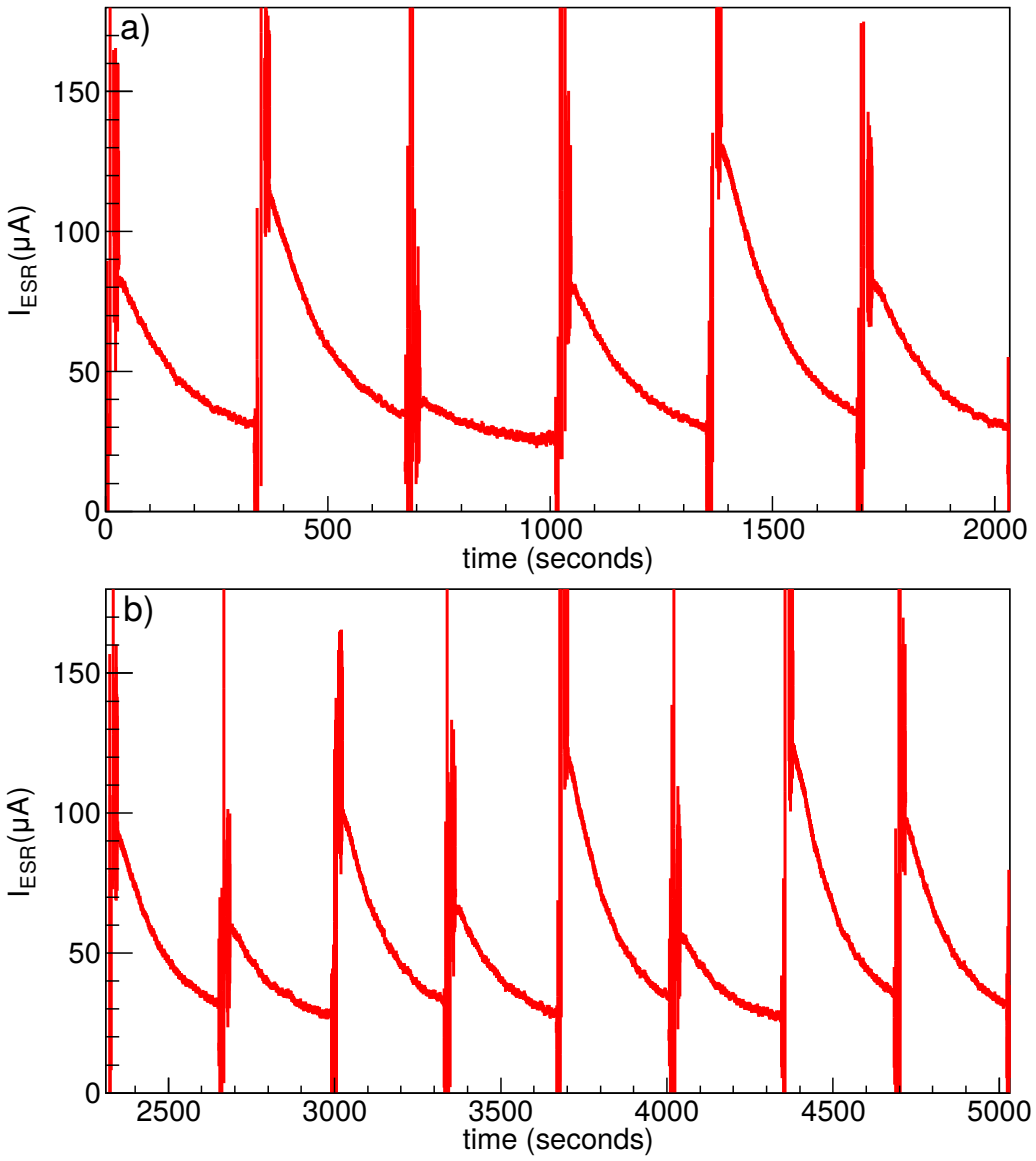

Figure 6.1: All fourteen injection measurements with the H-like $^{206}Pb^{81+}$ beam are shown. In this experiment, no target was used in the FRS and only $^{206}Pb^{81+}$ beam was stored in the ESR which was measured with the DCCT.

and form $^{206}Pb^{80+}$ (single-electron capture), $^{206}Pb^{79+}$ (double-electron capture)... ions. Single-electron captured $^{206}Pb^{80+}$ ions hit the MWPC detector placed in the outer pocket after the first dipole magnet downstream the gas jet target. Double- and higher-electron captured ions are bent stronger by the dipole magnet and do not hit the MWPC.

The position of the two particle detectors can be seen in Figure 4.5. With the $^{206}Pb^{81+}$ beam, there are in total fourteen injection cycle measurements. Figure 6.1 shows all fourteen injection cycles in terms of the beam current which is measured with the standard accelerator diagnostics, Direct-Current Current Transformer (DCCT) [85]. For all measurement cycles, the intensity of the injected beam was not the same. For example, the intensity of the third measurement cycle was low. During the experiment, there was a failure at the SIS-18 after the first six measurement cycles. The rest of the eight injection cycles were measured after the failure with the SIS-18 was solved.

To understand the data analysis of the two particle detectors, it is crucial to understand the response of each detector to ion hits. Thus, in the following sections, I describe the detector response one by one.

6.1 MWPC data analysis

A position-sensitive MWPC with the delay-line readout was employed in the experiment. Having an active area of 121×42 mm^2, the detector was used to count the number of single-electron captured $^{206}Pb^{80+}$ ions. For the MWPC, there are five readouts, Anode (A), x1, x2, y1 and y2 which are used to construct the position information. x1, x2, y1 and y2 are the positive signals induced on the adjacent orthogonal (X and Y direction) cathodes and A is the fast negative anode signal. All the analog signals containing the timing information are sent to a CFD which generates logical signals for a TDC. In the experiment, no amplitude information was recorded for the MWPC.

The time difference between the two sides of the delay-line gives the position information of the hitting particle under the condition that the sum of the signals from the two sides is constant. To get the sum condition, x-sum (x1 + x2 - 2×A) and y-sum (y1 + y2 - 2×A) are plotted as shown in Figure 6.2 a). It can be seen that x-sum spot is smeared out to the right of the spectrum and a weak spot for y-sum appears which contains $\sim$ 4.99% of the total events. To understand this, x (x1 - x2) vs x-sum and y (y1 - y2) vs y-sum are plotted. For x vs x-sum (Figure 6.2 b)), the smearing of the spot can be seen more clearly. This can be explained by the fact that during the experiment, a weak x1 signal was observed which did not allow a clean signal processing by the CFD. For y vs y-sum (Figure 6.2 c)), the weak spot

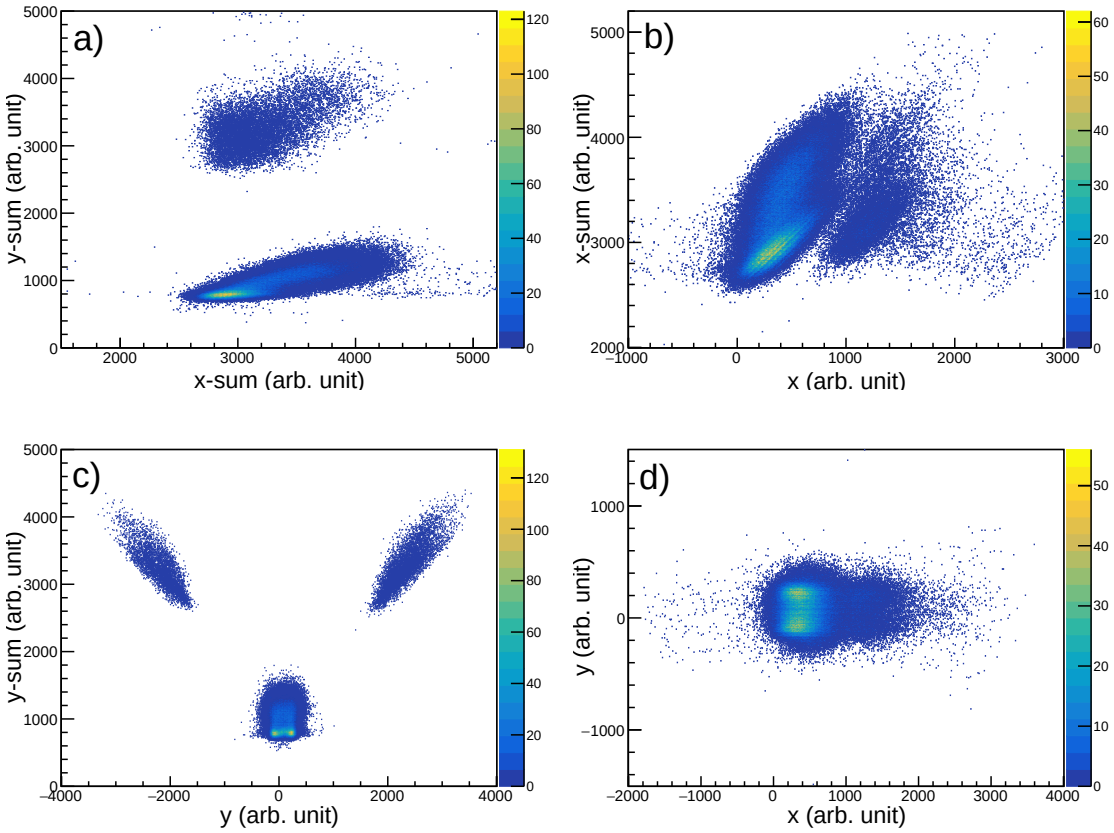

Figure 6.2: Different spectra for the MWPC are shown. In a), x-sum vs y-sum is plotted to constrain the sum condition for the detector. To understand the smearing of x-sum and additional band in y-sum, x vs x-sum and y vs y-sum are plotted in b) and c), respectively. In d), xy spectrum is obtained by considering the sum condition. For all plots, the first injection measurement cycle is used.

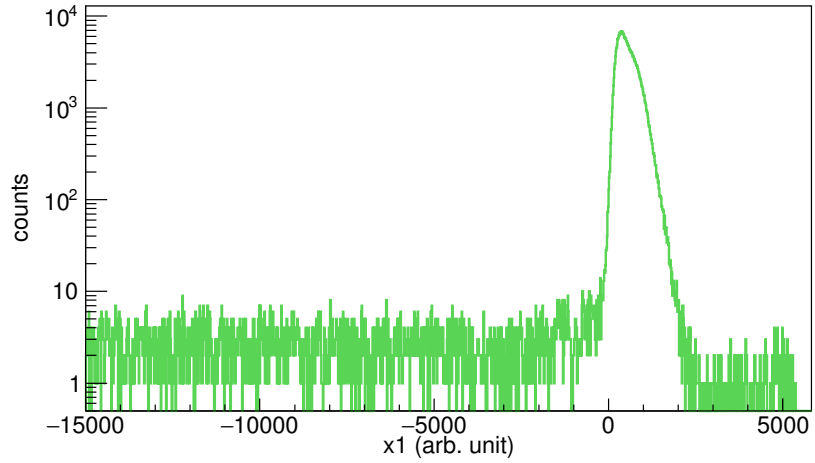

Figure 6.3: x1 signal from the first measurement cycle.

is split into two side bands equally. These side band events originate from signal reflections or multiple triggering of the CFD.

Considering the sum condition, Figure 6.2 d) shows a xy plot for the MWPC. $^{206}Pb^{80+}$ ions as the product of single-electron capture can be seen as a central spot in the figure containing $\sim$ 95.11% of the total events. One can observe a double peak in y which is likely due to a loose contact in the delay line. It is important to note that the position spectra are only used to ensure that the single-capture peak (as shown by x1 signal in Figure 6.3) is recorded and that it is the dominant component (95%). The anode signal used for the later analysis (scaler channel) is not affected by weak signals or reflections in the x/y channels. So, using the anode should give a reliable value for the single-capture, within a systematic offset of $\sim$ 5%.

A position calibration was not carried out during the experiment. MWPC stayed at -10 mm with respect to the nominal beam orbit (negative sign means outer orbit positions to the ring).

6.2 CsISiPHOS data analysis

CsISiPHOS is a complex ΔE-E telescope which was used for the purpose of counting the number of fully-stripped $^{206}Pb^{82+}$ ions. CsISiPHOS consists of six Si pads, a DSSD and a CsI scintillator crystal. The analysis for each component of the detector is described in the following sections.

6.2.1 DSSD

A double-sided silicon strip detector (DSSD) is used for the determination of the position of the particles hitting on it. The position information can be constructed by using equations 5.1 and 5.2. For the DSSD, there are four readouts, from the Left (L), Right (R), Top (T) and Bottom (B) sides with the condition that the sum of the signals from both the p- and n-sides is constant. Also, the same convention, x = (L - R)/(L + R) and y = (T - B)/(T + B) is used for the plots in this Chapter.

In order to constrain the sum condition, the sum of L + R (p-side) vs T + B (n-side) is plotted as shown in Figure 6.4. On the x- and y-axes are twice the channel number. We are using a 12-bit ADC in the DAQ and thus for each readout, we have 4096 channels. From Figure 6.4, we obtain the condition:

1. 2250 channel number < L + R < 2600 channel number
2. 2250 channel number < T + B < 2700 channel number

which is used to construct all the DSSD plots. The events below channel

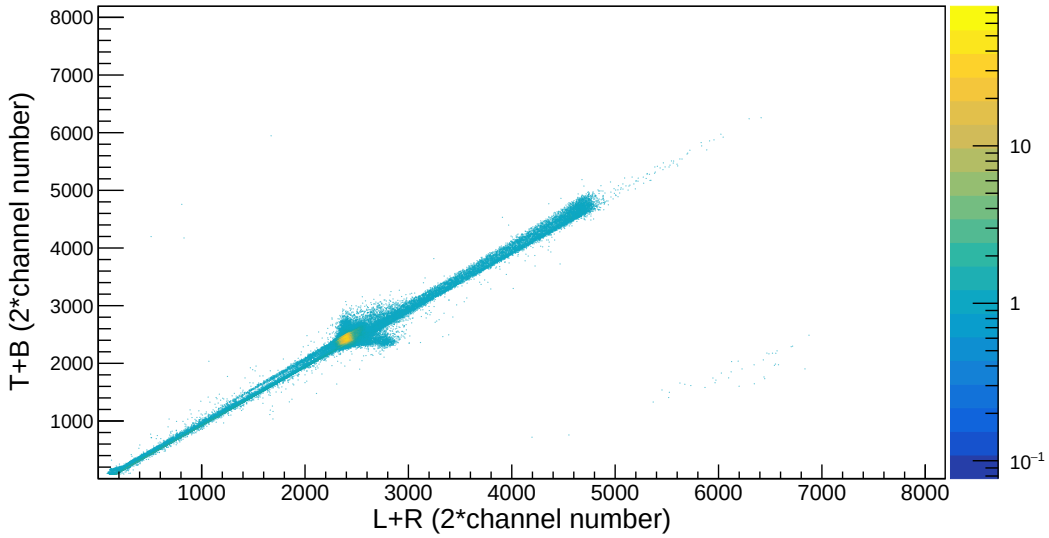

Figure 6.4: Spectrum of the sum of Left and Right sides (p-side) vs the sum of Top and Bottom sides (n-side). The sum for p- and n-sides should be constant, when the incident particles are monoenergetic.

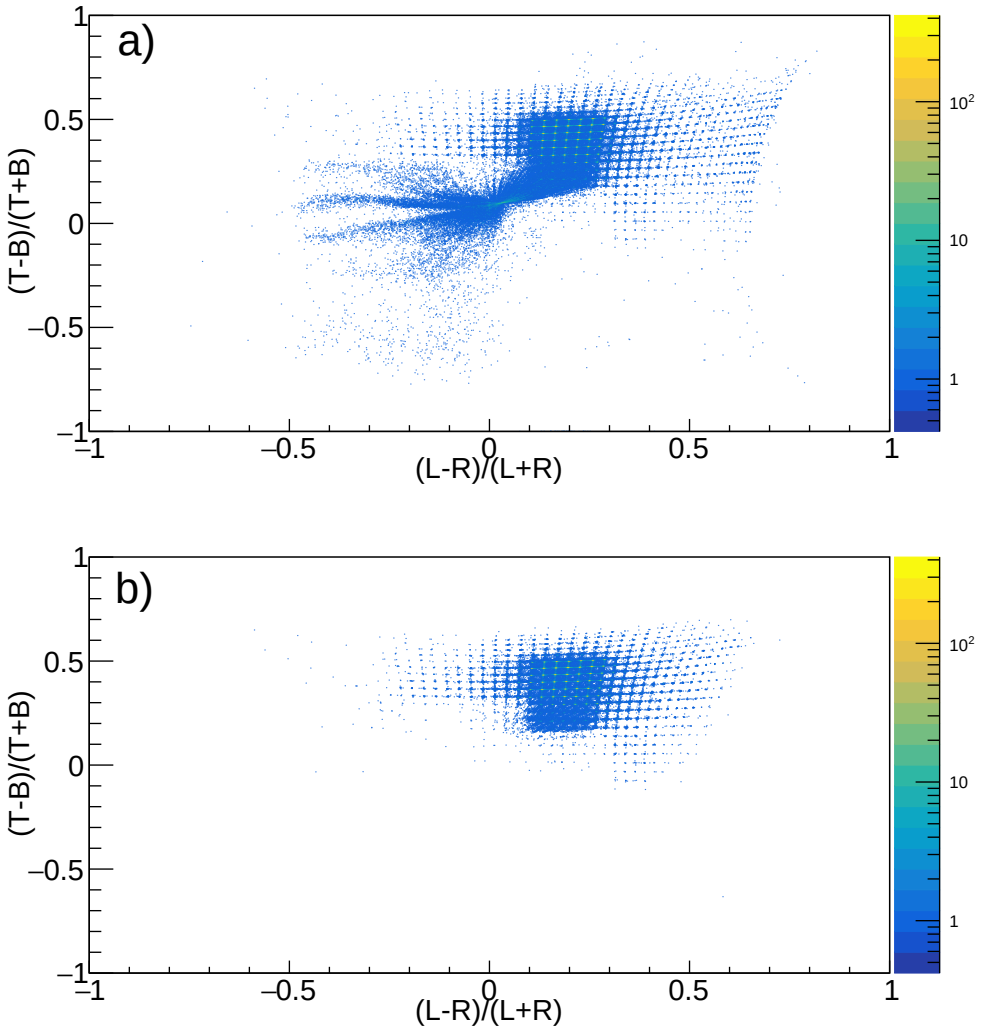

Figure 6.5: xy spectra for the DSSD. In a), no sum condition is used which shows the $^{206}Pb^{82+}$ beam spot with lots of background events. Using the sum condition, the spectrum in b) is cleaned and only good events hitting the DSSD can be seen.

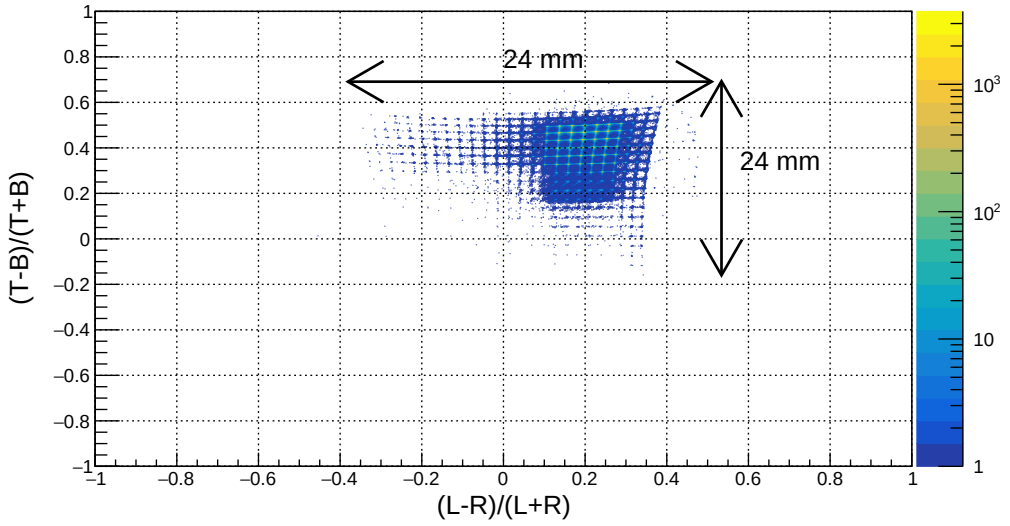

Figure 6.6: For the position calibration of the spectrum, the events that hit the DSSD and the CsI are selected. For the CsI, the dimensions are known from which the calibration is performed.

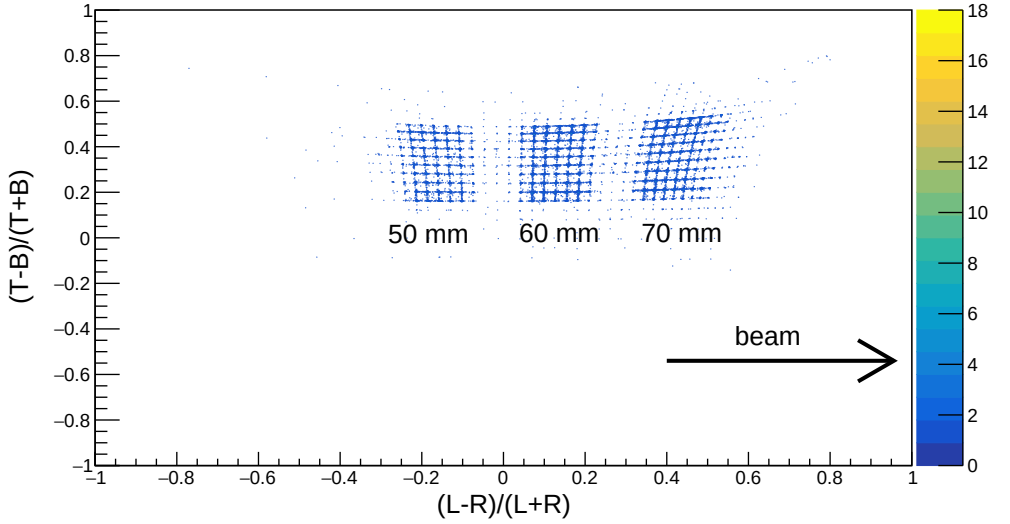

Figure 6.7: The particle detector was moved to different positions which can be seen in the above spectrum.

number $\sim$ 2200 are due to the bad signal processing and above channel number $\sim$ 2800 corresponds to the pile-up region (during high rate).

Figure 6.5 shows a xy spectrum obtained from the DSSD. In a), the sum condition is not applied and thus, a lot of bad and non-identified events can be seen. In b), a xy spectrum is obtained with the sum condition, wherein, one can see good events hitting the DSSD. One can also see the beam spot of fully-stripped $^{206}Pb^{82+}$ ions hitting the DSSD.

The next step is to do the position calibration of the xy spectrum obtained from the DSSD. For this purpose, the CsI, for which the dimensions are well known, is used. A thick CsI crystal having an area of 24×24 mm^2 (smaller than the DSSD) is used in the detector. By only selecting the events that hit the DSSD and the CsI, the xy spectrum is roughly calibrated. In Figure 6.6, one can see the events that hit both the DSSD and the CsI for all fourteen injection measurement cycles. From this, the xy spectrum for the DSSD is calibrated. One can also roughly obtain the size of the $^{206}Pb^{82+}$ beam hitting the detector which is $\sim$ 7×7 mm^2 as seen in Figure 6.6.

CsISiPHOS was placed in the inner pocket after the first dipole magnet downstream the internal gas jet target. For the data taking purpose, the detector was placed at +60 mm, where the positive sign indicates the x position to the inside of the ESR with 0 mm as the nominal beam orbit. While adjusting the position of the detector in the pocket, the detector was moved at positions +50 mm, +60 mm and +70 mm as shown in Figure 6.7. The position +70 mm is farther away from the beam in the inside direction, and one can see that the beam is to the right of the spectrum. This can be understood as when the detector is moved out of the ring, the position of the produced $^{206}Pb^{82+}$ beam spot is closer to the detector.

6.2.2 Si pads

The particle detector consists of six Si pads which are used for the energy loss ΔE measurement. For each Si pad, the p-side has 7 strips with no segmentation on the n-side. Thus, for each Si pad, there are 7 (for p-side) + 1 (for n-side) readouts. All the p-side (7×6) readouts are sent to MPR-32 preamplifier modules and the n-side (1×6) readouts to a MSI-8 preamplifier module.

For the analysis discussion, the n-sides of six Si-pads are defined as n1, n2, n3, n4, n5 and n6. For the p-sides of all Si pads, the analysis is not discussed. This is due to the fact that during the experiment, the sensitivity of MPR-32 preamplifier modules was set to 1 GeV. MPR-32 preamplifier modules have two sensitivity modes: 1 GeV and 5 GeV. From the ATIMA code [86] calculations, $^{206}Pb^{82+}$ beam at 400 MeV/u has an energy loss of

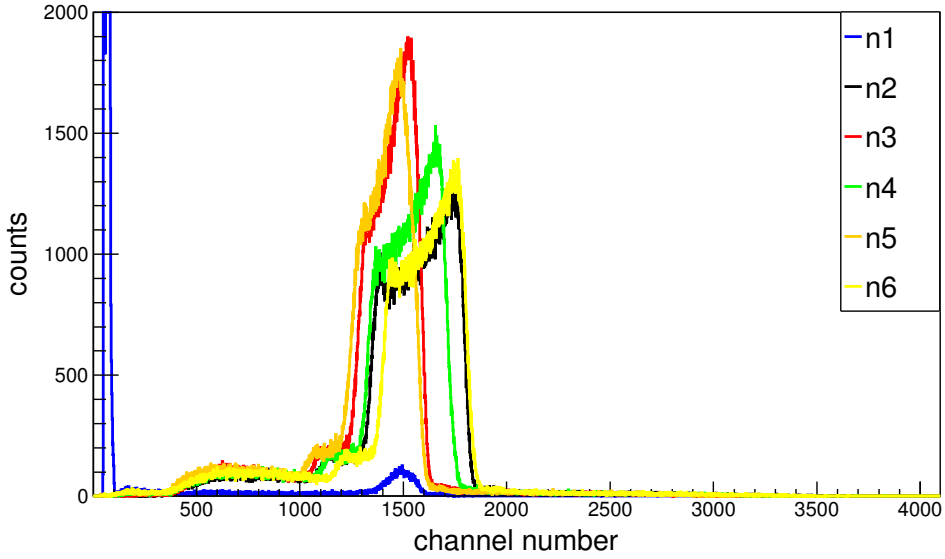

Figure 6.8: The signal from all n-sides of Si pads are plotted for the first measurement cycle.

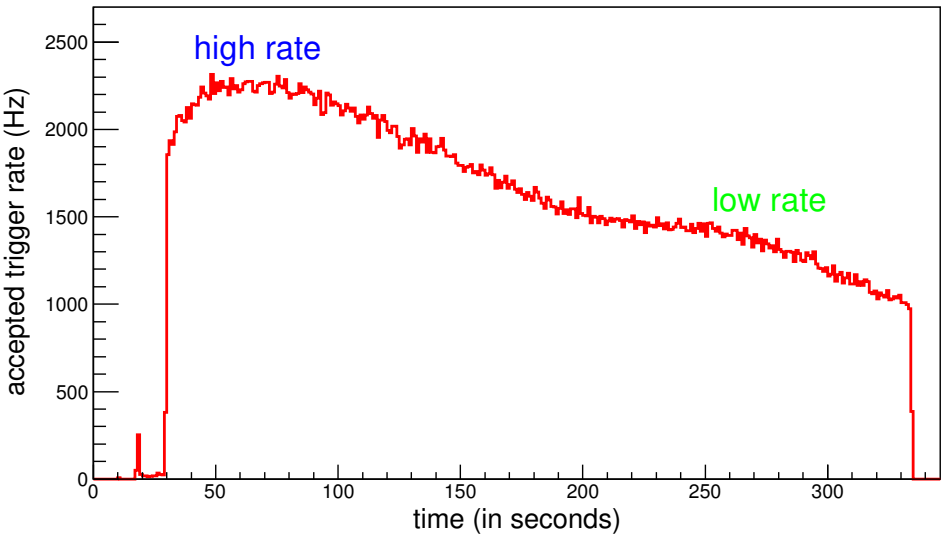

Figure 6.9: The accepted trigger rate for the CsISiPHOS for the first measurement cycle. It can be seen that the rate is initially high and it then decreases. The incoming raw trigger rate is plotted in Figure 6.13.

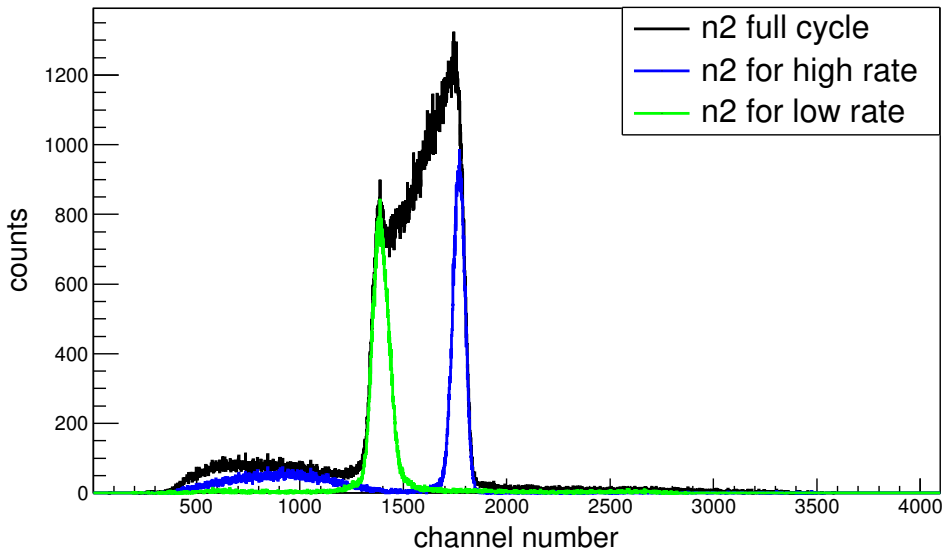

Figure 6.10: n2 signal is plotted for high and low rate separately.

$\sim$ 10 MeV/u in a Si-pad which corresponds to an incoming signal of $\sim$ 2.05 GeV. Since the sensitivity switch was adjusted to 1 GeV, the amplitude of incoming signals was not recorded correctly.

Figure 6.8 shows the n-side signals from all Si pads. One can clearly see a small signal from the n1 which is possibly due to the radiation damage during the setting of the experiment. The shape of the peaks of the n-side signals deviates from the expected Gaussian shape. To understand this deviation, the accepted trigger rate for the CsISiPHOS is plotted for the first injection measurement cycle as shown in Figure 6.9. It can be seen that the trigger rate is initially high and with time it decreases which affects the performance of the CsISiPHOS. To check this, the n-side spectrum for different rates is plotted on the top of the full measurement cycle as shown in Figure 6.10. A time window of 50 seconds is taken for high rate (40-90 s) and for low rate (280-330 s). The peak at low rate looks as expected which clearly suggests that the response of the detector is rate dependent. This is also confirmed for other n-sides and for the rest of the measurement cycles.

6.2.3 CsI

To completely stop the particles, a 10 mm thick CsI crystal is used in the particle detector which is coupled to a Si photodiode. The charged particles

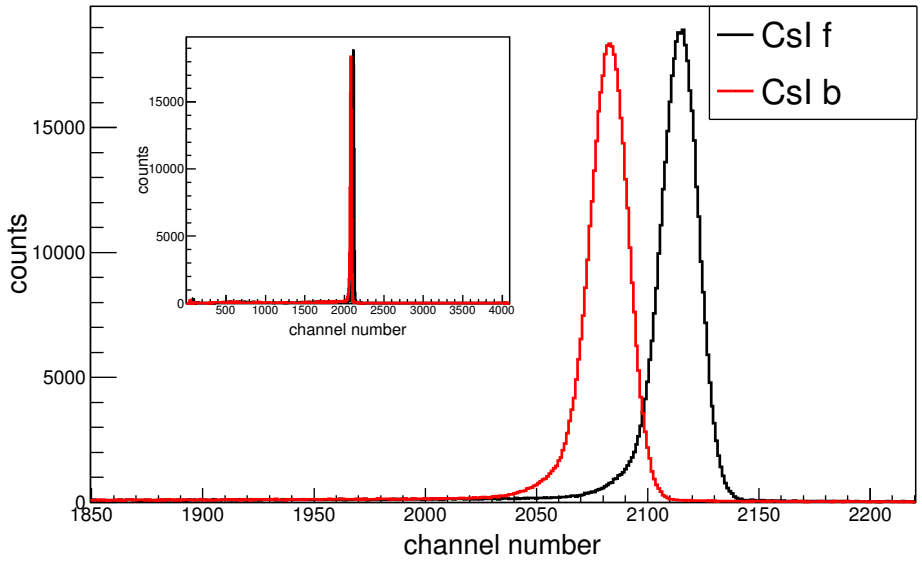

Figure 6.11: Spectra of the CsI from the front and the back side of the photodiode zoomed to the peak region. The inset plot shows the full range.

which lose their energy inside the CsI produce photons that are collected by the photodiode. For the Si photodiode, there are two readouts, from the front and the back side, defined as CsI f and CsI b for the analysis discussed here.

Figure 6.11 shows the spectra from the front and the back side of the photodiode which looks as expected. For plotting ΔE-E plots, the n-side of the last Si pad i.e. n6 and CsI f are used. In principle, one can consider any n-side of the Si pads which represents the energy loss ΔE. $^{206}Pb^{82+}$ ions are fully stopped in the CsI which represents the energy E.

In Figure 6.12 a), one can see a typical ΔE-E plot for one of the measurement cycles. The next step is to calibrate the ΔE-E spectrum. For this purpose, the ATIMA code [86] from LISE ++ [87] package is used to calculate the energy loss of $^{206}Pb^{82+}$ ions at 400 MeV/u hitting the detector. The energy loss of produced $^{206}Pb^{82+}$ ions in each detector component is given in Table 6.1. It is to be noted that for the calculations, the effect due to tilting of the detector components by 3° is not considered. From these calculations, the energy loss of ions in a Si-pad is $\sim$ 2.3 GeV and in the CsI crystal is $\sim$ 44 GeV. The calibrated ΔE-E spectrum is shown in Figure 6.12 b).

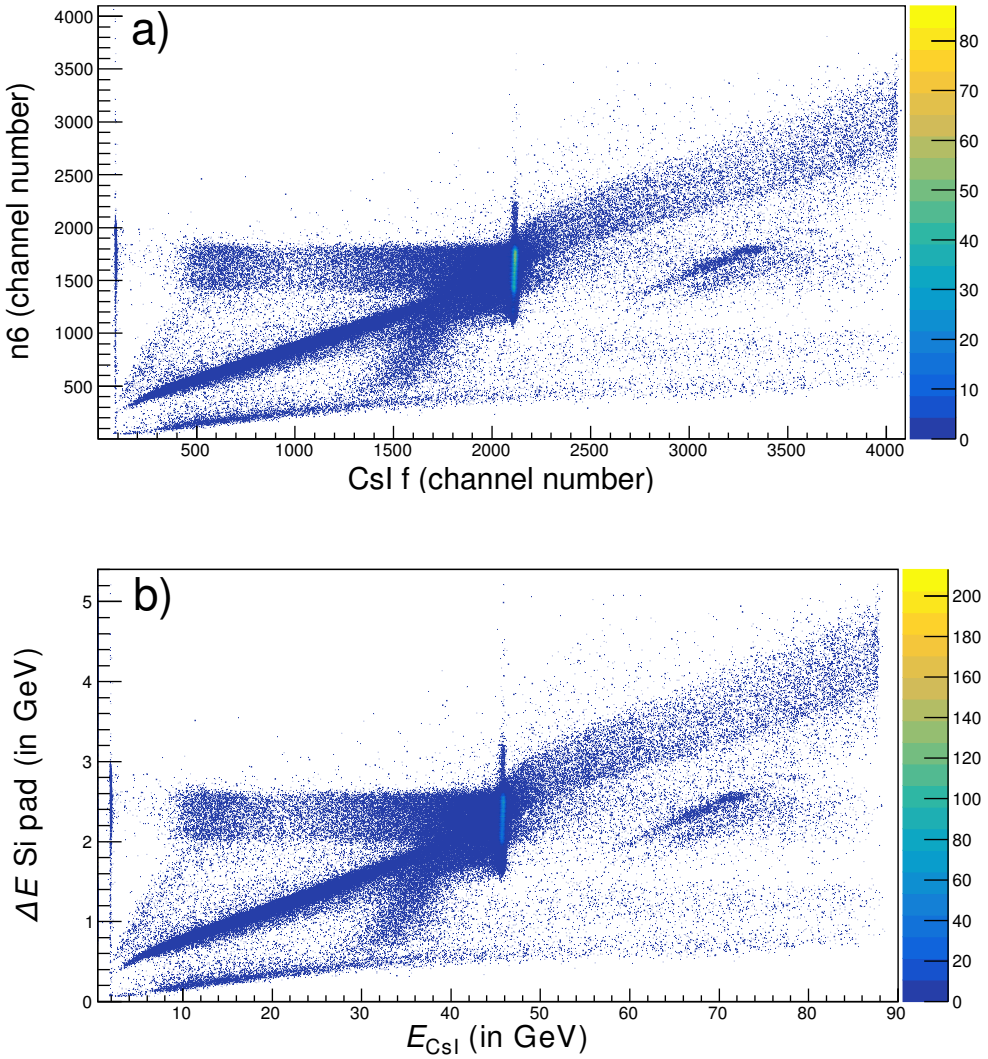

Figure 6.12: ΔE-E spectrum for one of the measurement cycles. The top spectrum is without the energy calibration and the bottom one is after the calibration.

Table 6.1: Energy loss in the CsISiPHOS calculated using the ATIMA code [86, 87].

CsISiPHOS	
Detector components	Energy loss (MeV/u)
Si pad	9.847
DSSD	5.955
Si pad	10.009
Si pad	10.118
Si pad	10.235
Si pad	10.359
Si pad	10.492
Ta	110.185
CsI	222.8

6.3 Dead time of DAQ

For both, the CsISiPHOS and the MWPC, a common DAQ system was used. A master trigger, which is the OR of triggers from the CsISiPHOS and the MWPC was used for triggering the DAQ. Due to the dead time of the DAQ, the accepted trigger rates and the incoming raw trigger rates from the CsISiPHOS and the MWPC are different. Dead time of the DAQ depends on the conversion rate of ADC modules and on the readout time for all other modules (TDC, scaler).

Figure 6.13 shows the accepted and raw trigger rates for one of the measurement cycles, where

a) Trigger 1 raw is the incoming raw trigger for the CsISiPHOS,
b) Trigger 2 raw is the incoming raw trigger for the MWPC,
c) Trigger 1 is the accepted trigger for the CsISiPHOS and
d) Trigger 2 is the accepted trigger for the MWPC.

From Figure 6.13, one can see that as soon as the gas jet target is switched on, the incoming raw trigger rates are high for both the detectors and decrease with decreasing beam intensity over time. However, the accepted trigger rates are low and one can estimate the dead time for both the detectors at

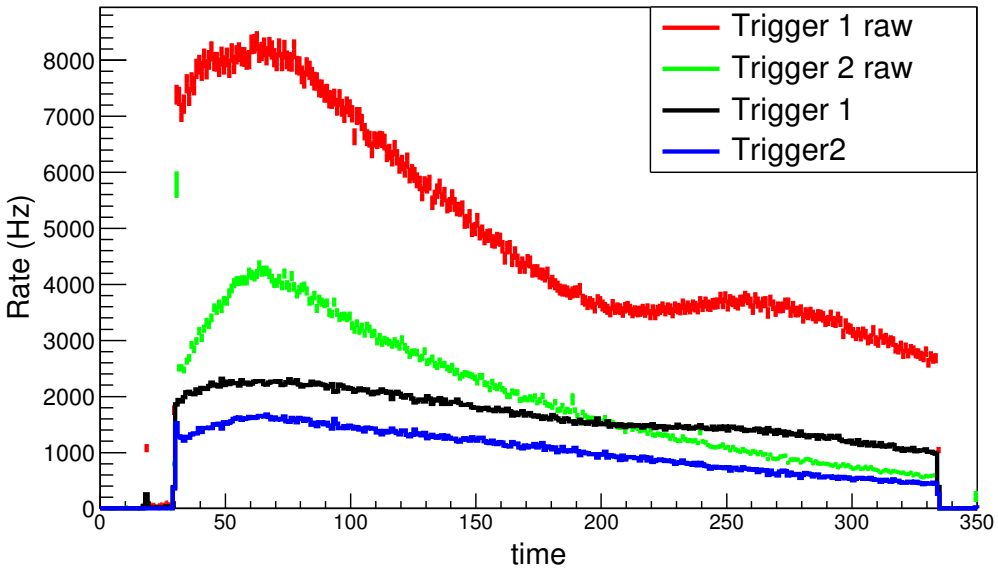

Figure 6.13: Different trigger rates for the first injection measurement cycle.

different rates using the following expression

$$\text{dead time } (\%) = 1 - \frac{\text{accepted trigger}}{\text{incoming raw trigger}} \quad . \tag{6.1}$$

For high rate, dead time for the CsISiPHOS and the MWPC is $\sim$ 72% and $\sim$ 61% and for low rate is $\sim$ 63% and $\sim$ 33%, respectively.

Another approach to estimate the dead time is to plot the number of events in any one of the components of the CsISiPHOS vs time between the last trigger events. This is done for n6 and is shown in Figure 6.14. In this plot, the nominal energy loss events are visible around the channel number $\sim$ 1750. For short time periods to the last trigger, the expected pile-up distribution is clearly observable above this channel. At short time periods, an additional intense amplitude reduction effect shows up. This is caused by a preamplifier saturation effect which builds up on a longer time scale and introduces a shift of the signal baseline below 0 Volt and results in a lowered amplitude measurement. At lower detector rates this effect slowly disappears again (see also Figure 6.15).

To get the dead time per event, the x-axis is zoomed in for 0-1 ms as shown by the inset plot in Figure 6.14. The empty white space is due to the dead time of the DAQ which is $\sim$ 150 µs.

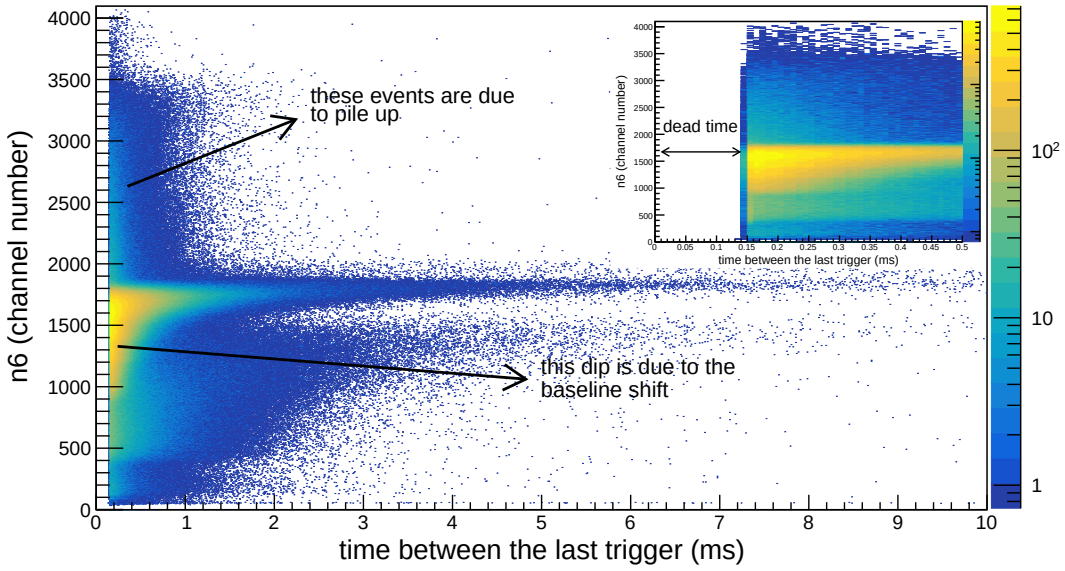

Figure 6.14: n6 vs time between the last trigger.

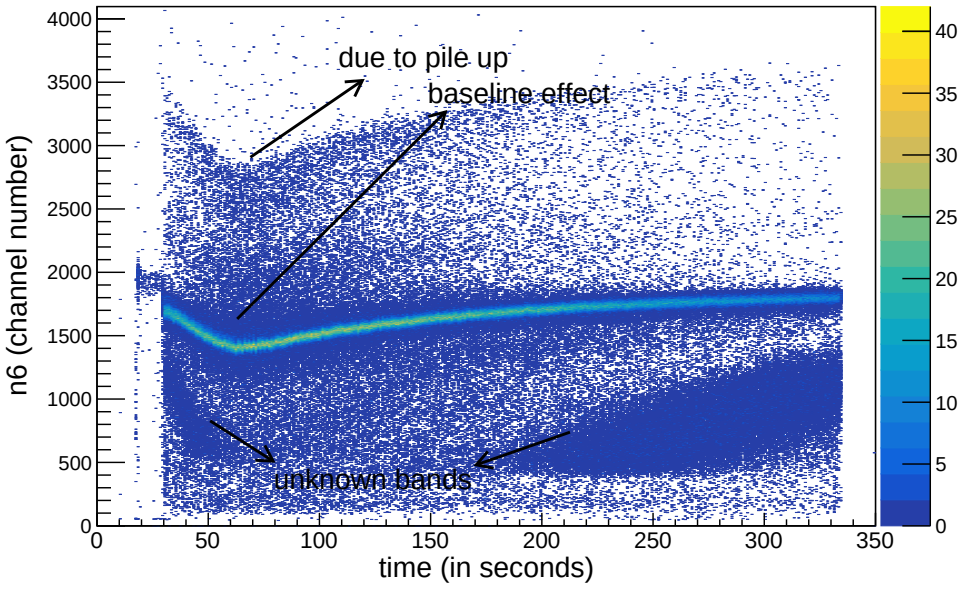

Figure 6.15: Propagation of events hitting on the n6 with time.

6.4 Unknown low energy band

While plotting ΔE of n6 vs time, an unknown band appears at low energy whose origin is not fully understood. This can be seen in Figure 6.15 where only the first injection measurement cycle is shown. One can clearly see the appearance of these low energy bands, which are seen for all detector components of the CsISiPHOS, and for all measurement injection cycles (see Appendix A). The contribution of these unknown bands in the spectrum is about $\sim 10\%$ of the total events.

The next approach was to look into the Schottky data which was recorded by a 245 MHz Schottky resonator during the experiment. The analysis details of the Schottky data are discussed in Chapter 7. It is interesting to see the appearance of huge side bands during one of the storage measurements with the $^{206}Pb^{81+}$ beam at electron cooler current $I_e = 200$ mA. In this measurement, the aim was to store H-like $^{206}Pb^{81+}$ beam for 2 hours and measure its storage decay constant. Figure 6.16 shows a two-dimensional Schottky spectrum where sizeable side bands are visible.

During the entire experiment with the $^{206}Pb^{81+}$ beam, the stochastic cooling was active in the outer orbit of the ESR and it could not be technically

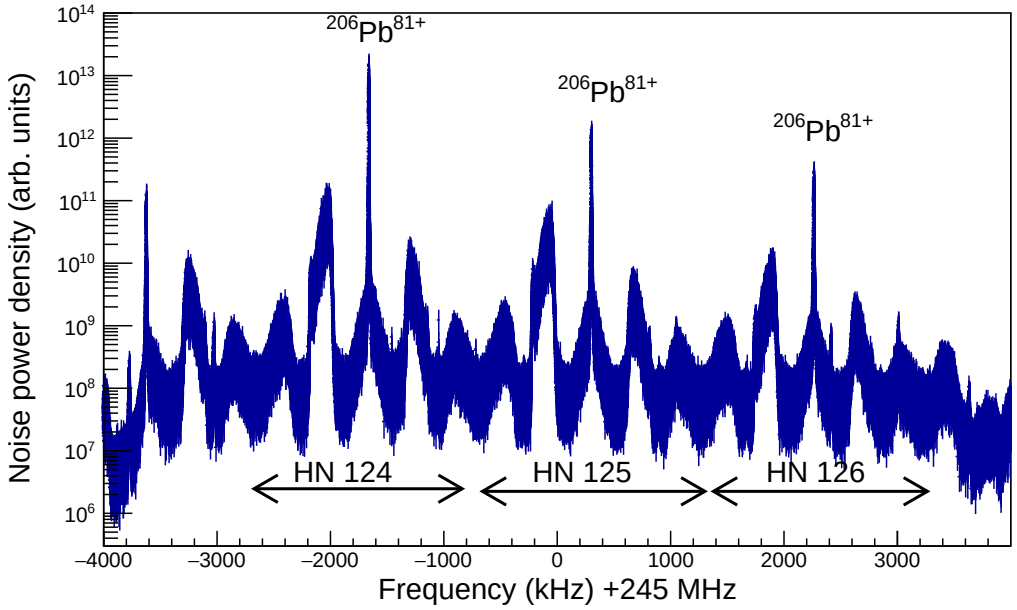

Figure 6.16: Appearance of side bands along with the main $^{206}Pb^{81+}$ beam can be seen for three harmonics in the Schottky spectrum.

switched off. For each measurement cycle, $^{206}Pb^{81+}$ ions were first injected into the stochastic cooling region on the outer orbit, then the ions were shifted to the inner orbit where the electron cooling was active and finally the gas jet target was switched on. A possible explanation for the side bands is that a fringe effect of stochastic cooling continuously kicks ions out of their nominal orbit. Instead of losing those ions after several turns, electron cooling keeps at least a part of them within the acceptance of the ring. These resulting exotic orbits might be responsible for the frequency side bands and possibly also for the low energy bands in the CsISiPHOS.

6.5 Determination of the ratio

Unfortunately, reliable ion counting with the CsISiPHOS detector, as needed for the ionization cross section determination, is impossible considering the high rates and the accompanying effects of pile-up, baseline shift and appearance of low energy bands. However, in the experiment, data from the DCCT [85] was also recorded from which the total particle number in the ring can be determined. This means that the sum of the counts on the CsISiPHOS and the MWPC should match with the reacted particle number measured with

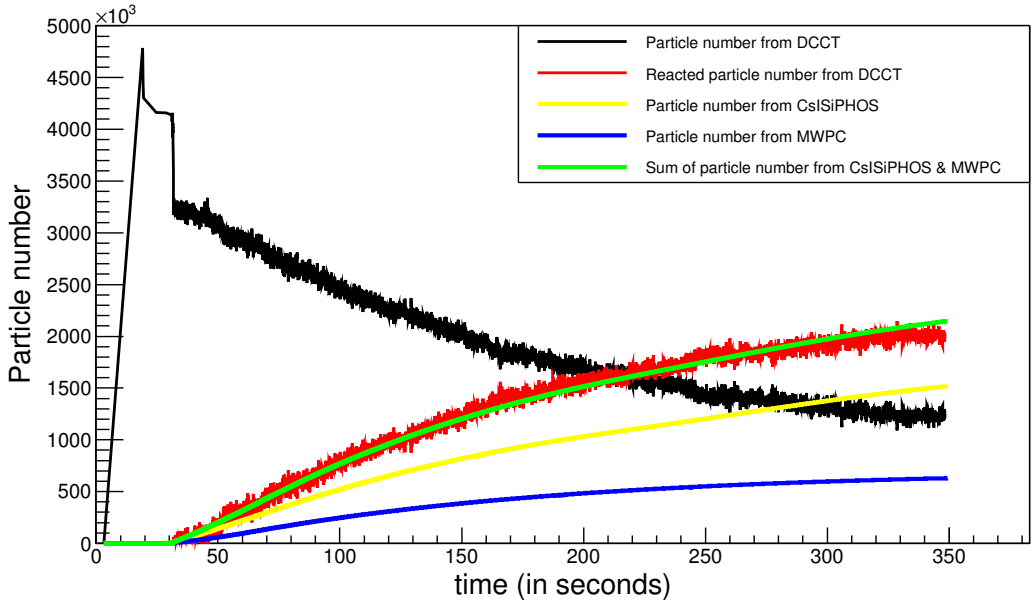

Figure 6.17: Particle number measured from CsISiPHOS, MWPC and DCCT for the first measurement cycle.

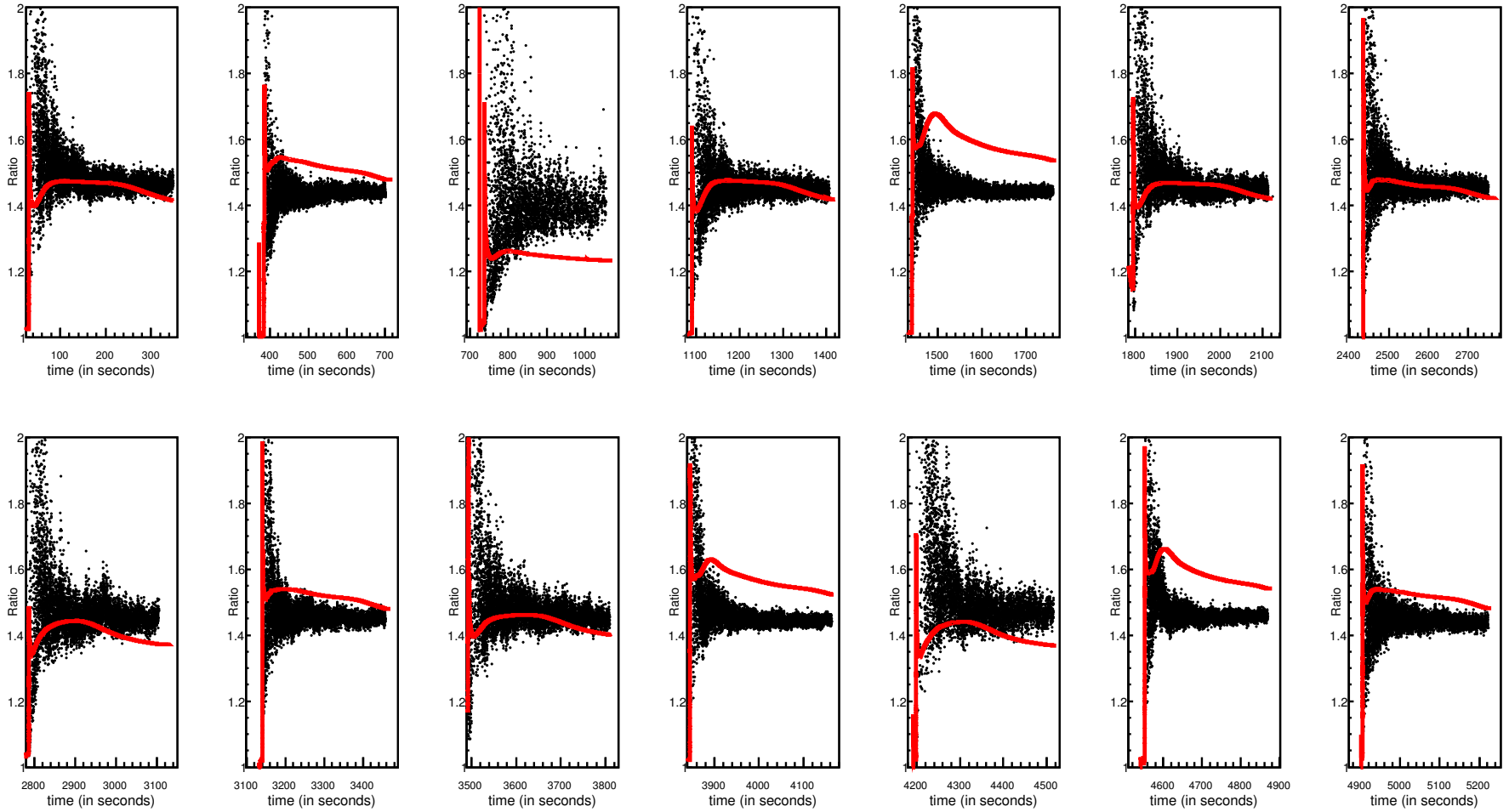

Figure 6.18: Comparison of the ratio obtained from equation 6.3 (red line) and equation 6.4 (black points) for all fourteen injection cycles.

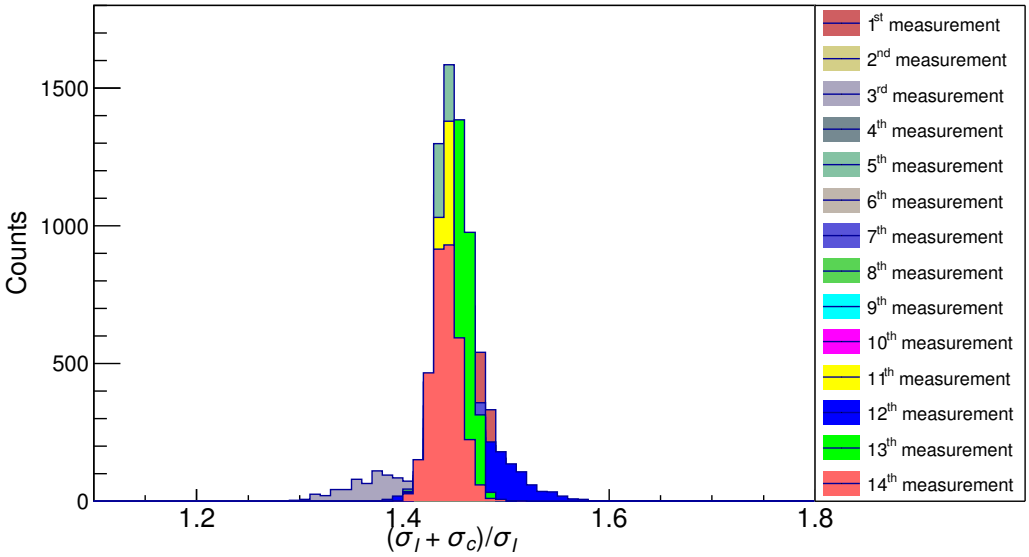

Figure 6.19: Ratios obtained from all fourteen measurements.

the DCCT, with the assumption that the electron capture and ionization are the only dominant losses for the $^{206}Pb^{81+}$ beam.

This is confirmed for one of the measurement cycles as shown in Figure 6.17. It can be seen that the sum of the raw triggers from the two particle detectors (shown with green line) agrees very well with the reacted particle number obtained from the DCCT using

$$N_{\text{DCCT Reacted}} = N_0(1 - e^{-\lambda t}) \ , \tag{6.2}$$

where N_0 is the particle number at the beginning of the measurement cycle measured by the DCCT, λ is the decay constant and t is the time during which the gas jet target is active ($t = 300$ s). DCCT measures ion current continuously for the entire acceptance of the ring and has a certain offset value (a few µA). As the reacted particle number is measured using equation 6.2, the offset value does not affect $N_{\text{DCCT Reacted}}$. It is also important to note that the agreement between the sum of the raw triggers from the two particle detectors and the reacted particle number is not observed for all fourteen injections (see Appendix A) as the response of the CsISiPHOS is rate dependent.

With this approach, one can obtain the ratio $(\sigma_{I,\text{Pb}} + \sigma_{c,\text{Pb}})/\sigma_{I,\text{Pb}}$ using

either CsISiPHOS and MWPC or DCCT and MWPC by

$$\frac{(\sigma_{I,\mathrm{Pb}} + \sigma_{c,\mathrm{Pb}})}{\sigma_{I,\mathrm{Pb}}} = \frac{N_{\mathrm{CsISiPHOS}} + N_{\mathrm{MWPC}}}{N_{\mathrm{CsISiPHOS}}} \ , \tag{6.3}$$

$$\frac{(\sigma_{I,\mathrm{Pb}} + \sigma_{c,\mathrm{Pb}})}{\sigma_{I,\mathrm{Pb}}} = \frac{N_{\mathrm{DCCT\ Reacted}}}{N_{\mathrm{DCCT\ Reacted}} - N_{\mathrm{MWPC}}} \ . \tag{6.4}$$

This is done for all fourteen measurement cycles as shown in Figure 6.18. The red line is the ratio obtained from equation 6.3 and the black points are the ratio obtained from equation 6.4. One can note that due to the rate dependence of the CsISiPHOS, the red line is not constant. This is not the case for the DCCT as it is rate independent.

Using equation 6.4, a constant ratio value can be seen for all fourteen injection measurement cycles, where the DCCT and the raw anode signal from the MWPC are used to get the ratio. For each injection measurement, the last 150 s are taken and the obtained value of the ratio is

$$\frac{(\sigma_{I,\mathrm{Pb}}+\sigma_{c,\mathrm{Pb}})}{\sigma_{I,\mathrm{Pb}}} = 1.449(4)_{\mathrm{stat}} \ .$$

The above is the mean value of the ratio obtained from all fourteen measurements which are shown in Figure 6.19. The error in the above value is purely statistical. To account for the contribution of the systematic error σ_{syst}, normalized χ_n value is calculated using

$$\chi_n = \sqrt{\frac{1}{n}\sum_{i=1}^{n} \frac{(\mathrm{ratio}_i - \mathrm{mean\ ratio})^2}{\sigma_i^2 + \sigma_\mu^2 + \sigma_{\mathrm{syst}}^2}} \ , \tag{6.5}$$

where n = 14, ratio_i is the value of the ratio for i^{th} measurement cycle with σ_i as its error, mean ratio = 1.449 and $\sigma_\mu = 0.004$. The obtained value of $\chi_n = 3.46$ is out of the expected range of $\chi_n = 1\pm0.24$, which means that an additional systematic error $\sigma_{\mathrm{syst}} = 0.015$ must be added. Thus,

$$\frac{(\sigma_{I,\mathrm{Pb}}+\sigma_{c,\mathrm{Pb}})}{\sigma_{I,\mathrm{Pb}}} = 1.449(4)_{\mathrm{stat}}(15)_{\mathrm{syst}} \ .$$

The systematic uncertainties can arise from the frequency channel to beam current conversion and the losses of $^{206}Pb^{81+}$ ions due to interaction with the electron cooler and the residual gas in the ring. Other unknown sources during the experiment may contribute to it. It is vital to emphasize that the ratio can also be evaluated using the rate instead of the particle number (in equation 6.4).

Since the DCCT and the anode signal from the MWPC are used for counting the ion number for the ratio, one does not need to consider the

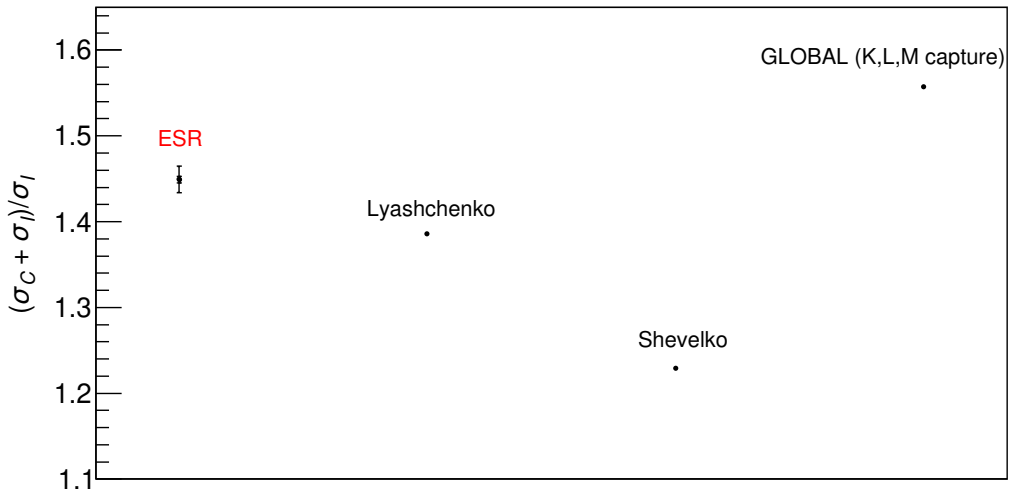

Figure 6.20: The comparison of our result with theoretical values.

efficiency (ϵ) of the detectors. For trigger rates below 10 kHz, as here, one can safely assume $\epsilon = 1$. Nonetheless, there are still analog dead time effects (signal overlap) or gas quenching effects (lowered amplitude).

To compare our result, three theoretical values are used. First value is obtained by using the GLOBAL code [87] by considering K-($\sigma_c = 5.57\times10^2$ barn), L-($\sigma_c = 1.34\times10^2$ barn) and M-shell ($\sigma_c = 4.45\times10$ barn) single electron capture and ionization ($\sigma_I = 1.32\times10^3$ barn) and value of the ratio is 1.557. It is to be noted that the GLOBAL cross section values have large uncertainties ranging from $\sim$ 10 % to $\sim$ 20 %. For the second theoretical value, electron capture ($\sigma_c = 3.94\times10^2$ barn) and ionization ($\sigma_I = 1.72\times10^3$ barn) cross sections are provided by V. P. Shevelko (see Figure A.11). For the third theoretical value, electron capture ($\sigma_c = 5.19\times10^2$ barn) and ionization ($\sigma_I = 1.34\times10^3$ barn) cross sections are provided by Konstantin N. Lyashchenko. The comparison between the values is shown in Figure 6.20.

The experimentally measured value of the ratio is used for the final determination of the half-life of the bound-state beta decay of $^{205}Tl^{81+}$ ions which is discussed in details in the next Chapter.

Chapter 7

Schottky resonator data analysis and results

7.1 Treatment of raw data

Schottky data for the entire experiment were recorded by the NTCAP in the form of complex samples of IQ in the time domain. The data is stored in the form of Technical Data Management Streaming (TDMS) format with each file containing 4096 (2^{12}) frames and each frame containing 262144 (2^{18}) data points. The data in the time domain is converted into the frequency domain by applying the Fast Fourier Transform (FFT) [88] technique which involves the following steps:

1. Rectangular windowing function is applied to the digitized IQ points per frame. Windowing is done in order to avoid the appearance of strong side lobes ("spectral leakage") around the frequency peaks after the FFT is performed. Applying a windowing function means that a part of the original data is discarded before the FFT is performed. The smoother the windowing is, the more the data is discarded and thus an appropriate choice of the windowing function must be made.

2. The "windowed" IQ points per frame are Fourier transformed using [88]

$$X(m) = \sum_{n=0}^{N-1} x(n) e^{-\frac{i2\pi nm}{N}} \quad , \tag{7.1}$$

$$X(m) = \sum_{n=0}^{N-1} x(n) \Big(\cos(2\pi nm/N) - i \sin(2\pi nm/N) \Big) \quad , \tag{7.2}$$

where n, m = 0, 1, 2,.... N-1, and N are the number of IQ points per frame (i.e. 2^{18}). A special algorithm, FFT is used to decrease the computing time needed to perform the Fourier Transform.

After going through steps 1 & 2, we get a frequency spectrum with 2^{18} = 262144 frequency channels and a frequency resolution of 30.52 Hz/channel. For each TDMS file, 4096 such spectra are obtained with the observation time of each spectrum to be 32.77 ms. In order to attain a better signal-to-noise ratio, the averaging technique is employed. Averaging cancels the fluctuations from random noise where the following relation applies to the noise background [89]

$$\frac{\sigma_I}{I} = \frac{1}{\sqrt{N_{aver}}} \ , \tag{7.3}$$

where I is the intensity of a channel in the frequency spectrum, σ_I is the standard deviation of the intensity, N_{aver} is the number of frames averaged to produce the frequency spectrum. For the current data analysis, 8 spectra (N_{aver} = 8) are averaged together after performing the FFT, and one is left with 512 spectra in a TDMS file with the observation time of each spectrum to be 262.14 ms.

By increasing the number of IQ points per frame (before performing the FFT), the width of any channel in the frequency spectrum is decreased or in other words, the frequency resolution is increased. The width δf is related to the observation time δt of any spectrum used by the FFT algorithm to produce the corresponding frequency spectrum by the Nyquist relation as

$$\delta f = 1/\delta t \ .$$

It may be noted that by increasing the frequency resolution, the observation time of each spectrum increases which is not optimal for experiments where produced radioactive nuclei have shorter half-lives. Since for the current experiment, $^{205}Tl^{81+}$ ions are long-lived, increasing the frequency resolution is not a problem.

7.2 Evaluation of spectra

As described in Section 5.3.1, for the experiment, an IQ rate of 8 MS/s was used which covers 8 MHz of bandwidth. This contains three Schottky Harmonic Numbers (HNs) namely HN 124, HN 125 and HN 126 with a carrier frequency of $\sim$ 245 MHz. Figure 7.2 shows a full frequency spectrum with the frequency ranging from 241 MHz to 249 MHz and containing 262.14 ms of measurement time.

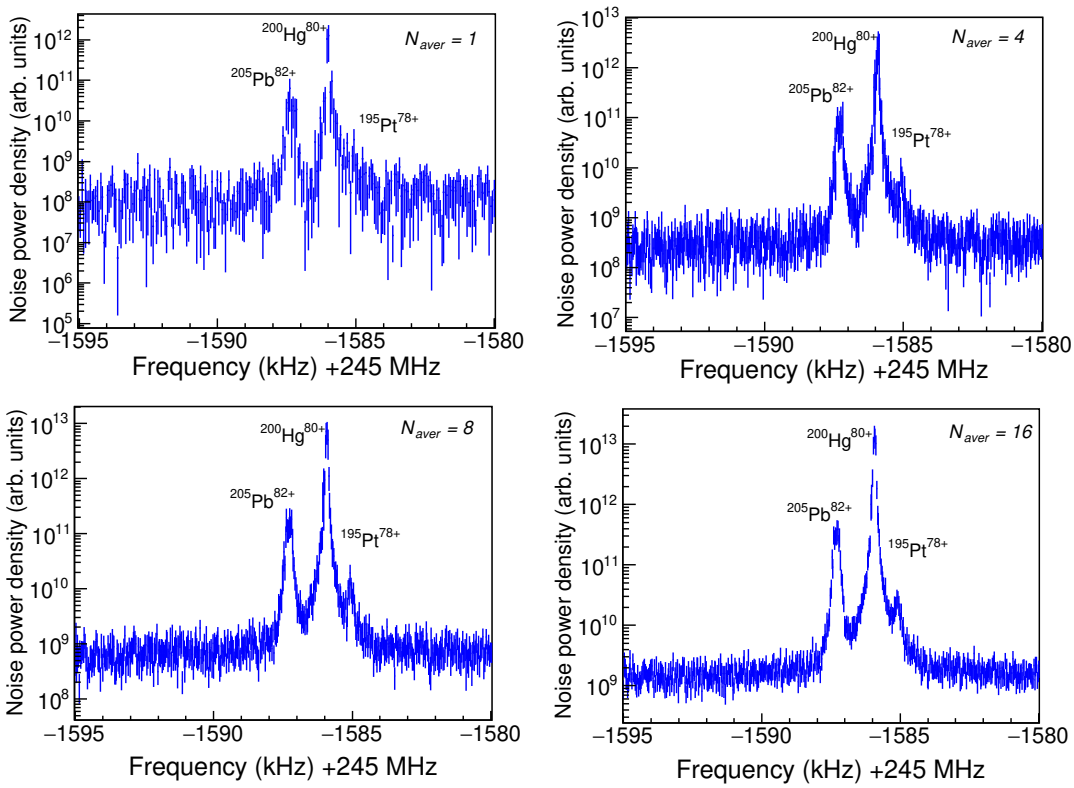

Figure 7.1: Comparison of the frequency spectra produced from the same data, but with different numbers of averaging. With increasing N_{aver}, the noise background level decreases. $N_{aver} = 8$ is chosen for the data analysis as the noise background level is considerably low which leads to the unambiguous determination of frequency peak signals. The spectra are zoomed into the frequency range of the daughter ions for HN 124.

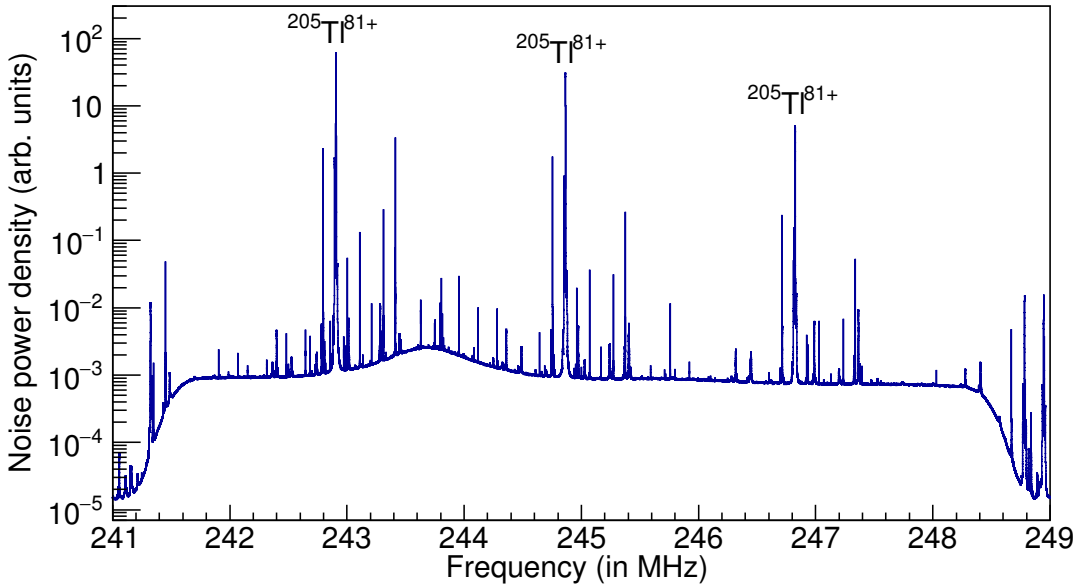

Figure 7.2: Full frequency spectrum obtained after the FFT. It depicts three Schottky harmonics HN 124, HN 125 and HN 126. The main peak in all three harmonics is of $^{205}Tl^{81+}$ ions.

The kinetic energy of 400 MeV/u of the stored $^{205}Tl^{81+}$ ions corresponds to a relativistic γ-factor of 1.429(2) with an ion velocity of 71% of the speed of light ($\beta = 0.714$ c). Thus, the mean revolution frequency of stored $^{205}Tl^{81+}$ ions in the ESR (circumference = 108.36 m) reaches up to $\sim$ 1.97 MHz. For the current experiment, a non-destructive resonant Schottky cavity with a resonance frequency $\sim$ 243.7 MHz was employed for the data taking. Schottky noise signal of 124^{th}, 125^{th} and 126^{th} harmonics of the revolution frequencies that are close to the resonance frequency of the resonator were recorded.

7.3 Steps of measurement

For the experiment, $^{205}Tl^{81+}$ ions were produced via the projectile fragmentation technique in the FRS and after being well separated from the same A/Z $^{205}Pb^{81+}$ contaminant ions, $^{205}Tl^{81+}$ ions were stored in the ESR for the measurements. Due to the radioactive technique adopted for the production of $^{205}Tl^{81+}$ ions, many other ions were produced as well which were then stored with the main $^{205}Tl^{81+}$ ions in the ESR. Different produced ions are

shown in Appendix B. Very close to the frequency of $^{205}Tl^{81+}$ ions are mixed hydrogen-like (H-like) $^{200}Hg^{79+}$ and fully-stripped $^{200}Au^{79+}$ ions which were stored during the measurement. For the current data analysis, each storage measurement is divided into four steps:

a) Step 1:

After sufficient accumulation of $^{205}Tl^{81+}$ ions in the inner orbit of the ESR, stacked $^{205}Tl^{81+}$ ions were shifted to the outer orbit and then a storage measurement started. For the start of the measurement, time is defined as $t = 0$ seconds (s). Then, $^{205}Tl^{81+}$ ions were stored for different storage times t_s as per the requirement of the storage measurement. The electron cooler current during the storage period was $I_e = 20$ mA, which was kept low in order to minimize the recombination rates between the stored ions and the electrons in the cooler.

b) Step 2:

At the end of each storage measurement i.e. at $t = t_s$, the internal argon (Ar) gas jet target was switched on for ~ 600 s. This was done in order to ionize/strip off the last electron from the β_b decayed H-like $^{205}Pb^{81+}$ daughter ions to produce fully-stripped $^{205}Pb^{82+}$ ions which were then separated in frequency and can be detected. In this step, $I_e = 200$ mA which enables proper cooling of different ions in the ring.

c) Step 3:

After the gas jet target being active for ~ 600 s, at this step, the target was switched off. The electron cooler current remains 200 mA as the fully-stripped $^{205}Pb^{82+}$ ions were still mixed with $^{200}Hg^{80+}$ ions in frequency. After some time, the daughter ions were cooled and can thus be counted.

d) Step 4:

At the very last step of the measurement, the ions were completely cooled and were well separated in frequency. The counting of the parent and the daughter ions is done after 100 s (until 110 s) after step 3 for a fixed time interval of 10 s.

Figure 7.3 shows an example of one of the storage measurements performed in the ESR. In this measurement, step 1 ($t = 0$ s) is the start time of the

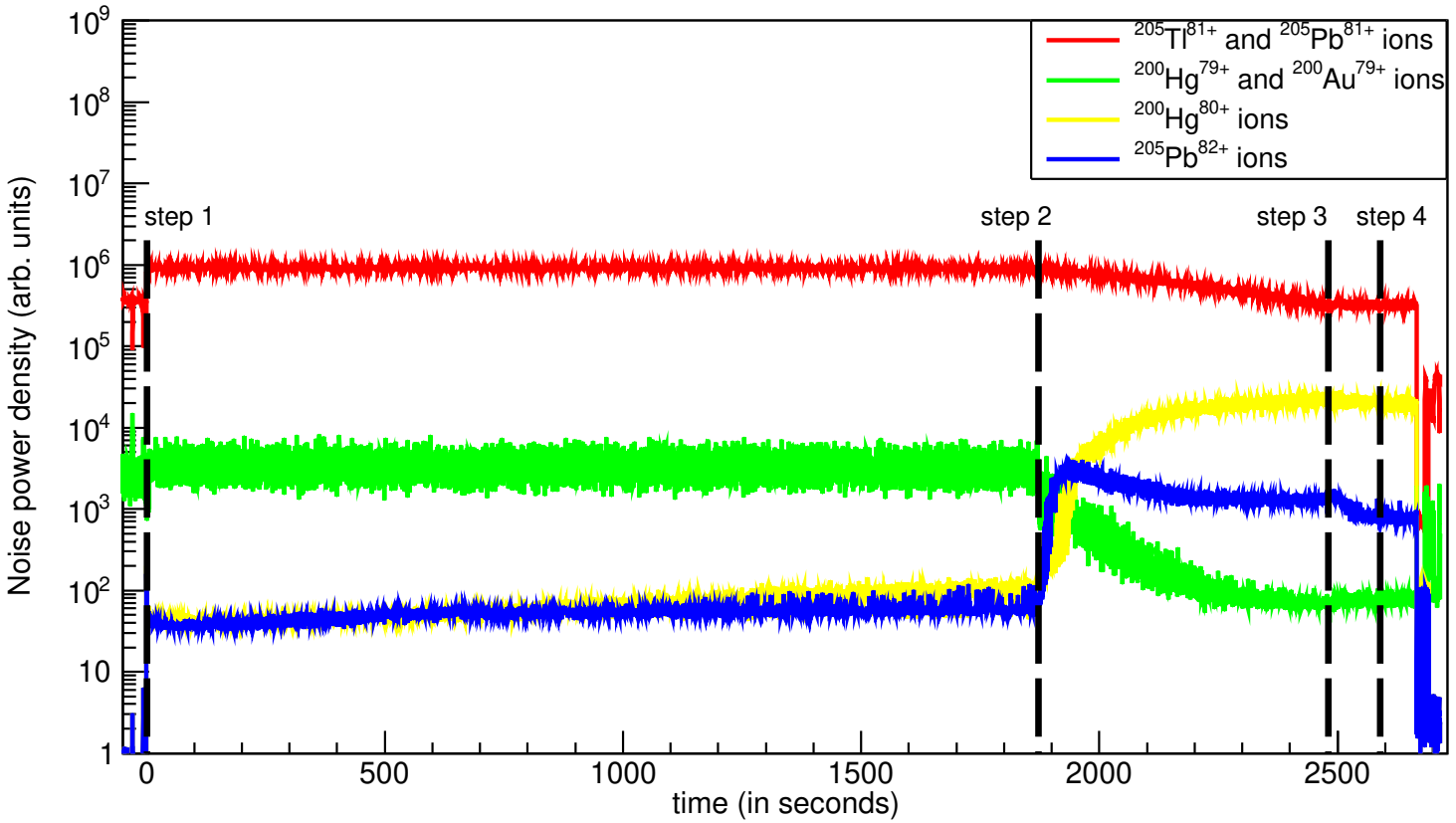

Figure 7.3: Measurement steps from half an hour storage measurement for HN 126 are shown above. Storage measurement starts at step 1, the gas jet target is switched on and off at step 2 and step 3, respectively, and the cooled ions are counted at step 4.

measurement and $^{205}Tl^{81+}$ ions are stored for t_s = 1872 s (0.52 hour) i.e. until step 2. At step 3, the internal Ar gas jet target is switched on for $\sim$ 600 s and fully-stripped $^{205}Pb^{82+}$ ions start to appear. At step 3, the target is switched off and the ions are cooled and are counted at step 4.

7.4 Counting of ions

For the determination of the half-life of β_b decay, the ratio of the number of daughter to the number of parent ions is to be determined. In this Section, I discuss how the counting of the ions is done.

Parent $^{205}Tl^{81+}$ ions:

In Figure 7.4, step 2 and step 4 are shown from a 5 hours storage measurement for HN 126, wherein, the frequency range is zoomed in near the parent ions. For the counting purpose, it has to be made sure that the ion peaks are well separated in frequency. At step 4, parent ions are counted by taking the integral of the two-dimensional projection spectrum in the frequency range for a fixed time interval of 10 s.

Daughter $^{205}Pb^{82+}$ ions:

As soon as the gas jet target is switched on, the very last electron from $^{205}Pb^{81+}$ ions is stripped off and we get $^{205}Pb^{82+}$ ions. This can be very clearly seen in Figure 7.5 a) which is also from a 5 hours storage measurement for HN 126. At the end of the storage measurement $t = t_s$, produced $^{205}Pb^{82+}$ ions are heavily mixed with $^{200}Hg^{80+}$ ions in frequency which are needed to be cooled and well separated for the counting purpose. At step 3, the gas jet target is switched off but still, $^{205}Pb^{82+}$ ions are not completely cooled as can be seen in Figure 7.5 b). Thus, with the electron cooler still on (with I_e = 200 mA), the daughter ions are allowed to cool for a few hundreds of seconds and once they are well separated in frequency, the number of daughter ions are counted at step 4.

It has to be mentioned that for both, the parent and the daughter ions, counting is done for the same fixed interval of measurement time (10 s) in order to obtain the ratio. The two-dimensional projection is taken at step 4 and integration of the peak is done to get the relative ion number. One does not need to consider the calibration of the noise power density obtained from the spectrum as we are interested in the determination of the ratio.

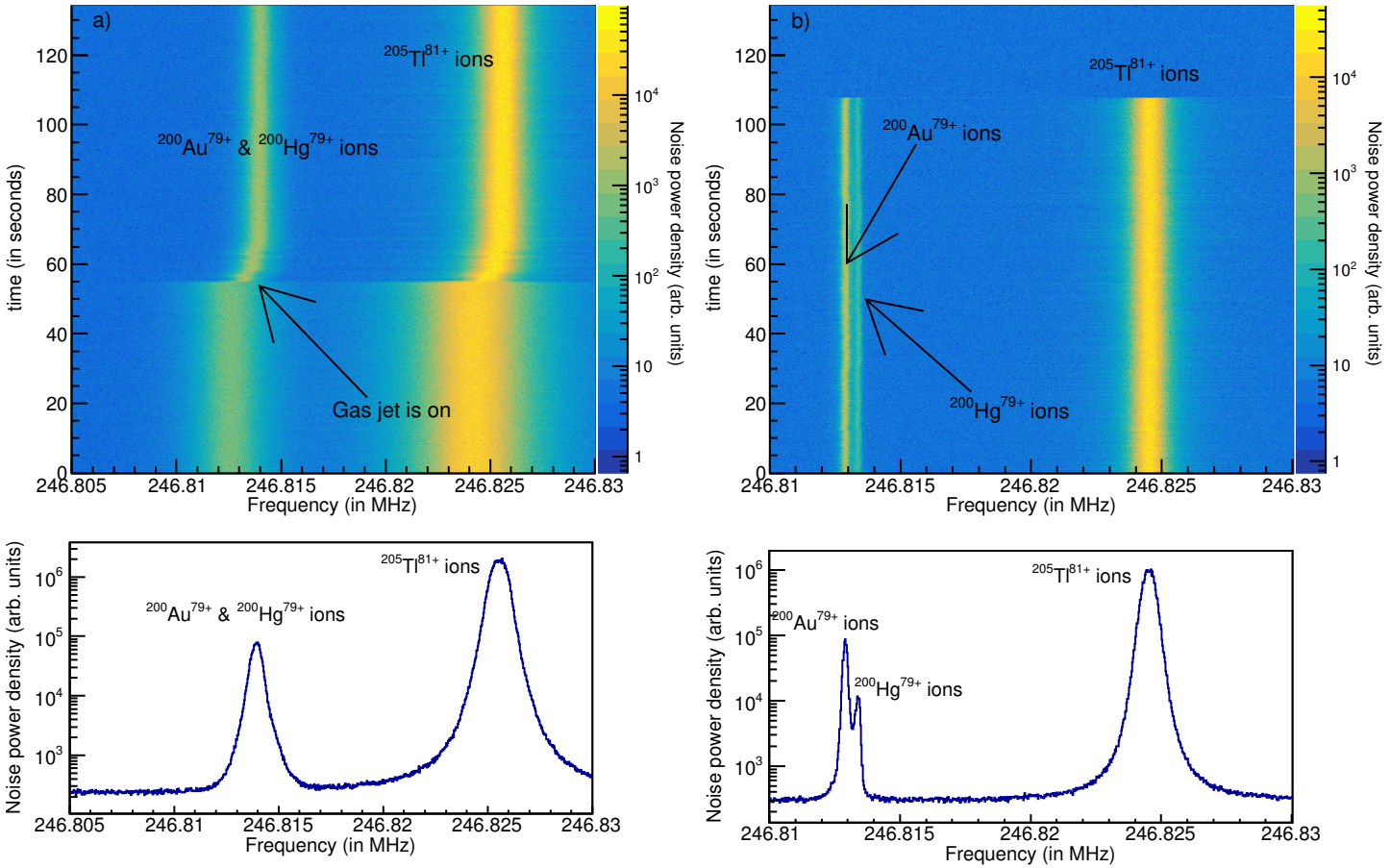

Figure 7.4: Zoomed in the frequency for the parent ions for HN 126. Left (a): The parent ions are shown at step 2 when the gas jet target is active. Right (b): The parent ions are shown at step 4 where the counting of the ions is done.

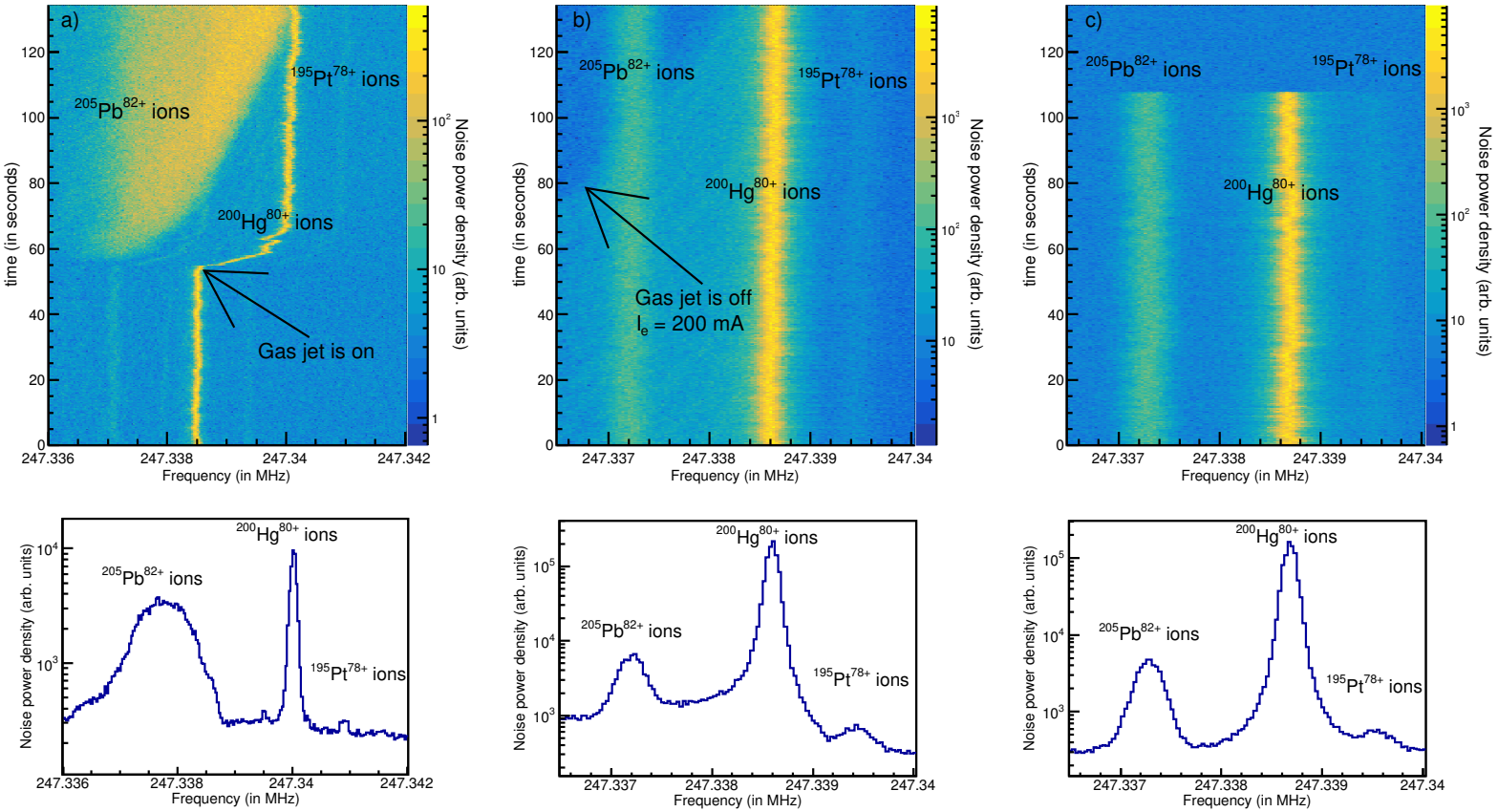

Figure 7.5: Zoomed in the frequency for the daughter ions for HN 126. Left (a): The daughter ions are shown at step 2 when the gas jet target is active where $^{205}Pb^{82+}$ & $^{200}Hg^{80+}$ ions are heavily mixed. Middle (b): The daughter ions are shown at step 3 where they are still mixed and are not completely cooled. Right (c): The daughter ions are shown at step 4 where the counting of the ions is done.

Figure 7.6 shows a two-dimensional projection taken at step 4 for 10 s of time (N_{aver} = 305.17). The plot is from the same 5 hours storage measurement for HN 126. As can be seen from Figure 7.6 and Figure 7.7 it is very crucial to subtract the linear background from the peak in order to obtain the correct integral value for the ratio. For this purpose, the experimental peaks are fitted with a function which is a sum of a Gaussian function and a polynomial function of first degree:

$$G(f) = a_0 \exp\left\{-\frac{1}{2}\left(\frac{f-a_1}{a_2}\right)^2\right\} + a_3 + a_4 \cdot f \quad , \tag{7.4}$$

where parameters a_0, a_1, a_2, a_3 and a_4 are the fitting parameters. After obtaining the fitting parameters, the linear background is subtracted. The area is determined by integrating the peaks over $f_{mean} \pm 5\sigma$ where f_{mean} is the mean frequency value of the peak and σ is the standard deviation.

It is important to accentuate that the subtraction of the background is crucial for the daughter ions where the linear background is quite substantial in amount (up to $\sim 30\%$, see Figure 7.7). For the parent ions, this is not so critical.

The above method is employed for all storage measurements to find the ratio of daughter to parent ions at step 4 for all harmonics. Thus, the discussed measured ratio at step 4 is

$$\text{ratio}_{\text{step 4}} = \left(\frac{N_{\text{Pb}}}{N_{\text{Tl}}}\right)_4 \quad . \tag{7.5}$$

7.5 Resonance response of the Schottky cavity

As discussed in previous Section and shown in Figure 7.2, there is a resonance effect for the Schottky resonator which was used for the data taking in the experiment. The resonance frequency of the resonator is $\sim$ 243.7 MHz and thus, the frequency peaks near the resonance region are over-amplified. This means that the same number of parent and daughter ions are different for different harmonics which gives different ratios at step 4.

To correct this effect, different stacked ion species in the inner and outer orbit of the ESR are considered. With $^{205}Tl^{81+}$ ions, mixed $^{200}Hg^{79+}$ & $^{200}Au^{79+}$ ions, mixed $^{203}Hg^{80+}$ & $^{203}Tl^{80+}$ ions are also stored within the acceptance of the ring (see Appendix B). For each measurement, $^{205}Tl^{81+}$

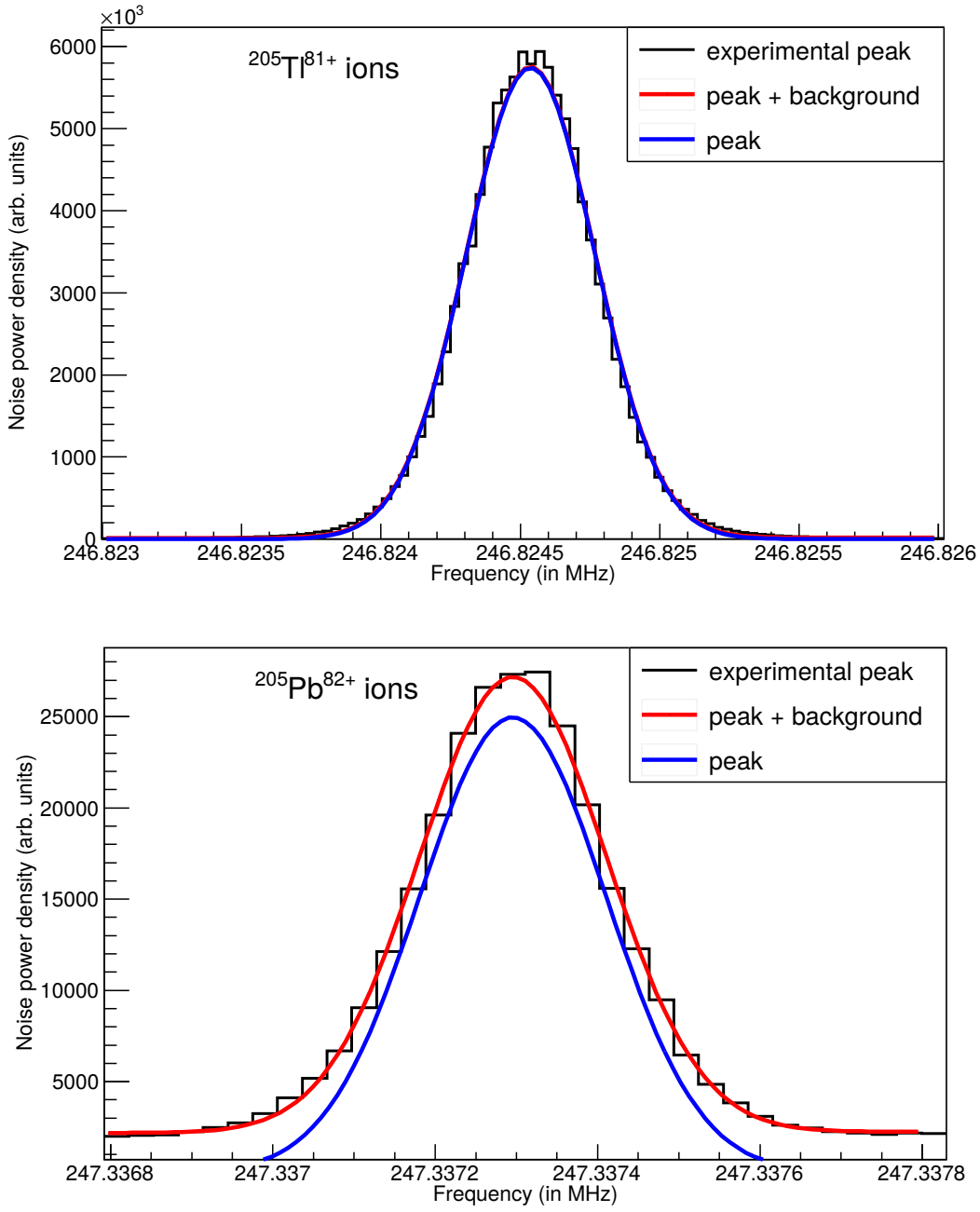

Figure 7.6: Background subtraction for the parent (above) and the daughter (below) ions. The experimental peak at step 4 is fitted with a function (equation 7.4) and the linear background is subtracted to count the ions.

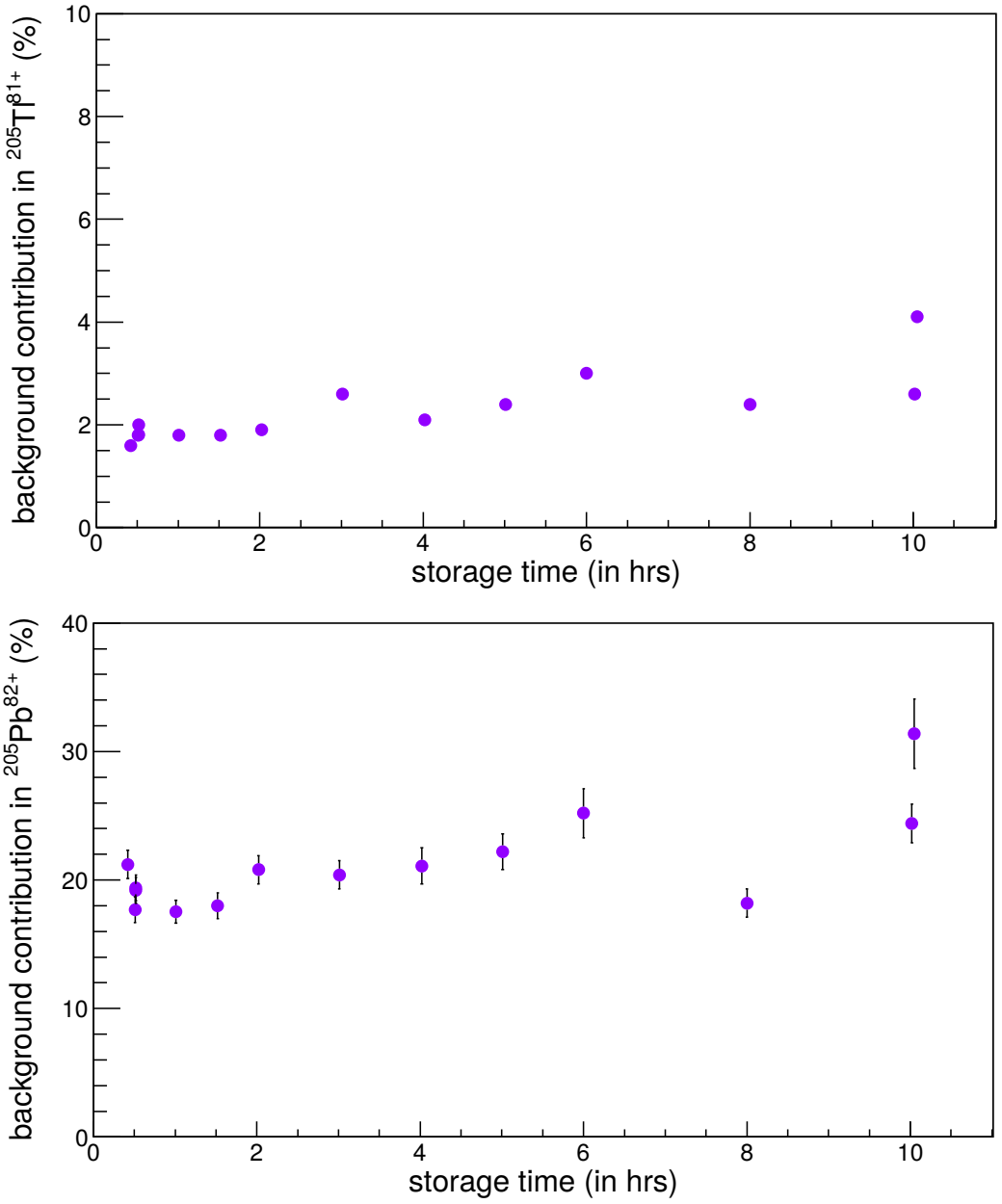

Figure 7.7: Background contribution (in %) in the parent (above) and the daughter (below) ions for different storage measurements. Background contribution is the ratio of the background to the experimental peak.

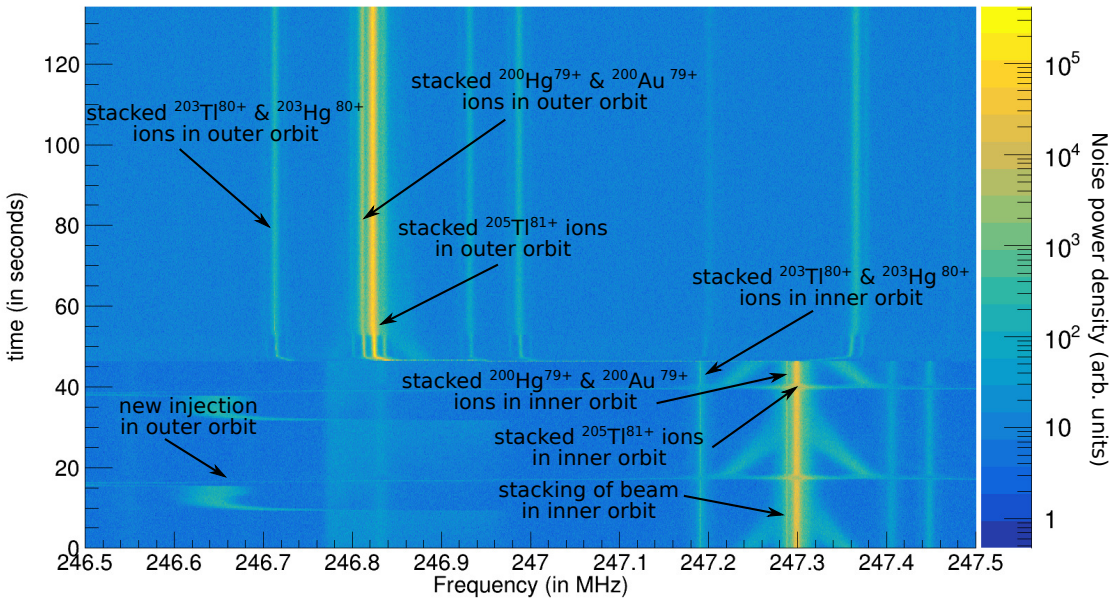

Figure 7.8: Different stacked ions are shown in the inner and outer orbit of the ESR for HN 126.

ions (along with other ion species) are first stacked in the inner orbit, until the desired intensity is achieved. The stacked $^{205}Tl^{81+}$ ions are then shifted to the outer orbit via the ramping of the dipole magnets of the ESR, from where a storage measurement starts i.e. at step 1 ($t = 0$ s). Figure 7.8 shows different ion species before and after shifting the orbit. The three-dimensional spectrum is from a 10 hours storage measurement for HN 126.

It is to be emphasized that the frequency of stacked $^{205}Tl^{81+}$ ions in the inner orbit is approximately the same frequency where $^{205}Pb^{82+}$ ions are seen when the gas jet target is active which makes the correction quite simple. For the correction purpose, different stacked ion species are counted for a fixed time interval of 3 s just before and after changing the orbit. In this way, we get the same number of ion species at two different frequencies and for all three harmonics. For e.g., in Figure 7.9 the same number of $^{205}Tl^{81+}$ ions for different harmonics from a 10 hours storage measurement can be seen. This is done for different ion species for all storage measurements and for all three harmonics as shown in Figure 7.10.

Due to the resonance effect of the Schottky resonator, the Amplification

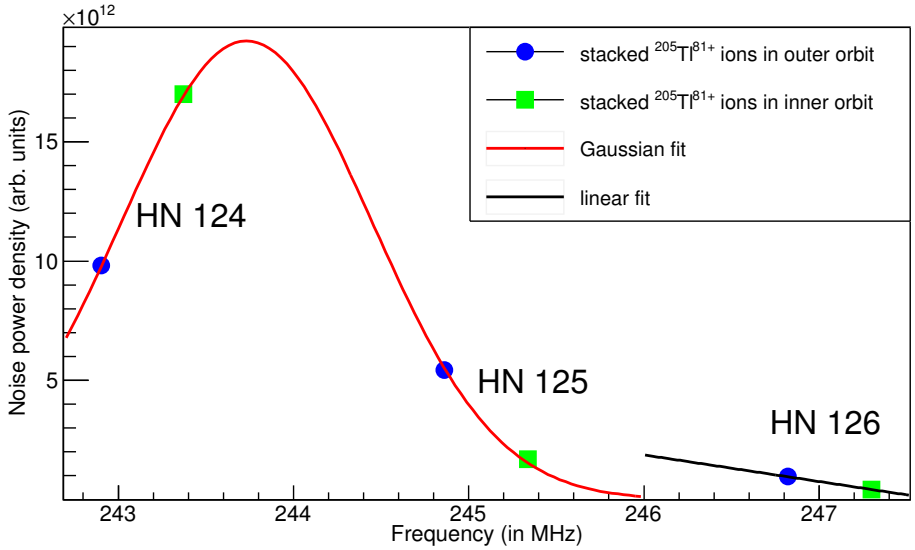

Figure 7.9: Resonance curve obtained by using the stacked $^{205}Tl^{81+}$ ions in the inner and outer orbit from a 10 hours storage measurement.

Factor (AF) is defined as:

$$\text{AF} = \frac{\text{number of stacked ions in the inner orbit}}{\text{number of stacked ions in the outer orbit}} \quad . \tag{7.6}$$

AF is determined for different ion species and for all storage measurements as shown in Figure 7.10. This is used to correct for the resonance effect for the ratio obtained at step 4. The values of the obtained AFs for different ion species and for different harmonics are given in Table 7.1.

Due to the saturation effect (discussed in Section 7.8, 7.10), the AF ob-

Table 7.1: Amplification factors obtained from different stacked ion species.

	AF from Figure 7.10 a)		AF from Figure 7.10 b)		AF from Figure 7.10 c)		**AF from Figure 7.10 d)**	
HN	Mean	S.D.(σ)	Mean	S.D.(σ)	Mean	S.D.(σ)	**Mean**	**S.D.(σ)**
124	1.72	0.03	1.31	0.07	1.83	0.12	**1.58**	**0.09**
125	0.33	0.01	0.29	0.01	0.39	0.03	**0.30**	**0.02**
126	0.44	0.02	0.40	0.01	0.50	0.03	**0.39**	**0.03**

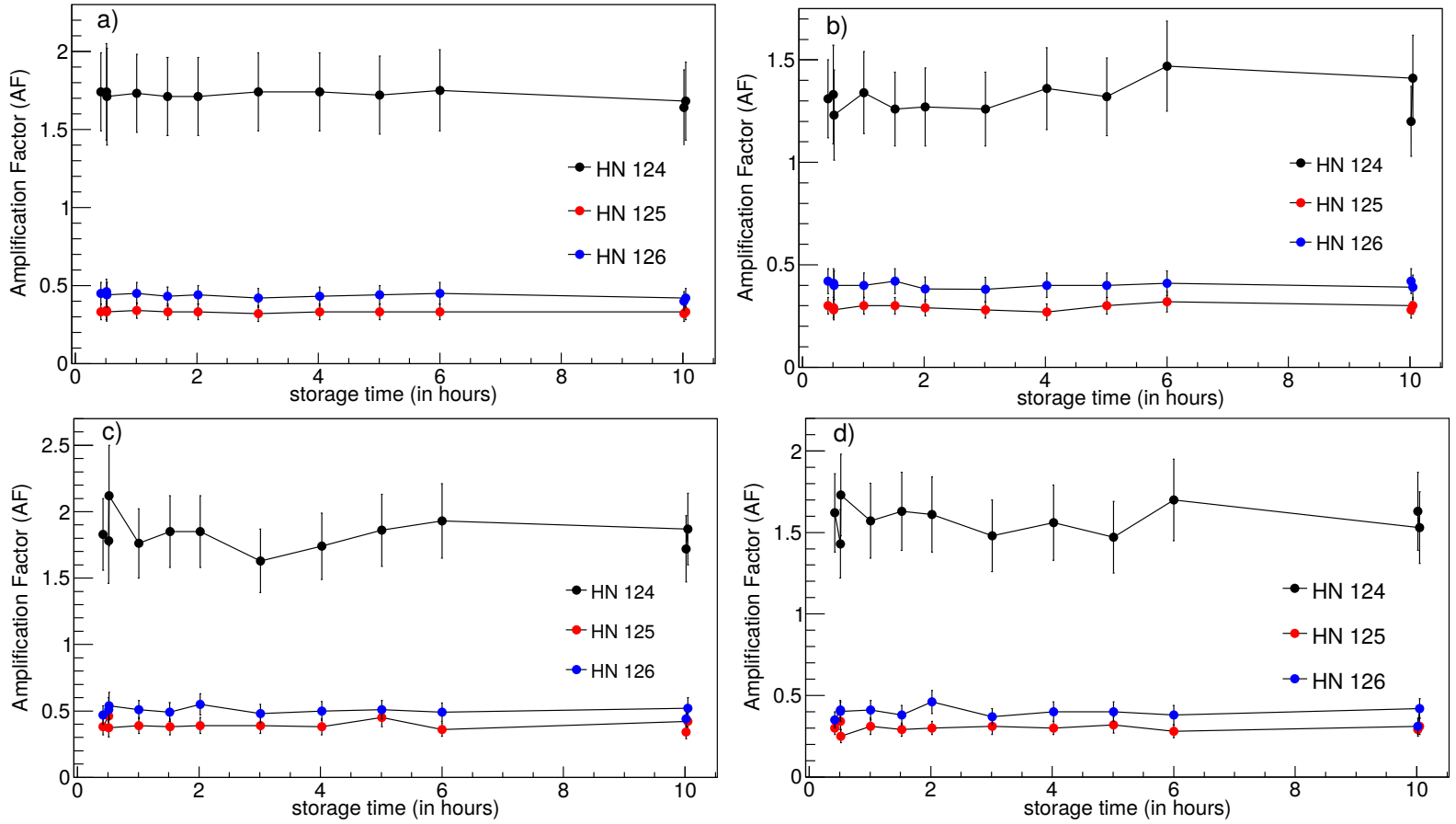

Figure 7.10: Amplification factor (AF) for different storage measurements and for different harmonics obtained using stacked a) $^{205}Tl^{81+}$ ions, b) mixed $^{200}Hg^{79+}$ & $^{200}Au^{79+}$ ions and c) mixed $^{203}Hg^{80+}$ & $^{203}Tl^{80+}$ ions, respectively. In d), the AF obtained at the frequency of $^{205}Tl^{81+}$ ions from mixed $^{203}Hg^{80+}$ & $^{203}Tl^{80+}$ ions is shown.

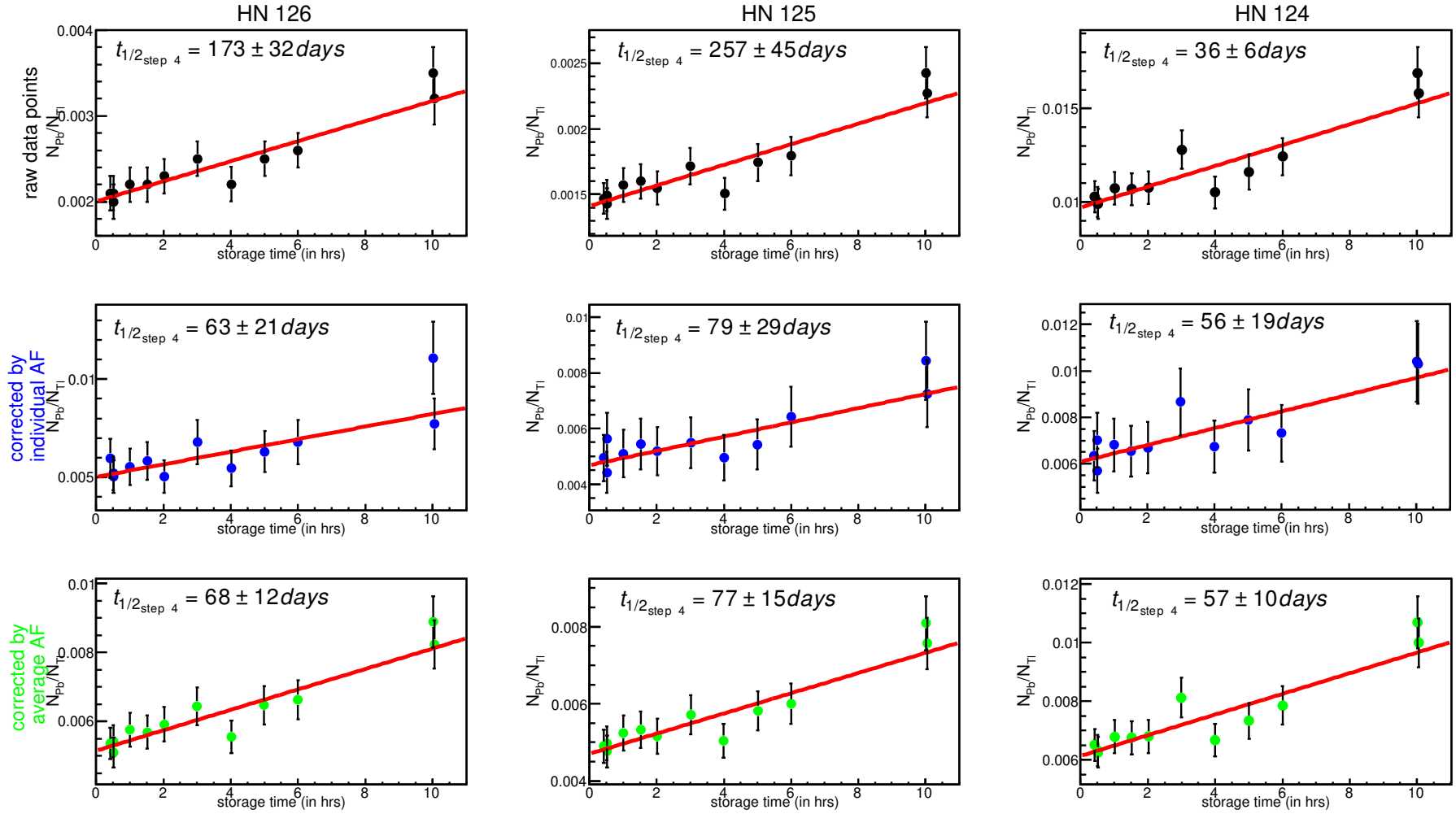

Figure 7.11: Comparison between $t_{1/2_{\text{step 4}}}$ obtained from the raw data points, corrected data points by the individual AF and corrected data points by the average AF for the three harmonics. After the AF correction, $t_{1/2_{\text{step 4}}}$ is consistent for the three harmonics.

tained from Figure 7.10 d) is considered for the correction purpose. In Figure 7.11, the ratio of the daughter and the parent ions obtained at step 4 with no resonance effect correction, with the resonance effect correction by evaluating the individual AF and with the resonance effect correction by taking the average AF for all the three harmonics is shown. For the plots in Figure 7.11, $t_{1/2_{\text{step 4}}}$ is calculated using

$$t_{1/2_{\text{step 4}}} = \frac{0.693}{\gamma \times 24 \times k} \quad , \tag{7.7}$$

with

$$k_0 + k \cdot t_s = \left(\frac{N_{\text{Pb}}}{N_{\text{Tl}}}\right)_4 \quad , \tag{7.8}$$

where γ is the Lorentz relativistic factor, k_0 (constant) and k (slope) are the fitting parameters of a first degree polynomial function. It is vital to emphasize that $t_{1/2_{\text{step 4}}}$ calculated here is not the half-life of the bound-state beta decay which we aim to measure. We are still at step 4 and for the measurement of the half-life of β_b decay, we need to determine the ratio at step 2.

From Figure 7.11, it is quite evident that the resonance effect correction leads to a consistency in $t_{1/2}$ values obtained at step 4 for all three harmonics.

7.6 Ratio at step 2

In order to evaluate the half-life of the bound-state beta decay, the end of the storage measurement must be considered. From equation 4.19, we have

$$\left(\frac{N_{\text{Pb}}(t_s)}{N_{\text{Tl}}(t_s)}\right)_2 = \frac{\lambda_{\beta_b}}{\gamma} t_s \left(1 + \frac{1}{2}(\lambda^{cc}_{\text{Tl}} - \lambda^{cc}_{\text{Pb}})t_s\right) \quad , \tag{7.9}$$

which means that the ratio is to be determined at step 2 i.e. at $t = t_s$. What we identify at step 4 with the help of the Schottky resonator is the number of reacted daughter ions ($N_{\text{Pb}_4} = N_{\text{Pb}_2} \frac{\sigma_{I,\text{Pb}}}{\sigma_{I,\text{Pb}} + \sigma_{c,\text{Pb}}} (1 - e^{-\lambda_2^{\text{Pb}} t_2}) e^{-\lambda_3^{\text{Pb}} t_3}$) and unreacted parent ions ($N_{\text{Tl}_4} = N_{\text{Tl}_2} e^{-\lambda_2^{\text{Tl}} t_2} e^{-\lambda_3^{\text{Tl}} t_3}$) as shown in Figure 7.12. Thus, the ratio at step 2 and step 4 is related as

$$\left(\frac{N_{\text{Pb}}}{N_{\text{Tl}}}\right)_4 = \left(\frac{N_{\text{Pb}}}{N_{\text{Tl}}}\right)_2 \cdot \frac{\sigma_{I,\text{Pb}}}{\sigma_{I,\text{Pb}} + \sigma_{c,\text{Pb}}} \cdot \frac{1 - e^{-\lambda_2^{\text{Pb}} t_2}}{e^{-\lambda_2^{\text{Tl}} t_2}} \cdot \frac{e^{-\lambda_3^{\text{Pb}} t_3}}{e^{-\lambda_3^{\text{Tl}} t_3}} \quad , \tag{7.10}$$

where λ_2^{Pb}, λ_2^{Tl} are the stripping decay constants for $^{205}\text{Pb}^{81+}$ and $^{205}\text{Tl}^{81+}$ ions, respectively, when the gas jet target is switched on at step 2 for t_2

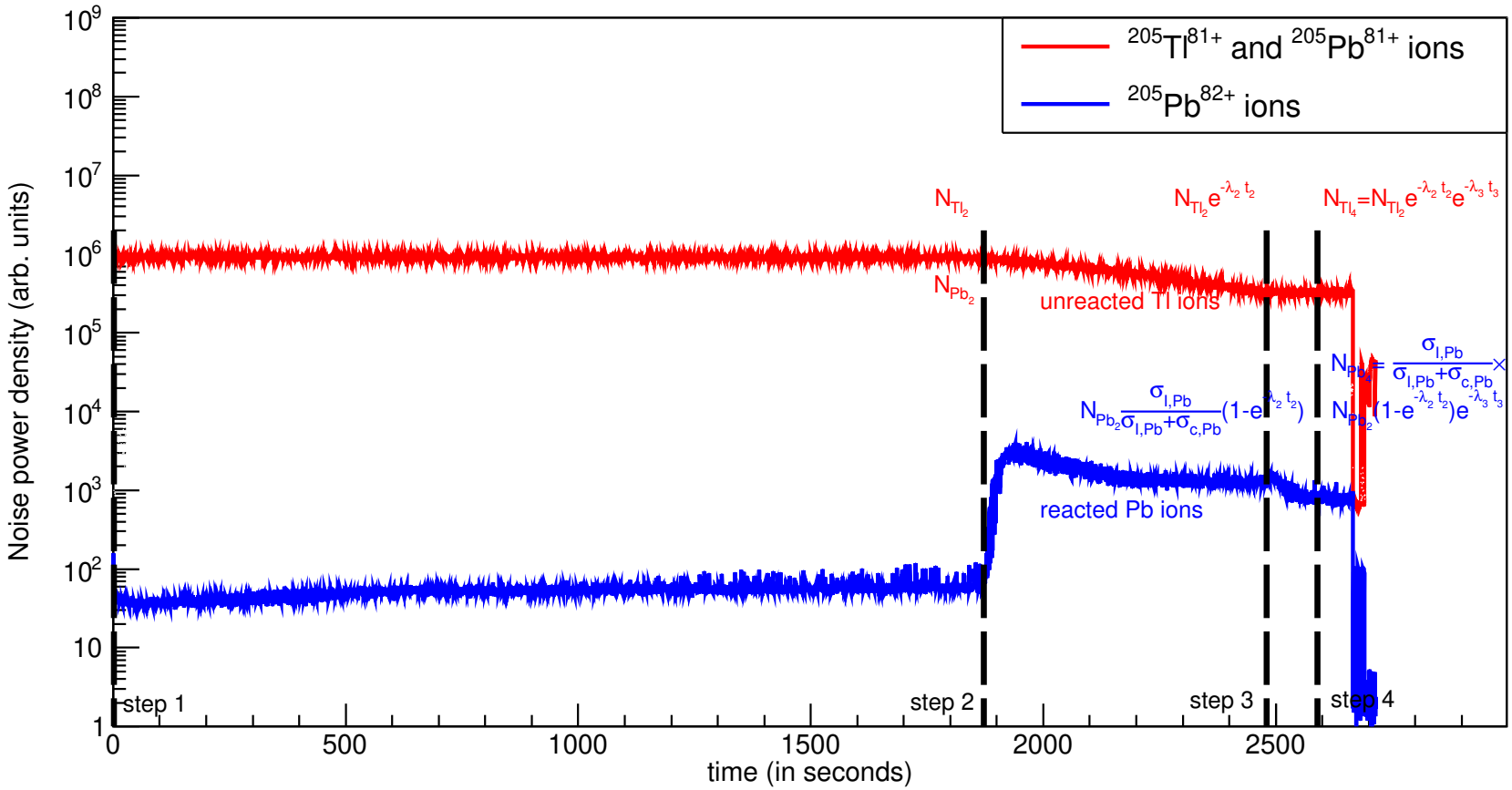

Figure 7.12: Parent and daughter ions at step 2 and step 4 from half an hour storage measurement for HN 126.

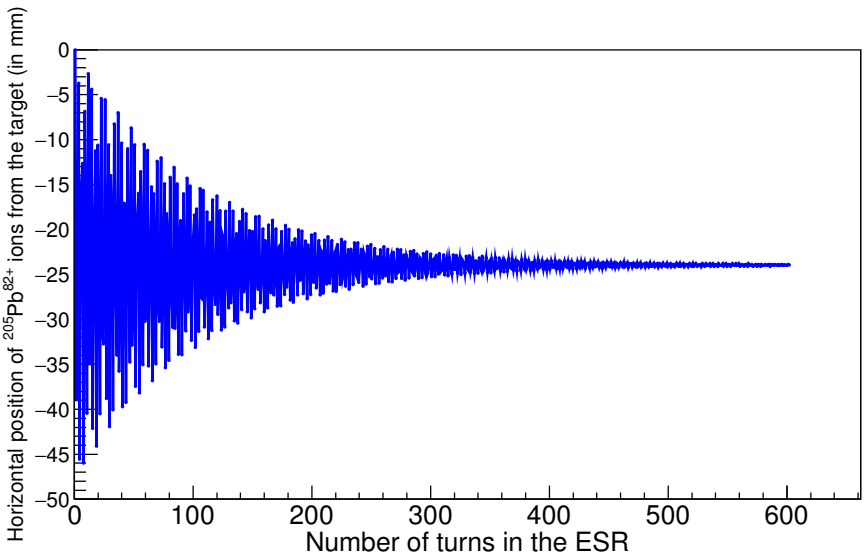

Figure 7.13: The result from a simulation showing the horizontal position of $^{205}Pb^{82+}$ ions vs the number of turns in the ESR. Horizontal position 0 mm represents the nominal $^{205}Tl^{81+}$ beam position and turn number 0 represents the time when the gas jet target is active.

$\sim$ 600 s. λ_3^{Pb}, λ_3^{Tl} are the decay constants for $^{205}Pb^{82+}$ and $^{205}Tl^{81+}$ ions, respectively, for the interaction with the electron cooler $I_e = 200$ mA when the gas jet target is switched off. Also, $\lambda_2^{\mathrm{Pb}} \approx \lambda_2^{\mathrm{Tl}} = \lambda_2$ and $\lambda_3^{\mathrm{Pb}} \approx \lambda_3^{\mathrm{Tl}} = \lambda_3$ as they scale with the square of the atomic number Z. However, for equation 7.10 to be valid, it is pivotal to confirm whether the fully-stripped $^{205}Pb^{82+}$ ions also interact with the gas jet target or not.

For this purpose, a simulation calculation is carried out, wherein the horizontal position of $^{205}Pb^{82+}$ ions is calculated using the ion optics of the ESR. From Figure 7.13, it is evident that approximately after 100 turns, the produced $^{205}Pb^{82+}$ ions revolve at around -25 mm position in the ring. Horizontal position 0 mm represents the nominal beam orbit of circulating $^{205}Tl^{81+}$ ions while overlapping with the internal gas jet target of diameter $\sim$ 5 mm. With the revolution frequency of the ions to be $\sim$ 2 MHz (2000000 turns), it is clear that there is no overlap of the gas jet target with $^{205}Pb^{82+}$ ions which verifies the correctness of the equation 7.10. Thus, from equations 7.9 and 7.10

$$\left(\frac{N_{\mathrm{Pb}}}{N_{\mathrm{Tl}}}\right)_4 \cdot \frac{\sigma_{I,\mathrm{Pb}} + \sigma_{c,\mathrm{Pb}}}{\sigma_{I,\mathrm{Pb}}} \cdot \frac{e^{-\lambda_2^{\mathrm{Tl}} t_2}}{1 - e^{-\lambda_2^{\mathrm{Pb}} t_2}} \cdot \frac{e^{-\lambda_3^{\mathrm{Tl}} t_3}}{e^{-\lambda_3^{\mathrm{Pb}} t_3}} = \frac{\lambda_{\beta_b}}{\gamma} t_s \left(1 + \frac{1}{2}(\lambda_{\mathrm{Tl}}^{cc} - \lambda_{\mathrm{Pb}}^{cc}) t_s\right) \quad . \tag{7.11}$$

Now, the next step is to determine the stripping decay constant λ_2 and $\lambda^{cc}_{\mathrm{Tl}} - \lambda^{cc}_{\mathrm{Pb}}$.

7.7 Stripping decay constant

As soon as the gas jet target is switched on, the parent $^{205}\mathrm{Tl}^{81+}$ ions capture one or more electrons but no stripping/ionization occur as they are fully-stripped. So, what we see for the parent ions in the Schottky spectra are the number of unreacted ions ($N = N_0 e^{-\lambda t}$) as the ones which react and capture electron(s) hit the MWPC placed in the outer pocket.

For the determination of λ_2, it has to be made sure that the gas jet density for different storage measurements is constant as λ_2 is given by

$$\lambda_2 = \rho\, \sigma f \quad ,$$

where ρ is the gas jet target density, σ is the electron capture cross section and f is the revolution frequency of $^{205}\mathrm{Tl}^{81+}$ ions.

The gas jet density is measured as a function of S1, S2, S3 and S4 pressure parameters [90] which are directly proportional to the gas jet density. S2 pressure parameter was stored in one of the scaler channels in the DAQ system and is plotted in Figure 7.14 for different storage times. The constant trend of S2 clearly indicates that the gas jet target was stable during the experiment and one can determine the λ_2.

There are three ways to determine the value of the stripping decay constant λ_2 which are discussed below.

1. From the Schottky data:

The two-dimensional noise power density is plotted vs the stripping time and fitted with an exponential function. For this, the Schottky intensity between step 2 and step 3 is taken which corresponds to the time when the gas jet target is on. It is then fitted with an exponential function

$$G(t) = N_2 \exp(a_1 + a_2 \cdot t) \quad , \tag{7.12}$$

where N_2 are roughly the number of ions at step 2 and a_1 & a_2 = - λ_2 are the fitting parameters. This is done for all storage measurements. Figure 7.16 a) shows the noise power density vs the stripping time for all storage measurements. Each curve is fitted with the above defined exponential function to extract the value of λ_2. The obtained λ_2 values are plotted versus the storage time as shown in Figure 7.17 a).

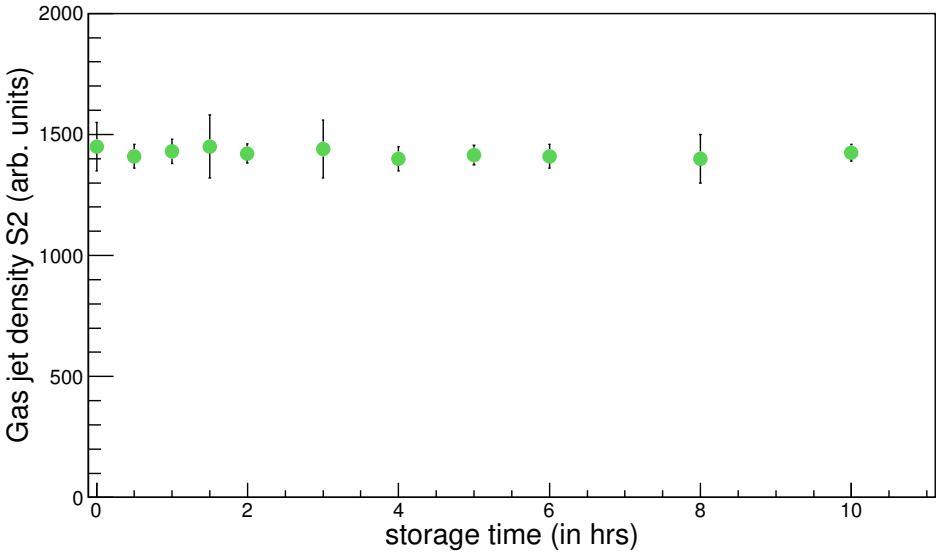

Figure 7.14: S2 parameter for different storage measurements.

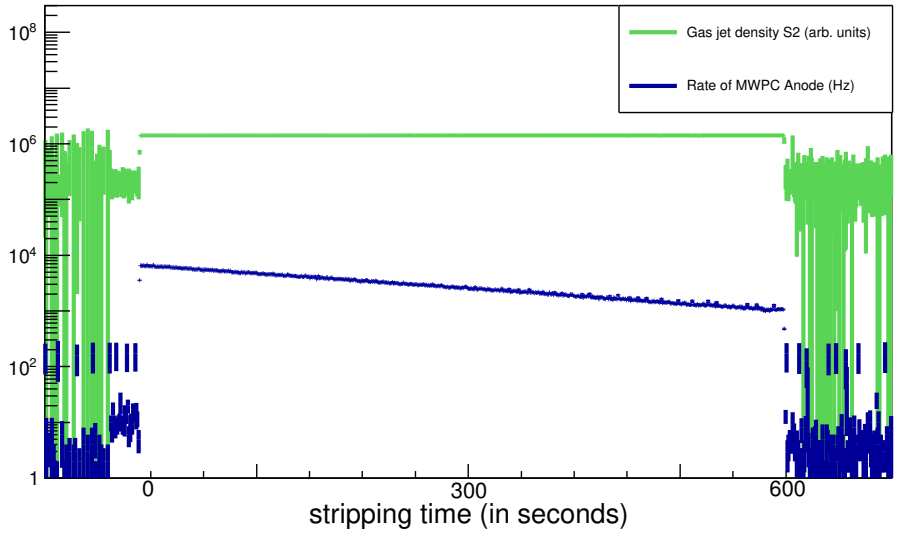

Figure 7.15: S2 parameter and the MWPC anode rate are shown when the gas jet target is active for one of the measurements.

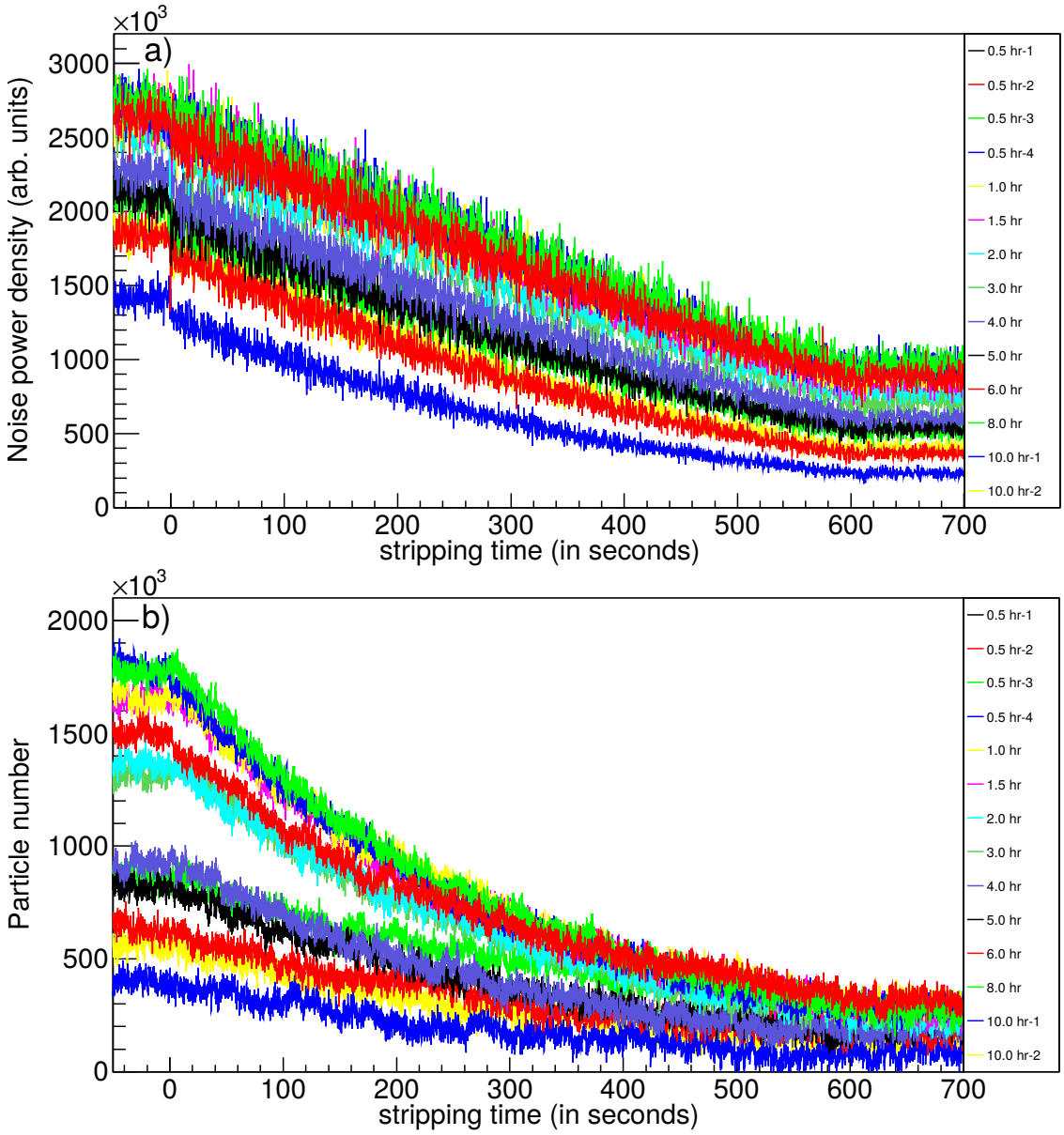

Figure 7.16: Top a): Noise power density obtained from the Schottky data for HN 126 and Bottom b): particle number obtained from the DCCT data for different storage measurements, respectively. Stripping time represents the time duration for which the gas jet target is active.

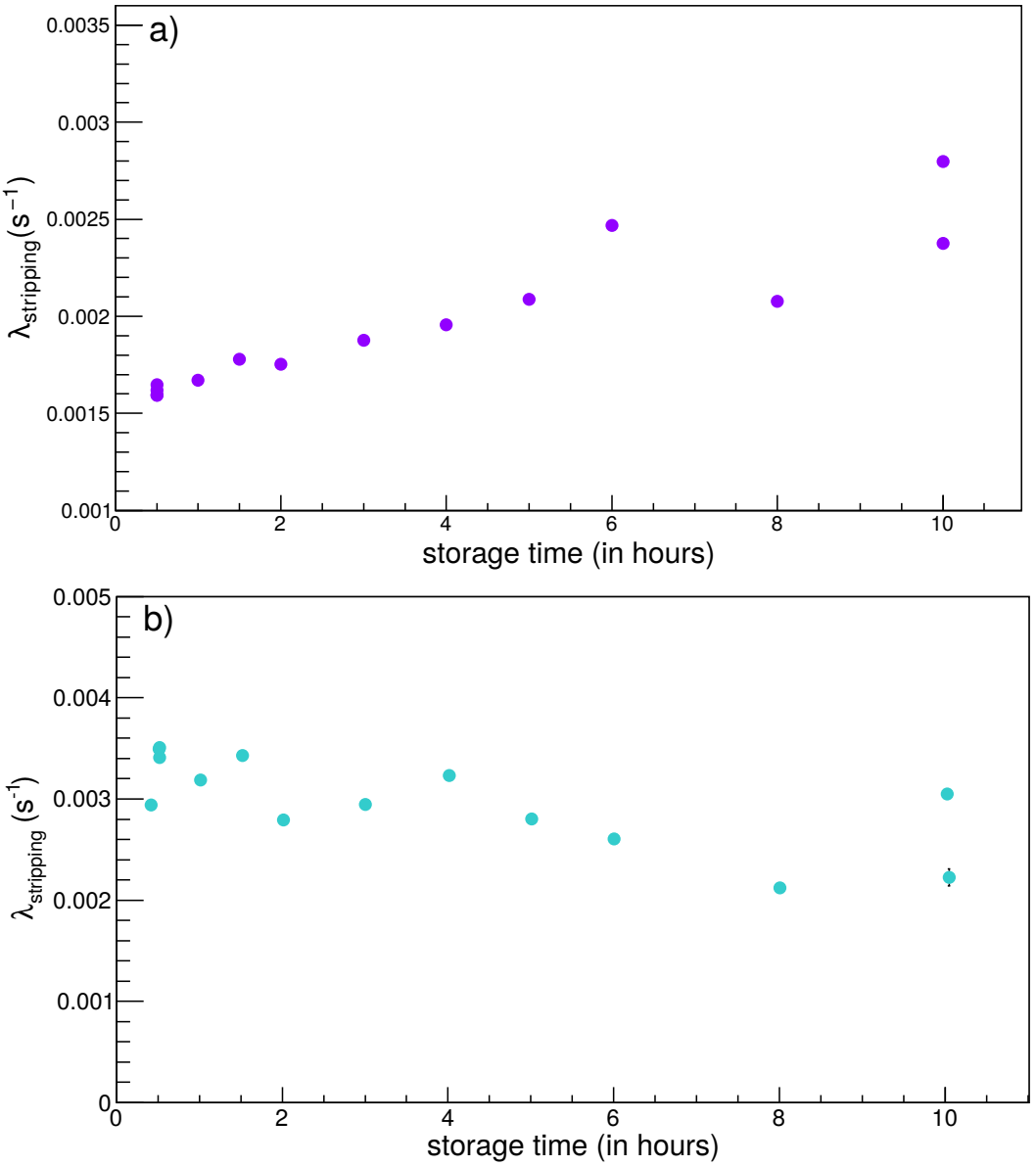

Figure 7.17: Stripping decay constant obtained by fitting the Schottky data and the DCCT data during the gas jet active mode are plotted in a) and b), respectively.

Not a constant value for different storage times was surprising as λ_2 should be independent of the storage time. The immediate step was to then look into the DCCT (Direct Current Current Transformer) data which was also recorded during the experiment.

2. From the DCCT data:

In an analogous approach as used above, the DCCT intensity is plotted vs the stripping time and fitted with an exponential function (using equation 7.12). This is done for all storage measurements as shown in Figure 7.16 b). It is to be mentioned that the DCCT measures absolute particle number and is not sensitive to low ion currents and thus has a certain offset value. The offset value (1.08×10^6) is subtracted in Figure 7.16 b). The values of the obtained λ_2 are then plotted versus the storage time as shown in Figure 7.17 b).

Figure 7.17 b) shows a constant trend for λ_2 except for long storage measurements. This is understandable as DCCT is not sensitive to low ion currents. In order to get an accurate and more precise value of λ_2, the next step was to look into the MWPC data.

3. From the MWPC data:

As discussed in Section 6.1, the MWPC detector was placed at position -10 mm (with respect to the nominal beam position). When the gas jet target is switched on, electron captured $^{205}Tl^{80+}$ ions ($N = N_0(1 - e^{-\lambda t})$) hit the MWPC which are then counted.

With turning on of the gas jet target for $\sim$ 600 s, the counts of the electron captured hits on the MWPC increases or the rate (counts per second) decreases with time, respectively. For plotting the MWPC rate, the anode signal from the MWPC is used. Figure 7.15 shows S2 and the MWPC rate in logarithmic scale for one of the storage measurements, where a constant value of S2 and exponentially decreasing MWPC count rate can be seen. MWPC anode rate is plotted for different storage measurements as shown in Figure 7.18 and Figure 7.19. Each of the storage measurements is fitted with an exponential function (using equation 7.12) to determine the value of λ_2.

Figure 7.20 show the obtained values of λ_2 for different storage measurements. λ_2 has a constant trend and is independent of the storage time as expected. Since a precise value of λ_2 is needed for the determination of the ratio at step 2, the value obtained from the MWPC is taken which is

$$\lambda_2^{\mathrm{Tl}} = 3.13(2)_{\mathrm{stat}} \times 10^{-3}\ \mathrm{s}^{-1}\ .$$

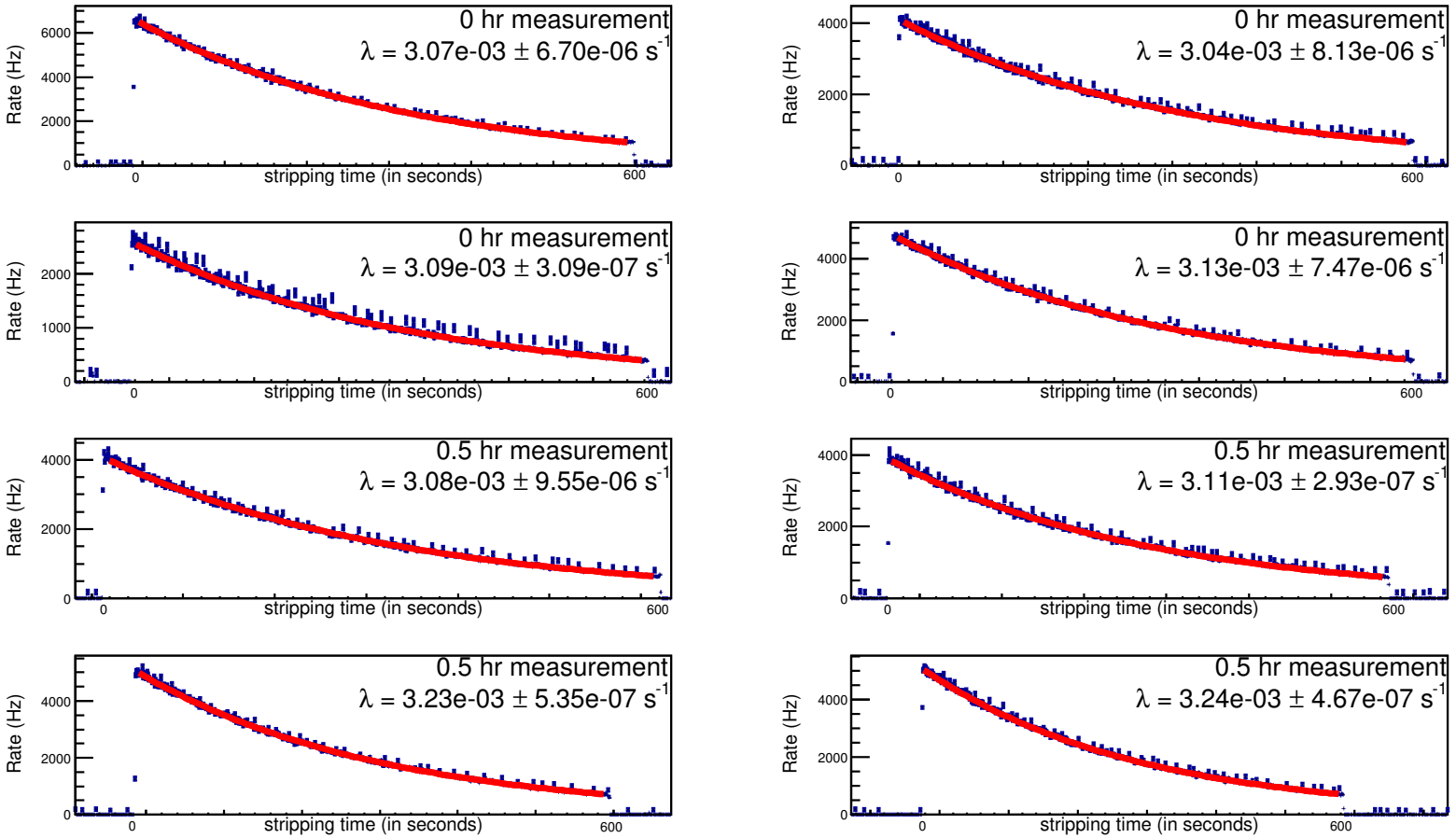

Figure 7.18: MWPC anode rate for different storage measurements when the gas jet target is active.

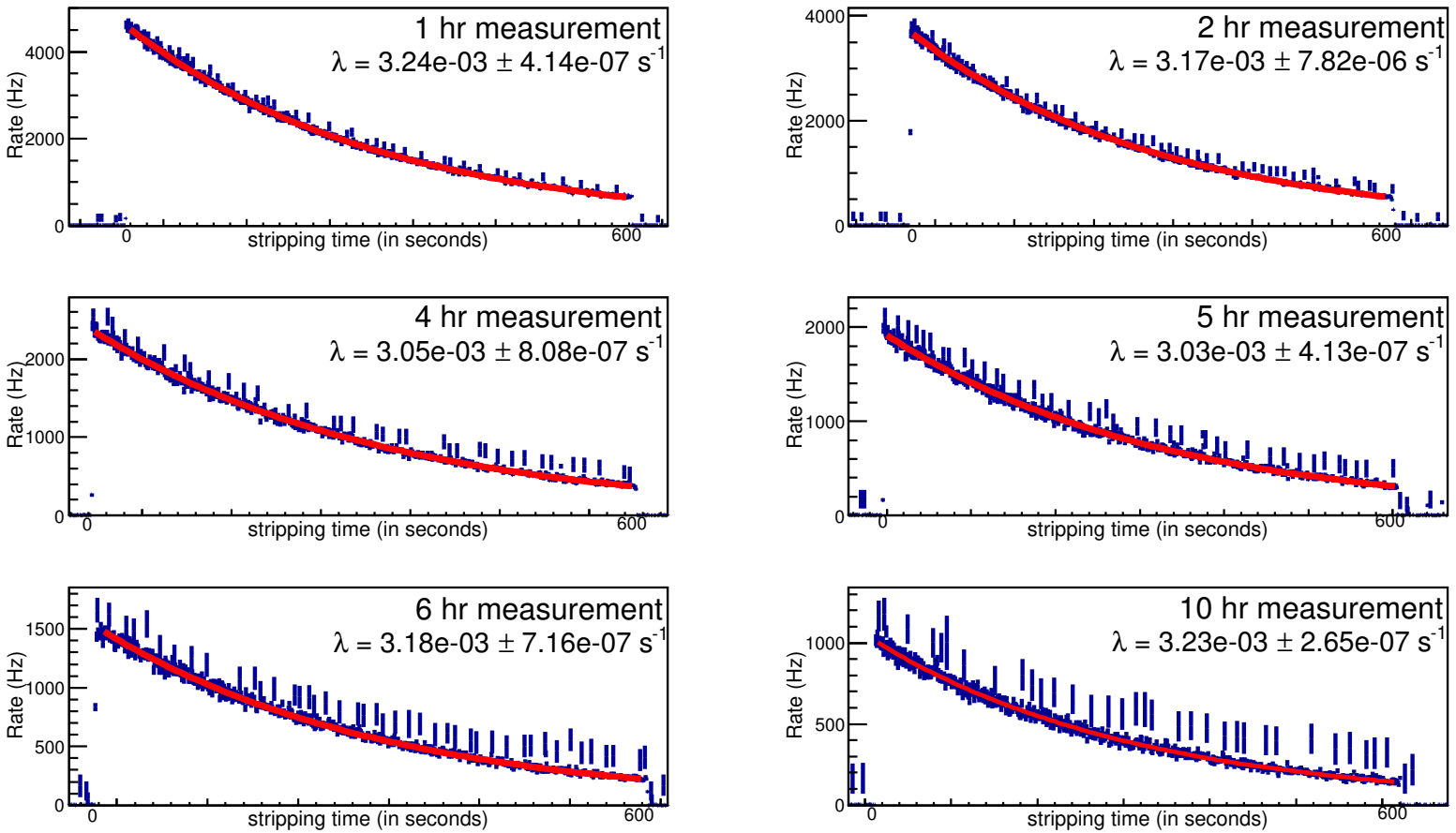

Figure 7.19: MWPC anode rate for different storage measurements when the gas jet target is active.

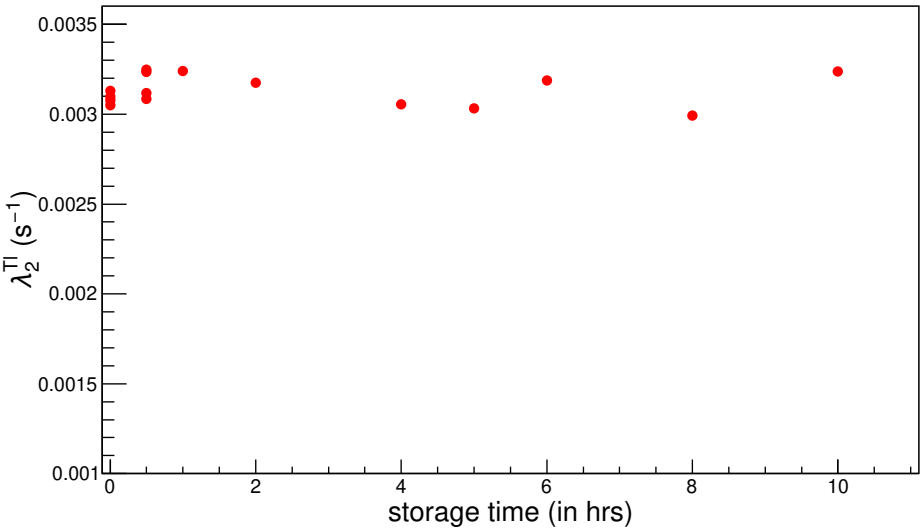

Figure 7.20: Stripping decay constant obtained from the MWPC data for different storage measurements.

The above value is obtained by taking the mean value of λ_2 acquired from different storage measurements. To account for the systematic uncertainty, normalized χ_n is calculated using equation 6.5. The obtained value of $\chi_n = 3.70$ is out of the expected range of $\chi_n = 1 \pm 0.24$. An additional systematic error $\sigma_{\text{syst}} = 0.08 \times 10^{-3}$ s^{-1} is added and thus,

$$\lambda_2^{\text{Tl}} = 3.13(2)_{\text{stat}}(8)_{\text{syst}} \times 10^{-3} \text{ s}^{-1} \quad .$$

In the experiment, there were no stripping measurements performed for the $^{205}Pb^{81+}$ ions. Nevertheless, λ_2^{Pb} ions can be obtained by proper scaling λ_2^{Tl} up by 2% as $\lambda_2 \propto Z^2$ which gives

$$\lambda_2^{\text{Pb}} = 3.21(2)_{\text{stat}}(8)_{\text{syst}} \times 10^{-3} \text{ s}^{-1} \quad .$$

λ_2^{Tl} and λ_2^{Pb} are used to evaluate the value of the Pb/Tl ratio at step 2.

7.8 Saturation effect

The unexpected trend of λ_2 obtained from the Schottky data was perplexing. The next step was to look into the storage measurements obtained by the Schottky data and the DCCT data and to compare them. Figure 7.21 shows the storage measurements obtained from the Schottky data and Figure 7.22

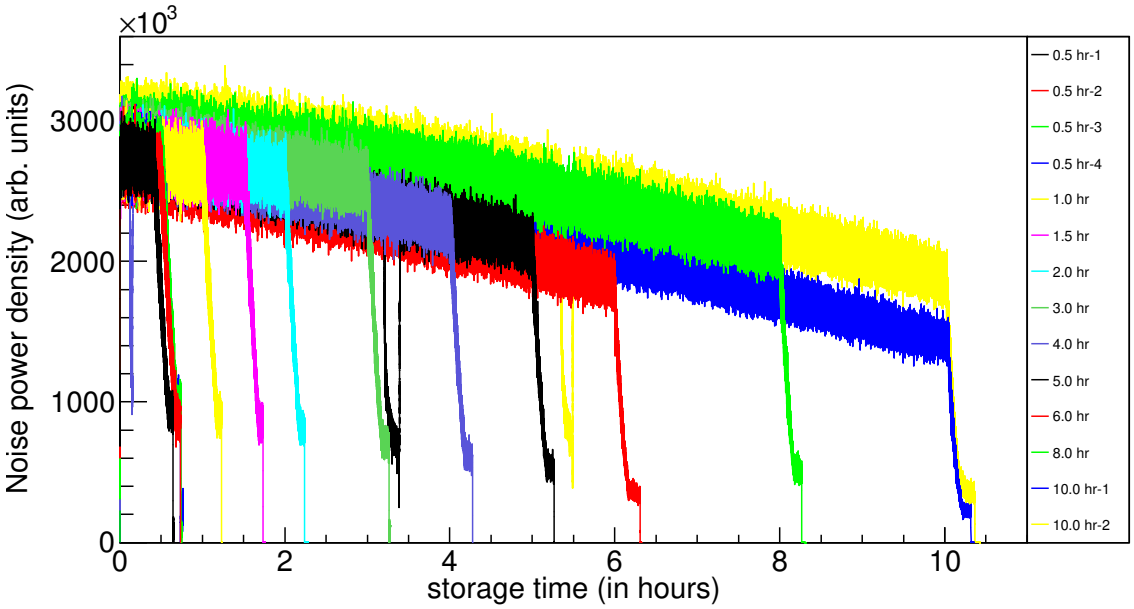

Figure 7.21: Different storage measurements are plotted from the Schottky data for HN 126.

shows the storage measurements obtained from the DCCT data. It can be seen that for the Schottky data, the intensities of the stored ions do not decrease exponentially with time as in the case of the DCCT data.

By looking at the shape of the intensities during the storage time (see Figure 7.21), it seems like the Schottky data are somehow "saturated" and this effect is termed as the "saturation effect". For the experiment, a resonant Schottky cavity was employed with the NTCAP as the DAQ system. The saturation effect can thus arise either from

1. the saturated behavior of the resonant Schottky cavity at high beam intensities, or/and
2. the NTCAP DAQ system.

The source of the saturation effect was crucial to confirm without which the interpretation of the Schottky data was arduous.

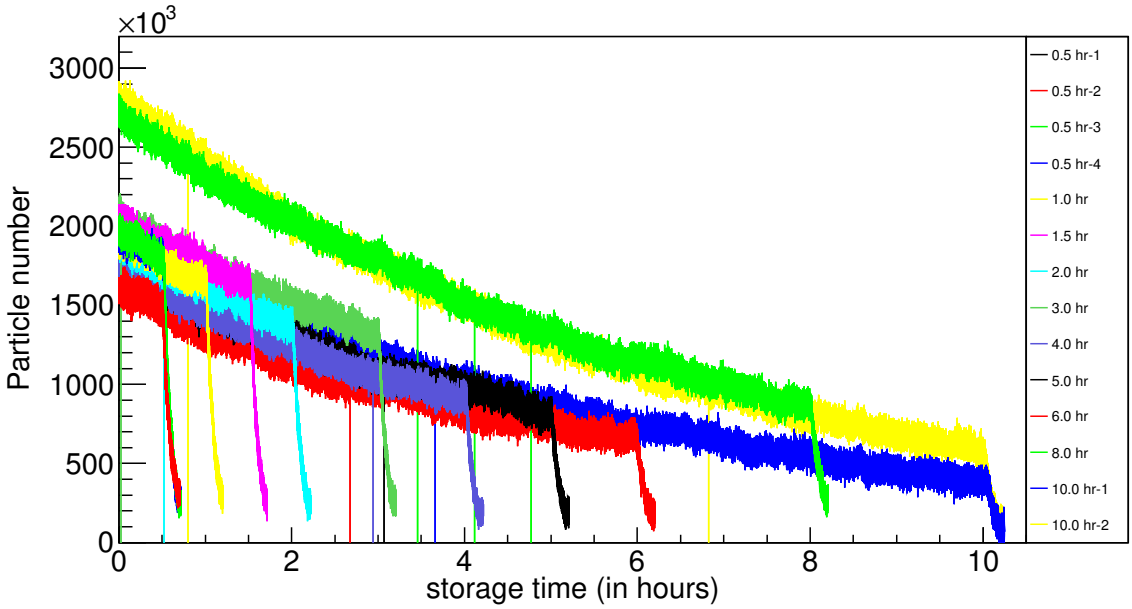

Figure 7.22: Different storage measurements are plotted from the DCCT data.

7.9 Auxiliary test with $^{238}U^{73+}$ beam

To understand the saturation effect seen in the Schottky data, a test experiment with $^{238}U^{73+}$ beam was carried out. $^{238}U^{73+}$ beam with $\sim 2\times10^7$ ions was stored in the ESR at 193.2 MeV/u. The very same resonant Schottky cavity (with resonance frequency $\sim$ 243.7 MHz) was employed. NTCAP with the same IQ rate 8 MS/s and a spectrum analyzer were used for the data taking purpose.

Schottky signal from the ESR goes to the main control room and in order to retain the signal strength, a series of amplifiers are used. During the data taking with the $^{238}U^{73+}$ beam, the amplifiers were switched on and off. The results of the measurement can be seen in Figure 7.23. The data recorded by the spectrum analyzer looks as expected as the decay (with storage half-life $\sim$ 20 minutes) of the beam in the ring is exponential. For the data recorded by the NTCAP, the onset of the saturation effect can be clearly seen in the case when one of the amplifiers (100 dB) is turned on, whereas the data recorded by the spectrum analyzer is not saturated. This is a clear indication that the response of the resonant Schottky cavity is not saturated even at high beam intensities. Rather, due to the dynamic range of the NTCAP DAQ system,

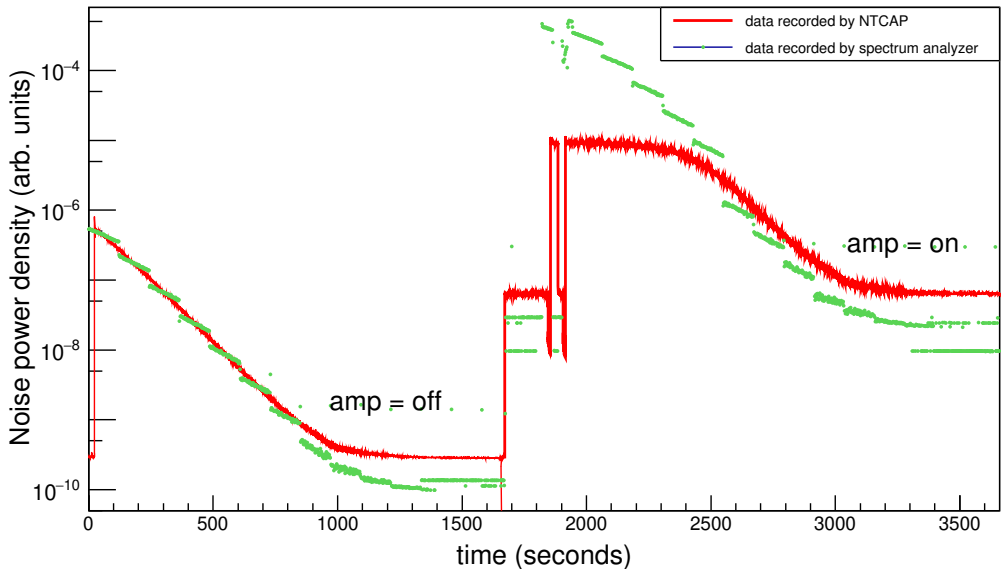

Figure 7.23: Data recorded by the NTCAP and the spectrum analyzer by using the $^{238}U^{73+}$ beam. When the amplifier (100 dB) is on, the saturation effect appears in the NTCAP data.

high noise power density signals were not accepted by the ADC and were distorted causing the saturation effect. For the experiment with the $^{205}Tl^{81+}$ beam, the amplifier (100 dB) was switched on which caused the saturation effect for the entire Schottky data recorded by the NTCAP.

7.10 Saturation correction

Until now, the Schottky data is used to get the Pb/Tl ratio at step 4 (see Section 7.4) which is corrected by the resonance effect in Section 7.5. Now the next correction to be applied is the saturation correction for the parent (Tl) and the daughter ions (Pb).

7.10.1 Saturation correction for $^{205}Pb^{82+}$ ions

The intensity of $^{205}Pb^{82+}$ ions which is determined by using the Schottky data is about four orders of magnitude lower than the saturated $^{205}Tl^{81+}$ ions. In order to confirm whether the daughter ions are saturated or not, it is important to understand the behavior of other low-intensity ion species in

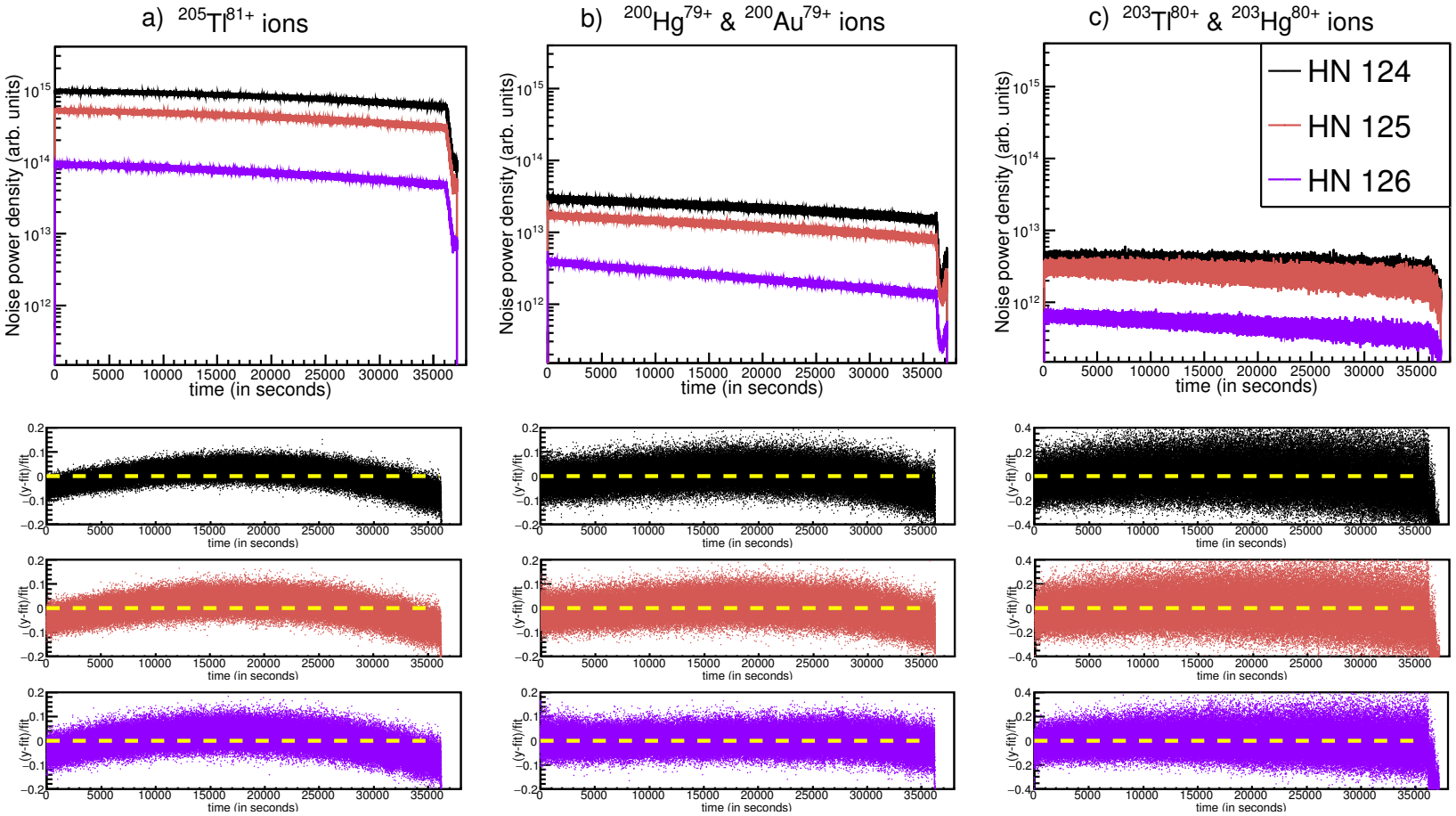

Figure 7.24: A ten hour storage measurement is shown. Left a): $^{205}Tl^{81+}$ ions are saturated at step 1 for all three harmonics which is evident by the bend in the residual plots. Middle b): mixed $^{200}Hg^{79+}$ & $^{200}Au^{79+}$ ions are saturated at step 1 for HN 124 and HN 125. The saturation effect is not evident for HN 126. Right c): mixed $^{203}Tl^{80+}$ & $^{203}Hg^{80+}$ ions are not saturated for any of the harmonics at step 1 as seen by the corresponding residual plots.

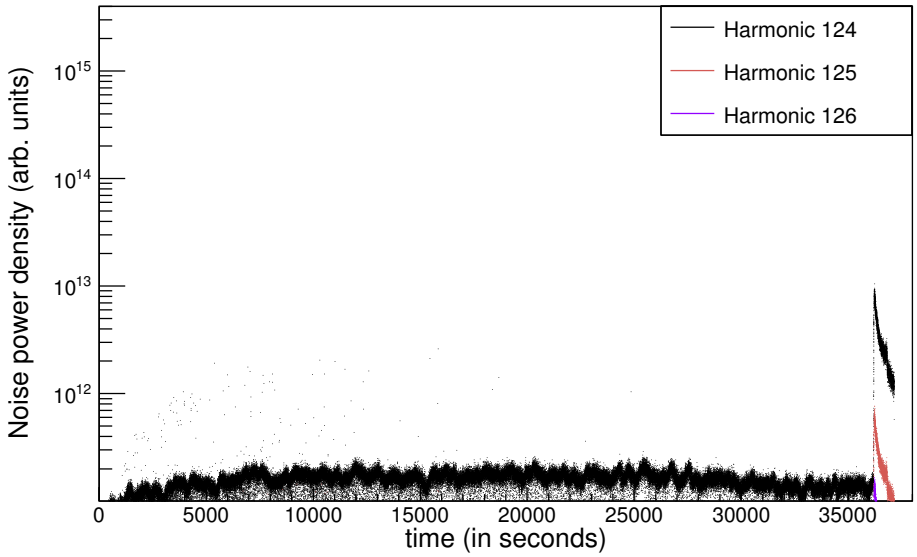

Figure 7.25: A ten hour storage measurement is shown for $^{205}Pb^{82+}$ ions for all three harmonics.

the ring. Along with $^{205}Tl^{81+}$ ions, mixed $^{200}Hg^{79+}$ & $^{200}Au^{79+}$ ions, mixed $^{203}Tl^{80+}$ & $^{203}Hg^{80+}$ ions are also stored which are ~ 1.5 and ~ 2.5 orders of magnitude lower in intensity than $^{205}Tl^{81+}$ ions, respectively.

In Figure 7.24 $^{205}Tl^{81+}$ ions (a), mixed $^{200}Hg^{79+}$ & $^{200}Au^{79+}$ ions (b) and mixed $^{203}Tl^{80+}$ & $^{203}Hg^{80+}$ ions (c) are plotted for a 10 hours storage measurement for all three harmonics. One can see three ion species for three harmonic numbers. Due to the interaction with the electron cooler ($I_e = 200$ mA) and the residual gas in the ring, the stored ions decay exponentially with time. Each ion species is fitted with an exponential function (using equation 7.12) for the 10 hours storage duration and the residual of the fit is shown as well. From Figure 7.24 a) one can see the bend in the residual of the fit for all three harmonics for $^{205}Tl^{81+}$ ions. This clearly indicates that $^{205}Tl^{81+}$ ions are saturated during the storage process. For mixed $^{200}Hg^{79+}$ & $^{200}Au^{79+}$ ions (Figure 7.24 b)), the bend is seen for HN 124 (close to the resonance of the Schottky cavity) and for HN 125 but not for HN 126 (away from the resonance of the Schottky cavity). For mixed $^{203}Tl^{80+}$ & $^{203}Hg^{80+}$ ions (Figure 7.24 c)) which are low in intensity, the bend disappears for all three harmonics indicating that they are not saturated in any of the harmonics. Due to this reason the AF for $^{205}Tl^{81+}$ ions obtained from mixed $^{203}Tl^{80+}$ & $^{203}Hg^{80+}$ ions is taken for the resonance correction in Section 7.5.

From the above discussion, it is clear that the saturation effect is dependent on ion intensity and low-intensity ion species are not affected by

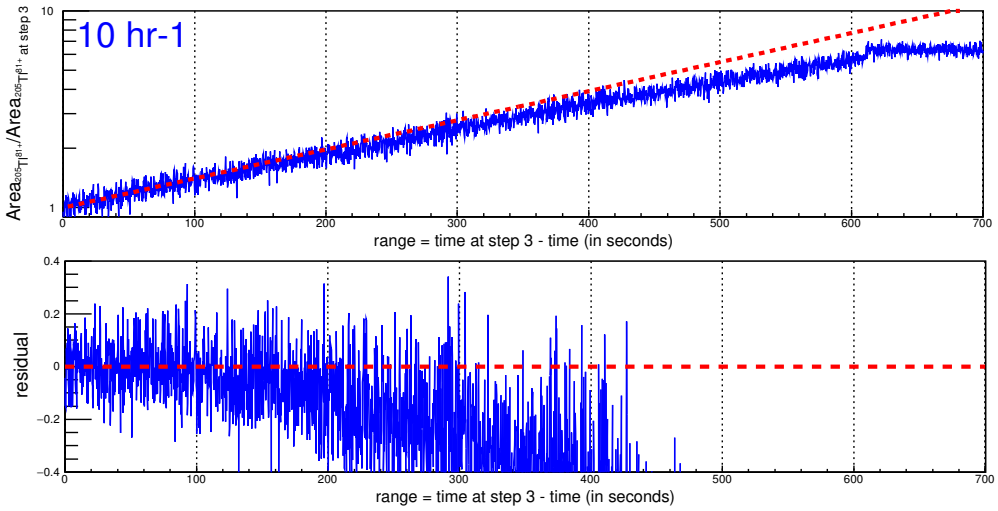

Figure 7.26: The ratio of the integral Schottky area to the integral Schottky area at step 3 for $^{205}Tl^{81+}$ ions vs range is plotted for 10 hr-1 storage measurement for HN 126.

it. $^{205}Pb^{82+}$ ions are shown in Figure 7.25 which are $\sim$ 2 orders of magnitude lower in intensity than that of mixed $^{203}Tl^{80+}$ & $^{203}Hg^{80+}$ ions. Hence, with this argument, $^{205}Pb^{82+}$ ions are not saturated and they can be safely counted (as done in Section 7.5) for all harmonics.

7.10.2 Saturation correction for $^{205}Tl^{81+}$ ions

$^{205}Tl^{81+}$ ions constitute the majority of the stored ions in the ESR. Also, bend in the residual of the fit in Figure 7.24 a) is a clear evidence of the persisting saturation effect in $^{205}Tl^{81+}$ ions which need to be corrected.

To get into the roots of understanding the saturation effect, the ratio of the integral Schottky area to the integral Schottky area at step 3 for $^{205}Tl^{81+}$ ions vs range is plotted for one of the 10 hours (10 hr-1) measurements (first and second 10 hour measurements are defined as 10 hr-1 and 10 hr-2, respectively) for HN 126, as shown in Figure 7.26. Here, the range is defined as the difference of time at step 3 (when the gas jet target is switched off) and time in seconds. Range = 0 s represents the end of the stripping time and range $\sim$ 600 s represents the start of the stripping time. The plot in Figure 7.26 is then fitted using an exponential function (equation 7.12). It

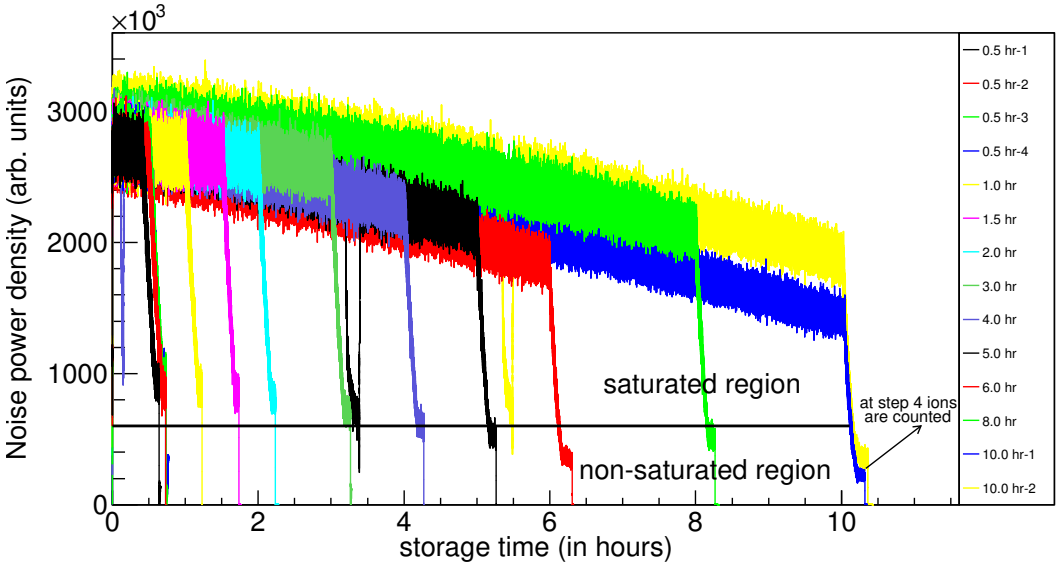

Figure 7.27: Saturated and non-saturated regions are depicted for the Schottky data for HN 126.

is interesting to see that till range $\sim$ 300 s, the plot agrees well with the fit which is more clearly shown by the residual plot below. This means, that for 10 hr-1 measurement, the Schottky intensities are saturated before 300 s of the stripping time, after which, the Schottky intensities enter into a non-saturated regime. Figure 7.27 shows more clearly the saturated and non-saturated regions for HN 126. However, the ion counting (as discussed in Section 7.4) is done at step 4.

From Figure 7.27, it is evident that small-storage hour measurements for $^{205}Tl^{81+}$ ions are even saturated at step 4 where the ion counting is done. To understand the saturation effect for small-storage hour measurements, the ratio of the integral Schottky area to the integral Schottky area at step 3 for $^{205}Tl^{81+}$ ions vs range is plotted for all storage measurements for HN 126 and is compared to 10 hr-1 measurement in Figure 7.28. Clear bend for small-storage hour measurements from the expected exponential fitting is a confirmation that these measurements are saturated at step 3 and demand a correction.

For the correction purpose, 10 hr-1 measurement is plotted for the stripping time and fitted using

$$G(t) = (p_1 + p_2 \cdot t) \cdot p_3 \exp(p_4 + p_5 \cdot t) \quad \text{for } 0 < t < 600\text{s} \ ,$$

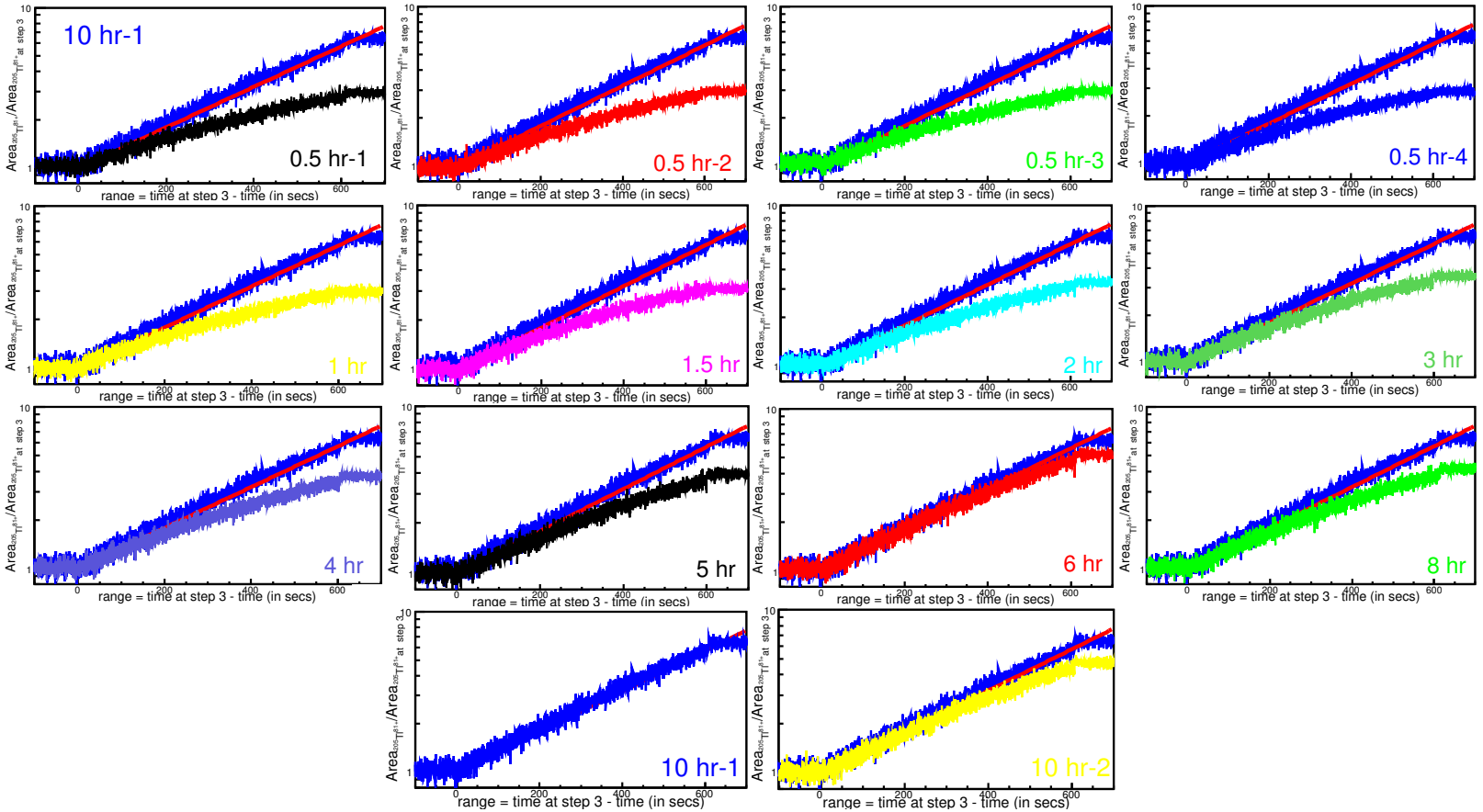

Figure 7.28: The ratio of the integral Schottky area to the integral Schottky area at step 3 for $^{205}Tl^{81+}$ ions vs range is plotted for different storage measurements for HN 126 and is compared with 10 hr-1 measurement.

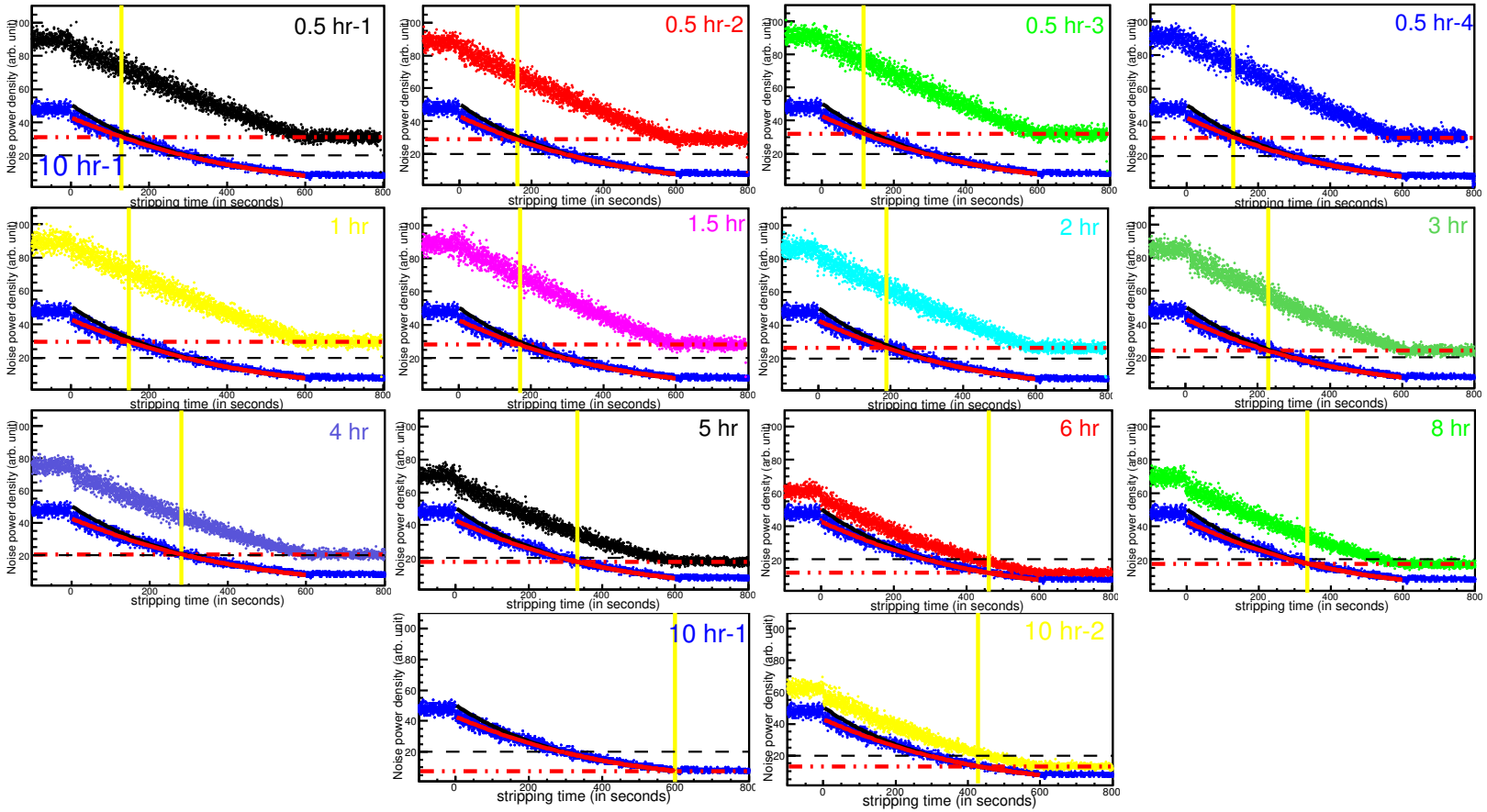

Figure 7.29: Saturation correction for different storage measurements for HN 126 is shown. 10 hr-1 measurement is taken as a reference for the correction.

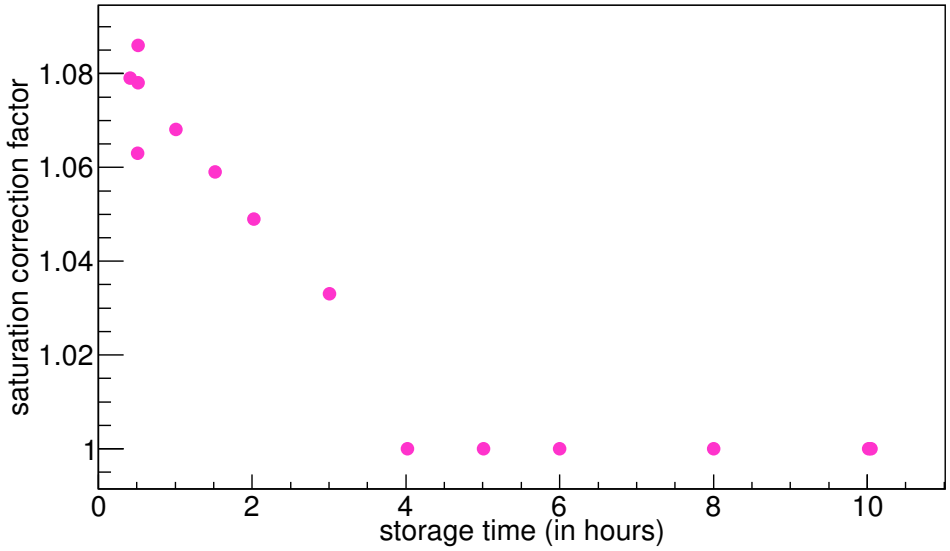

Figure 7.30: Saturation correction factor for different storage measurements for HN 126.

where p_1, p_2, p_3, p_4 and p_5 are the fitting parameters. $G(t)$ function is a product of a first degree polynomial function and an exponential function which fits the saturated curve. The fit is shown by a red fit line in Figure 7.29. Also, the MWPC data give the value of λ_2 from which, the Schottky intensity can be known at step 2 (N_2) if it is known at step 3 (N_3) as

$$N_3 = N_2 e^{-\lambda_2 t} \ .$$

This is shown by a black fit line in Figure 7.29 for 10 hr-1 measurement. Black and red fits agree very well for $300 < t < 600$ which is a consistency proof that after t=300 s, 10 hr-1 measurement is no longer saturated. By using the black fit, non-saturated particle number are obtained.

Now, to correct the number of $^{205}Tl^{81+}$ ions, black fit in 10 hr-1 measurement is taken as a reference and the saturated values are corrected. This can be seen in Figure 7.29 where all small-storage hour measurements are corrected for the saturation effect.

The saturation correction factor which is defined as

$$\text{saturation correction factor (SCF)} = \frac{\text{non saturated ion number}}{\text{saturated ion number}} \ , \quad (7.13)$$

is obtained, by using which, $^{205}Tl^{81+}$ ions are corrected. Figure 7.30 shows the saturation correction factor for different storage measurements. It is

to be emphasized that the number of $^{205}Tl^{81+}$ ions for small-storage hour measurements are suppressed by $\sim$ 5-8% due to the saturation effect which is now corrected for HN 126.

The saturation correction discussed for $^{205}Tl^{81+}$ ions in this Section is performed for HN 126. It is clearly reflected from Figure 7.24 a) that $^{205}Tl^{81+}$ ions are saturated even at step 4 for HN 124 and HN 125 due to which no reliable ion counting can be done.

7.11 Storage decay constant

In order to determine the half-life, storage decay constant for Tl ($\lambda^{cc}_{\mathrm{Tl}}$) and Pb ($\lambda^{cc}_{\mathrm{Pb}}$) ions are to be measured (see equation 7.9). $\lambda^{cc}_{\mathrm{Tl}}$ and $\lambda^{cc}_{\mathrm{Pb}}$ represents the losses due to interaction with the electron cooler and the residual gas in the ring for stored $^{205}Tl^{81+}$ and $^{205}Pb^{81+}$ ions, respectively.

Due to the saturation effect, the Schottky data cannot be used to determine the value of $\lambda^{cc}_{\mathrm{Tl}}$. The second way is to use the DCCT data. Relative intensities for all storage measurements are plotted as shown in Figure 7.31. These are fitted with an exponential function (using equation 7.12) to obtain the storage decay constant for each storage measurement, which is shown in Figure 7.32. $\lambda^{cc}_{\mathrm{Tl}}$ is constant as expected and the value obtained is

$$\lambda^{cc}_{\mathrm{Tl}} = 4.3(1)_{\mathrm{stat}} \times 10^{-5}\ \mathrm{s}^{-1}\ .$$

For systematic error contribution, χ_n is calculated using equation 6.5. χ_n = 1.59 is out of the expected range of $\chi_n = 1\pm0.24$ and thus an additional systematic error $\sigma_{\mathrm{syst}} = 0.1\times10^{-5}$ s^{-1} is added

$$\lambda^{cc}_{\mathrm{Tl}} = 4.3(1)_{\mathrm{stat}}(1)_{\mathrm{syst}} \times 10^{-5}\ \mathrm{s}^{-1}\ .$$

In the experiment, there were no storage measurements performed for the $^{205}Pb^{81+}$ ions. But, one can obtain $\lambda^{cc}_{\mathrm{Pb}}$ by proper scaling $\lambda^{cc}_{\mathrm{Tl}}$ up by 2% as $\lambda^{cc} \propto Z^2$ and thus

$$\lambda^{cc}_{\mathrm{Pb}} = 4.4(1)_{\mathrm{stat}}(1)_{\mathrm{syst}} \times 10^{-5}\ \mathrm{s}^{-1}\ .$$

For all storage measurements, $(\lambda^{cc}_{\mathrm{Tl}} - \lambda^{cc}_{\mathrm{Pb}}) \cdot t_s \leq 0.1$ and thus, equation 7.9 shows a linear dependence with storage time t_s and is given by

$$\left(\frac{N_{\mathrm{Pb}}(t_s)}{N_{\mathrm{Tl}}(t_s)}\right)_2 = \frac{\lambda_{\beta_b}}{\gamma} t_s\ . \tag{7.14}$$

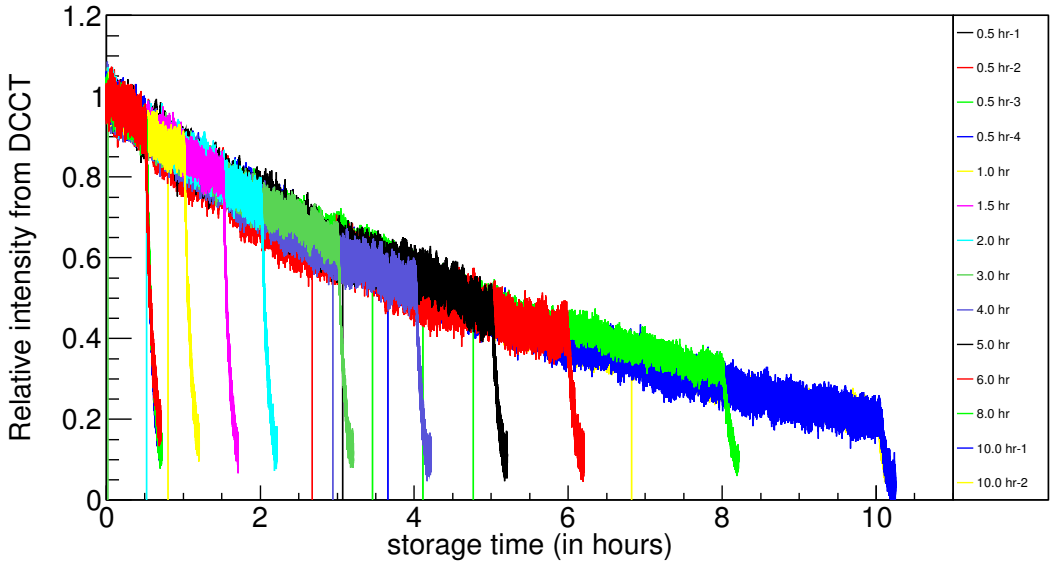

Figure 7.31: Relative DCCT intensities for different storage measurements are shown at step 1.

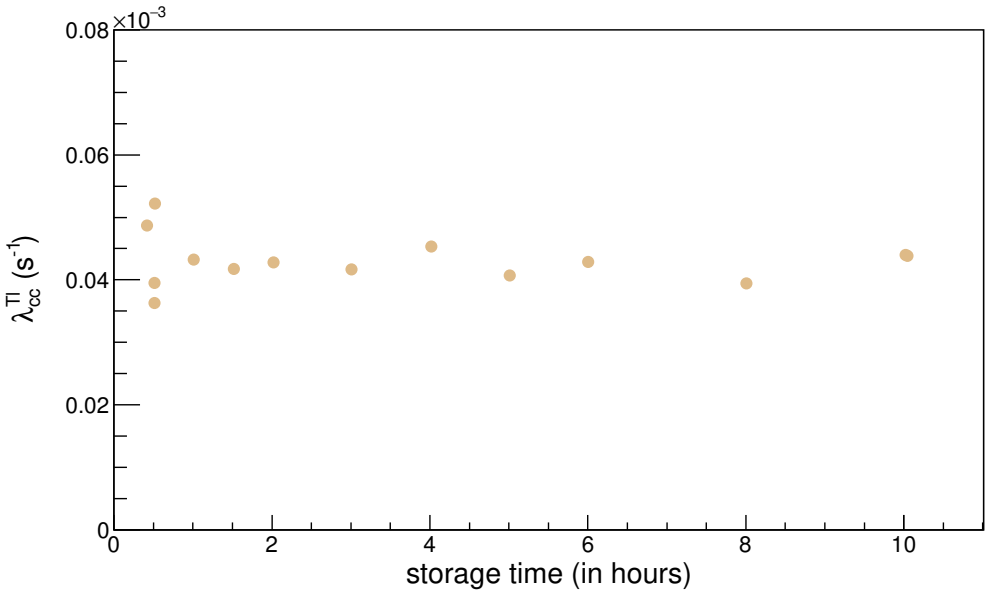

Figure 7.32: Storage decay constant ($\lambda_{\mathrm{Tl}}^{cc}$) for $^{205}\mathrm{Tl}^{81+}$ ions for different storage measurements.

7.12 Half-life of bound-state beta decay

After the resonance and the saturation correction, the ratio of Pb to Tl ions can be obtained at step 2 using

$$\left(\frac{N_{\mathrm{Pb}}}{N_{\mathrm{Tl}}}\right)_2 = \left(\frac{N_{\mathrm{Pb}}}{N_{\mathrm{Tl}}}\right)_4 \cdot \frac{e^{-\lambda_2^{\mathrm{Tl}} t}}{1 - e^{-\lambda_2^{\mathrm{Pb}} t}} \cdot \frac{\sigma_{I,\mathrm{Pb}} + \sigma_{c,\mathrm{Pb}}}{\sigma_{I,\mathrm{Pb}}} \quad . \tag{7.15}$$

The values obtained at step 2 for HN 126 are shown in Tables 7.2, 7.3, 7.4. The ratio at step 2 is plotted for different storage measurements and is fitted with a polynomial function of first degree as shown in Figure 7.33. The half-life is calculated using

$$t_{1/2_{\beta_b}} = \frac{0.693}{\gamma \times 24 \times \lambda} \quad , \tag{7.16}$$

with

$$\lambda_0 + \lambda \cdot t_s = \left(\frac{N_{\mathrm{Pb}}}{N_{\mathrm{Tl}}}\right)_2 \quad , \tag{7.17}$$

where λ_0 (constant) and λ_1 (slope) are the fitting parameters of the first degree polynomial function. Uncertainty of the half-life ($\Delta t_{1/2_{\beta_b}}$) is determined using

$$\Delta t_{1/2_{\beta_b}} = \frac{\Delta\lambda}{\lambda} \cdot t_{1/2_{\beta_b}} \quad , \tag{7.18}$$

with $\Delta\lambda$ being the error of λ. The half-life of the bound-state beta decay of bare $^{205}\mathrm{Tl}^{81+}$ ions is

$$t_{1/2_{\beta_b}} = 229 \pm 36 \text{ days} \; .$$

The above value incorporates error contribution coming from the amplification factor, λ_2^{Tl}, λ_2^{Pb} and $(\sigma_{I,\mathrm{Pb}}+\sigma_{c,\mathrm{Pb}})/\sigma_{I,\mathrm{Pb}}$. The error of $t_{1/2_{\beta_b}}$ is certainly large and also no systematic uncertainties are taken into account. The error can be further reduced by considering the following.

1) Windowing technique

Rectangular windowing technique is employed for the data analysis discussed in this thesis. The side lobes introduced due to the spectral leakage can affect the data produced after the FFT. Application of different windowing techniques such as Hamming windowing or alternatively a multi-taper method approach, etc. should be investigated.

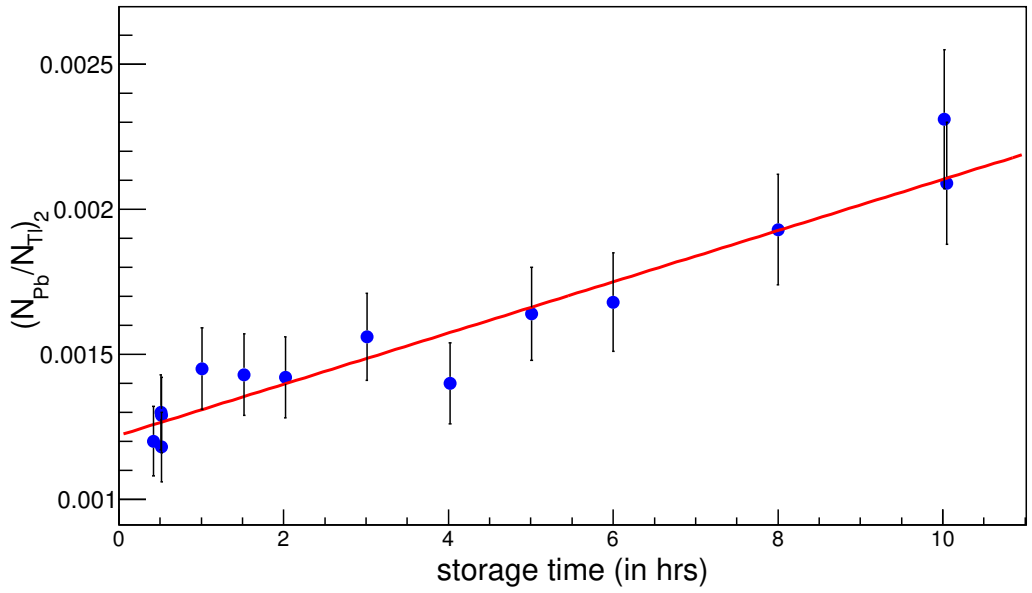

Figure 7.33: Pb to Tl ratio at step 2 as a function of storage time. First degree polynomial fit function is used to determine the decay constant for the bound-state beta decay β_b.

Step 4									
storage							Saturation		
time	$^{205}Tl^{81+}$		$^{205}Pb^{82+}$		Pb/Tl ratio		Correction	$^{205}Tl^{81+}$ after correction	
t_s (in hrs)	Mean	Error	Mean	Error	Mean	Error	SCF	Mean	Error
0.42	3.076×10^{13}	1.741×10^{12}	6.424×10^{10}	3.637×10^{9}	0.0021	0.0002	1.079	3.318×10^{13}	1.879×10^{12}
0.51	2.841×10^{13}	1.608×10^{12}	6.006×10^{10}	3.400×10^{9}	0.0021	0.0002	1.063	3.021×10^{13}	1.710×10^{12}
0.52	3.155×10^{13}	1.786×10^{12}	6.270×10^{10}	3.550×10^{9}	0.0020	0.0002	1.086	3.425×10^{13}	1.939×10^{12}
0.52	3.115×10^{13}	1.763×10^{12}	6.373×10^{10}	3.608×10^{9}	0.0020	0.0002	1.078	3.356×10^{13}	1.900×10^{12}
1.01	2.958×10^{13}	1.675×10^{12}	6.641×10^{10}	3.760×10^{9}	0.0022	0.0002	1.068	3.161×10^{13}	1.789×10^{12}
1.52	2.815×10^{13}	1.594×10^{12}	6.244×10^{10}	3.535×10^{9}	0.0022	0.0002	1.059	2.980×10^{13}	1.687×10^{12}
2.02	2.580×10^{13}	1.461×10^{12}	5.955×10^{10}	3.371×10^{9}	0.0023	0.0002	1.049	2.706×10^{13}	1.532×10^{12}
3.01	2.349×10^{13}	1.330×10^{12}	5.886×10^{10}	3.332×10^{9}	0.0025	0.0002	1.033	2.428×10^{13}	1.374×10^{12}
4.02	1.994×10^{13}	1.129×10^{12}	4.321×10^{10}	2.446×10^{9}	0.0022	0.0002	1.000	1.994×10^{13}	1.129×10^{12}
5.01	1.730×10^{13}	9.792×10^{11}	4.359×10^{10}	2.468×10^{9}	0.0025	0.0002	1.000	1.730×10^{13}	9.792×10^{11}
6.00	1.186×10^{13}	6.716×10^{11}	3.068×10^{10}	1.737×10^{9}	0.0026	0.0002	1.000	1.186×10^{13}	6.716×10^{11}
8.00	1.679×10^{13}	9.507×10^{11}	4.993×10^{10}	2.827×10^{9}	0.0030	0.0002	1.000	1.679×10^{13}	9.507×10^{11}
10.05	7.320×10^{12}	4.144×10^{11}	2.350×10^{10}	1.330×10^{9}	0.0032	0.0003	1.000	7.320×10^{12}	4.144×10^{11}
10.02	1.305×10^{13}	7.388×10^{11}	4.520×10^{10}	2.559×10^{9}	0.0035	0.0003	1.000	1.305×10^{13}	7.388×10^{11}

Table 7.2: Ratio at step 4 for HN 126.

Step 4						
	Resonance Correction AF=0.39(1)		$(\sigma_{I,\mathrm{Pb}} + \sigma_{c,\mathrm{Pb}})/\sigma_{I,\mathrm{Pb}}$=1.449(16)		With all corrections	
storage time	$^{205}Pb^{82+}$ after correction		$^{205}Pb^{82+}$		Pb/Tl ratio	
t_s (in hrs)	Mean	Error	Mean	Error	Mean	Error
0.42	1.647×10^{11}	1.024×10^{10}	2.387×10^{11}	1.507×10^{10}	0.0072	0.0006
0.51	1.540×10^{11}	9.571×10^{9}	2.231×10^{11}	1.409×10^{10}	0.0074	0.0006
0.52	1.608×10^{11}	9.992×10^{9}	2.330×10^{11}	1.470×10^{10}	0.0068	0.0006
0.52	1.634×10^{11}	1.016×10^{10}	2.368×10^{11}	1.495×10^{10}	0.0070	0.0006
1.01	1.703×10^{11}	1.058×10^{10}	2.467×10^{11}	1.557×10^{10}	0.0078	0.0007
1.52	1.601×10^{11}	9.950×10^{9}	2.320×10^{11}	1.464×10^{10}	0.0078	0.0007
2.02	1.527×10^{11}	9.490×10^{9}	2.213×10^{11}	1.397×10^{10}	0.0082	0.0007
3.01	1.509×10^{11}	9.380×10^{9}	2.187×10^{11}	1.380×10^{10}	0.0090	0.0008
4.02	1.108×10^{11}	6.886×10^{9}	1.605×10^{11}	1.013×10^{10}	0.0081	0.0007
5.01	1.118×10^{11}	6.946×10^{9}	1.620×10^{11}	1.022×10^{10}	0.0094	0.0008
6.00	7.867×10^{10}	4.889×10^{9}	1.140×10^{11}	7.195×10^{9}	0.0096	0.0008
8.00	1.280×10^{11}	7.957×10^{9}	1.855×10^{11}	1.171×10^{10}	0.0110	0.0009
10.05	6.026×10^{10}	3.745×10^{9}	8.731×10^{10}	5.511×10^{9}	0.0119	0.0010
10.02	1.159×10^{11}	7.203×10^{9}	1.679×10^{11}	1.060×10^{10}	0.0129	0.0011

Table 7.3: Ratio at step 4 for HN 126.

Step 2											
								$\lambda^{cc}_{\mathrm{Tl}}$=4.3(1)$\times10^{-5}$ s^{-1}			
storage	stripping	λ_2^{Tl} =3.13(8)$\times10^{-3}$ s^{-1}		λ_2^{Pb}=3.21(8)$\times10^{-3}$ s^{-1}				$\lambda^{cc}_{\mathrm{Pb}}$=4.4(1)$\times10^{-5}$ s^{-1}			
time t_s	time t	^{205}Tl^{81+}		^{205}Pb^{82+}		Pb/Tl ratio		$[1+1/2(\lambda^{cc}_{\mathrm{Tl}}-\lambda^{cc}_{\mathrm{Pb}})]t_s$		**Pb/Tl ratio**	
(in hrs)	(in sec)	Mean	Error	Mean	Error	Mean	Error	Mean	Error	**Mean**	**Error**
0.42	620	2.311×10^{14}	1.739×10^{13}	2.765×10^{11}	1.759×10^{10}	0.00120	0.00012	0.993	0.0011	**0.00120**	**0.00012**
0.51	604	2.001×10^{14}	1.489×10^{13}	2.606×10^{11}	1.659×10^{10}	0.00130	0.00013	0.9993	0.0013	**0.00130**	**0.00013**
0.52	608	2.297×10^{14}	1.714×10^{13}	2.715×10^{11}	1.728×10^{10}	0.00118	0.00012	0.9991	0.0013	**0.00118**	**0.00012**
0.52	595	2.161×10^{14}	1.598×10^{13}	2.779×10^{11}	1.769×10^{10}	0.00129	0.00013	0.9991	0.0013	**0.00129**	**0.00013**
1.01	590	2.003×10^{14}	1.477×10^{13}	2.904×10^{11}	1.849×10^{10}	0.00145	0.00014	0.9991	0.0026	**0.00145**	**0.00014**
1.52	593	1.907×10^{14}	1.409×10^{13}	2.726×10^{11}	1.736×10^{10}	0.00143	0.00014	0.9982	0.0039	**0.00143**	**0.00014**
2.02	610	1.826×10^{14}	1.365×10^{13}	2.576×10^{11}	1.639×10^{10}	0.00141	0.00014	0.9973	0.0051	**0.00142**	**0.00014**
3.01	610	1.638×10^{14}	1.225×10^{13}	2.546×10^{11}	1.620×10^{10}	0.00155	0.00015	0.9964	0.0077	**0.00156**	**0.00015**
4.02	610	1.346×10^{14}	1.006×10^{13}	1.869×10^{11}	1.189×10^{10}	0.00139	0.00014	0.9928	0.0102	**0.00140**	**0.00014**
5.01	609	1.164×10^{14}	8.691×10^{12}	1.887×10^{11}	1.201×10^{10}	0.00162	0.00016	0.9910	0.0128	**0.00164**	**0.00016**
6.00	609	7.980×10^{13}	5.960×10^{12}	1.328×10^{11}	8.450×10^{9}	0.00166	0.00016	0.9892	0.0153	**0.00168**	**0.00017**
8.00	611	1.137×10^{14}	8.502×10^{12}	2.159×10^{11}	1.374×10^{10}	0.00190	0.00019	0.9856	0.0204	**0.00193**	**0.00019**
10.05	611	4.955×10^{13}	3.706×10^{12}	1.016×10^{11}	6.465×10^{9}	0.00205	0.00020	0.9819	0.0256	**0.00209**	**0.00021**
10.02	604	8.642×10^{13}	6.432×10^{12}	1.962×10^{11}	1.248×10^{10}	0.00227	0.00022	0.9820	0.0255	**0.00231**	**0.00023**

Table 7.4: Ratio at step 2 for HN 126.

2) Averaging

Averaging minimizes the random noise fluctuations as described by equation 7.3. By increasing the number of frames (N_{aver}), σ_I can be further reduced.

3) Fitting functions

Gaussian function is used in Section 7.4 to fit and count the number of ions after the background subtraction which might introduce a tiny error. Also for most of the fittings, ROOT analysis software is employed.

4) MWPC

MWPC is used to determine λ_2^{Tl}, λ_2^{Pb} and $(\sigma_{I,\mathrm{Pb}} + \sigma_{c,\mathrm{Pb}})/\sigma_{I,\mathrm{Pb}}$ in the present work. More careful inspection is needed in order to understand and minimize the systematic error contribution.

5) $(\sigma_{I,\mathrm{Pb}} + \sigma_{c,\mathrm{Pb}})/\sigma_{I,\mathrm{Pb}}$

As derived in Chapter 6, particle number from the DCCT and the MWPC has been employed for the evaluation of the cross section ratio. An attempt must be made to get the ratio via the rates of DCCT & MWPC and compare them. It is also suggested to further investigate the analysis of the CsISiPHOS that might be put into use to estimate the cross section ratio.

6) Resonance curve

In order to acquire a more quantitative understanding of the resonance curve of the resonant Schottky cavity, it should be measured with a stable beam by changing its orbit in the ESR. It is planned to measure the resonance curve by using ^{78}Kr or ^{124}Xe beam in the ring.

7.13 Summary

It is exciting to see that ^{205}Tl neutral atom which is stable becomes unstable if all the electrons are stripped off. K. Takahashi *et al.* [54] gave the theoretical value of the decay constant for β_b to be 6.6×10^{-8} s^{-1} which corresponds

to $t_{1/2_{\beta_b}} = 122$ days with $\log(ft) = 5.4$. This work is the first experimental measurement of β_b in $^{205}Tl^{81+}$ ions with $t_{1/2_{\beta_b}} = 229 \pm 36$ days ($\log(ft) = 5.67(7)$) which agrees within 3σ with the theoretical value. The experimental measurement is crucial for the following studies.

1) LOREX project

LOREX is a long-time geochemical solar neutrino experiment [36, 37] that addresses the detection of the solar pp neutrino flux with an unprecedented low threshold of only 53 keV (as described in Section 3.1.1). With the extraction of the lorandite samples and quantitative determination of the $^{205}Pb/^{205}Tl$ ratio, the time integrated and energy averaged product of solar neutrino flux and neutrino capture cross section over 4.31(2) Myr can be determined [42]. Measurement of the bound-state beta decay in $^{205}Tl^{81+}$ ions is the only way to directly determine the essential nuclear matrix element from which the solar pp neutrino capture probability can be evaluated. With the first direct measurement of $t_{1/2_{\beta_b}}$ obtained in this thesis work, pp neutrino capture cross section can now be determined. The longer measured half-life will lead to a smaller nuclear matrix element and thus a smaller pp neutrino capture cross section, deviating from the theory. This will affect in the determination of the final mean solar pp neutrino flux which is decisive for the solar neutrino studies.

The final step for this project would then be to obtain the number of ^{205}Pb atoms in the lorandite samples which is properly corrected for the background events [36, 37]. For this purpose, an experiment is being prepared at the RIKEN facility and a dedicated Rapid Reaction Task Force (RRTF) [91] was organized under the flagship of ExtreMe Matter Institute (EMMI) from 12-13 December, 2019 at GSI where the future steps of the collaboration were addressed.

2) $^{205}Pb/^{205}Tl$ pair as an s-process cosmochronometer

Understanding the production and survival of ^{205}Pb in stars is pivotal as ^{205}Pb is the only short-lived radionuclide that is produced exclusively by s-process nucleosynthesis [38]. The study of short-lived s-process chronometer is essential for nuclear astrophysics as it could indicate the degree to which the last nucleosynthesis events contributing to the solar system abundances differed from the mean rate of s-process nucleosynthesis. As discussed in Section 3.1.2, the validity of the ^{205}Pb chronometer is strongly affected by the electron capture from the first excited state of ^{205}Pb ($E^* = 2.3$ keV), which

reduces the production of ^{205}Pb in the s-process. However, it was pointed out that the bound-state beta decay of ^{205}Tl [53] could counter-balance the reduction of ^{205}Pb. Now with the longer measured half-life of β_b, less destruction of ^{205}Tl to ^{205}Pb is expected in stellar plasmas. The electron capture decay from the 2.3 keV excited state in ^{205}Pb and β_b in $^{205}Tl^{81+}$ share the identical nuclear transition matrix element. As a consequence, the reduction of ^{205}Pb due to the electron capture decay from the 2.3 keV excited state is slower which influences the $P_{^{205}\mathrm{Pb}}/P_{^{204}\mathrm{Pb}}$ ratio. This might rule out injection from the Asymptotic Giant Branch (AGB) stars as the source of ^{205}Pb in the early solar system [51] and might bring the value from the continuous galactic chemical evolution model into better agreement with the meteoritic value [51]. Reduced electron capture decay from the 2.3 keV excited state of ^{205}Pb also raises questions to the validity of ^{205}Pb as an s-process cosmochronometer.

Chapter 8

Outlook

The ESR is an unique storage ring facility which offers unparalleled discovery potential. The ESR is suitable for nuclear and atomic physics experiments using highly charged and radioactive ion beams. Heavy ions can be stored with energies ranging from 4 MeV/u to 400 MeV/u according to the experimental requirements. Different physics cases, e.g., direct mass and half-life time measurements [33, 92, 93, 94, 95] of short-lived radionuclides, nuclear astrophysics experiments in the Gamow window [96], atomic physics experiments which aim to test the QED (Quantum Electrodynamics) at extreme electromagnetic fields [97, 98] etc. have been performed [99]. A new low energy storage ring CRYRING@ESR [99] has recently been installed which is optimized for operation of ions that can be stored with an energy range of 14 MeV/u down to several 100 keV/u and is in operation since last year.

The small acceptance at the injection channel for the fragment beams in the ESR limits the range of the accessible nuclei due to small production cross sections and hefty transmission losses. In order to overcome these problems and to provide higher beam intensities, a new facility FAIR (Facility for Antiproton and Ion Research) [74, 75] was approved which is now in the construction phase. Figure 8.1 shows the existing GSI facility in blue color and the future FAIR facility in red color, respectively. A new synchrotron SIS-100 will provide ion beams with intensities above 5×10^{11}/s for all stable elements up to uranium. A new Super-FRS (superconducting FRS) with high-acceptance will allow projectile fission fragments to be separated with higher efficiencies. Two new storage rings CR (collector ring) and HESR (high energy storage ring) will be built. The CR is designed to accept the full phase-space of the fragment beams from the Super-FRS which will be operated in the isochronous mode where physics cases of very short-lived nuclides will be addressed. On the contrary, the HESR is designed for the studies for longer-lived nuclides where the ions can be nicely cooled and

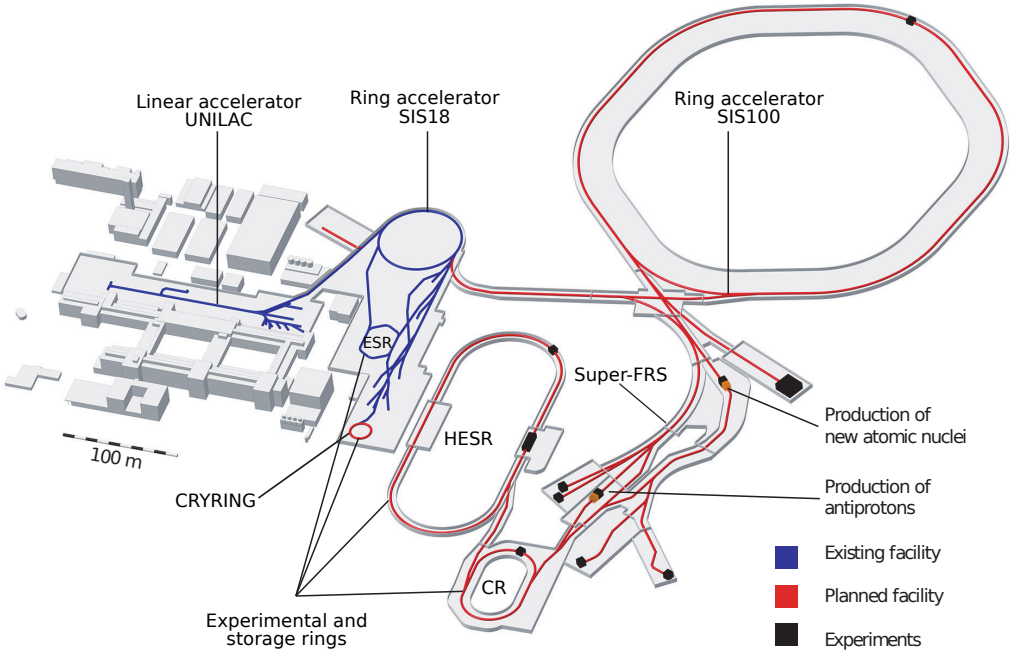

Figure 8.1: Visualization of the future FAIR accelerator facility [59].

stored for different studies.

The physics cases especially involving the search for new decay modes are promising in the ESR and the future proposed storage rings. One such example is the search for bound-state electron-positron pair [100]. For a photon, the $0^+ \rightarrow 0^+$ ($E0$) transitions via an emission of a single photon are prohibited as the photon is a boson. The decay can thus proceed via internal conversion, double gamma-ray emission or if the transition energy is larger than $2m_e$ via electron-positron pair decay in neutral atoms. For fully-ionized atom, internal conversion decay branch is impossible and if electron-positron pair decay is energetically disabled, one can see a bound-state electron-positron pair decay. One such prominent candidate for this yet unobserved decay mode is ${}^{194}_{82}\mathrm{Pb}^{82+}_{112}$ where the energy of the 0^+ state is less than $2m_e$. There are many other high potential physics cases with highly charged ions where nuclear decay properties can change dramatically and can be studied in the storage rings.

Appendices

Appendix A

Particle detector plots

For the analysis of the particle detectors discussed in Chapter 6, there are some important plots that are put in this Section.

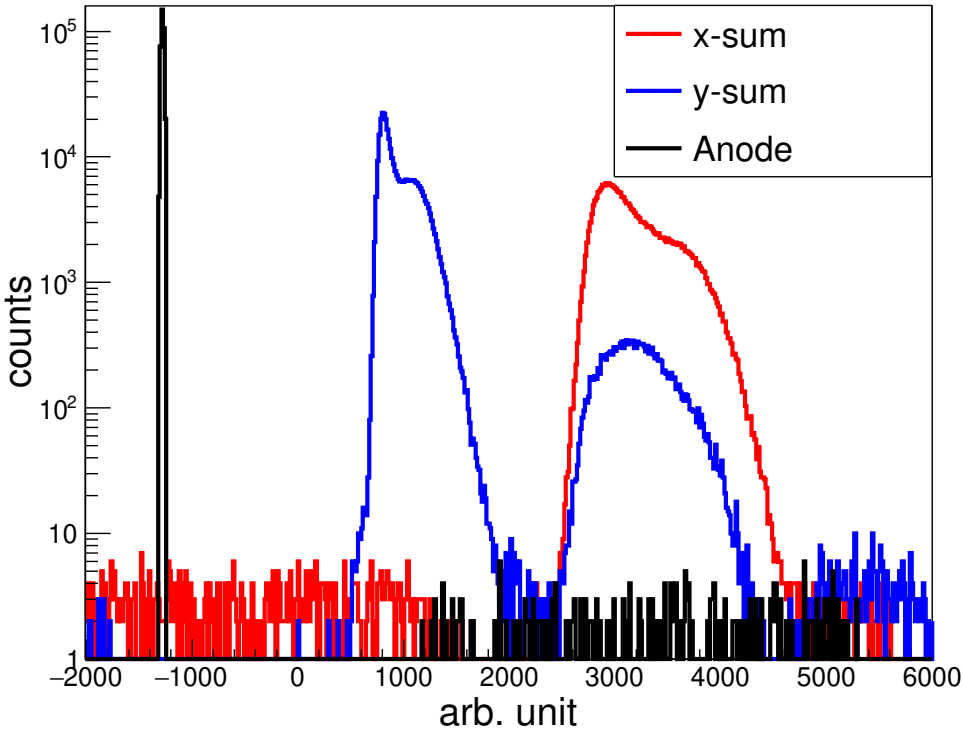

Figure A.1: Anode, x-sum and y-sum signals for a measurement cycle.

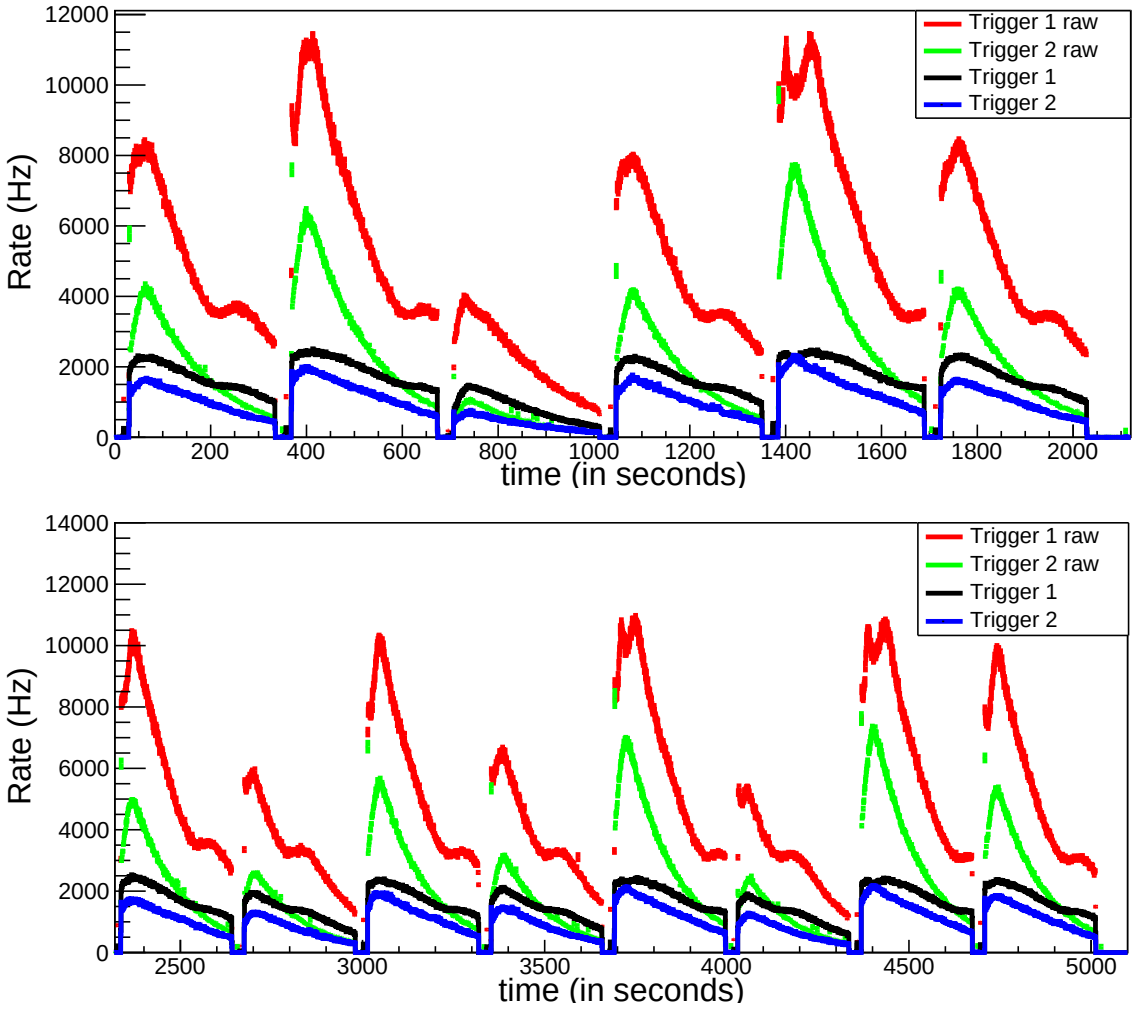

Figure A.2: Different trigger rates for all injection measurements.

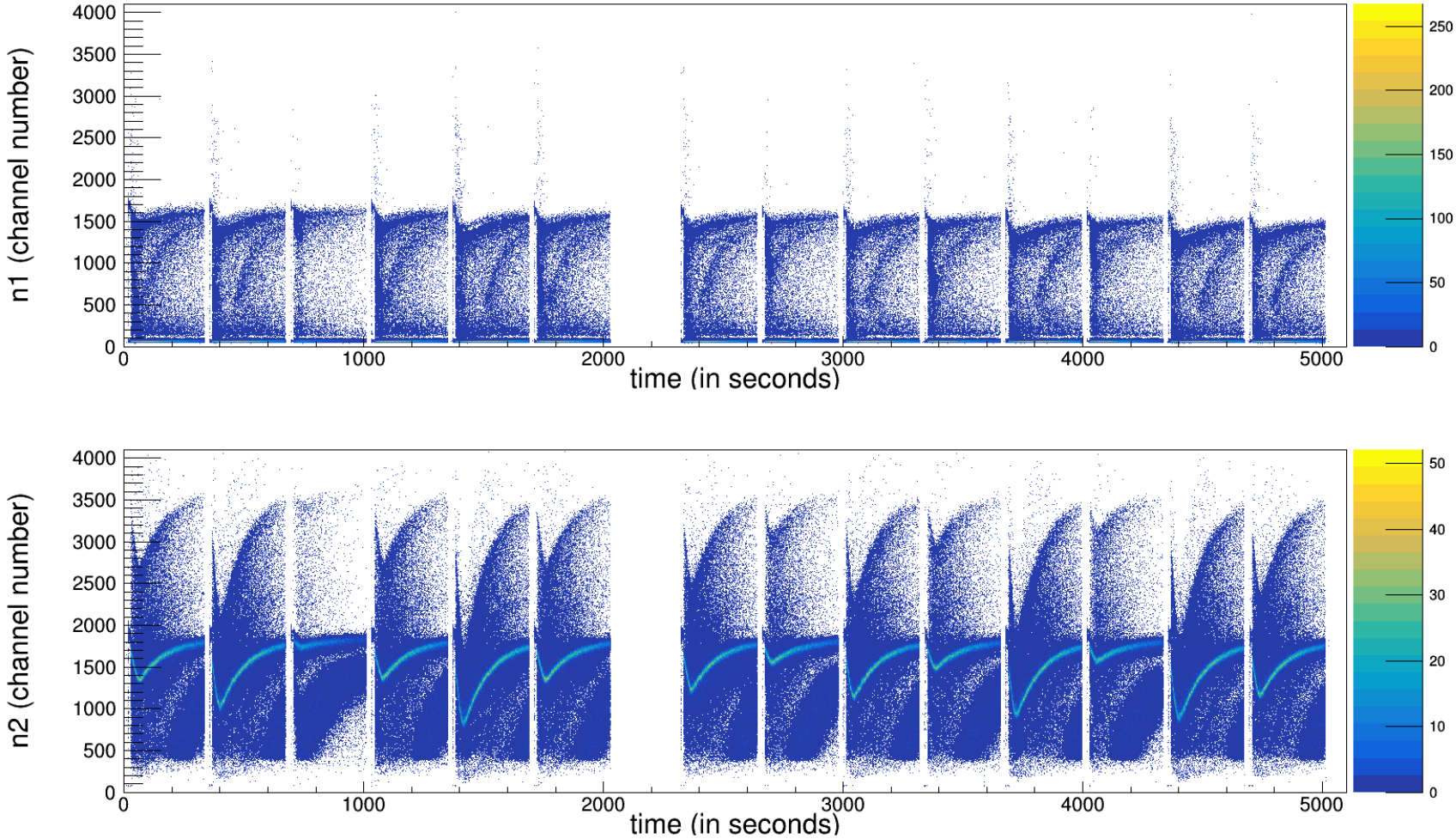

Figure A.3: Events hitting on the n1 and n2 for all injection measurements.

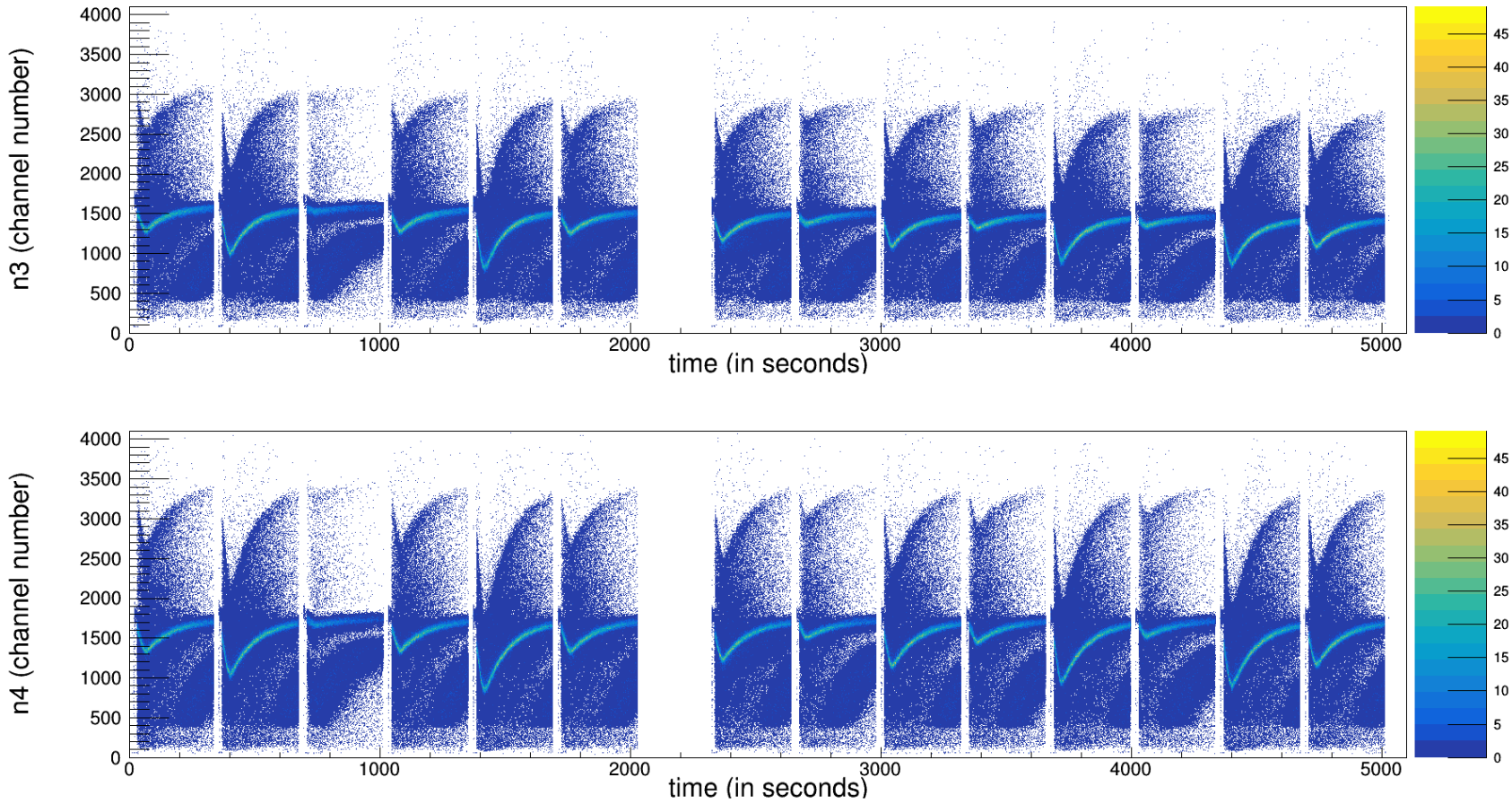

Figure A.4: Events hitting on the n3 and n4 for all injection measurements.

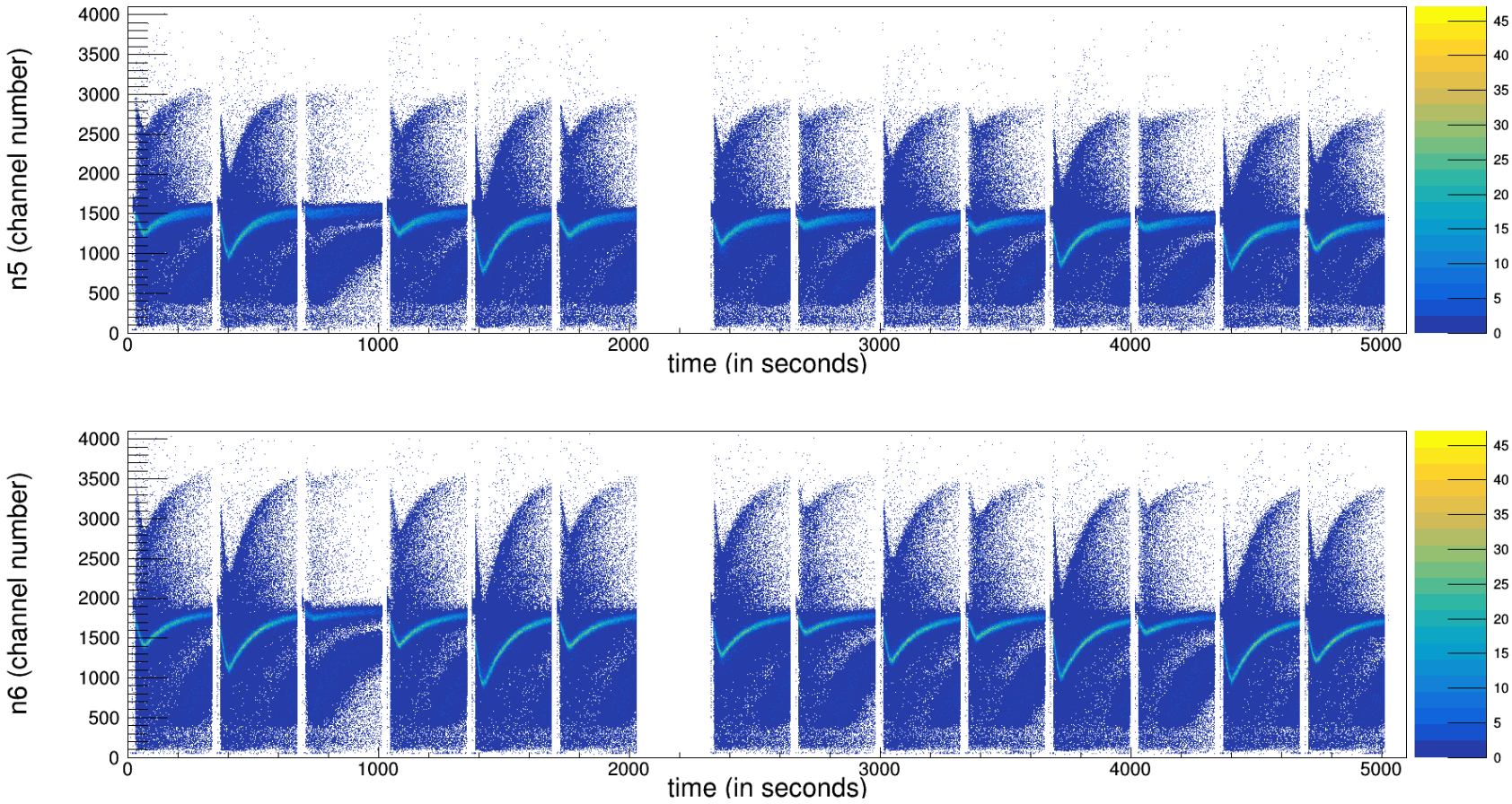

Figure A.5: Events hitting on the n5 and n6 for all injection measurements.

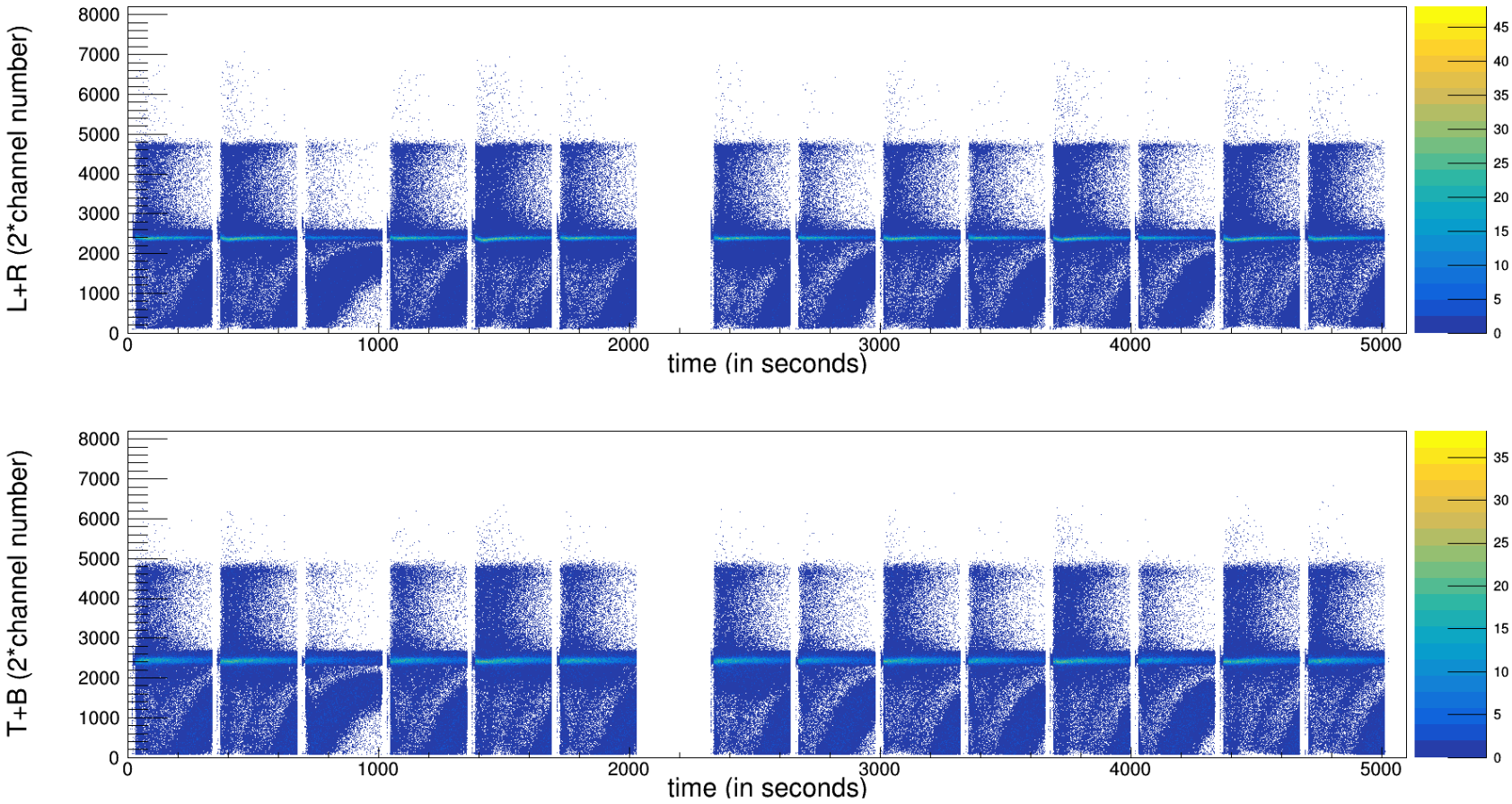

Figure A.6: Events hitting on the p- and n-side of the DSSD for all injection measurements.

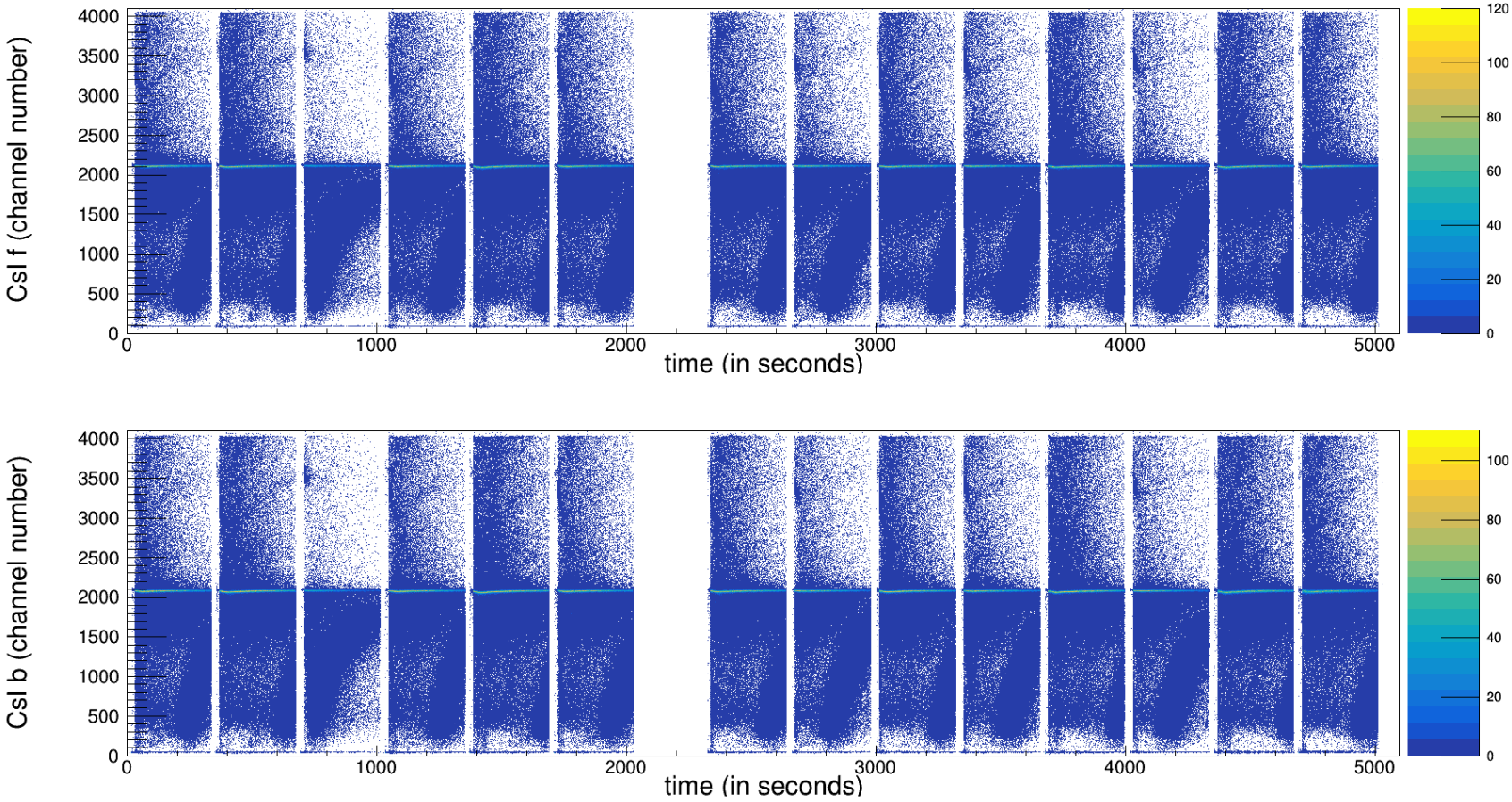

Figure A.7: Events hitting on the CsI f and CsI b for all injection measurements.

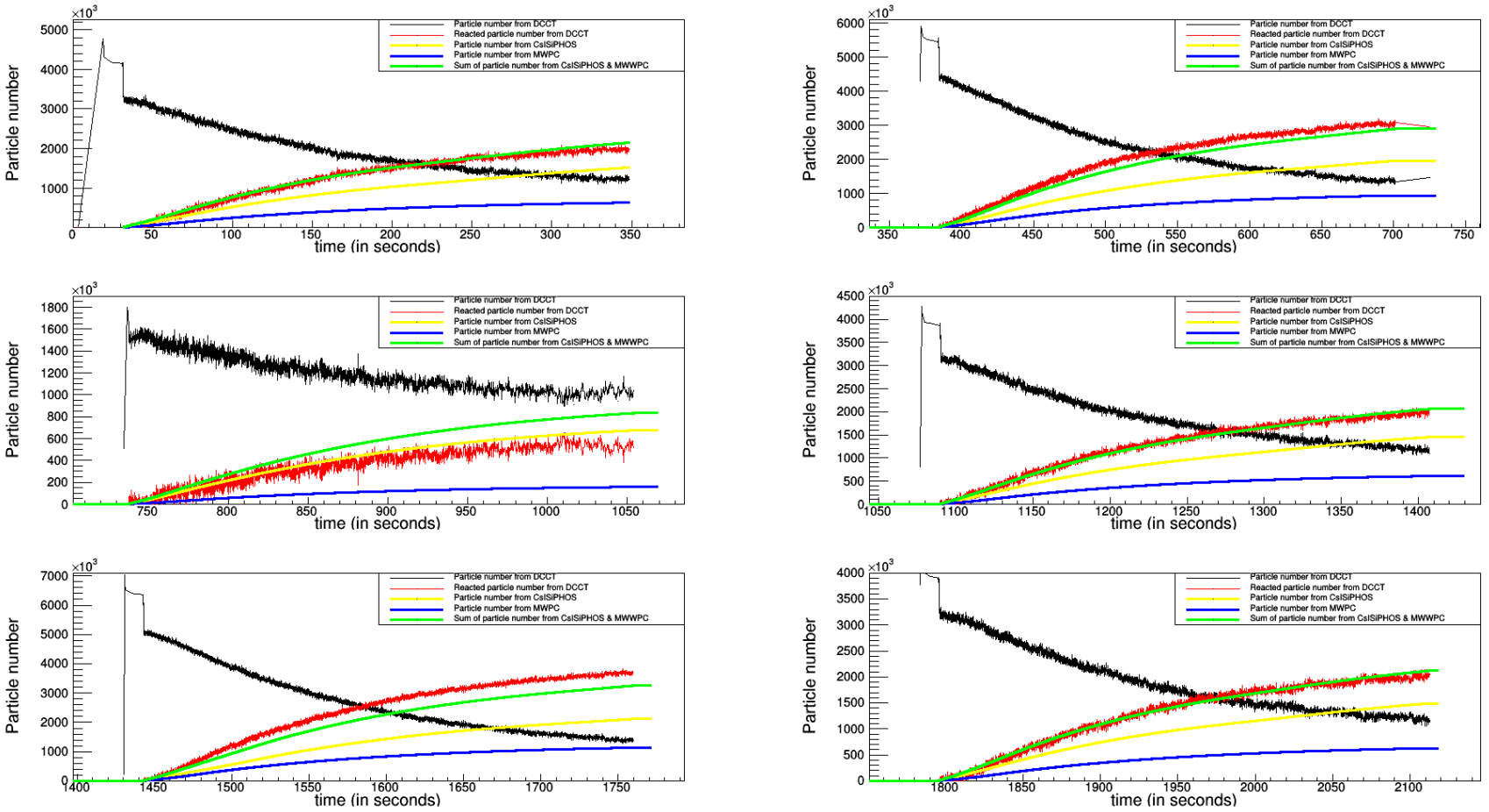

Figure A.8: Particle number measured from CsISiPHOS, MWPC and DCCT for the first six injection measurements.

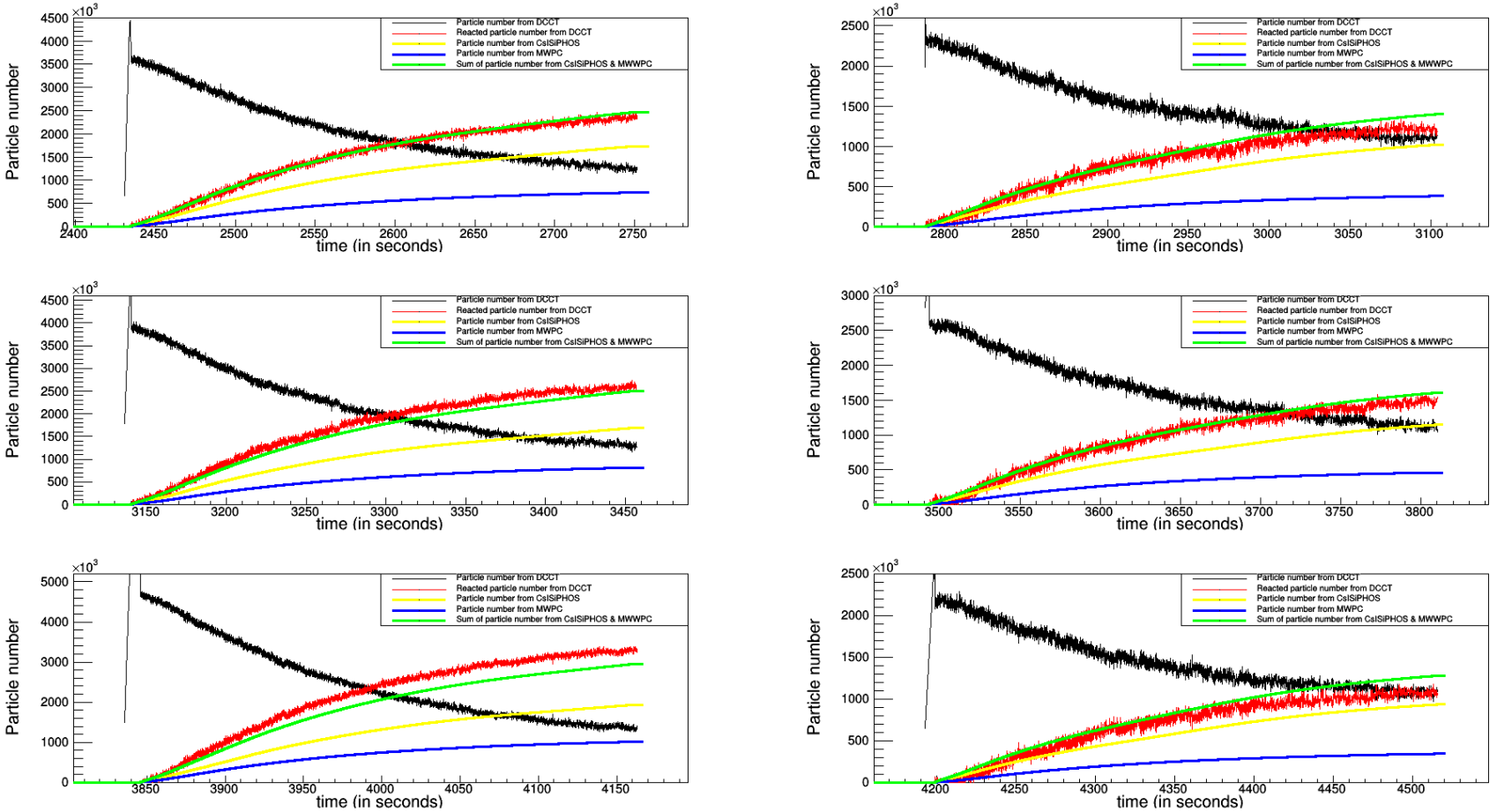

Figure A.9: Particle number measured from CsISiPHOS, MWPC and DCCT from seventh to twelfth injection measurements.

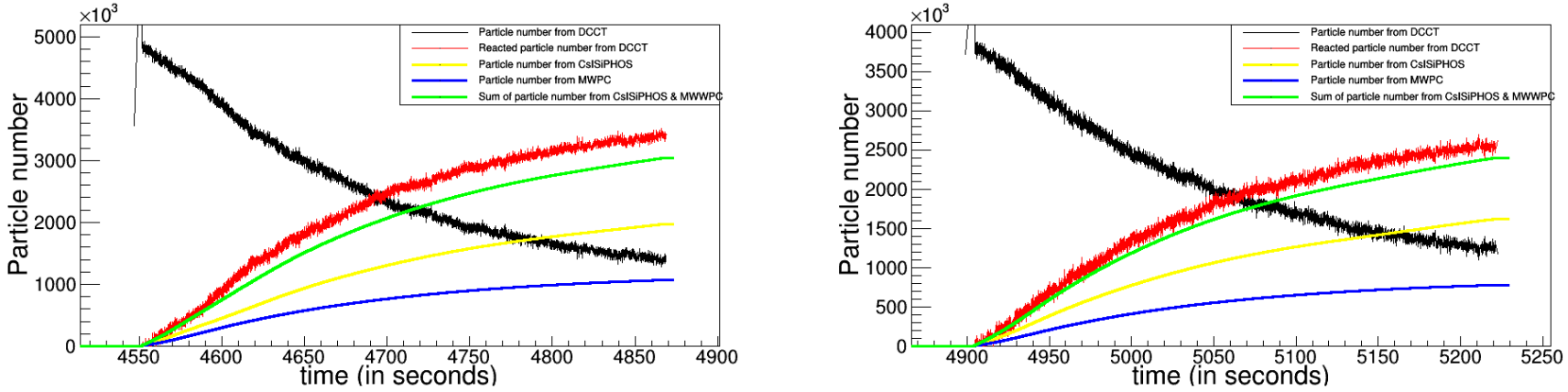

Figure A.10: Particle number measured from CsISiPHOS, MWPC and DCCT for the last two injection measurements.

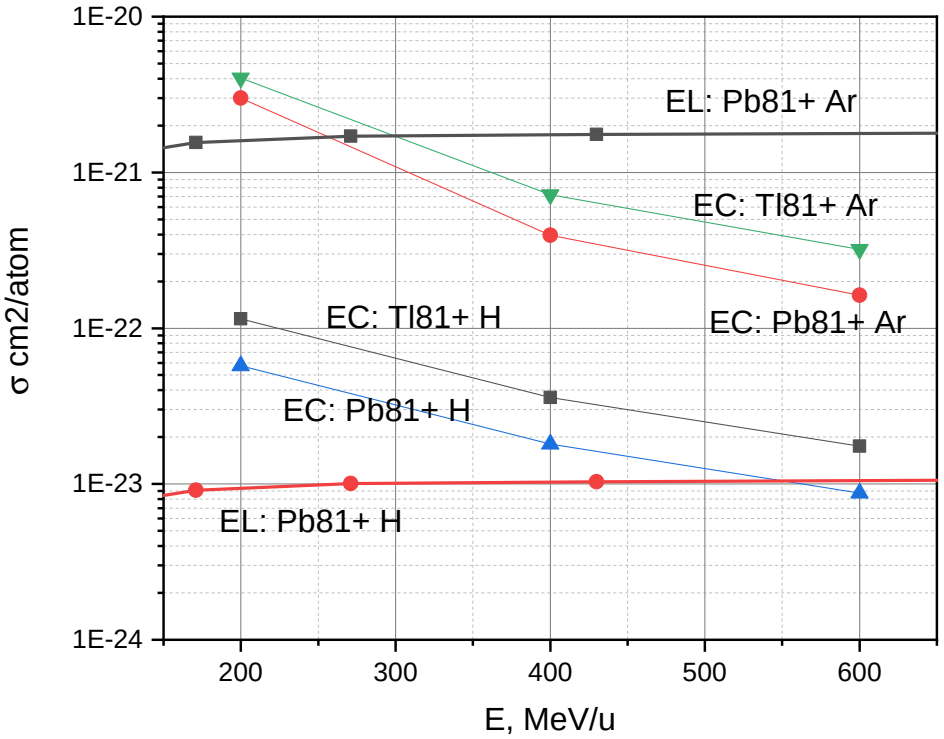

Figure A.11: Ionization (EL) and capture (EC) cross sections for $^{205}Tl^{81+}$ and $^{206}Pb^{81+}$ atoms interacting with hydrogen (H) and argon (Ar) atoms, respectively.
Courtesy: Prof. Dr. V. P. Shevelko.

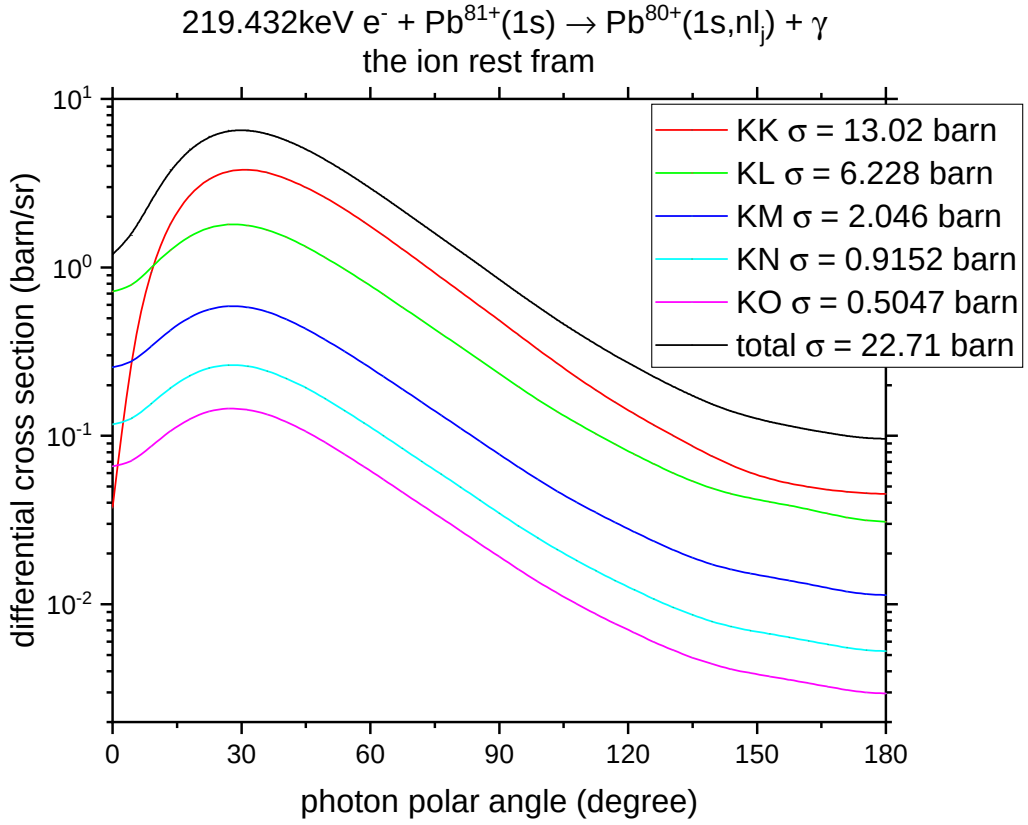

Figure A.12: Radiative Recombination (RR) cross sections for $^{206}Pb^{81+}$ atom at 400 MeV/u.
Courtesy: Dr. Konstantin N. Lyashchenko.

Appendix B

Full Schottky spectrum

Full Schottky spectra are shown for different storage measurement steps during the experiment.

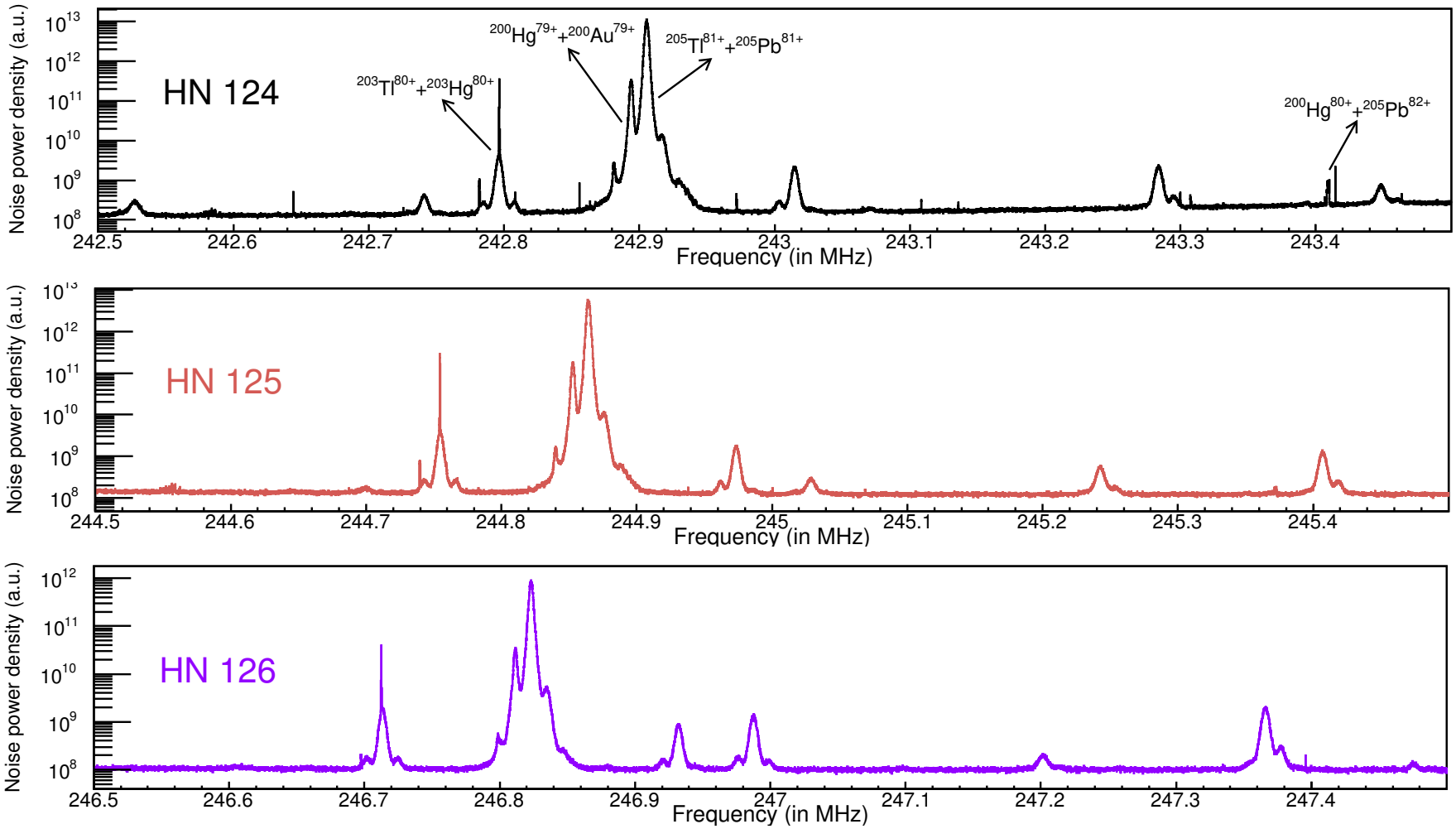

Figure B.1: Full Schottky spectrum at step 1 of the storage measurement.

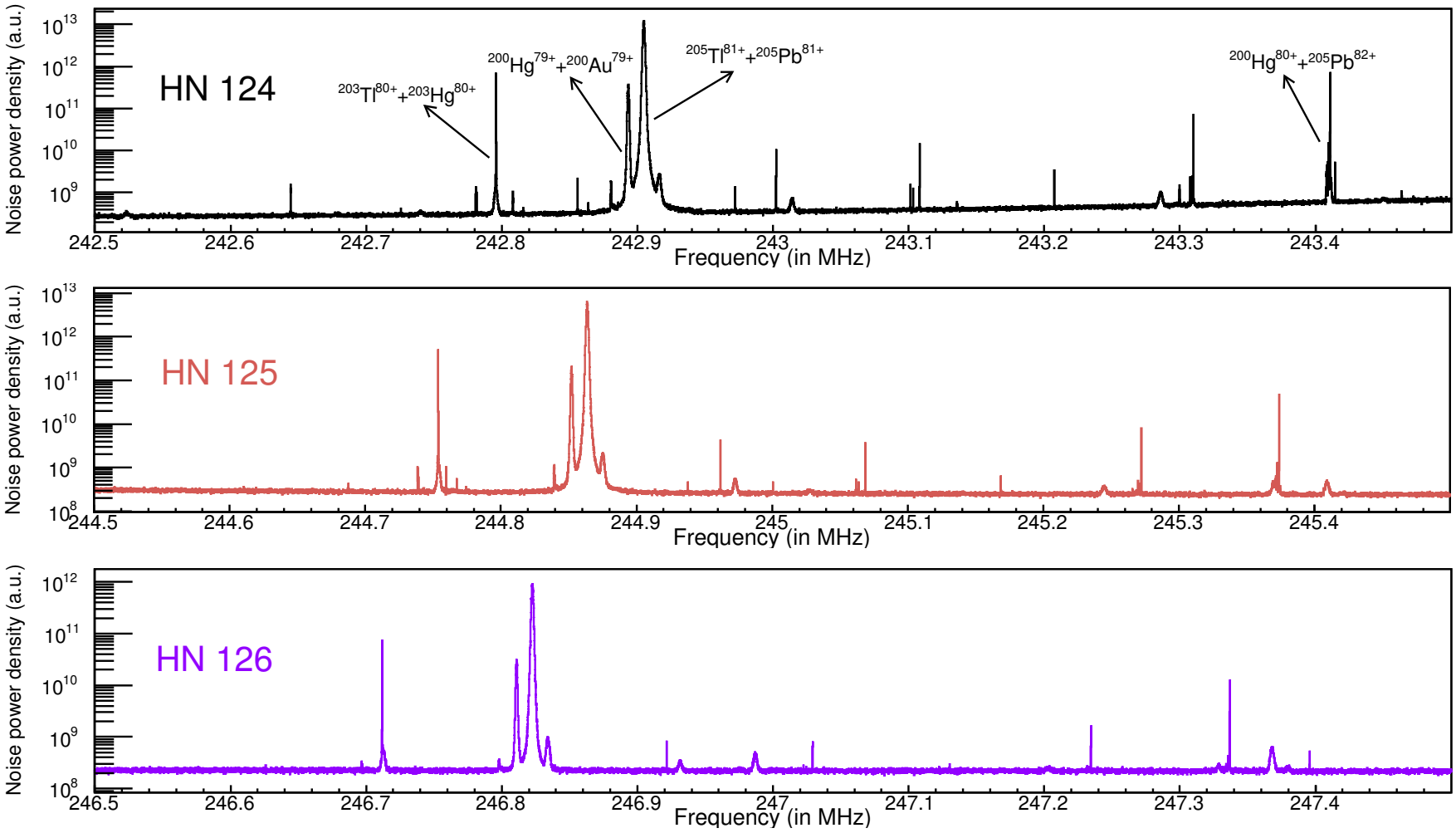

Figure B.2: Full Schottky spectrum at step 2 of the storage measurement.

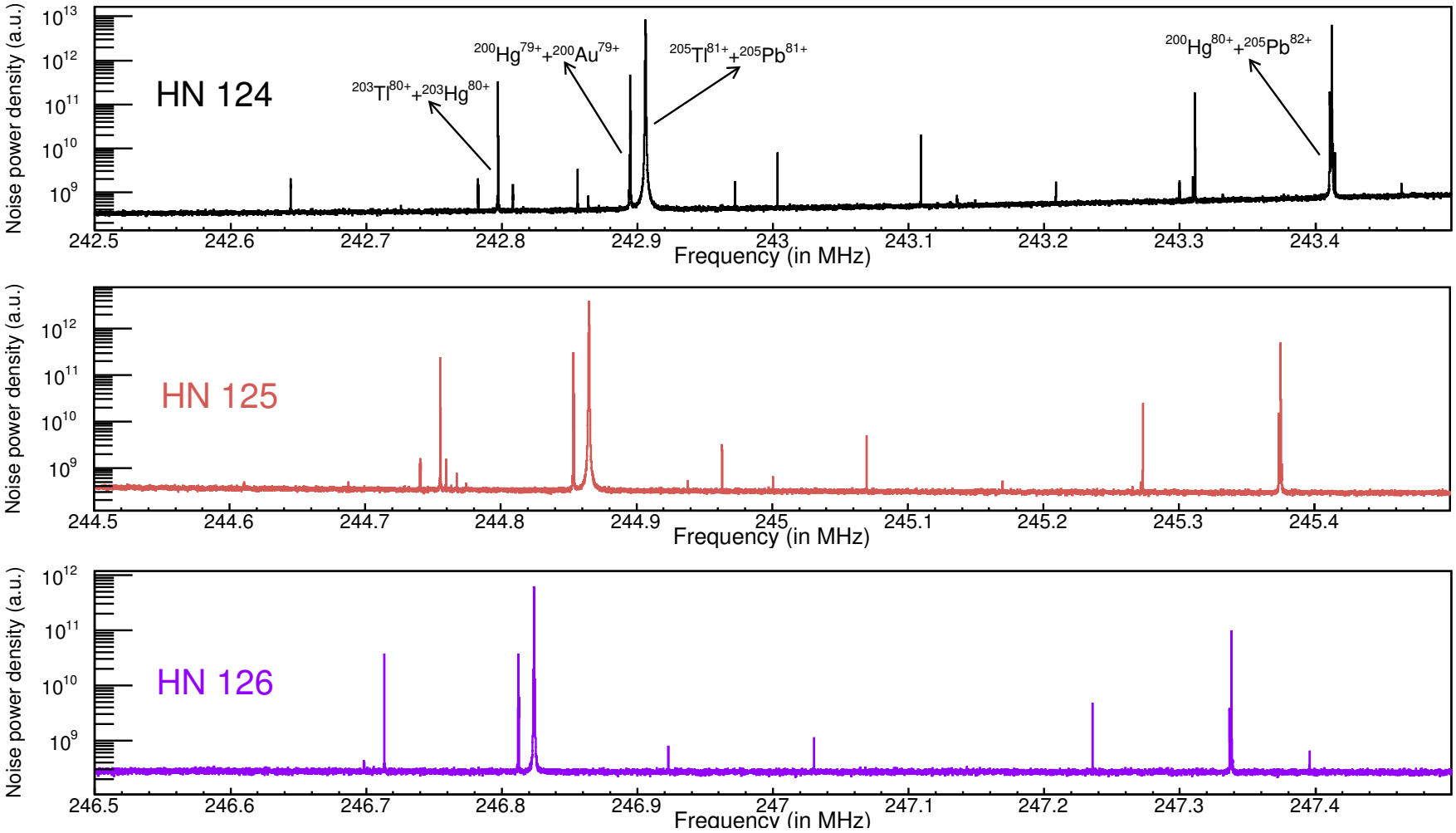

Figure B.3: Full Schottky spectrum at step 3 of the storage measurement.

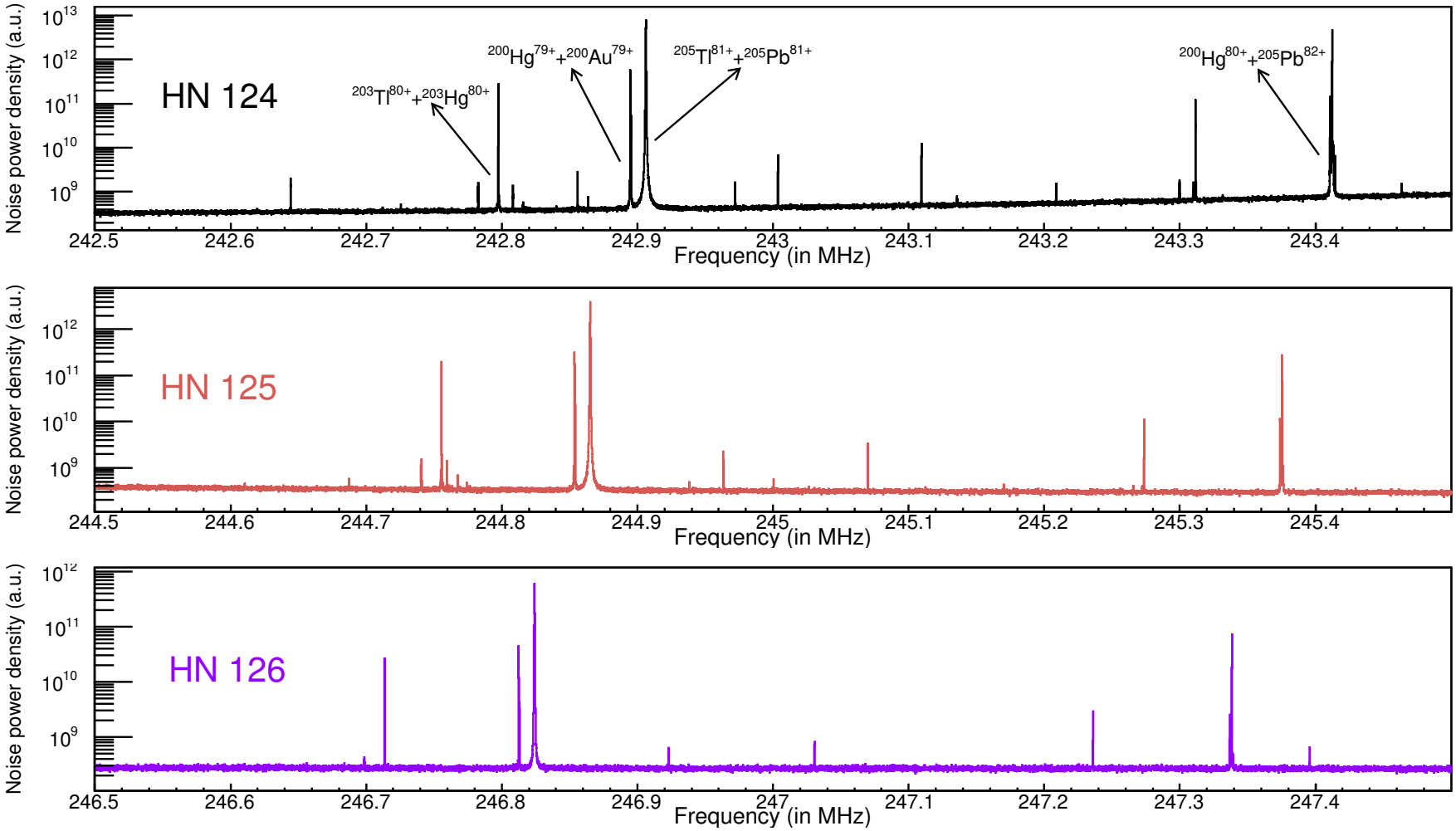

Figure B.4: Full Schottky spectrum at step 4 of the storage measurement.

Appendix C

Experimental settings

During the experiment, many techniques were employed in the ESR. Some of the ESR settings are shown in this Appendix.

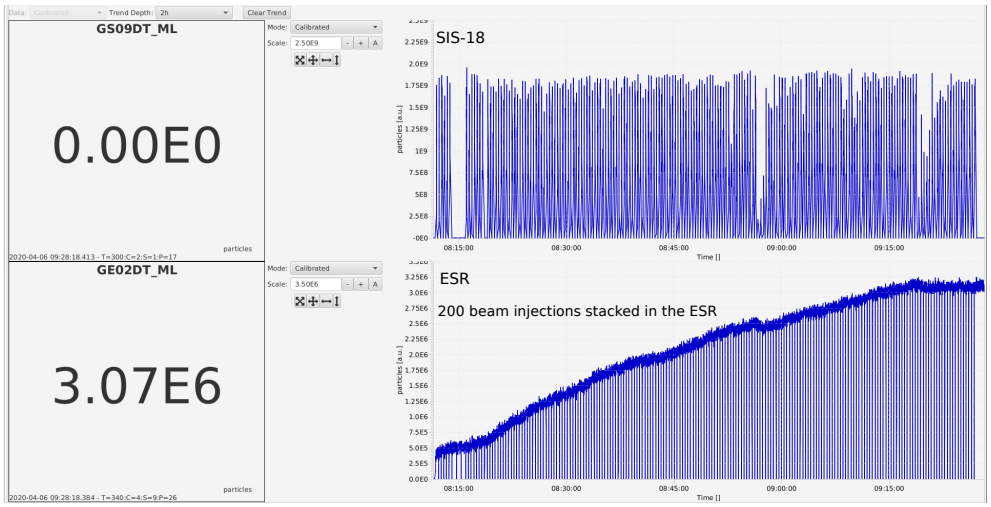

Figure C.1: Stacking of two hundred $^{205}Tl^{81+}$ beam injections in the ESR can be seen. Such a high stacking was achieved for the first time in the ESR.

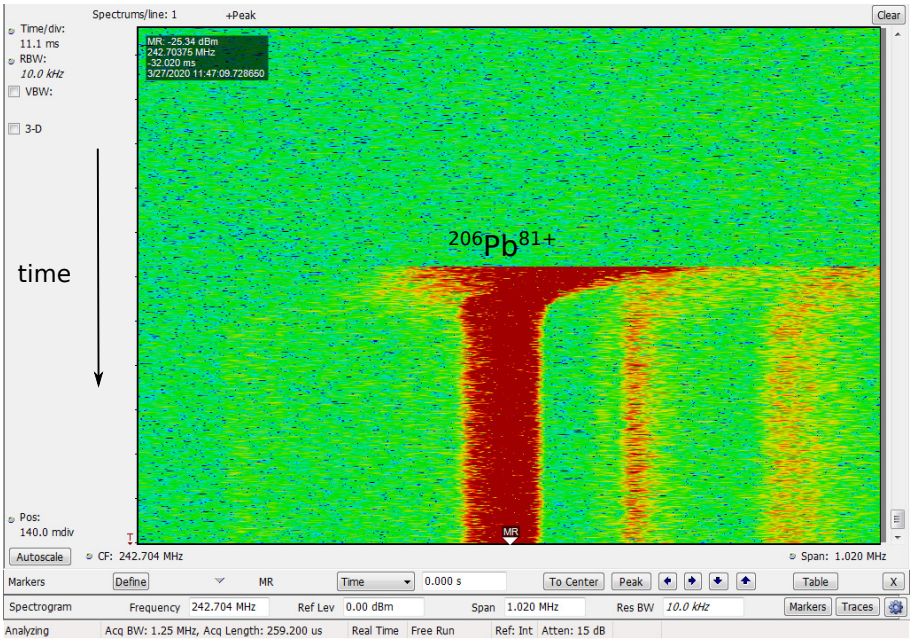

Figure C.2: $^{206}Pb^{81+}$ beam is stochastically cooled in the ESR at 400 MeV/u.

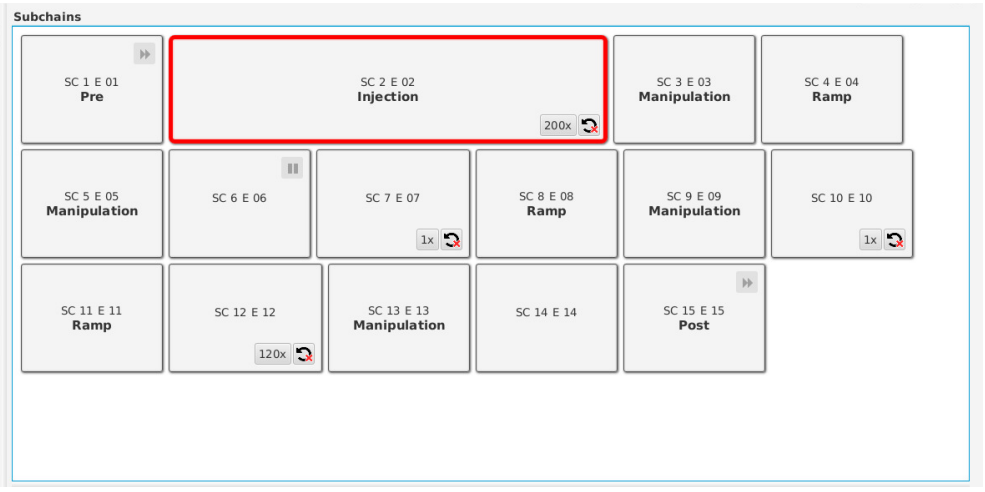

Figure C.3: Above is the ESR pattern with the $^{205}Tl^{81+}$ beam. SC 2: the beam stacking, SC 10: the beam is stored for different storage times, SC 12: the Ar gas jet target is on for 600 s and the rest are the beam manipulation steps.

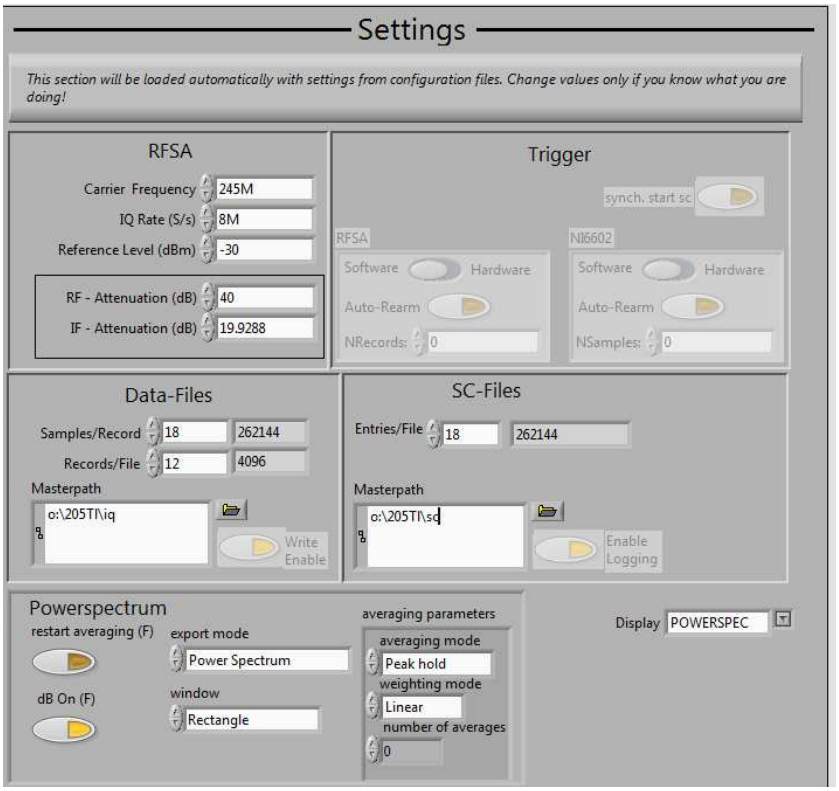

Figure C.4: NTCAP settings during the experiment.

List of Figures

List of Tables

Bibliography

[1] H. Becquerel, Comptes Rendus, **122**, 501, 1896.

[2] G. Gammow, Zeitschrift für Physik, **51**, 204, 1928.

[3] E. Fermi, Zeitschrift für Physik, **88**, 161, 1934.

[4] E. Rutherford, The London, Edinburgh, and Dublin Philosophical Magazine and Journal of Science, **5**, 177, 1903.

[5] E. Rutherford, The London, Edinburgh, and Dublin Philosophical Magazine and Journal of Science, **21**, 669, 1911.

[6] Emil Jan Konopinski, Reviews of Modern Physics, **15**, 209, 1943.

[7] Emil Jan Konopinski, Reviews of Modern Physics, **27**, 254, 1955.

[8] J. Chadwick, Verhandlungen der Deutschen Physikalischen Gesellschaft, **16**, 383, 1914.

[9] B. Pontecorvo, Zh. Eksp. Teor. Fiz., **53**, 1717, 1968.

[10] T. D. Lee and C. N. Yang, Phys. Rev., **104**, 254, 1957.

[11] C. S. Wu *et al.*, Phys. Rev., **105**, 1413, 1957.

[12] S. Weinberg, Phys. Rev., **52**, 134, 1937.

[13] Nathal Severijns *et al.*, Reviews of Modern Physics, **78**, 991, 2006.

[14] K. Nakamura *et al.*, Phys. G: Nucl. Part. Phys., **37**, 07021, 2010.

[15] L. W. Alvarez, Phys. Rev. Lett., **19**, 1264, 1967.

[16] R. Daudel *et al.*, J. Phys. Radium, **8**, 238, 1947.

[17] R. Daudel *et al.*, Comptes Rendus, **224**, 1427, 1947.

[18] R. Daudel *et al.*, Comptes Rendus, **225**, 290, 1948.

[19] K. S. Krane, Introductory Nuclear Physics, John Wiley & Sons, Inc., 1988.

[20] K. Heyde, Basic Ideas and Concepts in Nuclear Physics, Inst. of Phys. Publ., 2004.

[21] C. Iliadis, Nuclear Physics of Stars, WILEY-VCH, 2014.

[22] A. Bohr, B.R. Mottelson, Nuclear Structure, World Scientific Publ., 1998.

[23] J. N. Bahcall, Phy. Rev., **124**, 495, 1961.

[24] M. Jung *et al.*, Phys. Rev. Lett., **69**, 2164, 1992.

[25] M. Jung *et al.*, Nucl. Inst. and Meth. in Phys. Res., A, **553**, 309, 1993.

[26] Yu.A. Litvinov *et al.*, Rep. Progr. Phys., **74**, 016301, 2011.

[27] M. Born *et al.*, Zeitschrift für Physik, **38**, 803, 1926.

[28] T. Ohtsubo *et al.*, Phys. Rev. Lett., **95**, 052501, 2005.

[29] B. Franzke, Nucl. Inst. and Meth. in Phys. Res., B, **24/25**, 18, 1987.

[30] B. Franzke, Physica Scripta, **19**, 1988.

[31] F. Bosch *et al.*, Phys. Rev. Lett., **77**, 5190, 1996.

[32] F. Bosch *et al.*, Physica Scripta, **T156**, 014025, 2013.

[33] Yu. A. Litvinov *et al.*, Reports on Progress in Physics, **74(1)**, 016301, 2011.

[34] https://www.helmholtz.de/forschung/helmholtz-international/europaeische-projekte/saeule-1-excellent-science/erc/consolidatorgrants/astrum/

[35] Yu. A. Litvinov *et al.*, E121 experiment proposal, Measurement of the bound-state beta decay of bare ^{205}Tl ions, GPAC-GSI, 2017.

[36] M. K. Pavićević *et al.*, Nucl. Inst. and Meth. in Phys. Res., A, **895**, 62, 2018.

[37] M. K. Pavićević *et al.*, Nucl. Inst. and Meth. in Phys. Res., A, **621**, 278, 2010.

[38] J. B. Blake *et al.*, Nature, **242**, 98, 1973.

[39] E. G. Adelberger *et al.*, Review of Modern Physics, **83**, 195, 2011.

[40] J. N. Bahcall and R. K. Ulrich, Review of Modern Physics, **60**, 297, 1988.

[41] Till A. Kirsten, Review of Modern Physics, **71**, 1213, 1999.

[42] M. S. Freedman *et al.*, Science, **193**, 1117, 1976.

[43] G. Bellini *et al.*, Nature, **512**, 383, 2014.

[44] M. Agostini *et al.*, Nature, **562**, 505, 2018.

[45] G. R. Huss *et al.*, Geochym. Cosmica Acta, **73**, 4922, 2009.

[46] F. Käppeler *et al.*, Review of Modern Physics, **83**, 157, 2011.

[47] F.-K. Thielemann *et al.*, In Astronomy with Radioactivitiess, 153, Springer, 2011.

[48] B. S. Meyer and D. D. Clayton, Space Science Reviews, **92**, 133, 2000.

[49] G. J. Wasserburg *et al.*, Astroph. J., **466**, L109, 1996.

[50] D. D. Clayton, Astroph. J., **268**, 381, 1983.

[51] R. G. A. Baker, Earth and Planetary Science Letters, **291**, 39, 2010.

[52] J. B. Blake and D. N. Schramm, Astroph. J., **197**, 615, 1975.

[53] K. Yokoi *et al.*, Astron. and Astrophys., **145**, 339, 1985.

[54] K. Takahashi *et al.*, Phys. Rev. C, **36**, 1522, 1987.

[55] K. Takahashi *et al.*, Nucl. Phys. A, **404**, 578, 1983.

[56] X. Campi *et al.*, Phys. Rev. C, **24**, 2199, 1981.

[57] A. S. Goldhaber, Phys. Lett. B, **53**, 306, 1974.

[58] D. R. Napoli *et al.*, Phys. Lett. B, **210**, 61, 1988.

[59] https://www.gsi.de/en/press/media_center

[60] Image by courtesy of Dr. R. M. Alarcon Sanchez, GSI Helmholtzzentrum für Schwerionenforschung, Darmstadt, Germany.

[61] https://web-docs.gsi.de/ weick/epax/

[62] H. Geissel *et al.*, Nucl. Inst. and Meth. in Phys. Res., B, **70**, 286, 1992.

[63] H. Geissel *et al.*, Phys. Rev. Lett., **68**, 3412, 1992.

[64] N. Iwasa *et al.*, Nucl. Inst. and Meth. in Phys. Res., B, **126**, 284, 1997.

[65] https://web-docs.gsi.de/ weick/mocadi/

[66] Markus Steck, Yuri A.Litvinov, Progress in Particle and Nuclear Physics, **115**, 103811, 2020.

[67] Helmut Wiedemann, Particle Beams and Phase Space, Springer International Publishing, 2015.

[68] M. Steck *et al.*, Nucl. Inst. and Meth. in Phys. Res., A, **532**, 357, 2004.

[69] M. Steck *et al.*, Phys. Rev. Lett., **77**, 3803, 1996.

[70] M. A. Najafi *et al.*, Nucl. Inst. and Meth. in Phys. Res., A, **836**, 1, 2016.

[71] O. Klepper *et al.*, Nucl. Inst. and Meth. in Phys. Res., B, **204**, 553, 2003.

[72] F. Nolden *et al.*, Nucl. Inst. and Meth. in Phys. Res., A, **659**, 69, 2011.

[73] https://fair-center.eu/for-users/experiments/nustar/experiments/ilima.html

[74] https://fair-center.eu/

[75] FAIR GmbH, GSI,Green Paper, The Modularized Start Version: FAIR Facility for Antiproton and Ion Research, GSI-2013-04816, Darmstadt, Germany (2009).

[76] A. Dolinskii *et al.*, Proceedings of the COOL'07 conference, 2007.

[77] M. S. Sanjari, Resonant pickups for non-destructive single-particle detection in heavy-ion storage rings and first experimental results, PhD Thesis, Johann Wolfgang Goethe-Universität, 2013.

[78] ZANG Yong-Dong *et al.*, Chinese Physics C, **35**, 1124, 2011.

[79] F. Caspers, Schottky signals for longitudinal and transverse bunched-beam diagnostics, in CAS - CERN Accelerator School: Course on Beam Diagnostics, CERN, 2009.

[80] F. Nolden *et al.*, Proc. COOL05, AIP Conf. Proc., **821**, 211, 2006.

[81] F. Nolden, Proc. COOL09, 123, 2009.

[82] C. Trageser *et al.*, Physica Scripta, **T166**, 014062, 2015.

[83] C. Trageser, Aufbau einer Datenaufnahme zur Integration von Schottky-Signalen in Atomphysikexperimenten an Speicherringen, PhD Thesis, Justus-Liebig-Universität Gießen, 2018.

[84] https://www.ni.com/pdf/product-flyers/pxi-vector-signal-analyzers.pdf

[85] H. Reeg *et al.*, GSI Scientific Report '90, Darmstadt, March 1991.

[86] http://web-docs.gsi.de/ weick/atima/

[87] http://lise.nscl.msu.edu/lise.html

[88] Richard G. Lyons, Understanding digital signal processing, Pearson Education, Inc., 2011.

[89] B. Schlitt, Schottky Mass Spectroscopy at the Heavy Ion Storage Ring ESR, PhD Thesis, Ruprecht-Karls-Universität, 1997.

[90] Nikolaos Petridis, The internal multiphase target for storage ring experiments, PhD Thesis, Johann Wolfgang Goethe-Universität, 2014.

[91] https://indico.gsi.de/event/9673/

[92] Yu. A. Litvinov *et al.*, Nucl. Inst. and Meth. in Phys. Res., B, **317**, 603, 2013.

[93] Yu. A. Litvinov *et al.*, Nucl. Phys. A, **756**, 3, 2005.

[94] F. Bosch *et al.*, Reports on Progress in Physics, **73**, 84, 2013.

[95] Y. H. Zhang *et al.*, Physica Scripta, **91(7)**, 073002, 2016.

[96] J. Glorius *et al.*, Phys. Rev. Lett., **122**, 092701, 2019.

[97] Th. Stöhlker *et al.*, Phys. Rev. Lett., **85**, 3109, 2000.

[98] A. Gumberidze *et al.*, Phys. Rev. Lett., **94**, 223001, 2005.

[99] M. Lestinsky *et al.*, Eur. Phys. J. Special Topics, **225**, 797, 2016.

[100] F. Bosch *et al.*, EPJ Web of Conferences, **123**, 04003, 2016.

List of Publications

1. Ragandeep Singh Sidhu, J. Glorius, Yu. A. Litvinov, M. K. Pavićević, M. S. Sanjari, T. Stöhlker, and the ILIMA, SPARC, LOREX, and NucAR Collaborations, Electroweak Decays of Highly Charged Ions, EPJ Web of Conferences, **178**, 01003, 2018.

2. F. C. Ozturk *et al.*, New test of modulated electron capture decay of hydrogen-like ^{142}Pm ions: Precision measurement of purely exponential decay, Physics Letters B, **797**, 134800, 2019.

3. R. S. Sidhu, R. J. Chen, Yu. A. Litvinov, Y. H. Zhang, and the FRS-ESR Collaboration, Revisiting the Analysis of the Isochronous Mass Measurements of Uranium Fission Fragments at the ESR, EPJ Web of Conferences, **227**, 02012, 2020.

4. X. Zhou *et al.*, In-ring velocity measurement for isochronous mass spectrometry, Physical Review Accelerators and Beams, **24**, 042802, 2021.

In addition, Chapters 6 and 7 summarize the new results obtained in this work by the author for the first time.

Acknowledgments

Here, I would like to express my deep gratitude to all the people who supported and helped me during my PhD journey.

First of all, I am grateful to my Doktorvater Prof. Dr. Yuri A. Litvinov who gave me the best opportunity to do my PhD thesis at GSI. I am thankful for the wealth of experience I could gather about everyday science and life during the past years. Yuri, your enthusiasm for storage rings is infectious, it created a wonderful learning environment for me to grow and gave me a lot of motivation. I thank you for the encouragement and the intellectual freedom which you have provided me during the past years.

I am thankful to Prof. Dr. Klaus Blaum who agreed to be my second thesis advisor. You were just a zoom away whenever I needed your help. Klaus, you have taught me how excellence and hard work can do magic in science. I am grateful to you for your guidance and for teaching me the ion trap physics. You have always been and will be an inspiration for me and for this invaluable experience, I am deeply thankful.

I am thankful to Prof. Dr. Adriana Pálffy who kindly agreed to be the second referee for the thesis and to Prof. Dr. André Butz who kindly agreed to be one of the examiners.

I would not have accomplished this work without the help and support of Dr. Rui-Jiu Chen. Many thanks for accompanying me through the last three and a half years. Your patience to carry out this project together is applaudable.

I am thankful to Dr. Jan Glorius and Dr. Pierre-Michel Hillenbrand from whom I learned a lot about particle detectors. I want to thank Dr. Shahab Sanjari, Prof. Dr. Robert Grisenti and Dr. Nikos Petridis for helping with the Schottky detector and the gas jet target. I am thankful to Prof. Dr. V. P. Shevelko and Dr. Konstantin N. Lyashchenko for providing the theoretical calculations which are used in this work.

I owe my thanks to the FRS-ESR team, Dr. Markus Steck, Dr. Helmut Weick, Dr. Sergey Litvinov, Dr. Ronald Joseph, Dr. Ulrich Popp, and other members who helped to provide a stable ring operation for the experiment.

I want to thank Prof. Dr. Paolo Giubellino for providing an excellent and world-class research platform at GSI. Your visits to HKR during the beam

time were encouraging. I am grateful to Prof. Dr. Thomas Stöhlker, an outstanding group leader for hosting me in the Atomic Physics department. I also want to thank Prof. Dr. H.-J. Kluge for the joyful weekend physics and life discussions we had. I would like to thank the people of the AP who made it a pleasure to work at GSI. I want to thank Prof. Dr. Thomas Faestermann, Prof. Dr. Wolfgang Quint, Prof. Dr. Phil Woods, Prof. Dr. Iris Dillmann, Prof. Dr. René Reifarth, Prof. Dr. Wolfram Korten, Prof. Dr. Hans Geissel, Prof. Dr. Christoph Scheidenberger, Prof. Dr. Taka Yamaguchi, Prof. Dr. M. K. Pavićević, Prof. Dr. G. Amthauer, Prof. Dr. Beatriz Jurado, Prof. Dr. Roman Gernhäuser, Prof. Dr. Wilfried Nörtershäuser, Dr. Alexandre Gumberidze, Dr. Zoran Andelkovic, Dr. Michael Lestinsky, Dr. Rodolfo Sánchez, Dr. Carlo Bruno, Dr. Uwe Spillmann, Dr. Frank Herfurth, Dr. Günter Weber, Dr. S. Trotsenko, Dr. Gleb Vorobjev, Dr. Tatiana Litvinova, Lea Wunderlich and all the other members of the AP department at GSI. I would also like to acknowledge all the collaborators with whom I have worked.

I grateful to Prof. Dr. Yuhu Zhang, Prof. Dr. Meng Wang, Dr. Rui-Jiu Chen, Dr. Yuanming Xing, X. Zhou and colleagues at the Institute of Modern Physics (IMP) for inviting me to Lanzhou in December 2018 and 2019 and for their hospitality. Special thanks to Prof. Dr. Yuri A. Litvinov for providing DAAD funds for the visits.

This thesis work has received funding from the European Research Council (ERC) under the EU Horizon 2020 research and innovation programme (ERC CG 682841 "ASTRUm"). I am thankful to Prof. Dr. Yuri A. Litvinov for providing me funding via this project. I also want to thank HGSFP and HGS-HIRe graduate schools for the perfect coordination of courses and the structured PhD tenure. I am indebted to Stiftung Giersch for honoring with the Giersch-Excellence-Grant 2020.

I would like to thank my fellow Phd's Dmytro Dmytriiev, László Varga, Ivan Kulikov, Esther Menz and Kanika with whom I have shared my PhD journey. I would like to say a big "thank you" to my friend Tayyab who made my life in Germany so pleasant. Special thanks to my friends Saakshi, Shaifali and the RARARAA who were always there for me.

Last but not least, I would like to thank my parents Late S. Rukmani Devi and S. Harjit Singh Sidhu. Today I stand tall because of your immense sacrifices. I miss you Mom and I hope that you will be proud to see me from heaven. I am grateful to the Almighty who has always blessed me with the best. I would like to thank Amrit, Meelu Di and all my family members.